NASA TECHNICAL NOTE

NASA TN D-8039

c.1

NASA TN D-8039

THE EFFECTS ON PROPULSION-INDUCED AERODYNAMIC FORCES OF VECTORING A PARTIAL-SPAN RECTANGULAR JET AT MACH NUMBERS FROM 0.40 TO 1.20

Francis J. Capone

Langley Research Center
Hampton, Va. 23665

NATIONAL AERONAUTICS AND SPACE ADMINISTRATION • WASHINGTON, D. C. • DECEMBER 1975

1. Report No. NASA TN D-8039	2. Government Accession No.	3. Recipient's Catalog No.

4. Title and Subtitle THE EFFECTS ON PROPULSION-INDUCED AERODYNAMIC FORCES OF VECTORING A PARTIAL-SPAN RECTANGULAR JET AT MACH NUMBERS FROM 0.40 TO 1.20	5. Report Date December 1975
	6. Performing Organization Code
7. Author(s) Francis J. Capone	8. Performing Organization Report No. L-10352
	10. Work Unit No. 505-04-11-01
9. Performing Organization Name and Address NASA Langley Research Center Hampton, Va. 23665	11. Contract or Grant No.
	13. Type of Report and Period Covered Technical Note
12. Sponsoring Agency Name and Address National Aeronautics and Space Administration Washington, D.C. 20546	14. Sponsoring Agency Code

15. Supplementary Notes

16. Abstract

An investigation has been conducted in the Langley 16-foot transonic tunnel to determine the induced lift characteristics of a vectored-thrust concept in which a rectangular jet-exhaust nozzle was located in the fuselage at the wing trailing edge. The effects of nozzle deflection angles of 0° to 45° were studied at Mach numbers from 0.4 to 1.2, at angles of attack up to 14°, and with thrust coefficients up to 0.35. Separate force balances were used to determine total aerodynamic and thrust forces as well as thrust forces which allowed a direct measurement of jet turning angle at forward speeds. Wing pressure loading and flow characteristics using oil-flow techniques were also studied. The Reynolds number per meter varied from 8.20×10^6 to 13.12×10^6.

17. Key Words (Suggested by Author(s)) Vectored thrust Induced lift Rectangular nozzle Transonic	18. Distribution Statement Unclassified – Unlimited Subject Category 02

19. Security Classif. (of this report) Unclassified	20. Security Classif. (of this page) Unclassified	21. No. of Pages 249	22. Price* $7.50

*For sale by the National Technical Information Service, Springfield, Virginia 22161

THE EFFECTS ON PROPULSION-INDUCED AERODYNAMIC FORCES OF VECTORING A PARTIAL-SPAN RECTANGULAR JET AT MACH NUMBERS FROM 0.40 TO 1.20

Francis J. Capone
Langley Research Center

SUMMARY

An investigation has been conducted in the Langley 16-foot transonic tunnel to determine the induced lift characteristics of a vectored-thrust concept in which a rectangular jet-exhaust nozzle was located in the fuselage at the wing trailing edge. The effects of nozzle deflection angles of 0° to 45° were studied at Mach numbers from 0.4 to 1.2, at angles of attack up to 14°, and with thrust coefficients up to 0.35. Separate force balances were used to determine total aerodynamic and thrust forces as well as thrust forces which allowed a direct measurement of jet turning angle at forward speeds. Wing pressure loading and flow characteristics using oil-flow techniques were also studied. The Reynolds number per meter varied from 8.20×10^6 to 13.12×10^6.

The results indicate that significant increases in thrust-induced lift up to Mach number 0.95 and substantial decreases in drag up to Mach number 1.20 were achieved during the vectoring operation. A lift-augmentation factor of 4.15 was reached with 45° nozzle deflection at a Mach number of 0.90 with an angle of attack of 0°. The overall ability of this vectored-thrust model to increase lift and to reduce drag for all the deflected nozzles was generally maintained up to a Mach number of 0.9 and to angles of attack where flow-separation effects dominate. Deflection of the jet was instrumental in reducing afterbody flow separation at Mach numbers of 0.9 and 0.95.

INTRODUCTION

Supercirculation effects induced from thrust vectoring have indicated a potential both for improving cruise performance and for increasing maneuverability of fighter aircraft (refs. 1 to 4). The experimental studies of references 1 to 3 used a vectorable rectangular exhaust nozzle located in the fuselage of the aircraft at the wing trailing edge. The effect of the exhaust is similar to that of a jet flap and induces lift caused by supercirculation. In contrast to the jet flap, this concept permits the use of all the engine exhaust to simulate the jet flap, avoids ducting through the wing, and limits mechanical articulation of the exhaust nozzles. Two-dimensional jet-flap results (refs. 5 to 7) have been applied to an advanced fighter configuration (ref. 8); large lift gains were obtained. However, any fighter configuration would require that the engine supply an adequate mass flow for the operation of jet flaps in the wings. Given in reference 9 is an indication of the potential problems associated with bleeding fan-jet engines to provide the exhaust gases for jet flaps.

The vectored-thrust concept originally proposed in references 1 and 2 utilized a highly swept wing (66.8°). Two advantages were cited: (1) the aerodynamic center could be placed at the nozzle exit and (2) improved lift augmentation was anticipated with the outboard panels of the highly swept wing placed in a stronger induced upwash field created by the deflected jet. However, the results of reference 1 indicated that most of the induced lift was developed on the inboard portion of the wing panels forward of the nozzle exit.

Consequently, the design philosophy for the model of the present investigation was to choose a configuration with a wing planform and airfoil thickness ratio typical of current high-performance twin-engine fighter airplanes. A canard could be used to trim the jet-induced pitching moments.

Reference 3 summarizes a parametric investigation that included a study of the effects of the nozzle deflection angle, nozzle exit location, nozzle shape, and wing camber on the aerodynamic characteristics of a wing-afterbody configuration. This report presents detailed information from that investigation on the effects of varying the nozzle deflection angle from 0° to 45°. The investigation was conducted in the Langley 16-foot transonic tunnel at Mach numbers from 0.4 to 1.2, at angles of attack up to 14°, and at thrust coefficients up to 0.35. The average Reynolds number per meter varied from 8.20×10^{6} to 13.12×10^{6}.

SYMBOLS

Model forces and moments are referred to the axis system shown in figure 1 with the model moment-reference center located at $0.25\bar{c}$, the point which corresponds to fuselage station 117.64 cm. A discussion of the data-reduction procedure and definitions of the aerodynamic force and moment terms and propulsion relationships used herein are given in appendixes A and B. All aerodynamic coefficients are nondimensionalized with respect to $q_{\infty}S$ or $q_{\infty}S\bar{c}$ except at static conditions where p_a is substituted for q_{∞}.

A_{base}	total cross-sectional area at nozzle exit including vane and nozzle base area, 78.513 cm^2
A_e	exhaust nozzle exit area, 51.322 cm^2
A_{max}	maximum cross-sectional area of afterbody, 284.784 cm^2
A_n	total exit area for eight sonic air-supply nozzles, 3.433 cm^2
$A\!\!R$	wing aspect ratio, 3.0
A_{seal}	cross-sectional area enclosed by seal strip, 266.000 cm^2
b	span, 88.32 cm
C_A	axial-force coefficient (fig. 1 and appendix A)
C_D	drag coefficient (fig. 1 and appendix A)
$C_{D,i}$	induced drag coefficient (eq. (A14), appendix A)
$C_{D,min}$	average jet-off minimum drag coefficient determined from several data runs for all nozzles tested
$C_{(F-A)}$	thrust-minus-axial-force coefficient (fig. 1)
$C_{(F-D)}$	thrust-minus-drag coefficient (fig. 1)
$C_{F,j}$	nozzle thrust coefficient along tailpipe center line (fig. 1)
C_L	total lift coefficient (fig. 1)
$C_{L,j}$	jet lift coefficient (fig. 1)
$C_{L,o}$	jet-off lift coefficient
$(C_{L,o} + C_{L,\Gamma})_M$	lift corresponding to $C_{D,min}$

C_{L_α}	lift-curve slope per degree
$C_{L,\Gamma}$	jet-induced supercirculation lift coefficient
ΔC_L	incremental lift, $C_{L,\Gamma} + C_{L,j}$
C_m	total pitching-moment coefficient (fig. 1)
$C_{m,j}$	jet pitching-moment coefficient (fig. 1)
C_N	normal-force coefficient (fig. 1)
$C_{N,j}$	jet normal-force coefficient
$C_{N,o}$	jet-off normal-force coefficient
$C_{N,\Gamma}$	jet-induced supercirculation normal-force coefficient
C_p	wing pressure coefficient, $\frac{p_l - p_\infty}{q_\infty}$
$C_{p,aft}$	afterbody pressure coefficient
$C_{p,cr}$	critical pressure coefficient adjusted for wing sweep
C_T	gross thrust coefficient along jet axis (fig. 1)
$C_{T,i}$	ideal isentropic gross thrust coefficient
c	local chord, cm
$\bar{c}$	mean geometric chord, 32.28 cm
c'	average wing chord, 29.44 cm
$c_{d,c}$	effective discharge coefficient
c_n	wing section normal-force coefficient
e	wing efficiency factor at jet-off conditions

F_A	axial force, N
$F_{A,mom}$	momentum tare force due to bellows, N
$F_{A,Mbal}$	axial force measured by main balance along main balance axis, N
$F_{A,Tbal}$	axial force measured by thrust balance along thrust-balance axis, N
F_i	ideal isentropic gross thrust, N
$F_{i,c}$	total ideal isentropic gross thrust determined using chamber mass-flow rate, N
$F_{i,con}$	ideal convergent nozzle thrust, N
$F_{i,p}$	total ideal isentropic gross thrust determined using measured mass-flow rate, N
F_j	thrust component along tailpipe or body axis, N
FS	fuselage station, cm
G	gain factor (eq. (A12), appendix A)
l	length of model, 138.68 cm
M	Mach number
$\dot{m}_c$	chamber mass-flow rate, kg/sec
$\dot{m}_i$	ideal mass-flow rate, kg/sec
$\dot{m}_p$	measured mass-flow rate, kg/sec
N_{Re}	Reynolds number per meter
p_a	ambient pressure, N/m^2
p_c	chamber pressure measured in supply pipe, N/m^2

$\bar{p}_{es}$	average static pressure at external seal, N/m^2
$\bar{p}_i$	average internal static pressure, N/m^2
p_l	local static pressure, N/m^2
$p_{t,j}$	average jet total pressure, N/m^2
p_∞	free-stream static pressure, N/m^2
q_∞	free-stream dynamic pressure, N/m^2
R	gas constant (for $\gamma = 1.4$), 287.3 N-m/kg-K
S	wing reference area including projection to model center line, 2599.89 cm^2
T_c	chamber temperature, K
T_{rec}	thrust recovery (eq. (A13), appendix A)
T_t	free-stream stagnation temperature, K
$T_{t,j}$	jet total temperature, K
w	half-width of body, 11.43 cm
X	afterbody length (fig. 8), 24.82 cm
x,y,z	body or wing ordinate, cm
α	angle of attack (fig. 1), deg
α_{jo}	jet-off angle of attack, deg
α_n	angle of attack of tailpipe center line (fig. 1), deg
γ	ratio of specific heats, 1.40 for air

δ	effective jet turning angle, deg
δ_d	design or nominal nozzle deflection angle, deg

APPARATUS AND PROCEDURE

Model

A sketch showing the external geometry of the model is presented in figure 2(a); photographs are shown in figure 2(b). The wing had a leading-edge sweep of 50°, streamwise NACA 64A406 airfoil sections, an aspect ratio of 3.0, taper ratio of 0.3, and a reference area of 2599.89 cm^2. The wing had no twist or dihedral.

The fuselage had rectangular cross sections with rounded corners and had an effective fineness ratio of 7.28. As shown in figure 3, the body lines were chosen in order to enclose the internal propulsion system and to fair into the afterbody enclosing the nozzles. The afterbody boattail angle was 12.5°. The maximum width and height of the body were 22.86 cm and 12.7 cm, respectively, and the maximum body cross-sectional area was 284.78 cm^2. Table I presents ordinates for both the fixed nonmetric forebody and the metric afterbody. A 0.16-cm annular gap between the forebody and afterbody was required to prevent fouling between the nonmetric and metric portions of the model. A flexible Teflon strip inserted into slots was used as a seal to prevent internal flow in the model. (See fig. 3.) The low coefficient of friction of Teflon minimized restraint between the metric and nonmetric portions of the model. Only that portion of the configuration aft of the metric break at fuselage station 99.06 cm was supported by the main-force balance and hereafter is referred to as the wind-tunnel model.

Twin-Jet Propulsion Simulation System and Exhaust Nozzles

A sketch of the twin-jet propulsion simulation system is presented in figures 3 and 4; photographs without the force balances are shown in figure 5. Appendix B presents the method for analysis and results of static tests to determine the propulsion system internal-performance characteristics.

An external high-pressure air system provides a continuous flow of clean, dry air at a controlled temperature of about 306 K. This high-pressure air is brought through the support strut by six tubes into a high-pressure chamber. (See fig. 3.) Here the air is divided into two separate flows and is passed through flow-control valves. These manually operated valves are used to balance the exhaust nozzle total pressure in each duct. As shown in figure 4, the air in each supply pipe is then discharged perpendicularly to the model axis through eight sonic nozzles equally spaced around the supply pipe.

This method is designed to eliminate any transfer of axial momentum as the air is passed from the nonmetric to metric portion of the model. Two flexible metal bellows are used as seals and serve to compensate for the axial forces caused by pressurization. The cavity between the supply pipe and bellows is vented to the model internal pressure. The tailpipes are connected to the thrust balance, whose loads are then transmitted to the main balance through the wing and thrust-balance support block. (See fig. 3.)

The air is then passed through the tailpipes to the exhaust nozzles as shown in figure 6. A transition section, located between fuselage stations 122.44 cm and 124.97 cm, was used to transform the exhaust flow from axisymmetric to two dimensional. The nozzle internal cross-sectional area was held constant from fuselage stations 126.75 cm to 134.62 cm. Four sets of nozzles, each with a total exit area of 50.322 cm^2 at fuselage station 138.62 cm, were investigated with design turning angles of 0°, 15°, 30°, and 45° as defined by δ_d in figure 6. The aspect ratio of the twin nozzles was 5.99°; the nozzle aspect ratio is defined as the maximum nozzle width divided by the maximum depth including vanes. Nozzle mass-flow and static force and moment characteristics are shown in figures 7 and 8, respectively. The variation of measured thrust coefficient with nozzle pressure ratio is given in figure 9.

Thrust vectoring was obtained by using circular-arc turning vanes located in the nozzle exhaust flow. These turning vanes were arranged so that they would be completely washed by the jet flow in order to minimize the influence of the external flow on vectored nozzle performance. Initially, these turning vanes were constructed with the vanes faired smooth to a point as shown in the following sketch:

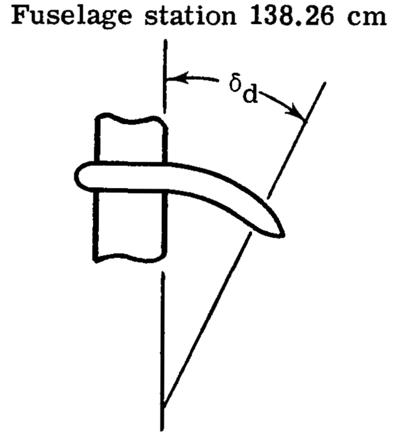

However, static tests with the 30° nozzle indicated an effective turning angle that varied from 22° at low nozzle pressure ratio to about 56° at maximum pressure ratio. This turning was largely influenced by Coanda turning of the jet flow over the sharp curvature at the end of the vanes. (The angle of vane tip on top was approximately 60°.) One design objective was to use nozzles which had a constant static turning angle over the pressure ratio range. It was found that blunting the vanes (see fig. 6) nearly accomplished this design objective by eliminating the Coanda turning at the vane trailing edge. Figure 8 indicates that static turning was approximately 65 to 80 percent of the design turning angle for $\delta_d > 0^{o}$.

Wind Tunnel and Support System

This investigation was conducted in the Langley 16-foot transonic tunnel, which is a single-return atmospheric wind tunnel with a slotted octagonal test section and continuous air exchange. The wind tunnel has continuously variable airspeed up to a Mach number of 1.30. Test-section plenum suction is used for speeds above a Mach number of 1.10. From the calibration of the wind tunnel, the test-section wall divergence is adjusted as a function of the airstream dewpoint. The adjustment eliminates any longitudinal static-pressure gradients in the test section; such gradients might occur because of condensation of atmospheric moisture. A complete description of the wind tunnel and operating characteristics can be found in reference 10.

The model was supported by a sting strut with the model center of rotation indicated in figure 2. The strut had a 45^{o} leading-edge sweep, a 50.8-cm chord, and a 5-percent-thick hexagonal airfoil in the streamwise direction. The model blockage ratio was 0.0015 (ratio of model cross-sectional area to test-section area), and the maximum blockage ratio including the support system was 0.0020. Strut interference effects were considered to be small on this model afterbody because the boattail angle was 12.5^{o}. Reference 11 indicates that strut interference may be large for models with boattail angles in excess of 15^{o}, depending on the proximity to the strut trailing edge.

Instrumentation

External aerodynamic and internal nozzle forces and moments were each measured by internal, six-component strain-gage balances (fig. 3). Eight external static pressures were measured at the sealed gap at approximately fuselage station 100.00 cm as shown in figure 10. Four of these pressure orifices were located on the nonmetric forebody and four were located on the metric afterbody at meridian angles of every 90^{o}. These pressure measurements were used to correct the measured axial forces for pressure-area force tares as described in appendix A. (See refs. 12 and 13.) Four internal pressures were measured in the vicinity of the sealed gap, and four internal pressures were located on the top and bottom of the nozzles approximately at fuselage station 125.00 cm. The internal pressures are also used for determining pressure area force tares. One internal pressure measurement was made near the nose of the model. Additional tests were conducted with 24 pressure orifices, each located on the top and bottom of the nozzles from fuselage stations 125.00 cm to 138.62 cm. These tests indicated uniform internal pressure inside the model at any given Mach number, angle of attack, and pressure ratio tested. Similar results were found in references 12 and 13.

A turbine flowmeter (external to the wind tunnel) was used to measure the total mass-flow rate to the nozzles. In addition, the pressure and temperature in each supply pipe were measured prior to the discharge of the flow through the eight sonic nozzles; the measurements determined the mass-flow rate to each nozzle. These flow measurements were used independently to check the measurement determined by the flowmeter. Two total pressures and one total temperature were measured at one axial location in each nozzle. These measurements were made at fuselage station 133.50 cm or 5.38 cm forward of the nozzle exit.

Afterbody pressure distributions were measured on the top and bottom of the afterbody along axial rows located at the model center-line plane and at 8.89 cm from the center line during all force tests as indicated in figure 10. Wing pressures were measured at four span stations (fig. 10) on an additional set of wings separate from the force tests. On the right wing, pressures were measured along two streamwise chords located at $\frac{y}{b/2} = 0.325$ and $\frac{y}{b/2} = 0.60$. On the left wing, pressure orifices were located at $\frac{y}{b/2} = 0.45$ and $\frac{y}{b/2} = 0.80$. (Note that fig. 10 shows the span locations on only one wing panel.) All pressures were measured with individual pressure transducers except those on the wings; these pressures were measured with pressure scanning devices. Temperatures were measured with iron-constantan thermocouples.

At each test condition, approximately 10 samples of data were recorded on magnetic tape over a period of about 10 seconds. The average of the 10 samples is used for computational purposes. In those tests during which wing-loading characteristics were determined, 48 samples of data were recorded over a period of 45 seconds with only a single sample of each wing pressure being made because of the pressure scanning devices used.

Tests

Four nozzles with geometric turning angles δ_d of 0°, 15°, 30°, and 45° were tested at Mach numbers from 0 to 1.2 and at angles of attack from -2° to 14°. Some tests were conducted with the wings off. Wing loadings were determined with nozzle deflection angles of 0° and 30° only; flow characteristics for $\delta_d = 30^\circ$ were determined using the fluorescent oil technique. The average Reynolds number per meter, the free-stream dynamic pressure, and the stagnation temperature are summarized in the following table:

M	N_{Re} per meter	q_{∞}, kN/m^2	T_t, K
0.40	8.20×10^6	10.14	302.6
.70	11.68	24.96	316.5
.80	12.30	29.78	323.1
.90	12.63	33.92	328.7
.95	12.80	35.71	331.5
1.20	13.12	41.92	344.3

Balance load limits on the pitching moment restricted the maximum angle of attack at high Mach numbers; the maximum obtainable jet pressure ratio for the nozzles with the larger deflection angles was also restricted.

All tests were conducted with 0.25-cm-wide boundary-layer transition strips consisting of No. 100 silicon carbide grit sparsely distributed in a thin film of lacquer. In accordance with the recommendations of references 14 and 15, these strips were located 2.54 cm from the tip of the forebody nose and on both the upper and lower surfaces of the wings at 5 percent of the wing chord at the wing-fuselage juncture to 10 percent of the local streamwise chord at the wing tip.

PRESENTATION OF RESULTS

The results of this investigation are presented in plotted coefficient form in the following figures:

	Figure
Basic aerodynamic characteristics:	
$\delta_d = 0^\circ$	11
$\delta_d = 15^\circ$	12
$\delta_d = 30^\circ$	13
$\delta_d = 45^\circ$	14
Basic nozzle thrust characteristics:	
$\delta_d = 0^\circ$	15
$\delta_d = 15^\circ$	16
$\delta_d = 30^\circ$	17
$\delta_d = 45^\circ$	18
Wing pressure distributions:	
$\delta_d = 0^\circ$	19
$\delta_d = 30^\circ$	20

DISCUSSION

Basic Force Characteristics

External aerodynamic characteristics.- The basic longitudinal aerodynamic characteristics including thrust forces for the model with nozzle deflection angles of 0^o to 45^o are presented in figures 11 to 14. Shown in variation with thrust coefficient C_T are the total lift coefficient C_L, thrust-minus-drag coefficient $C_{(F-D)}$, pitching-moment coefficient C_m, and angle of attack α. Each curve on these figures, as well as on subsequent data figures, has been identified by the initial jet-off angle of attack α_{jo}. Ideally, the angle of attack would be fixed as the pressure ratio or thrust coefficient is varied, but this condition was not possible because of the method of model support.

In general, figures 11 to 14 show an increase in lift coefficient with increasing thrust coefficient at approximately the same angle of attack. This increase, especially for the model with $\delta_d > 0^o$, is the result of the contribution of both the jet lift and jet-induced supercirculation lift.

Thrust-minus-drag coefficient varies almost linearly with thrust coefficient at approximately the same angle of attack. At a constant thrust coefficient, the decrease in $C_{(F-D)}$ with increasing α is caused by the increase in drag at lifting conditions.

Reference 3 showed that the model is statically stable at jet-off conditions and that there is no change in stability caused by jet operation $\left(dC_m/dC_L\right.$ at constant C_T is equal to dC_m/dC_L at $\left.C_T = 0\right)$. When cross plots of C_m versus C_L are made at constant C_T, the effect of the nozzle deflection angle is to add to the jet-off pitch curves a constant increment in C_m over the entire lift range. This increment, which is a function of the nozzle deflection angle, is similar in magnitude to the nose-down pitching moments caused by a 10° to 15° deflection of a full-span trailing-edge flap found on typical fighter aircraft. A canard would be an ideal surface to trim a configuration employing this vectored-thrust system. Trimming would require an upload on the canard; such an upload would increase the overall lift of the configuration.

Nozzle thrust characteristics.- Basic nozzle thrust characteristics for the model with nozzle deflection angles of 0° to 45° are shown in figures 15 to 18. Shown are the variation with thrust coefficient of the measured jet normal force $C_{N,j}$, jet thrust component along the tailpipe center line $C_{F,j}$, and the pitching moment caused by the jet $C_{m,j}$. The variation with C_T of the angle of attack α_n of the tailpipe center line is also shown. At jet-off conditions $\alpha_n = \alpha$; however, at power-on conditions, the internal propulsion system deflects with respect to the main force balance and to the external aerodynamic surfaces. (See fig. 1 and appendix A.) In the upper left corner of each figure is shown the effective turning angle which is determined from $C_{F,j}$ and $C_{N,j}$. (See appendix A.)

Figures 15 and 16 indicate that the effective turning angles δ for the 0° and 15° nozzles are about the same as the static values given in figure 9. The effect of the angle of attack on the effective turning angle is generally small except at $M = 0.9$ and $M = 0.95$. There is a significant increase in δ over the static turning angle (fig. 9) for both the 30° and 45° nozzles at low C_T (figs. 17 and 18). For example, this increase is about 7° to 10° for the 30° nozzle at low thrust coefficients. One explanation is that this difference between the static and wind-on turning angles may be associated with the jet flow over the top turning vane. In this particular nozzle design, it is implicit that full Coanda turning of the jet flow over the turning vanes is achieved. Apparently this turning may not happen at static conditions for the two nozzles with the longer top turning vanes, that is, the 30° and 45° nozzles. However, at wind-on conditions the external flow along the afterbody may help to keep the jet flow attached to the turning vane at low thrust coefficients. As the thrust coefficient is increased, the increase in jet velocity probably causes the flow to separate again over the top of the turning vane. The separation then results in a decrease in the wind-on effective turning angle that approaches the static values.

Wing-Loading Characteristics

In order to gain some insight into the basic flow phenomena occurring from the interaction of the deflected jet and wing flow fields, pressure distributions were measured on the wing for the model with the 0° and 30° nozzles. These pressure distributions are presented in figures 19 and 20 and the resulting span-load characteristics are shown in figure 21. The critical pressure coefficient was adjusted for wing sweep (ref. 16) and is indicated in figures 19 and 20.

Jet-off characteristics.- Jet-off pressure distributions are typical for a wing of this type. The data indicate that an increasing angle of attack increases the planform induced loading at the wing tip. This increased loading is a result of swept wings having no twist. (See, for example, fig. 19(c), $M = 0.70$ and $\alpha = 5.4^{\circ}$.) By $\alpha = 9.1^{\circ}$ at $M = 0.7$ (fig. 19(d)), the flow over the outboard portion of the wing is separated; further increases in the angle of attack move this flow-separation area progressively inboard. This separated area can be seen by examining the oil-flow patterns shown in the photographs of figure 22(a). At $M = 0.90$ and $M = 0.95$, the pressure distributions indicate the presence of a strong shock at $x/c > 0.7$. Behind the shock the flow is separated, especially at $\frac{y}{b/2} > 0.45$. (See photographs of figs. 22(b) and 22(c).)

Power effects, $\delta_d = 0^{\circ}$.- In general, the power effects of the model with $\delta_d = 0^{\circ}$ are small. This fact is best illustrated by examining the span-load characteristics of figure 21; these characteristics show little or no effect of power at $M = 0.7$ and $M = 0.8$. However, at $M = 0.9$ and $M = 0.95$, jet operation does improve the inboard wing loading at the higher angles of attack. The improvement may be caused by entrainment effects of the jet.

Power effects, $\delta_d = 30^{\circ}$.- Jet operation for the model with the 30° deflected jet affects wing-loading characteristics out to the tip except where flow separation occurs. At $M = 0.7$ and $M = 0.8$, the jet exerts a greater influence over the airfoil lower surface than over the upper surface in that the lower surface is pressurized almost to the airfoil leading edge. At those angles of attack where flow separations occur, the jet has no effect and therefore no induced lift is generated. This effect can best be seen, for example, from pressure distributions of figure 20 and the span-loading characteristics of figure 21 for $M = 0.7$ and $\alpha = 9.1^{\circ}$.

At $M = 0.90$ and $M = 0.95$, where supersonic flow exists over a large portion of the airfoil, a smaller region of the airfoil is affected by the jet. On the top there is generally a small forward shift of the wing shock wave with jet operating at the initial jet-on condition. Further increases in thrust coefficient generally move the shock back to a position downstream from the initial jet-off location. On the inboard lower surface of the wing the rapid expansion of the flow is reduced by jet operation.

Comparison of integrated and measured induced lift.- A comparison of integrated and measured induced lift coefficients is shown in figure 23. The variation of $C_{L,\Gamma}$ (appendix A) with the angle of attack is shown at two Mach numbers for two thrust coefficients. The integrated values of $C_{L,\Gamma}$, including allowance for body carryover and the measured body-alone data, show good agreement with the measured induced lift except at $M = 0.9$ and $C_T = 0.06$.

Afterbody Pressure Distributions

Afterbody pressure distributions for the model with nozzle deflection angles of 0° to 45° are presented for selected Mach numbers and angles of attack in figures 24 to 27. These pressure distributions show typical results of a large expansion at the start of the afterbody boattail and a recompression along the afterbody. Nearly free-stream conditions exist at the end of the afterbody for jet-off conditions. At $M = 0.70$ and $M = 0.80$, the results generally show that, for $\delta_d > 0^\circ$, some lift is being generated on the afterbody because the effect of the jet is to pressurize the lower surface of the afterbody and to reduce the recompression on the upper surface.

At $M = 0.90$ and $M = 0.95$, the operation of the jet generally causes the shock on the upper surface of the afterbody to move downstream and the shock on the lower surface to move upstream. The flow on the top of the afterbody can be seen more clearly by once again examining the oil-flow photographs of figure 22. At $M = 0.9$ and $C_T = 0$, there is a clearly defined bell-shaped shock where the axial location of the shock on the outer edge of the afterbody is being influenced by the shock on the wing. There also appears to be an area of separated flow behind this shock. As C_T is increased, the shock moves downstream and the separation area is reduced ($\alpha \approx 3^\circ$ in fig. 22(b)). Similar effects are seen at $M = 0.95$, where operation of the jet at $\alpha \approx 3^\circ$ appears to eliminate completely the separation on the afterbody upper surface.

Lift Characteristics

Total lift.- Figure 28 presents the variation of total lift coefficient with angle of attack at constant values of thrust coefficient for the model with nozzle deflection angles of 0° to 45°. These data are obtained from cross plots of the basic data of figures 11 to 14. The average jet-off variation of the lift coefficient with the angle of attack is also shown by the dashed line. These jet-off curves were determined from averaging the measured jet-off lift data for the model with the four nozzles.

As can be seen in figure 28, increasing the thrust coefficient for a particular nozzle or increasing the nozzle deflection angle at a constant thrust coefficient results in an increase in the lift coefficient caused by effects of both jet lift and jet-induced supercirculation lift.

Lift-curve slope.- The variation of the ratio of jet-on to jet-off lift-curve slope is presented in figure 29 for the model with nozzle deflection angles of 0° to 45° at selected thrust coefficients. Lift-curve slopes were determined over the most linear portion of the lift curves from $\alpha = 0^{\circ}$ (range from 0° to about 4°) because of the nonlinearity of the lift curves that exists from -2° to 0° at the higher Mach numbers. The jet-off lift-curve slope is also shown at the top of figure 29.

In general, there is a 4- to 6-percent increase in lift-curve slope as thrust coefficient is increased from 0.05 to 0.2; the increase is caused mainly by the increase in jet lift. The sharp decrease in the power-on lift-curve slope at $M = 0.9$ and $C_T \leqq 0.1$ may be attributed to the flow-separation characteristics shown in figure 22. At $M = 0.95$, the reduced flow separation at jet-on conditions results in an increase in C_{L_α}.

Induced and incremental lift.- The total lift of a propulsive lift system can be broken down into three parts which include basic jet-off $C_{L,o}$, jet lift $C_{L,j}$, and jet-induced supercirculation lift $C_{L,\Gamma}$. The variation $C_{L,j}$ and $C_{L,\Gamma}$ with thrust coefficient for the model with nozzle deflection angles of 0° and 45° is presented in figures 30 to 33. The variation of ΔC_L (sum of $C_{L,\Gamma}$ and $C_{L,j}$) is also shown.

For the model with the 0° nozzle, there is an increase in $C_{L,\Gamma}$ with both increasing angle of attack and Mach number except at $M = 1.2$. It was shown in figure 21 that at $M = 0.7$ and $M = 0.8$, the induced lift is being generated on the wing at $y/b/2$ from about 0.4 to 0.6; whereas, at $M = 0.9$ and $M = 0.95$, the induced lift is a result of a filling in of the defect in the span loading caused by the body.

For the vectoring case of this wing-body model, induced lift is most affected by deflection angle and thrust coefficient, whereas the effects of either Mach number or angle of attack are small. However, at $\alpha < 0^{\circ}$ for the nozzle with $\delta_d = 15^{\circ}$ and $M = 0.95$ (fig. 31(b)), no lift is induced up to $C_T = 0.1$ after which there is a sharp increase in $C_{L,\Gamma}$. Similar results are reported in reference 3 for the same model with an NACA 64A006 airfoil over a wider range of all test variables. Reference 3 inferred that at $M = 0.9$ there was a sudden rearward shift of the shock on the afterbody. This shift occurred at those thrust coefficients at which the measured force data indicated an increase in $C_{L,\Gamma}$. Since there is no lift induced at $M = 1.2$ for the 30° nozzle (fig. 32(c)), subsequent discussions are confined to Mach numbers up to 0.95.

A summary of the variation of incremental lift with the angle of attack at selected Mach numbers and thrust coefficients is presented in figure 34. For the 0° and 15° nozzles, the increase in incremental lift with the increasing angle of attack is caused by increases in both $C_{L,j}$ and $C_{L,\Gamma}$. For example, about one-third of the incremental lift for the 0° nozzle at $M = 0.7$ and $\alpha = 13.5^{\circ}$ is induced lift (fig. 30(a)). For the 30° and 45° nozzles, increases in incremental lift are primarily caused by increasing jet lift with increasing angle of attack.

Lift-augmentation factor.- For the present investigation, a lift-augmentation factor $\Delta C_L/C_{L,j}$ is used rather than the lift gain factor as used in references 1 and 17. This augmentation factor depends upon the measured wind-on jet lift and not on the jet lift that is predetermined from the static turning angle as is usually done for gain factor. Note that these two terms differ only in the $C_{L,j}$ used and that both are based on a measured ΔC_L. The variation of the lift-augmentation factor with the thrust coefficient is presented in figure 35 for wings off and in figures 36 to 38 for the model, wings on, with nozzle deflection angles of 15° to 45°.

The results with the wings off indicate that a small part of the total induced lift is developed on the body with the exception of $M = 0.7$ and $\delta_d = 15^{\circ}$, where almost 50 to 60 percent of the total induced lift is generated on the body at low values of the thrust coefficient. This single result is similar to that of reference 1.

Lift-augmentation factors generally decrease with either increasing the thrust coefficient or the angle of attack (figs. 36 to 38). This decrease is because jet lift increases more rapidly than $C_{L,\Gamma}$ with increases in both of these variables. A lift-augmentation factor of 4.15 was achieved at $\alpha \approx 0^{\circ}$ for the model with $\delta_d = 45^{\circ}$ at $M = 0.90$ at $C_T = 0.056$ (fig. 38).

Lift-augmentation factors are summarized in figure 39, which shows that these factors increase up to $M = 0.9$. The sharp drop in lift augmentation for $\delta_d = 15^{\circ}$ at $M = 0.95$ and $C_T = 0.1$ is caused by the nature of the induced lift variation with C_T for this particular condition (fig. 31(b)). It is evident that the nozzle with $\delta_d = 30^{\circ}$ has the lowest performance; the exact reasons for this fact are unknown at this time. Reference 3 showed that ΔC_L varied linearly with effective turning angle δ up to 28° (corresponds to $\delta_d = 30^{\circ}$); after that point there is a sharp increase and again a linear variation up to 42°. Incremental lift variations obtained in this investigation with δ up to about 30° are similar to those of reference 1. Jet lift $C_{L,j}$ is linear with δ up to 42°. The increase in ΔC_L between 28° and 42° indicates a sharp improvement in induced lift $C_{L,\Gamma}$ as the nozzle design angle is increased from 30° to 45° and might indicate that the vectored thrust at these higher deflection angles acts more like a classic jet flap.

It is significant that the results show no degradation in lift-augmentation performance for any of the deflection angles tested up to $M = 0.9$. This lack of degradation is probably because of the wing thickness ratio and airfoil shape. A thicker airfoil or one designed for low speeds would probably reach maximum lift-augmentation ratios at lower Mach numbers.

Comparisons with other data.- In order to compare the lift-augmentation performance of the current system with the performance of other types of jet flaps, the customary gain factor, based on static turning and adjusted for partial-span effects (ref. 18), is used. The static turning angle is used because jet turning is only measured at static conditions for the investigations in this comparison. The variation of adjusted gain factor with ideal thrust coefficient is shown in figure 40 for the present investigation and for several previous investigations. The two areas used for the partial-span adjustment are also defined in the upper left corner of figure 40. Note that for the present investigation, the total area is somewhat larger than the reference area used; however, since gain factor is a ratio, it is a function of lift only. The 30° nozzle was chosen because this nozzle deflection angle was similar to that of other investigations.

The empirical two-dimensional results of reference 19 are used as a basis for comparison where ΔC_L was found to be proportional to the product of $\sqrt{C_{T,i}}$ and $\sin \delta_d$ (up to 65°). In reference 19 the constant of proportionality was given for two cases: (1) the pure jet flap, shown by solid line and (2) blown flap shown by dashed line (blowing over the upper surface of a flap). The empirical result of reference 19 was used because of the agreement with the theory of reference 20 for a pure jet flap.

When adjustments for partial-span effects are made, both the results of the present investigation and that of reference 1 compare favorably with other data. (See fig. 40.) When compared to the theoretical two-dimensional jet flap, the results of the present investigation indicate a reduction in performance at $M = 0.4$ of about 40 percent at $C_{T,i} = 0.1$ to about 25 percent at $C_{T,i} = 0.3$. This reduction in performance is probably a jet thickness effect.

It is interesting to note that the different wing airfoil shapes of references 5 and 6 had little effect on the gain factor using two-dimensional wings. Reference 5 used an NACA 64A406 airfoil, whereas a 10-percent-thick supercritical airfoil was employed in the investigation of reference 6. The resulting small effect is similar to that reported in reference 3 where airfoil shape had little effect on lift augmentation for the configuration tested.

Thrust Minus Drag

One measure of airplane maneuvering performance is the specific excess power of the airplane (ref. 4). Since this parameter is a function of thrust minus drag, the potential of improving maneuvering capability caused by thrust vectoring can be assessed by examining the relationship between thrust minus drag and total lift. This relationship can be seen in figure 41 for the model with nozzle deflection angles of 0° to 45° at $M = 0.7$ and $M = 0.9$ and at $C_T = 0.05$ and $C_T = 0.2$. These results are typical and show that at maneuvering lift coefficients a crossover in $C_{(F-D)}$ occurs so that an increase in deflection angle increases maximum usable lift coefficient, that is, a larger lift coefficient at which $C_{(F-D)} = 0$.

Drag Characteristics

Drag coefficient.- The variation of drag coefficient C_D and the aerodynamic lift $C_{L,o} + C_{L,\Gamma}$ with thrust coefficient are presented in figures 42 to 45 for the model with deflection angles of 0^o to 45^o. (See appendix A for details concerning determination of aerodynamic lift and drag.) By cross-plotting these data, power-on drag polars at constant values of C_T are obtained and are shown in figure 46. Typical power drag increments, defined simply as the difference between jet-on and jet-off C_D at constant $C_{L,o} + C_{L,\Gamma}$, are given in figure 47. As indicated in figures 46 and 47, increasing nozzle deflection angles from 0^o to 45^o result in significant reductions in drag coefficient over the entire lift range up to $M = 1.2$. This reduction is primarily the result of increased supercirculation which is caused by the induced upwash field created by the deflected jet in front of the wing. The cause of the rather substantial decrease in drag at $M = 1.2$ because of jet is not known at this time.

Another source of drag reduction could be an improvement in the afterbody drag. The oil-flow photographs of figure 22 indicate that there is a reduction in afterbody flow separation with jet operation at $M = 0.9$ and $M = 0.95$.

Drag due to lift.- Drag reduction at some combinations of nozzle deflection angle and thrust coefficient is accomplished through improvements in the drag-to-lift characteristics $dC_D/d(C_{L,o} + C_{L,\Gamma})^2$ as shown in figure 48. For this study, $dC_D/d(C_{L,o} + C_{L,\Gamma})^2$ has been determined by fitting the equation

$$C_D = C_{D,min} + \frac{dC_D}{d(C_{L,o} + C_{L,\Gamma})^2}\left[(C_{L,o} + C_{L,\Gamma}) - (C_{L,o} + C_{L,\Gamma})_M\right]^2$$

to the drag polars of figure 46 up to about $(C_{L,o} + C_{L,\Gamma}) = 0.4$. (See ref. 21.) The value $(C_{L,o} + C_{L,\Gamma})_M$ corresponds to the lift coefficient at $C_{D,min}$. The conditions for theoretical zero suction $1/C_{L_\alpha}$ and for theoretical 100-percent suction $1/\pi A$ computed only at jet-off conditions are also presented. The values of $1/C_{L_\alpha}$ and $1/\pi A$ may not represent true upper and lower bounds with the jet operating. As can be seen, improvements in drag due to lift occur for all the nozzles at $C_T = 0.2$, with $dC_D/d(C_{L,o} + C_{L,\Gamma})^2$ approaching theoretical jet-off 100-percent suction for the 45^o nozzle at $M = 0.70$. The improvements in drag due to lift are probably because of improvements in span-loading characteristics.

The reader is cautioned that this analysis assumes classical theory; it is only valid for wings not operating in an induced upwash field. For example, reference 22 showed that for the case of a jet located forward and above a wing, a decrease in induced drag was achieved, even though power effects distorted the span loading.

Drag-rise characteristics.- The variation of drag coefficient with Mach number at both minimum conditions and at $C_{L,o} + C_{L,\Gamma} = 0.4$ is presented in figure 49 for two thrust coefficients. Again, these results show the reduction in drag caused by increasing deflection angle. The results also show that drag-rise characteristics are not affected by nozzle deflection angle or jet operation.

Thrust Recovery

The two-dimensional jet flap has been shown to be an effective means for significantly inducing lift while at the same time recovering a part of the thrust lost because of deflection of the jet. Thrust recovery is defined as that portion of the thrust recovered in the streamwise direction or as the amount of directed propulsive thrust converted to aerodynamic thrust. Thrust recovery for a three-dimensional configuration has already been demonstrated (ref. 1).

While the concept of recovery is the same, there are various methods used to determine it. (See appendix A.) For the present investigation, the method of reference 18 that determines a thrust ratio is chosen as the prime method because, for models employing force balances, this method requires the measurement of thrust minus drag only. This requirement is typical of most investigations. For comparative purposes, the method of reference 23, which requires additional measurements to determine drag or thrust, and the method of reference 1, developed for data taken at $\alpha = 0^{\circ}$, are used.

The variation of thrust recovery with thrust coefficient for the model with deflection angles of 0° to 45° is presented in figures 50 to 53. From these data and the effective turning angles obtained from figures 15 to 18, thrust recovery is plotted as a function of the thrust vector angle $\alpha + \delta$ for two Mach numbers and thrust coefficients in figure 54. The line of no thrust recovery $\cos(\alpha + \delta)$ is also shown. (See appendix A.) Each nozzle recovers thrust until viscous effects, such as flow separations, develop on the wing. The point at which a nozzle does not have any recovery represents the lift coefficient at which the power-on polar departs from being parabolic and at which the definition of the induced drag (appendix A, eq. (A14)) is no longer valid.

As deflection angle is increased, the amount of thrust recovered in the streamwise direction increases. This recovered thrust is actually the drag reduction previously noted. An envelope curve could be drawn through the points of maximum thrust recovery and can serve as a guide to the operational potential of the current system. For example, these data indicate that the 15° nozzle would provide attractive improvements in cruise performance since nearly all of the directed thrust is recovered, that is, the aerodynamic thrust term is approximately $1 - \cos(\alpha + \delta)$.

A comparison of thrust recovery defined by references 18 and 23 is made in figure 55 where the variation of thrust recovery in percent thrust coefficient (see appendix A) with the aerodynamic lift coefficient $C_{L,o} + C_{L,\Gamma}$ is given. As shown, the maximum usable lift coefficient has been increased from 0.46 to 0.59, a 28-percent improvement. Good agreement with the two methods is also shown.

Figure 56 presents the variation of thrust recovery in percent thrust coefficient with Mach number for the 30° nozzle at $C_T = 0.1$ and $\alpha \approx 0^{\circ}$. Thrust recovery for this configuration is relatively insensitive to Mach number up to $M = 0.95$. This insensitivity indicates that the ability of this vectored-thrust system to reduce drag is maintained through transonic speeds.

CONCLUDING REMARKS

An investigation was conducted in the Langley 16-foot transonic tunnel to determine the induced lift characteristics of a vectored-thrust concept in which a rectangular jet-exhaust nozzle was located in the fuselage at the wing trailing edge. The effects of nozzle deflection angles of 0° to 45° were studied at Mach numbers from 0.4 to 1.2, at angles of attack up to 14°, and with thrust coefficients up to 0.35. The Reynolds number per meter varied from 8.20×10^6 to 13.12×10^6.

The results indicated that significant increases in thrust-induced lift up to Mach number 0.95 and substantial decreases in drag up to Mach number 1.20 were achieved during the vectoring operation. A lift-augmentation factor of 4.15 was reached with 45° nozzle deflection at a Mach number of 0.90 with an angle of attack of 0°. The overall ability of this vectored-thrust model to increase lift and to reduce drag for all the deflected nozzles was generally maintained up to a Mach number of 0.9 and to angles of attack where flow-separation effects dominate. Deflection of the jet was instrumental in reducing afterbody flow separation at Mach numbers of 0.9 and 0.95. Some reductions in drag due to lift were also found.

Langley Research Center
National Aeronautics and Space Administration
Hampton, Va. 23665
August 13, 1975

APPENDIX A

DATA REDUCTION PROCEDURE

Data Adjustments

External aerodynamic and internal nozzle forces and moments were each measured by separate internal six-component force balances as shown in figure 3. The main balance measured total lift, thrust-minus-axial force, and total pitching moment; the thrust balance sensed nozzle normal and axial forces and pitching moment. The center lines of these two force balances were located above and below the tailpipe center line (fig. 3) and the bellows flow-transfer system (fig. 4). Because of this offset, an interaction of loading one balance on the other existed; this interaction is primarily the result of the main balance acting on the thrust balance.

Consequently, single and combined loadings of the normal force and the pitching moment were made with and without the jets operating with the 0° nozzle. These calibrations were performed with the jets operating because this condition gave a more realistic effect of pressurizing the bellows rather than capping off the nozzles and pressurizing the flow system. Thus, in addition to the usual balance interaction corrections that are applied for a single force balance under combined loads, another set of interactions was made to the data from this investigation for the combined loading effects of one balance on the other. However, loadings were also made in the axial-force direction with the flow system capped off and pressurized; these loadings indicated no effect on the axial force measured by each balance.

In order to achieve desired thrust-minus-axial force (from main balance) and thrust (from thrust balance), the axial forces measured by both force balances must also be corrected for pressure-area tare forces acting on the model (similar to refs. 12 and 13), and for momentum tare forces caused by flow in the bellows. The external seal and internal pressure forces on the model were obtained by multiplying the difference between the average pressure (external seal or internal pressures shown in fig. 10) and free-stream static pressure by the affected projected area normal to the model axis. The momentum tare force was determined from calibrations prior to the wind-tunnel investigation using standard calibration nozzles (appendix B).

Gross thrust-minus-axial force was computed from the main balance axial force from the following relationship:

$$F_j - F_A = F_{A,Mbal} + (\bar{p}_{es} - p_{\infty})(A_{max} - A_{seal}) + (\bar{p}_i - p_{\infty})A_{seal} - F_{A,mom} \qquad \text{(A1)}$$

where $F_{A,Mbal}$ (positive upstream) includes all pressure and viscous forces, internal and external on both the afterbody and thrust system. The second and third terms account for the forward seal rim and interior pressure forces, respectively. In terms of an axial-force coefficient, the second term ranges from -0.0001 to -0.0007 and the third term varies ±0.0075 depending upon Mach number and pressure ratio. It was previously stated that internal pressure at any given set of test conditions was uniform throughout the inside of the model, thus indicating no flow. These results are similar to those of references 12 and 13. The fourth term is caused by the momentum tare correction and is a function of the average bellows internal pressure. At an internal pressure of 1380 kN/m^2 (corresponding to $p_{t,j}/p_\infty \approx 4.0$), this tare is approximately 5 percent of the maximum static thrust and its repeatability is 0.25 percent.

Gross thrust from the thrust balance is computed from a similar relationship:

$$F_j = F_{A,Tbal} - (\bar{p}_i - p_\infty)A_{base} - F_{A,mom} \tag{A2}$$

where $F_{A,Tbal}$ (positive upstream) includes nozzle thrust and the internal pressure forces acting on the thrust system.

Since both balances are offset from the model center line, similar adjustments are made to the pitching moments measured by both balances. These adjustments are necessary because both the pressure area and bellows momentum tare forces are assumed to act along the model center line. The pitching-moment tare is determined by multiplying the tare force by the appropriate moment arm and subtracting the value from the measured pitching moments.

External Forces Including Thrust

The adjusted forces and moments measured by the main balance are transferred from the main-balance axis to the body axis of the metric portion of the model where the body axis lies in the wing chord plane (fig. 1). Angle of attack α, which is the angle between the wing chord plane and the relative wind, was determined by applying deflection terms caused by model and balance bending under aerodynamic load to the sting pitch angle. Calibrations were made with the propulsion simulation system in place in order to account for any restraints that might occur across the force balances. It should also be noted that some difference in angle between the nonmetric and metric portions of the model exists because of balance deflection. No adjustment has been made for wind-tunnel flow angularity which is approximately 0.1° for most sting-supported models in the 16-foot transonic tunnel.

APPENDIX A

The total force and moment coefficients, including thrust about the body and stability axis, are shown in figure 1 where the moment reference center is at the quarter chord of the wing mean geometric chord (fuselage station 117.64 cm).

Nozzle Internal Forces

The adjusted forces and moments measured by the thrust balance are transferred from the thrust-balance axis to the parallel tailpipe center-line axis (fig. 1). The tailpipe center line will be at some angle with respect to the body axis because the thrust balance deflects, under load, relative to the body axis. Accordingly, α_n is defined as the angle between the tailpipe center line and the relative wind. This angle was determined by adding deflection terms to the previously determined value of angle of attack. Calibrations with the propulsion system in place were made in order to determine these deflection constants.

From the measured axial and normal components of the jet resultant thrust, the effective jet turning angle, thrust coefficient, and jet lift coefficient are defined, respectively, as

$$\delta = \tan^{-1} \frac{C_{N,j}}{C_{F,j}} \qquad \text{(A3)}$$

$$C_T = \sqrt{C_{N,j}^2 + C_{F,j}^2} \qquad \text{(A4)}$$

$$C_{L,j} = C_T \sin\left(\delta + \alpha_n\right) = C_{N,j} \cos \alpha_n + C_{F,j} \sin \alpha_n \qquad \text{(A5)}$$

Thrust Removal

Nozzle internal forces are transferred from the tailpipe center-line axis to the body axis and then subtracted from the external forces resulting in the following aerodynamic loads:

$$C_{N,o} + C_{N,\Gamma} = C_N - \left[C_{N,j} \cos\left(\alpha - \alpha_n\right) - C_{F,j} \sin\left(\alpha - \alpha_n\right)\right] \qquad \text{(A6)}$$

$$C_A = -C_{(F-A)} + \left[C_{F,j} \cos\left(\alpha - \alpha_n\right) + C_{N,j} \sin\left(\alpha - \alpha_n\right)\right] \qquad \text{(A7)}$$

and transferring to the wind axis

$$C_{L,o} + C_{L,\Gamma} = \left(C_{N,o} + C_{N,\Gamma}\right) \cos \alpha - C_A \sin \alpha \qquad \text{(A8)}$$

$$C_D = C_A \cos \alpha + \left(C_{N,o} + C_{N,\Gamma}\right) \sin \alpha \tag{A9}$$

where the normal force or lift coefficient with the subscript o refers to jet-off values and the subscript Γ refers to the jet-on normal or lift force induced as a result of supercirculation on the wing. The quantity $C_{L,o} + C_{L,\Gamma}$ represented the total aerodynamic lift of the wings.

Lift Augmentation

Generally, the total lift component is broken down into three parts: (1) jet-off lift, (2) jet-reaction lift, and (3) jet-induced supercirculation lift (refs. 1, 17, and 23). A gain factor is then defined as the ratio of supercirculation lift plus jet lift to the jet lift. Jet lift (not measured at forward speeds) is then defined as $C_{T,i} \sin\left(\alpha + \delta_{static}\right)$ where $C_{T,i}$ is an ideal thrust coefficient determined by measuring the total flow momentum at the nozzle exit (typical of two-dimensional tests). Other experimental setups usually have a single force balance and, thus, are only able to measure thrust and turning angle at static conditions. In this case, values of thrust coefficient at forward speeds can be determined based on these static thrust measurements. Since one of the purposes of the present investigation was to determine the components of the total lift, jet lift is measured directly with the thrust balance. However, first it was necessary to determine the jet-off or basic wing lift coefficient $C_{L,o}$. The basic wing lift varies with thrust coefficient and is different at each jet-on point since the model angle of attack is decreased with jet operation because of balance deflections. Figures 11 to 14 show the variation of α with C_T. Therefore, in order to determine $C_{L,o}$, the average jet-off lift variation with angle of attack at each Mach number was fitted to a third-order polynomial curve as a function of angle of attack; $C_{L,o}$ was then computed at each power-on point for the particular model angle of attack measured.

Incremental lift is then defined as

$$\Delta C_L = C_L - C_{L,o} = C_{L,\Gamma} + C_{L,j} \tag{A10}$$

and the lift-augmentation factor based on measured jet lift is simply

$$\frac{\Delta C_L}{C_{L,j}} = \frac{C_{L,\Gamma} + C_{L,j}}{C_{L,j}} \tag{A11}$$

For those tests (refs. 1 and 17) where jet lift is not directly measured but total lift is, the gain factor is defined as

$$G = \frac{\Delta C_L}{C_{T,i} \sin\left(\alpha + \delta_{static}\right)} \tag{A12}$$

APPENDIX A

Thrust Recovery

Thrust recovery has been defined as that portion of the total thrust recovered in the streamwise direction (refs. 17, 18, and 23) or as the amount of propulsive thrust converted to aerodynamic thrust. The prime method of defining thrust recovery for this investigation is similar to that of reference 18 and is

$$T_{rec} = \frac{C_{D,min} + C_{D,i} + C_{(F-D)}}{C_T} \tag{A13}$$

where T_{rec} is a thrust ratio. The average jet-off minimum drag coefficient $C_{D,min}$ is determined by averaging the data for all the nozzles. The induced drag coefficient $C_{D,i}$ is given in reference 20 as

$$C_{D,i} = \frac{\left(C_{L,o} + C_{L,\Gamma}\right)^2}{e\pi A\!\!\!R + 2C_T} \tag{A14}$$

where only the wing efficiency factor e determined at jet-off conditions is used to account for nonelliptic loading effects. Another efficiency factor can be applied to the entire denominator to account for jet effects; however, its value is not known.

In terms of the propulsive and aerodynamic thrust terms, thrust recovery is

$$T_{rec} = \frac{C_T \cos(\alpha + \delta) + C_{\Delta F}}{C_T} \tag{A15}$$

where $C_{\Delta F}$ is the aerodynamic thrust coefficient and represents the change in drag from the ideal jet-off drag polar. For no or zero thrust recovery, $C_{\Delta F} = 0$, and then

$$T_{rec} = \cos(\alpha + \delta) \tag{A16}$$

For complete thrust recovery, $T_{rec} = 1$ and then

$$C_{\Delta F} = C_T\left[1 - \cos(\alpha + \delta)\right] \tag{A17}$$

The aerodynamic thrust term can also be expressed as a ratio to C_T which then can be easily converted to percent thrust coefficient or, in ratio form,

$$\frac{C_{\Delta F}}{C_T} = T_{rec} - \cos(\alpha + \delta) \tag{A18}$$

A second method, used for limited comparison, is that of reference 23 where thrust recovery is defined as the ratio between the reduction in drag caused by jet-on induced effects and the thrust coefficient. This method (defined as Method 2) computes the aerodynamic thrust term as the difference between a jet-on drag polar and an ideal jet-off polar and is

$$\frac{C_{\Delta F}}{C_T} = \frac{C_{D,min} + C_{D,i} - C_D}{C_T} \tag{A19}$$

A third method (Method 3), also used for comparative purposes, was that of reference 1. Using equation (14) of reference 1 and replacing ideal thrust with measured thrust, thrust recovery also is defined as

$$\frac{C_{\Delta F}}{C_T} = \left\{\left[\frac{dC_{(F-D)}}{dC_T}\right]_{\delta} - \left[\frac{dC_{(F-D)}}{dC_T}\right]_{\delta=0}\right\} + 1 - \cos \delta \tag{A20}$$

This method was developed because the investigation of reference 1 could only be conducted at $\alpha = 0^{\circ}$. Note that, for purposes of this investigation, the effective turning angle is used instead of the measured static turning angle that was used in reference 1.

APPENDIX B

PROPULSION SIMULATION SYSTEM PERFORMANCE

Prior to the wind-tunnel investigation, the propulsion simulation system was checked out and the performance was determined on a static test stand. This static test stand utilizes the same air supply and has similar valving, filters, and heat exchanger (to operate the jet at a constant stagnation temperature) as the 16-foot transonic tunnel. Except for the turbine flowmeter, the same instrumentation, such as force balances, pressure transducers, and data recording system, was used in both facilities. This checkout was accomplished by attaching standard calibration nozzles as described in references 24 and 25 to each of the tailpipes at fuselage station 91.96 cm. (See fig. 57.) This appendix summarizes the results of this static checkout.

The total ideal isentropic gross thrust or exhaust jet momentum for both nozzles is

$$F_{i,p} = \dot{m}_p \sqrt{RT_{t,j} \frac{2\gamma}{(\gamma - 1)} \left[1 - \left(\frac{p_a}{p_{t,j}}\right)^{\frac{\gamma-1}{\gamma}}\right]} \tag{B1}$$

where $\dot{m}_p$ is the mass-flow rate measured by the turbine flowmeter and $p_{t,j}$ is the average jet stagnation pressure for both nozzles. The stagnation pressure in each nozzle is determined by a rake of four pressure probes manifolded together to indicate a single pressure. The turbine flowmeter is also calibrated using standard choked nozzles with different exit areas with average discharge coefficients of 0.995. Therefore,

$$\dot{m}_p = 0.995\dot{m}_i \tag{B2}$$

where $\dot{m}_i$ is the total ideal mass-flow rate and for a choked nozzle is

$$\dot{m}_i = A_e p_{t,j} \sqrt{\frac{\gamma}{RT_{t,j}} \left(\frac{2}{\gamma + 1}\right)^{\frac{\gamma+1}{\gamma-1}}} \tag{B3}$$

The variation of measured mass-flow rate $\dot{m}_p$ with pressure ratio for several runs is presented in figure 58.

The ideal isentropic gross thrust of each nozzle can also be determined if the mass-flow rate for each nozzle is known. The eight sonic nozzles forward of each of the nozzle tailpipes can be used for measuring mass-flow rate if an effective discharge coefficient for each is obtained. Since these nozzles are always choked, their ideal mass-flow rate is

$$\dot{m}_{i,c} = A_n p_c \sqrt{\frac{\gamma}{RT_c}\left(\frac{2}{\gamma + 1}\right)^{\frac{\gamma+1}{\gamma-1}}} \tag{B4}$$

where p_c and T_c are the chamber pressure and temperature measured in the supply pipes just ahead of the eight sonic nozzles. The effective discharge coefficient is

$$c_{d,c} = \frac{0.995\dot{m}_i}{\dot{m}_{i,c}} = \frac{\dot{m}_c}{\dot{m}_{i,c}} \tag{B5}$$

The variation of the effective discharge coefficients for both the left- and right-hand sets of sonic nozzles is shown in figure 59. Figure 60 presents mass-flow ratios determined by both the turbine flowmeter and from the chamber measurement.

The ideal isentropic gross thrust for the left nozzle is

$$F_i = c_{d,c}\left(\dot{m}_{i,c}\right)\sqrt{\left(RT_{t,j}\right)\frac{2\gamma}{\gamma - 1}\left(1 - \frac{p_a}{p_{t,j}}\right)^{\frac{\gamma-1}{\gamma}}} \tag{B6}$$

where measurements are made for the corresponding nozzle. The total ideal isentropic gross thrust is simply the sum of the ideal thrust computed for the left and right nozzle.

The flow control valves (fig. 3) are used to match up the jet stagnation pressure in each nozzle in order to equalize the thrust of each. Jet total pressure, ideal mass-flow rate, and ideal isentropic thrust can be matched to within 1 percent of each other as shown in figure 61.

At static conditions, both force balances measure thrust (drag equals zero) and these results are presented in figure 62. These results show excellent agreement between the measured values of thrust. Again, the various symbols represent several static runs. Static thrust ratios are presented in figure 63 where the values of F_j (measured thrust) were obtained from the thrust balance; the ratios presented are for the ideal isentropic thrust determined both by the turbine flowmeter (eq. (B1)) or from the chamber measurements (eqs. (B6) and (B7)). The ideal convergent nozzle thrust for choked conditions is computed from the following equation:

$$F_{i,con} = A_e p_{t,j}\left[\left(\frac{2}{\gamma + 1}\right)^{\frac{\gamma}{\gamma-1}}(\gamma + 1) - \frac{p_a}{p_{t,j}}\right] \tag{B7}$$

REFERENCES

1. Corson, Blake W., Jr.; Capone, Francis J.; and Putnam, Lawrence E.: Lift Induced on a Swept Wing by a Two-Dimensional Partial-Span Deflected Jet at Mach Numbers From 0.20 to 1.30. NASA TM X-2309, 1971.
2. Capone, Francis J.: Exploratory Investigation of Lift Induced on a Swept Wing by a Two-Dimensional Partial-Span Deflected Jet at Mach Numbers From 0.20 to 1.30. NASA TM X-2529, 1972.
3. Capone, Francis J.: Supercirculation Effects Induced by Vectoring a Partial-Span Rectangular Jet. AIAA Paper No. 74-971, Aug. 1974.
4. Pennington, Jack E.: Simulation Study of Effects of Thrust Vectoring and Induced Lift Due to Thrust Vectoring on Combat Effectiveness of a Fighter Aircraft. NASA TM X-3202, 1975.
5. Grahame, W. E.; Headley, J. W.; and Rogers, L. W.: Recent Experience in the Transonic Testing of Two-Dimensional Swept and Straight Wings With High Lift Devices. Facilities and Techniques for Aerodynamic Testing at Transonic Speeds and High Reynolds Number, AGARD-CP-83-71, Aug. 1971, pp. 6-1 – 6-17.
6. Peake, D. J.; Yoshihara, H.; Zonars, D.; and Carter, W.: The Transonic Performance of Two-Dimensional, Jet-Flapped Aerofoils at High Reynolds Numbers. Facilities and Techniques for Aerodynamic Testing at Transonic Speeds and High Reynolds Number, AGARD-CP-83-71, Aug. 1971, pp. 7-1 – 7-39.
7. Yoshihara, H.; Magnus, R.; and Zonars, D.: Transonic Drag Due to Lift of Planar Jet-Flapped Airfoils. Aerodynamic Drag. AGARD-CP-124-73, Oct. 1973.
8. Yoshihara, H.; Benepe, D. B.; and Whidden, P. D.: Transonic Performance of Jet Flaps on an Advanced Fighter Configuration. AFFDL-TR-73-97, U.S. Air Force, Sept. 1973. (Available from DDC as AD 913 798L.)
9. Parker, J. L.; and Ball, R. F.: An Analysis of the Effects of Internally Blown Jet Flaps on an Advanced Fighter Aircraft Design. AIAA Paper No. 74-970, Aug. 1974.
10. Corson, Blake W., Jr.; Runckel, Jack F.; and Igoe, William B.: Calibration of the Langley 16-Foot Transonic Tunnel With Test Section Air Removal. NASA TR R-423, 1974.
11. Reubush, David E.; and Runckel, Jack F.: Effect of Fineness Ratio on the Boattail Drag of Circular-Arc Afterbodies Having Closure Ratios of 0.50 With Jet Exhaust at Mach Numbers up to 1.30. NASA TN D-7192, 1973.

12. Berrier, Bobby Lee; and Wood, Frederick H., Jr.: Effect of Jet Velocity and Axial Location of Nozzle Exit on the Performance of a Twin-Jet Afterbody Model at Mach Numbers up to 2.2. NASA TN D-5393, 1969.

13. Lee, Edwin E., Jr.; and Runckel, Jack F.: Performance of Closely Spaced Twin-Jet Afterbodies With Different Inboard-Outboard Fairing and Nozzle Shapes. NASA TM X-2329, 1971.

14. Braslow, Albert L.; and Knox, Eugene C.: Simplified Method for Determination of Critical Height of Distributed Roughness Particles for Boundary-Layer Transition at Mach Numbers From 0 to 5. NACA TN 4363, 1958.

15. Braslow, Albert L.; Hicks, Raymond M.; and Harris, Roy V., Jr.: Use of Grit-Type Boundary-Layer-Transition Trips on Wind-Tunnel Models. NASA TN D-3579, 1966.

16. Shapiro, Ascher H.: The Dynamics and Thermodynamics of Compressible Fluid Flow. Vol. I. Ronald Press Co., c.1953.

17. Korbacker, G. K.; and Sridhar, K.: A Review of the Jet Flap. UTIA Rev. No. 14, Inst. Aerophys., Univ. of Toronto, May 1960.

18. Williams, J.; Butler, S. F. J.; and Ward, M. N.: The Aerodynamics of Jet Flaps. R. & M. No. 3304, Brit. A.R.C., 1963.

19. Poisson-Quinton, Ph.; and Lepage, L.: Survey of French Research on the Control of Boundary Layer and Circulation. Boundary Layer and Flow Control, Vol. 1, G. V. Lachmann, ed., Pergammon Press, Inc., 1961, pp. 21-73.

20. Maskell, E. C.; and Spence, D. A.: A Theory of the Jet Flap in Three Dimensions. Proc. Roy. Soc. (London), ser. A, vol. 251, no. 1266, June 9, 1959, pp. 407-425.

21. Igoe, William B.; Re, Richard J.; and Cassetti, Marlowe D.: Transonic Aerodynamic Characteristics of a Wing-Body Combination Having a 52.5° Sweptback Wing of Aspect Ratio 3 With Conical Camber and Designed for a Mach Number of $\sqrt{2}$. NASA TN D-817, 1961.

22. Putnam, Lawrence E.: An Analytical Study of the Effects of Jets Located More Than One Jet Diameter Above a Wing at Subsonic Speeds. NASA TN D-7754, 1974.

23. Lowry, John G.; Riebe, John M.; and Campbell, John P.: The Jet-Augmented Flap. Preprint No. 715, S.M.F. Fund Paper, Inst. Aeronaut. Sci., Jan. 1957.

24. Stratford, B. S.: The Calculation of the Discharge Coefficient of Profiled Choked Nozzles and the Optimum Profile for Absolute Air Flow Measurement. J. Royal Aeronaut. Soc., vol. 68, no. 640, Apr. 1964, pp. 237-245.

25. Sparkes, D. W.: A Standard Choked Nozzle for Absolute Calibration of Air Flowmeters. Aeronaut. J., vol. 72, no. 688, Apr. 1968, pp. 335-338.

TABLE I. - BODY ORDINATES

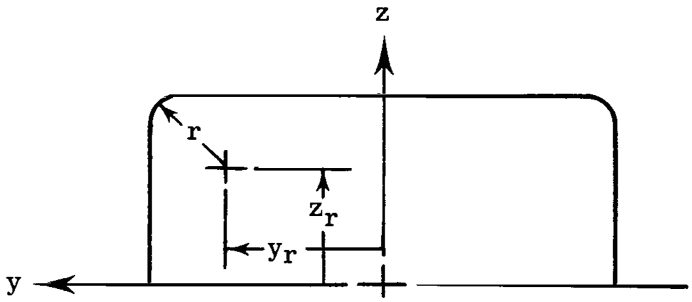

x, cm	y, cm	z, cm	r, cm	$\pm y_r$, cm	$\pm z_r$, cm
0	0	0	0	0	0
2.54	.914	.812	.812	.102	↓
5.08	1.816	1.603	1.603	.213	
7.62	2.695	2.360	2.360	.335	
10.16	3.551	3.078	3.078	.472	
15.24	5.192	4.379	4.379	.813	
20.32	6.711	5.420	5.420	1.290	
22.86	7.417	5.814	5.814	1.603	
25.40	8.082	6.109	6.109	1.974	
30.48	9.268	6.350	6.350	2.918	
38.10	10.262	↓	↓	4.270	
45.72	11.338			4.988	
49.53	11.430			5.080	
55.88	↓		4.618	6.812	1.732
63.50			2.540	8.890	3.810
98.90			2.540	8.890	3.810
99.16			2.540	8.890	3.810
119.38			2.540	8.890	3.810
120.65		6.266	2.540	8.867	3.701
121.92		5.994	2.403	9.027	3.592
127.00		4.877	1.717	9.713	3.160
132.08		3.749	1.026	10.404	2.723
138.68		2.286	.127	11.303	2.159

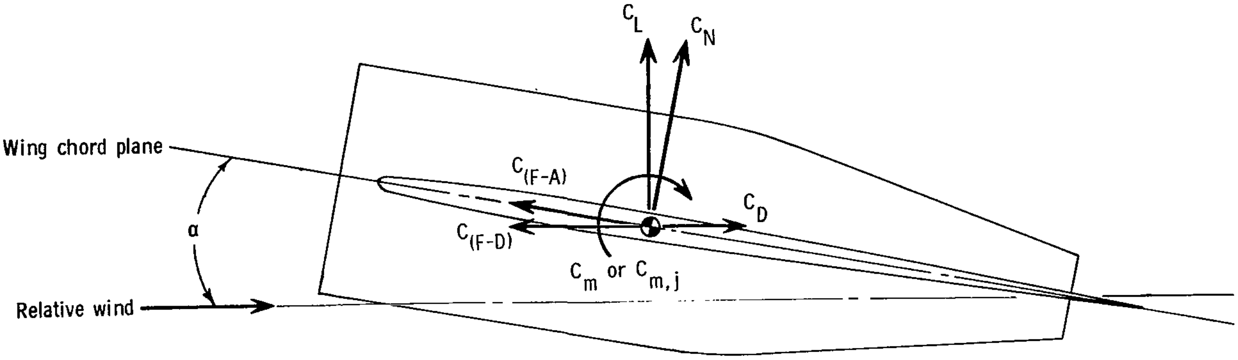

(a) External forces.

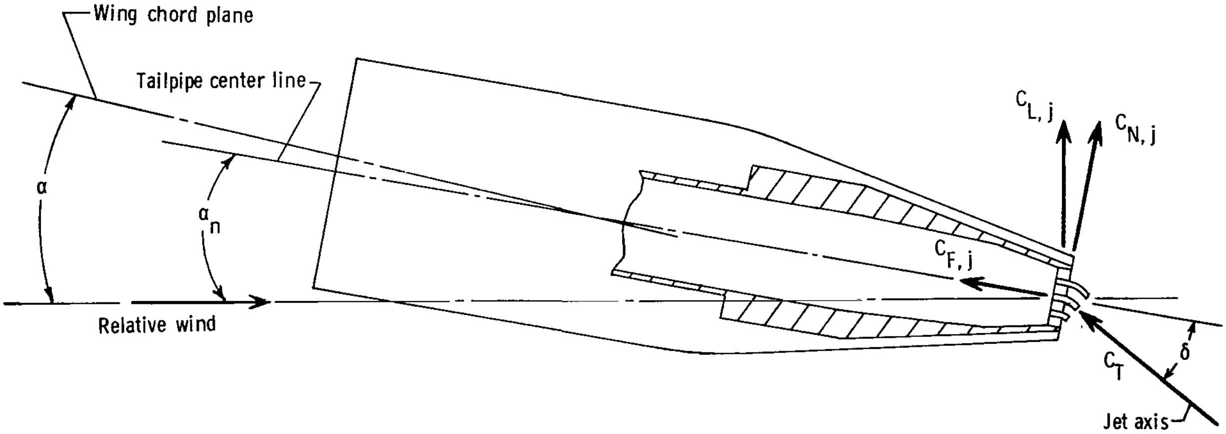

(b) Internal forces.

Figure 1.- Definition of model forces showing positive directions.

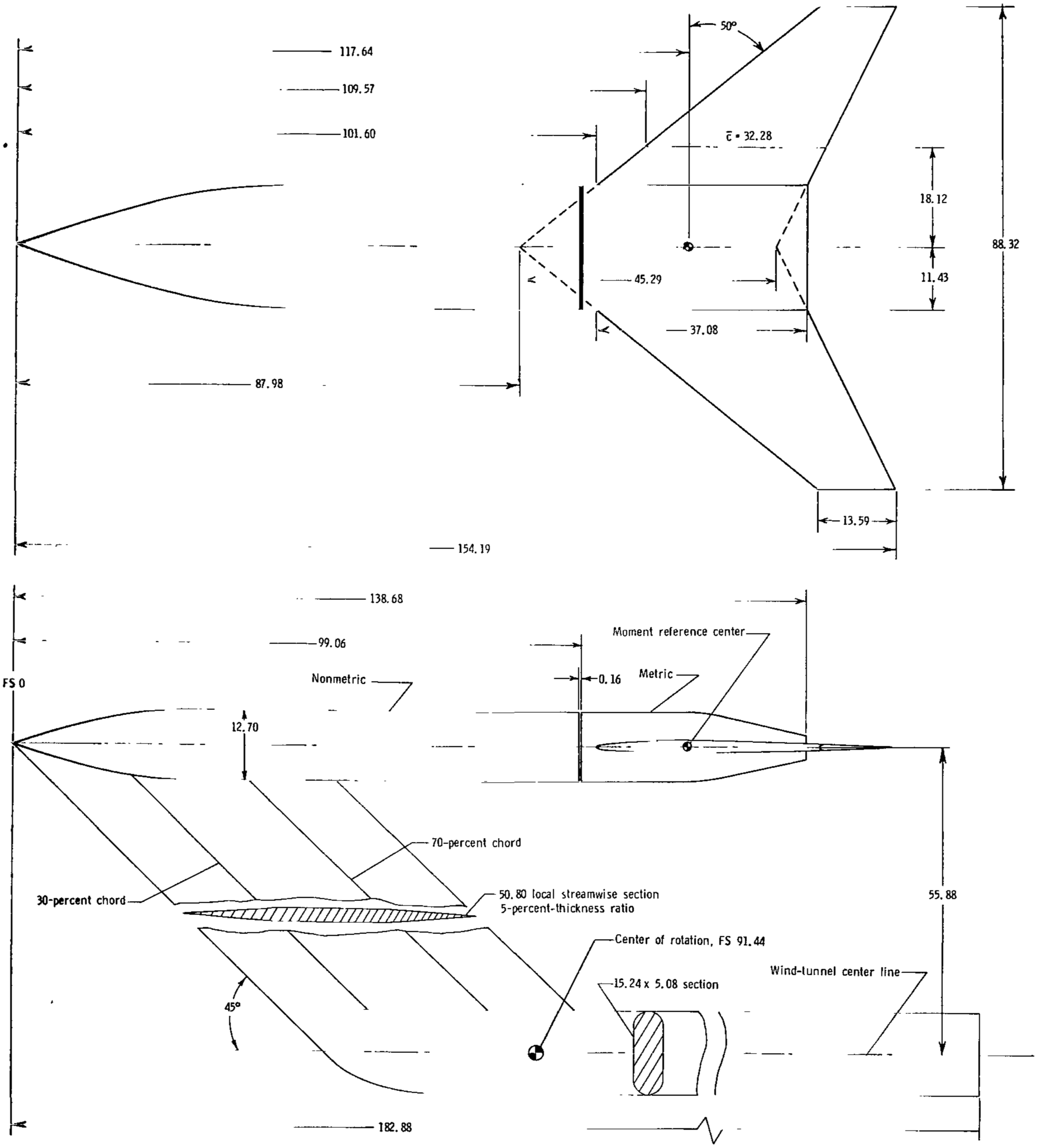

(a) Drawing of model.

Figure 2.- Model details. All dimensions in centimeters unless otherwise noted. FS denotes fuselage station.

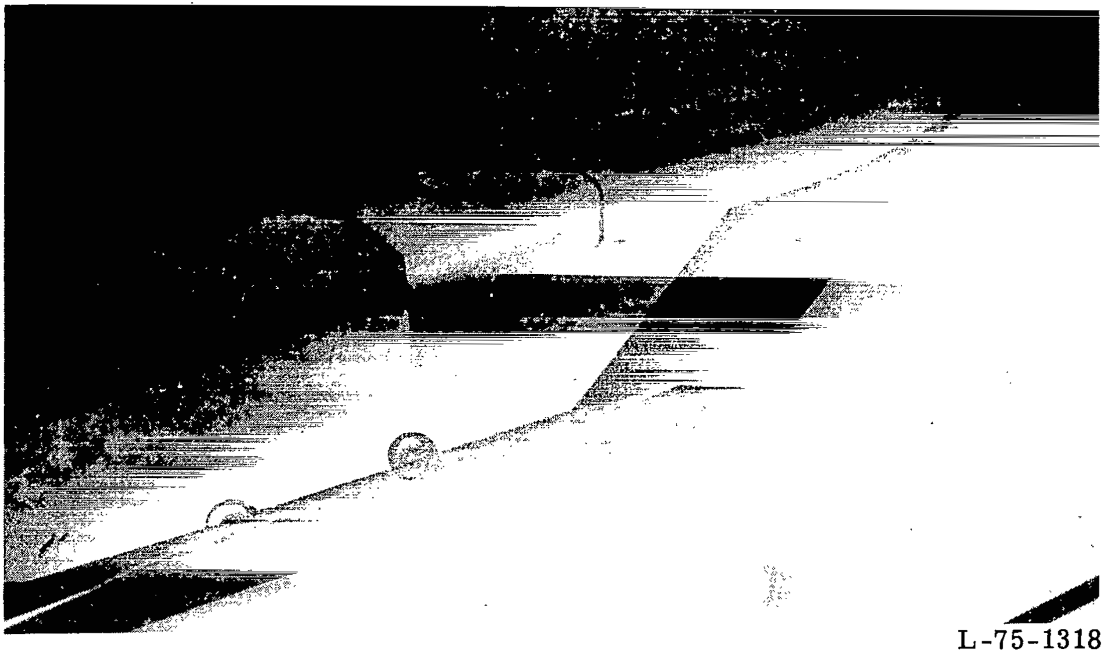

L-75-1318

Three-quarter rear view

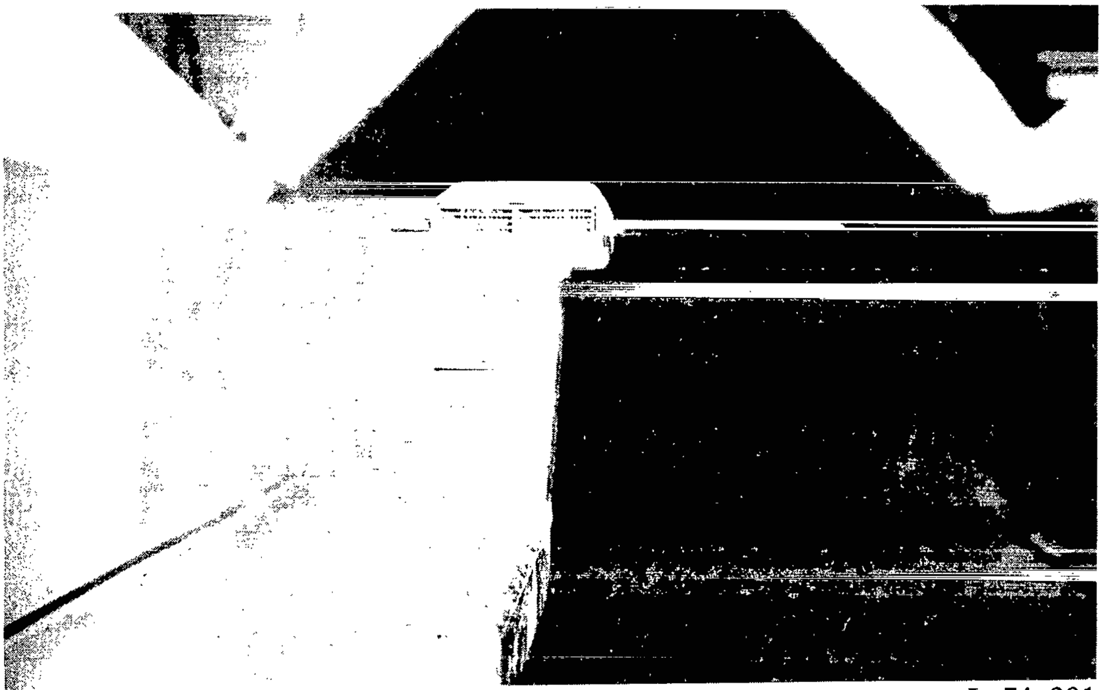

L-74-231

End view

(b) Photographs of model.

Figure 2.- Continued.

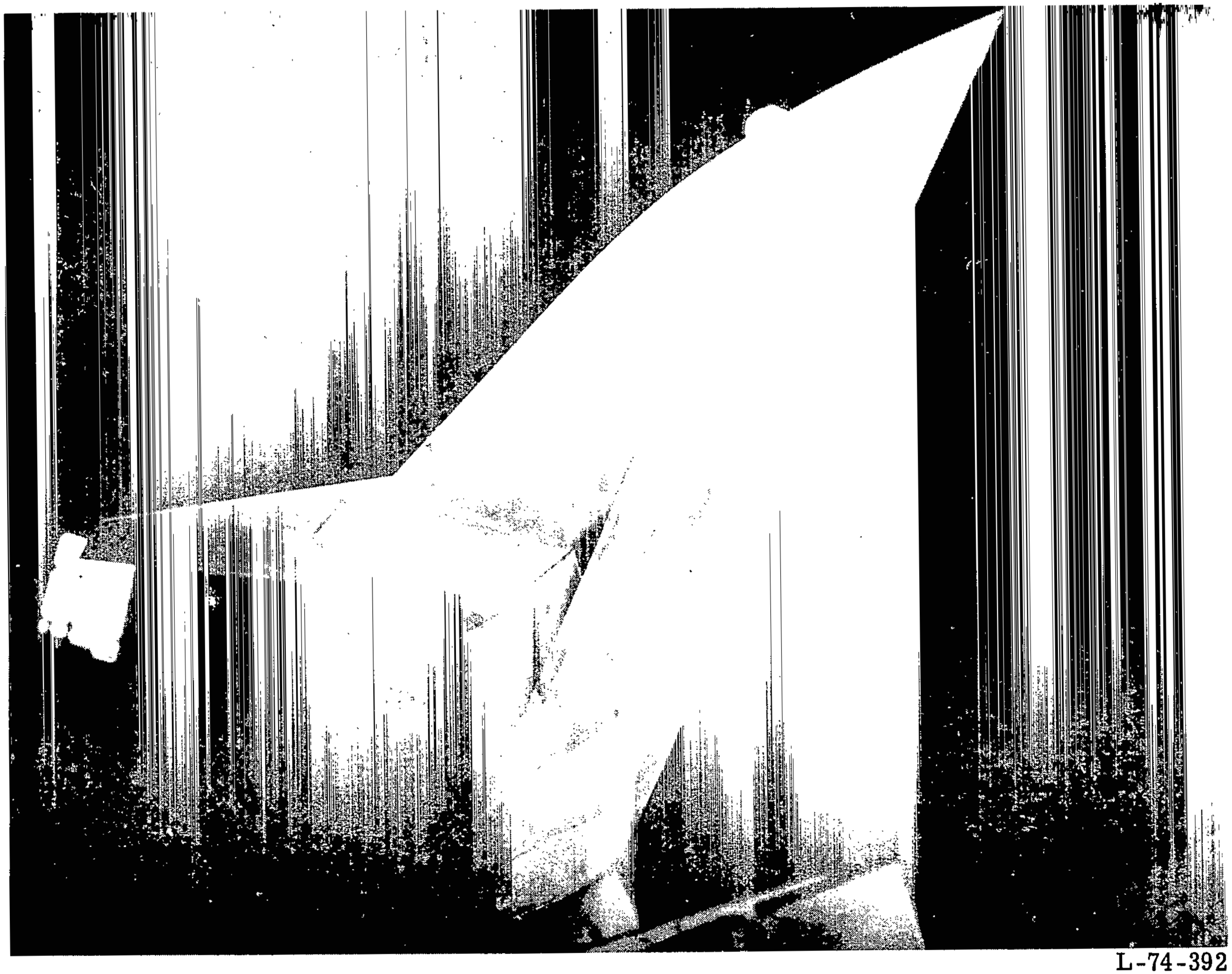

(b) Concluded.

Figure 2.- Concluded.

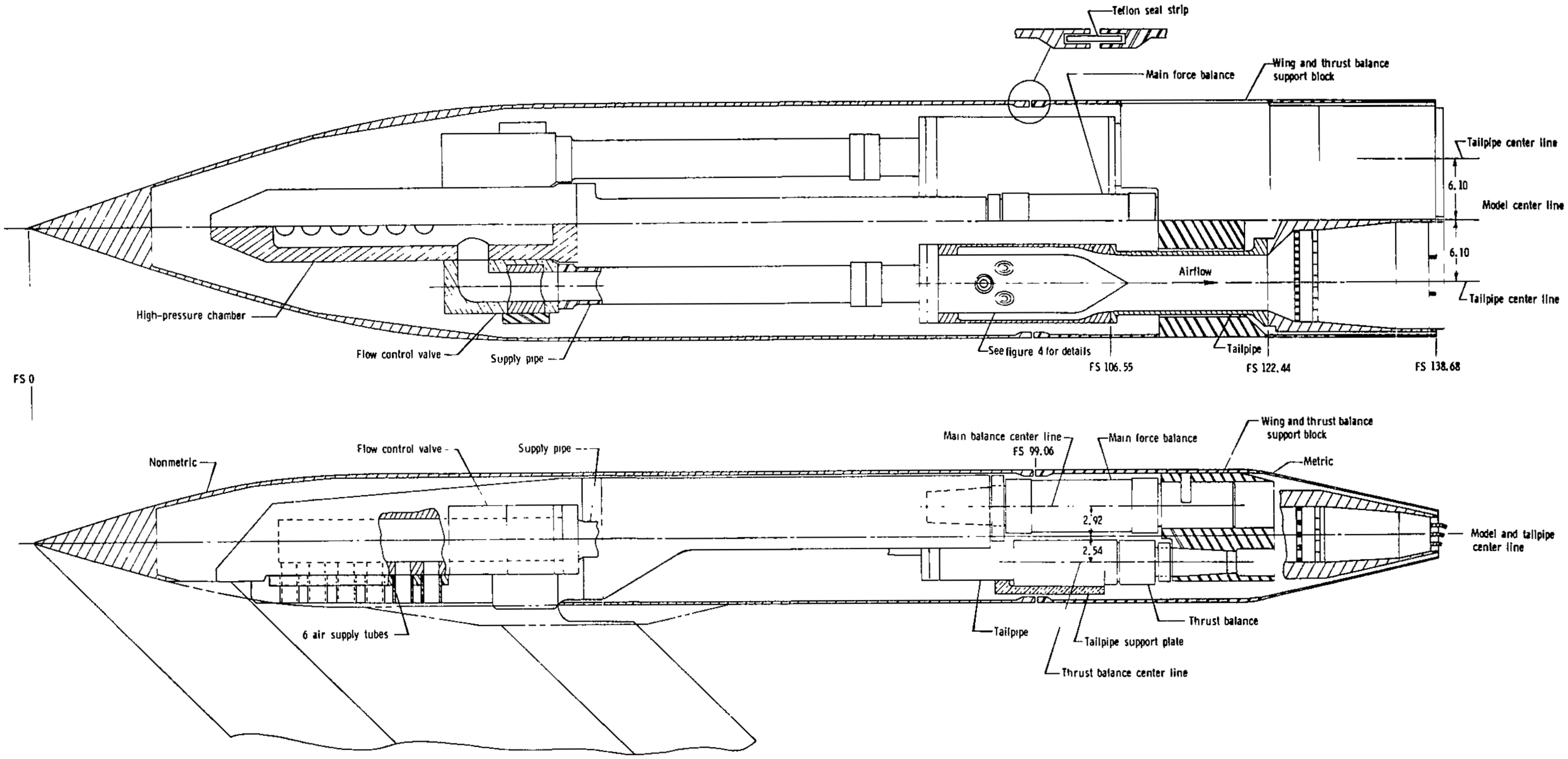

Figure 3.- Sketch of model and twin-jet exhaust nozzle simulation system. All dimensions are in centimeters.

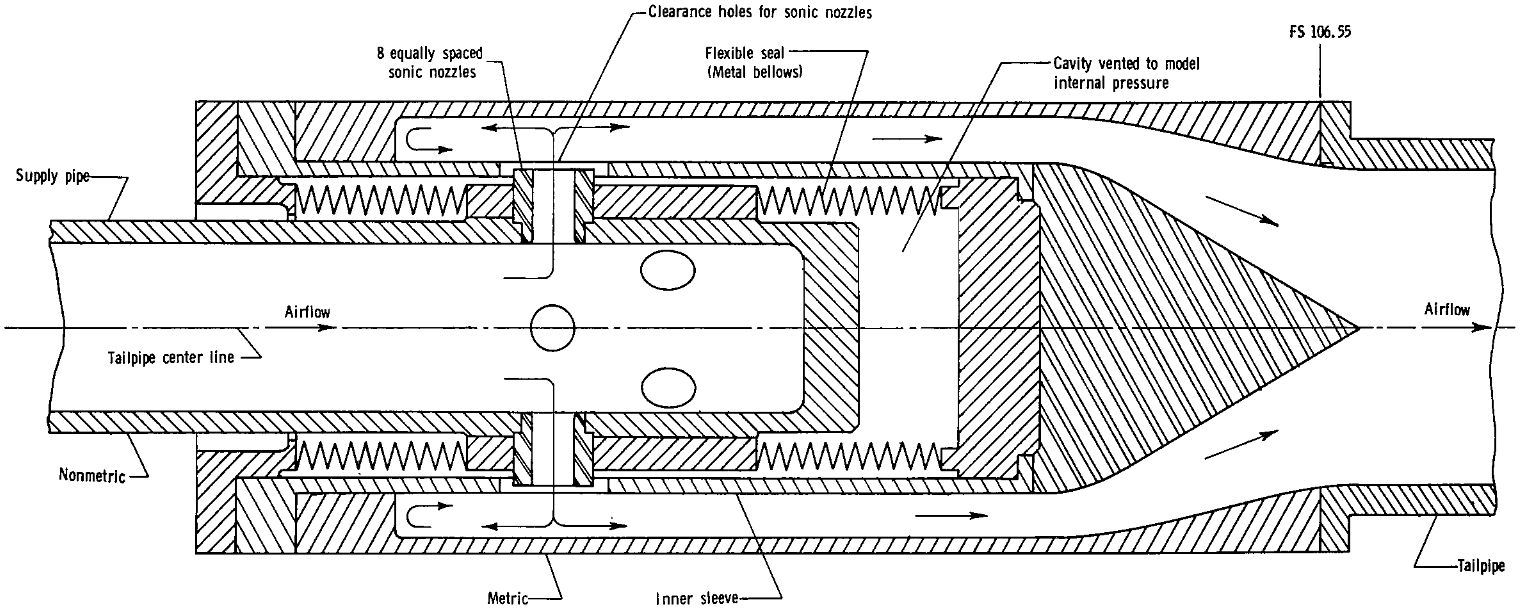

Figure 4.- Details of bellows arrangement used to transfer air from nonmetric to metric portions of model. Dimensions are in centimeters.

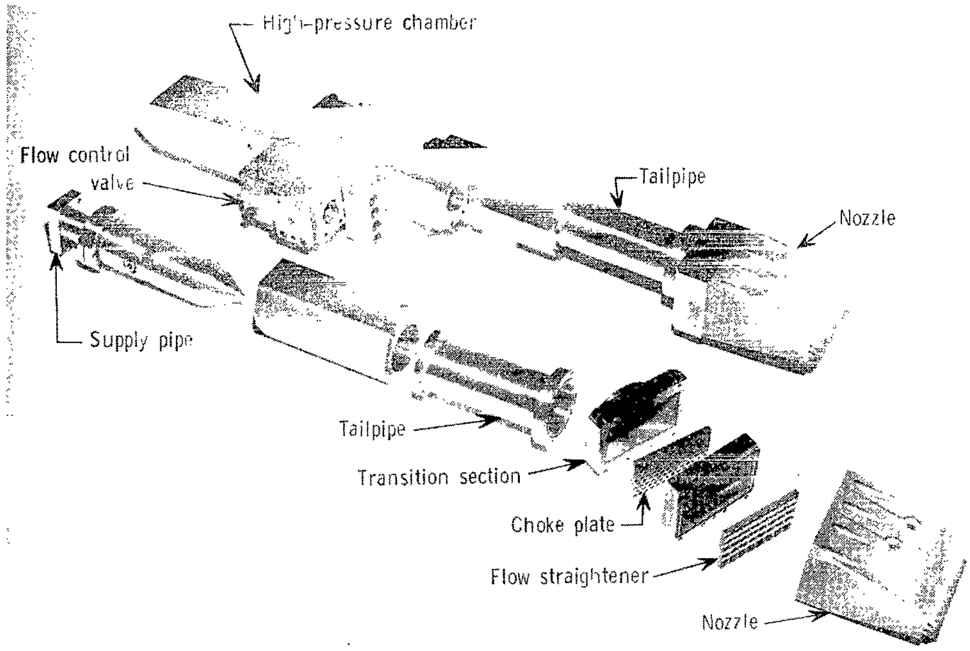

L-70-7604.1

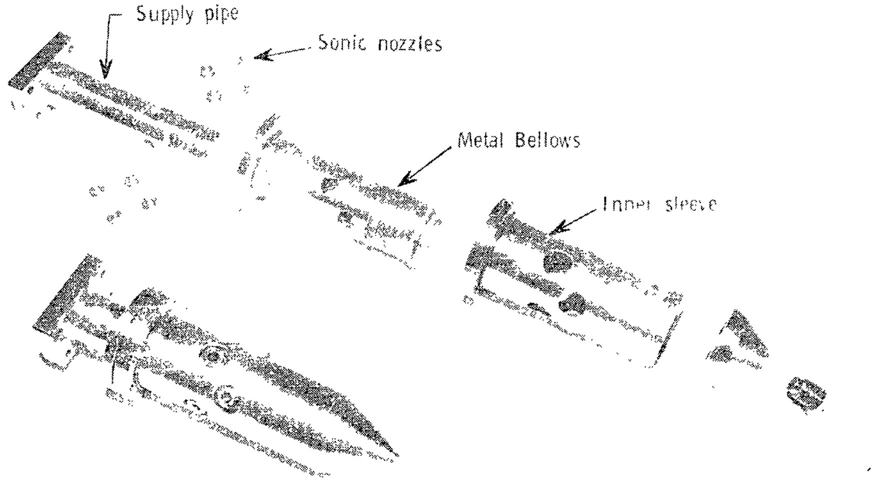

L-70-7605.1

Figure 5.- Photographs of propulsion simulation system.

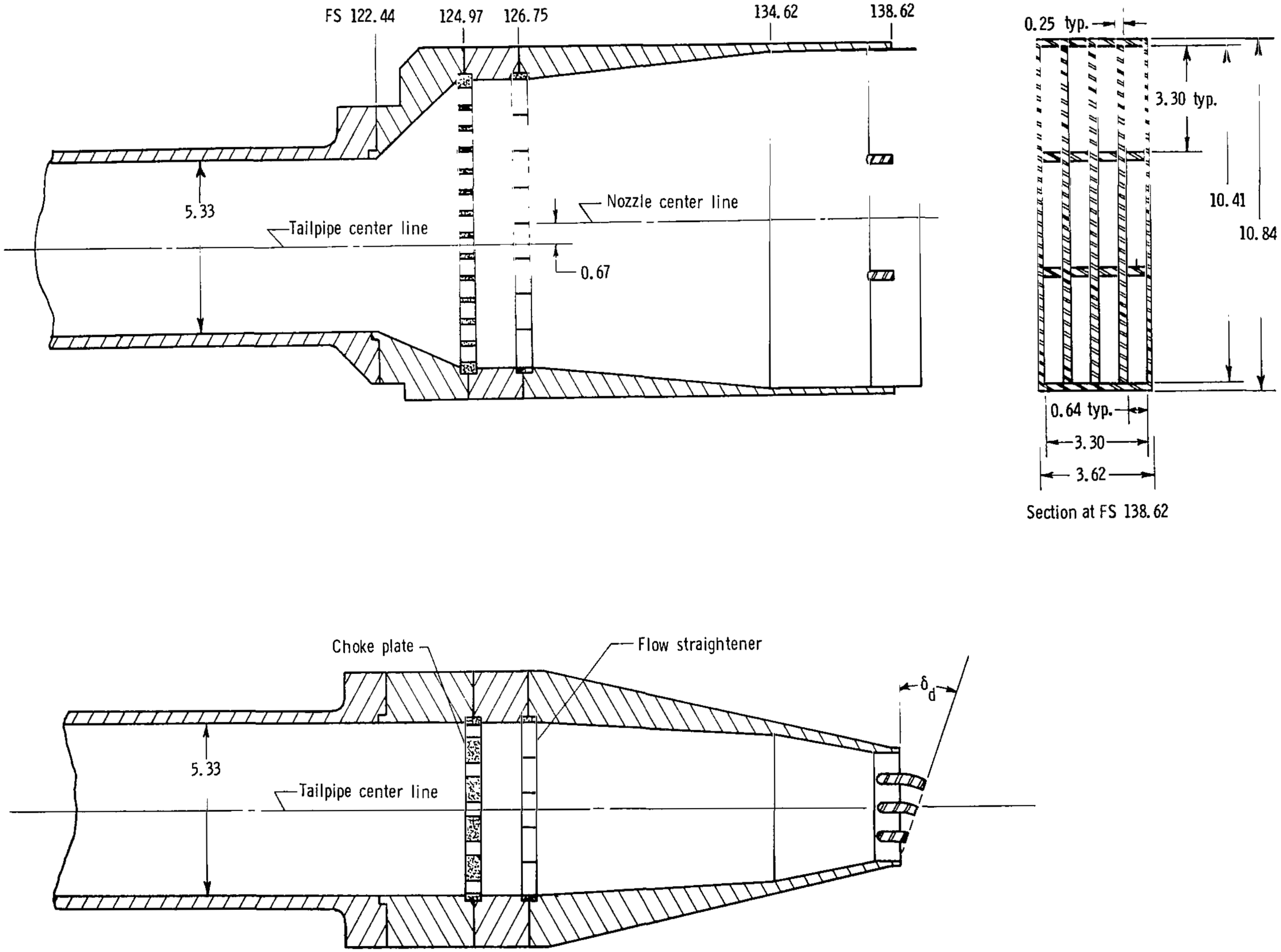

Figure 6.- Nozzle details. All dimensions are in centimeters except as noted.

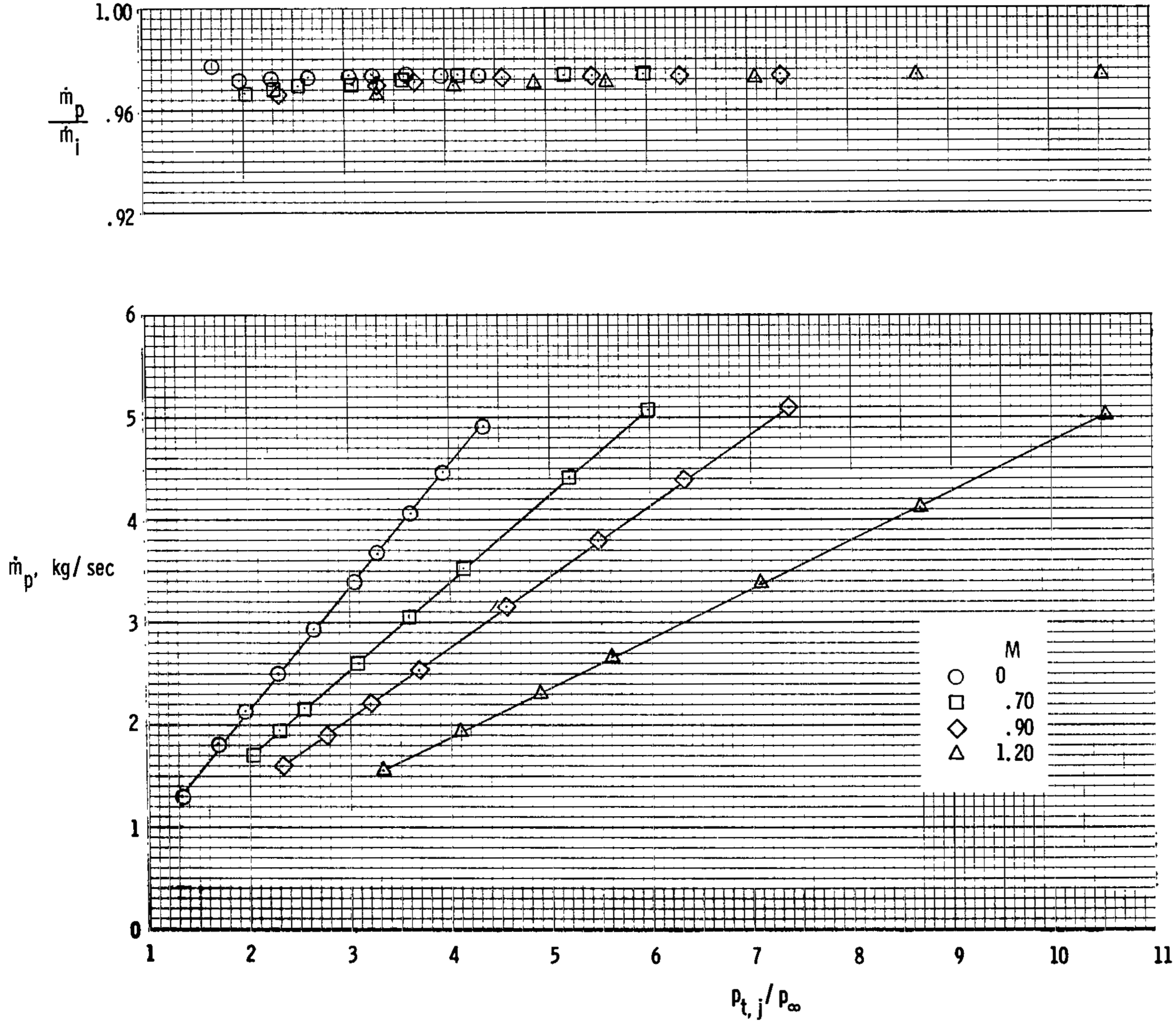

Figure 7.- Typical mass-flow rate and discharge coefficient characteristics.

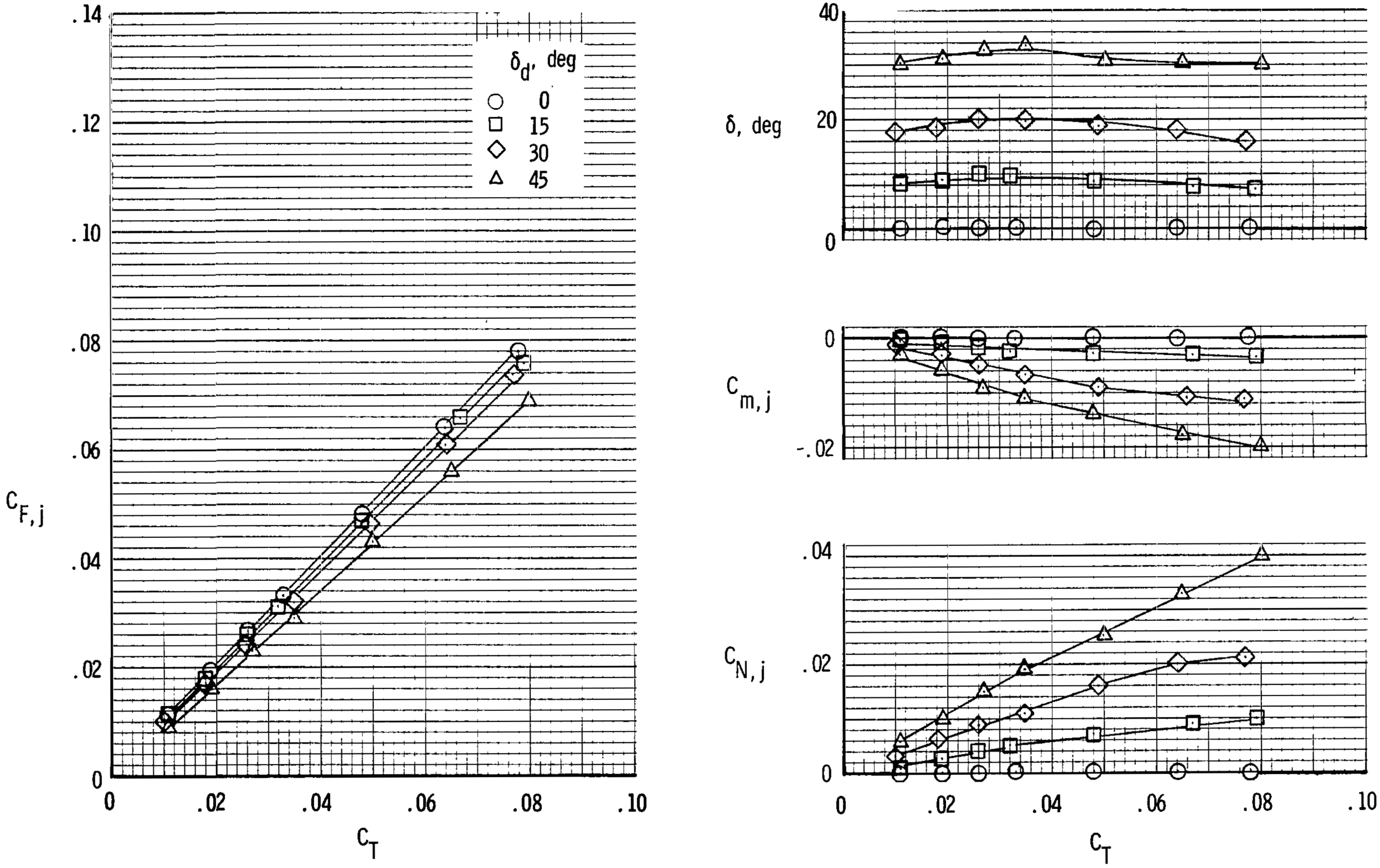

Figure 8.- Static thrust and effective turning-angle characteristics.

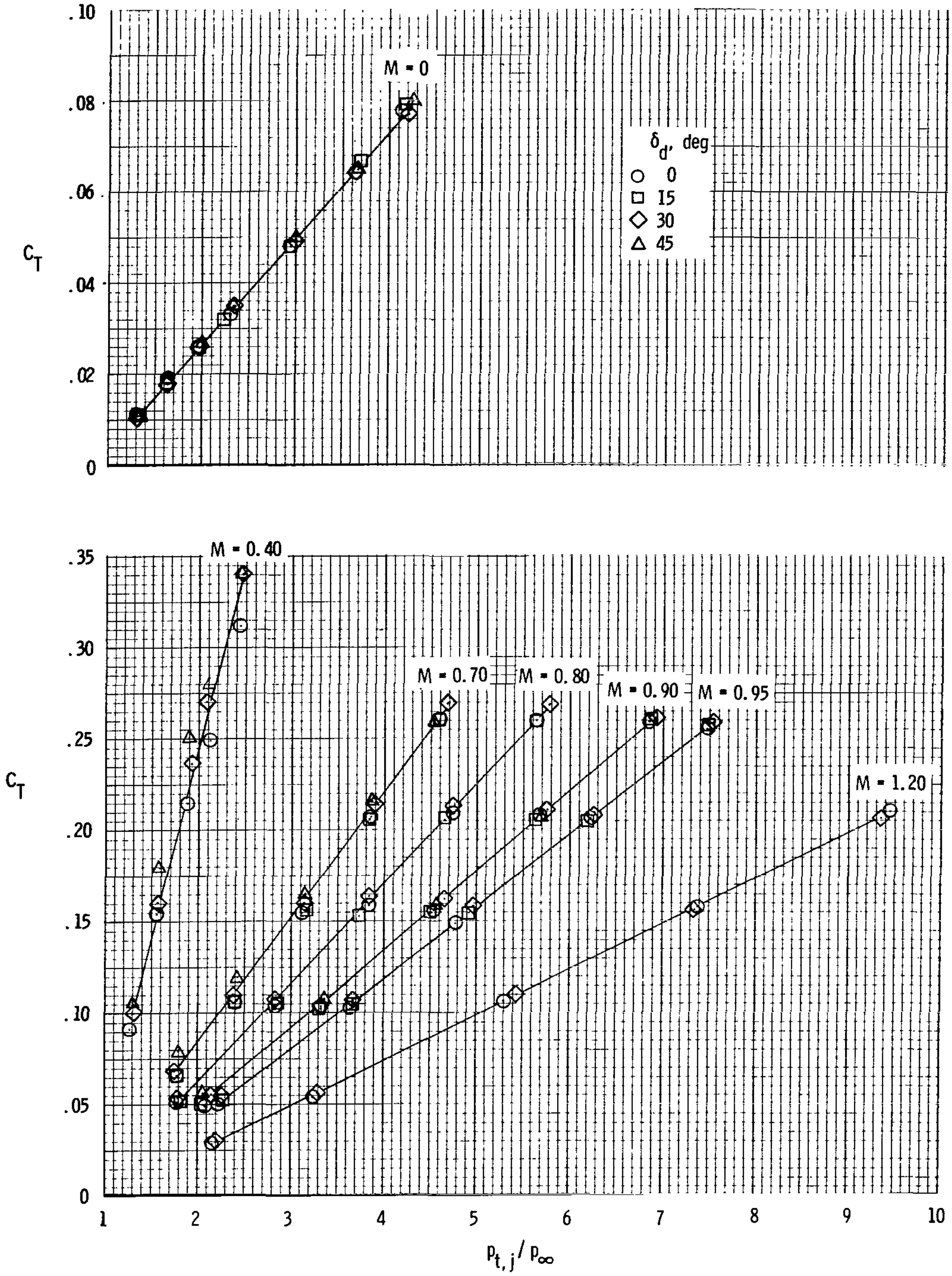

Figure 9.- Variation of measured thrust coefficient with nozzle pressure ratio.

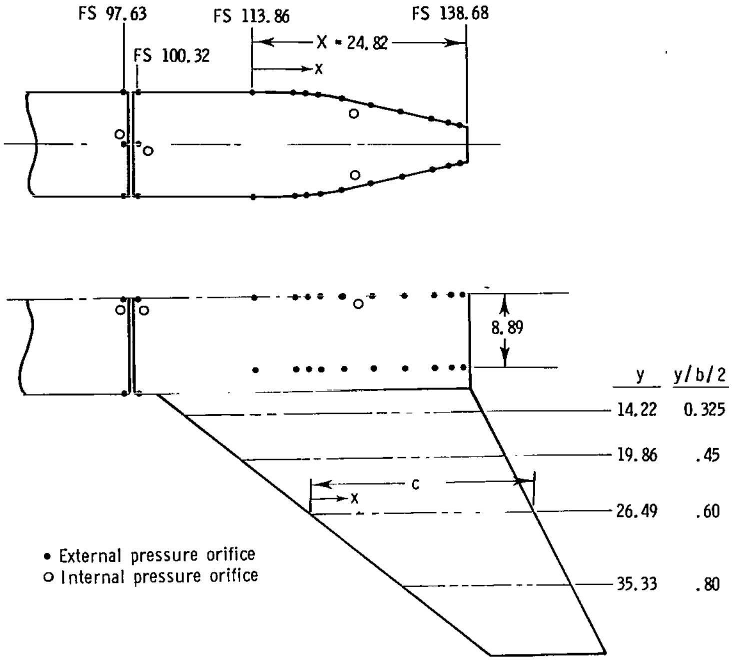

Afterbody pressure orifices

x, cm	x/X	$\frac{x + 113.86}{l}$
0.00	0.000	0.00
4.88	.200	.86
6.25	.257	.87
7.64	.315	.88
10.41	.429	.90
13.89	.572	.925
17.35	.714	.95
20.83	.858	.975
22.88	.943	.99
23.77	.98	.996

Wing pressure orifices

x/c	Upper	Lower
0.000	•	
.025	•	•
.05	•	•
.075	•	
.10	•	•
.15	•	
.20	•	•
.25	•	
.30	•	•
.35	•	
.40	•	•
.45	•	
.50	•	•
.55	•	
.60	•	•
.65	•	
.70	•	•
.75	•	
.80	•	•
.85	•	
.90	•	•
.95	•	•
1.00	•	

Figure 10.- Sketch showing locations of various pressure orifices. Typical internal pressures shown at approximate locations. All dimensions are in centimeters.

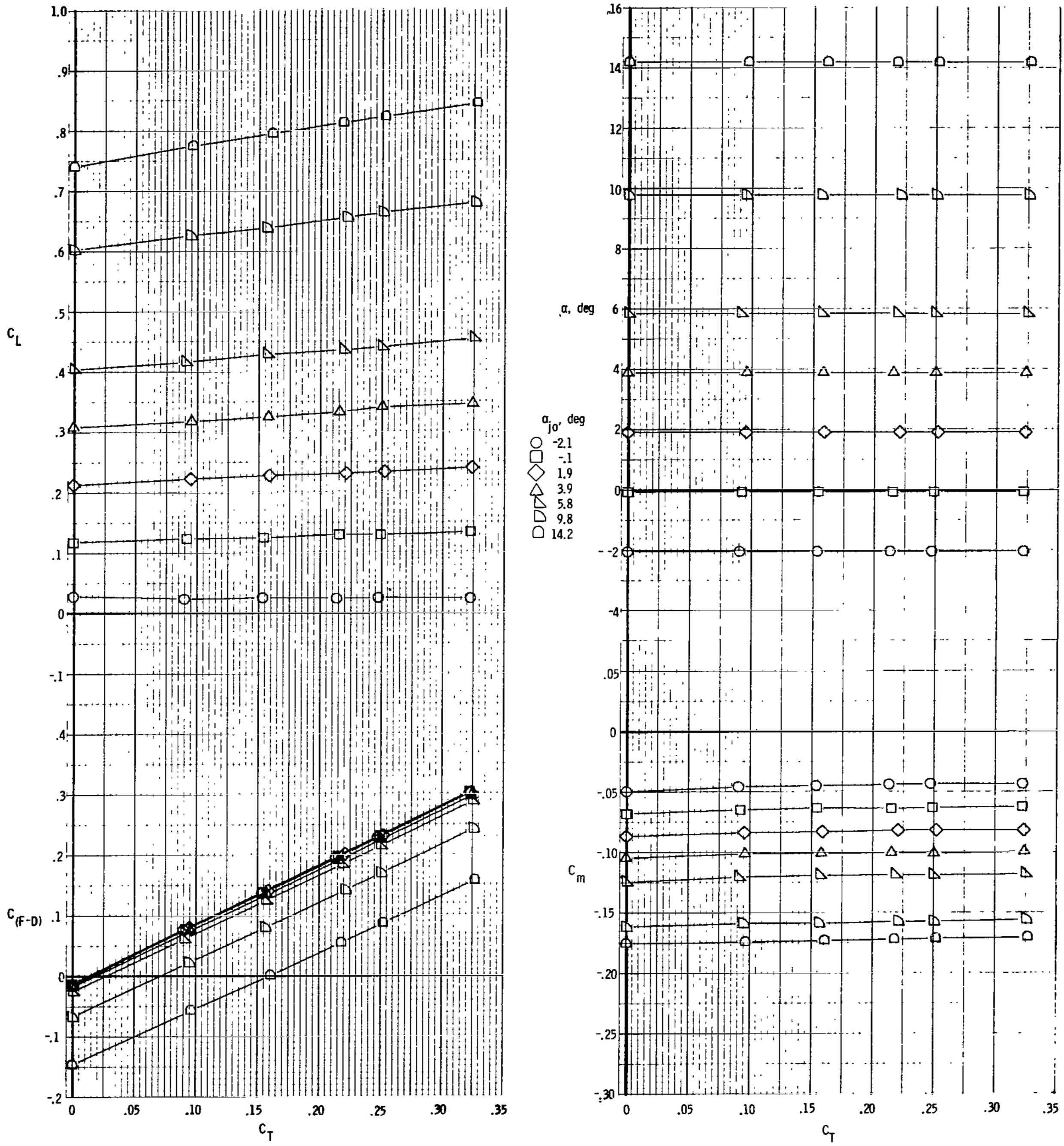

(a) M = 0.40.

Figure 11.- Basic aerodynamic characteristics. $\delta_d = 0^{\circ}$.

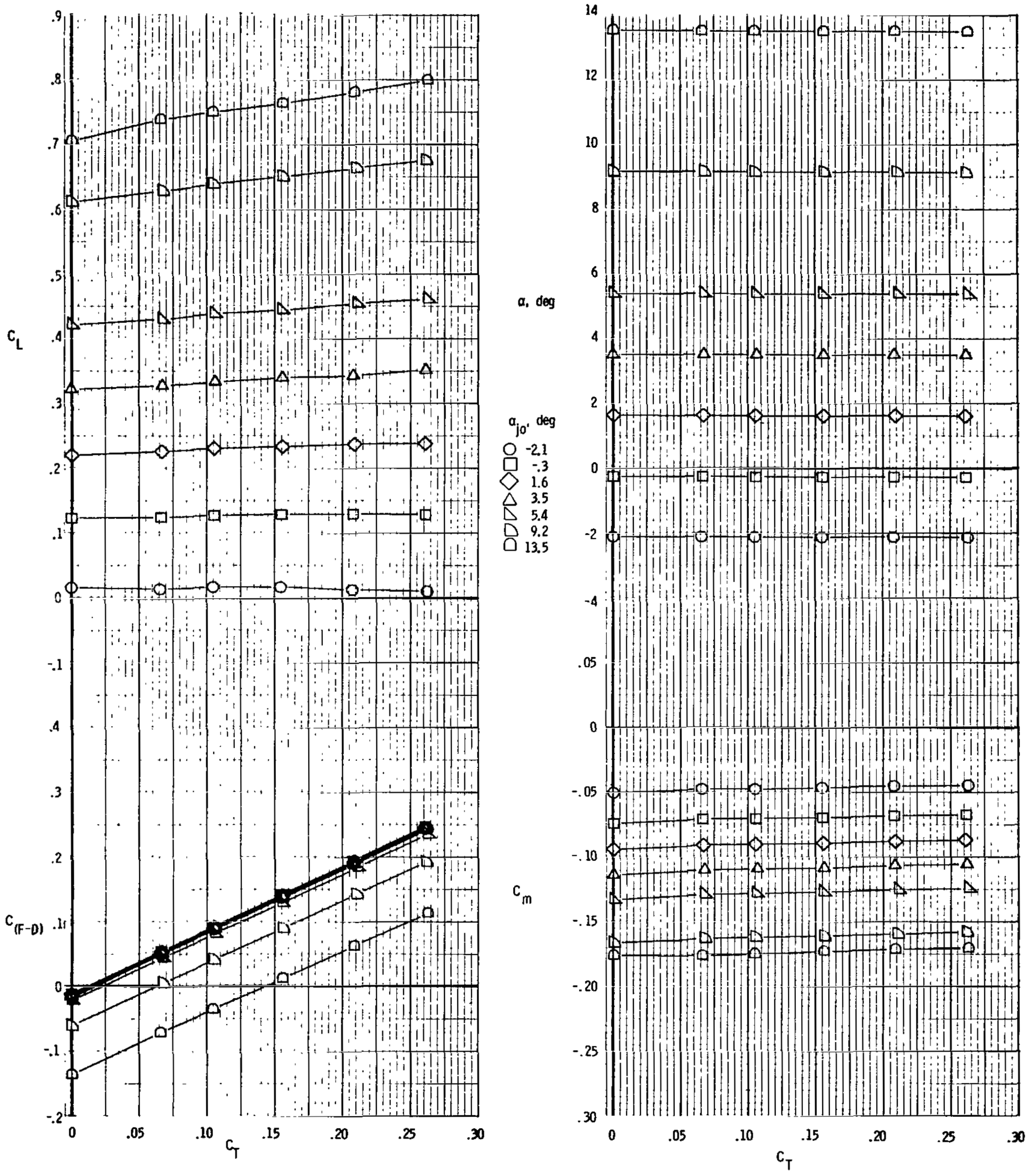

(b) M = 0.70.

Figure 11.- Continued.

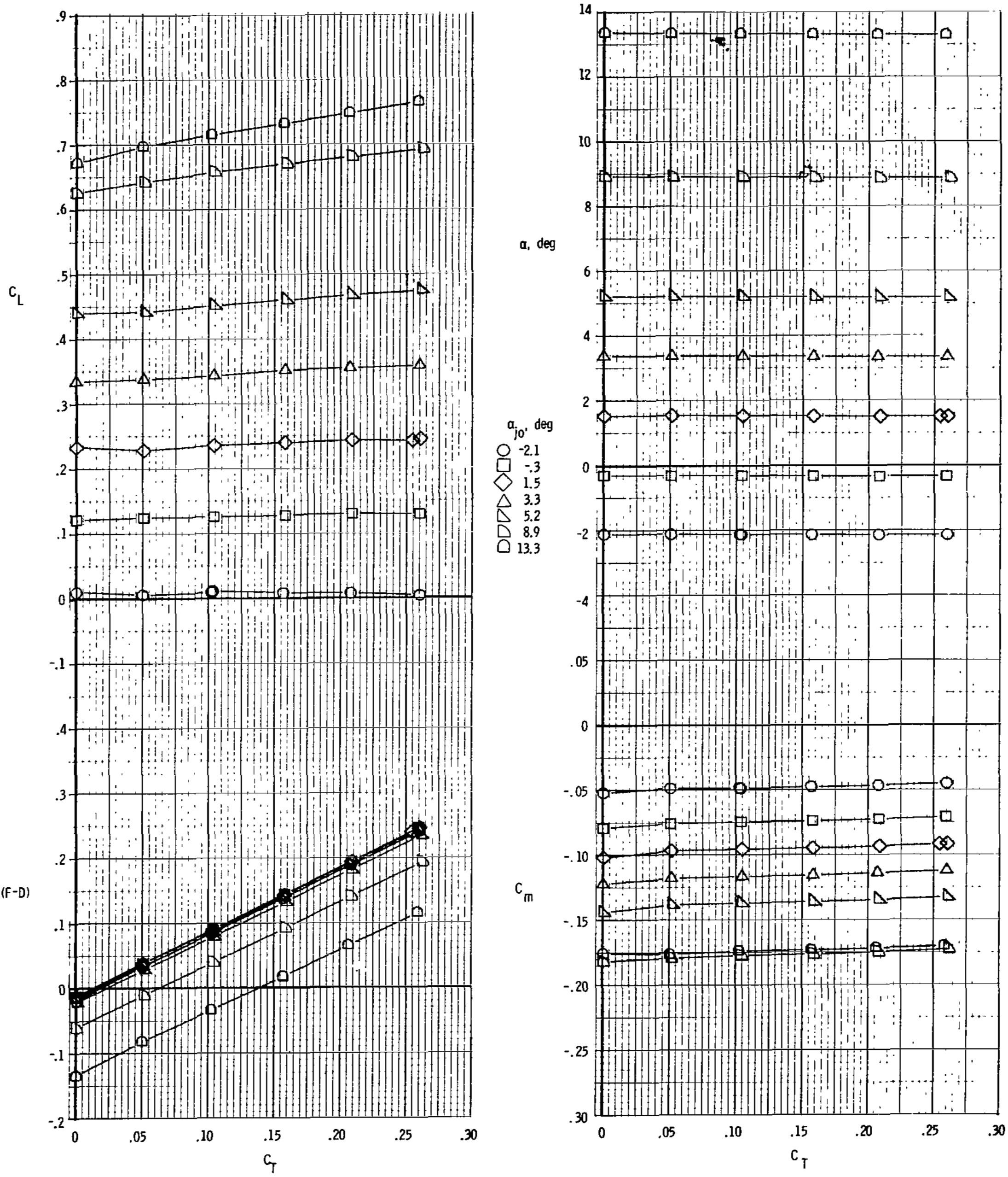

(c) M = 0.80.

Figure 11.- Continued.

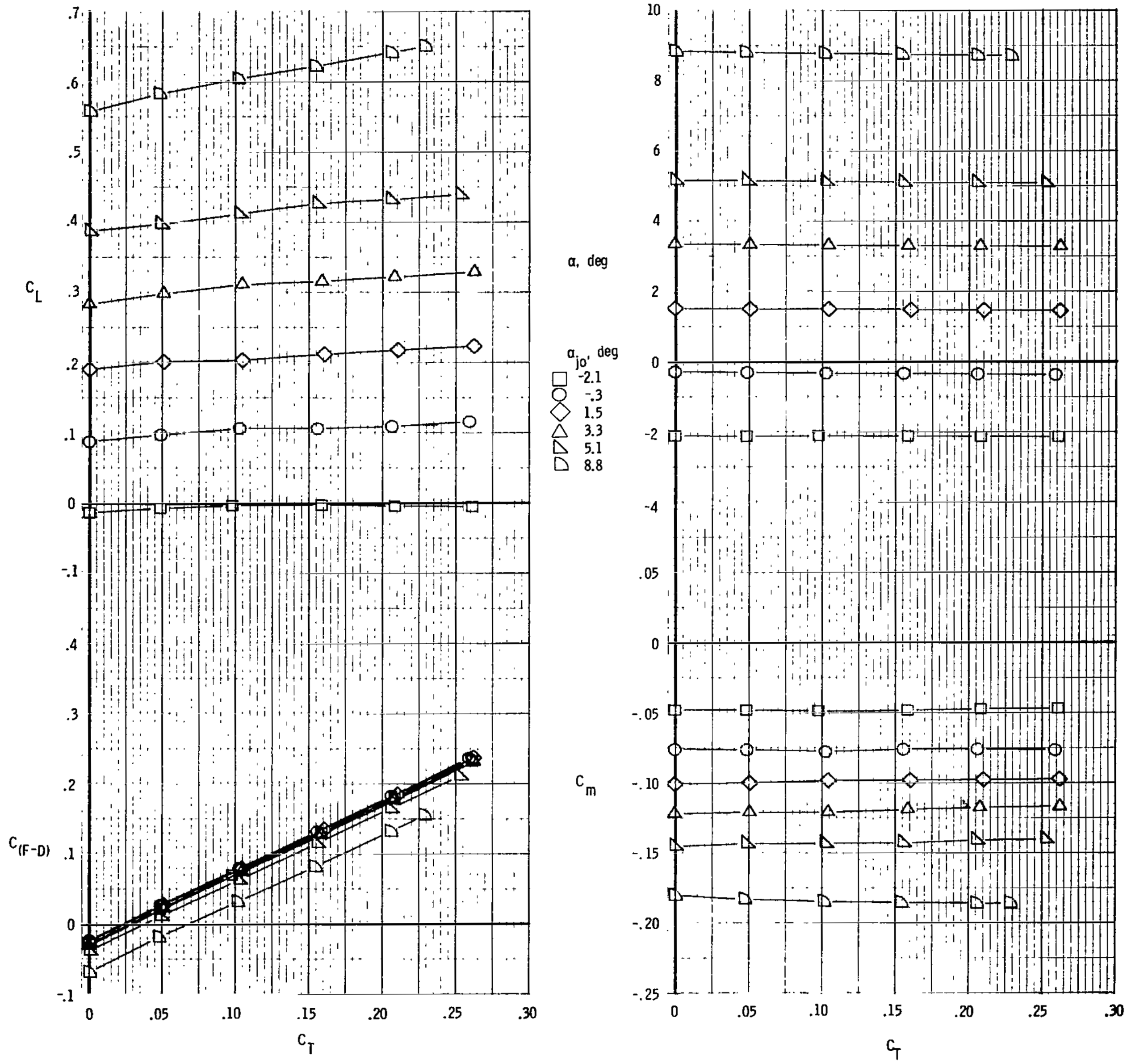

(d) M = 0.90.

Figure 11.- Continued.

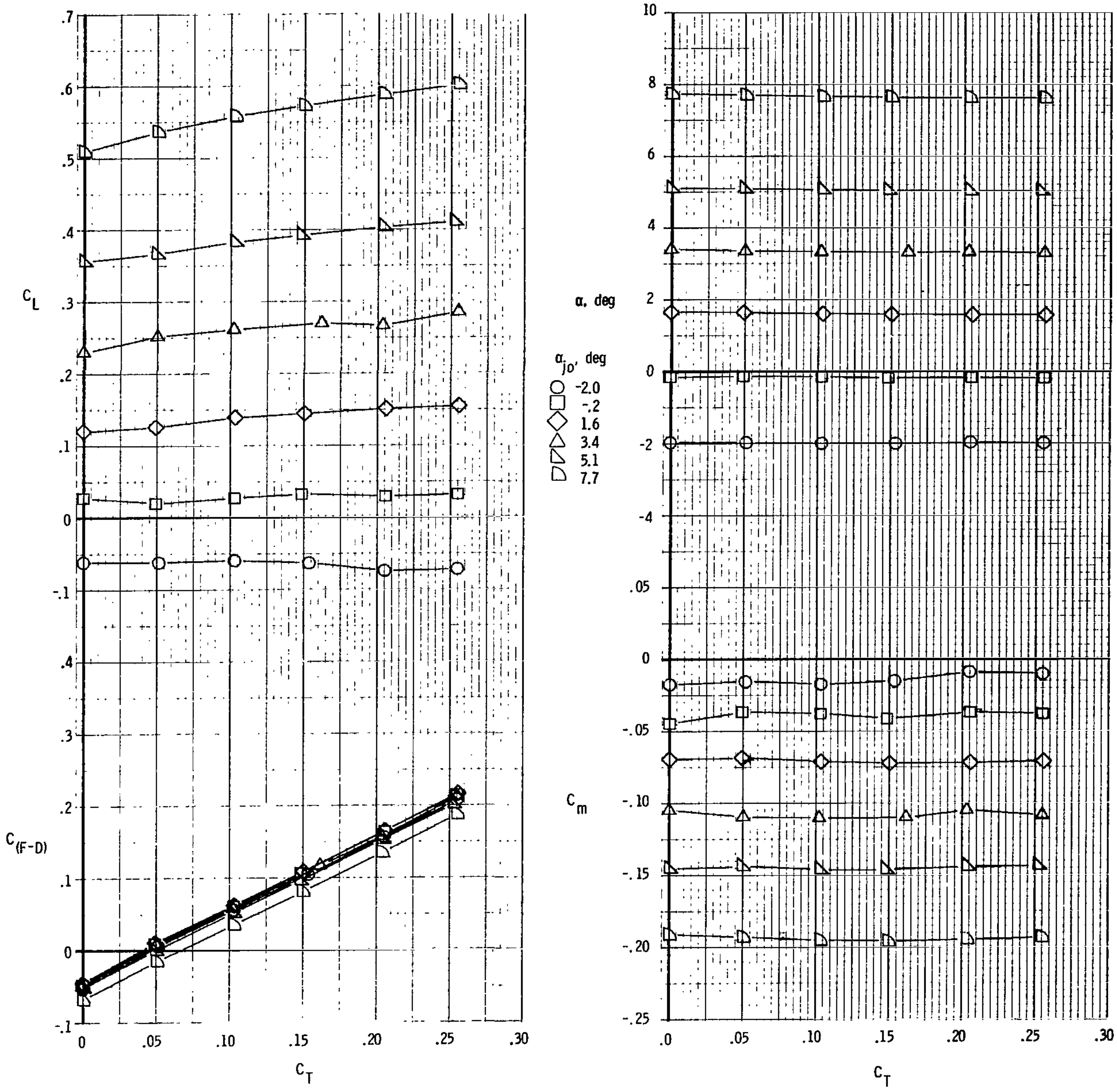

(e) M = 0.95.

Figure 11.- Continued.

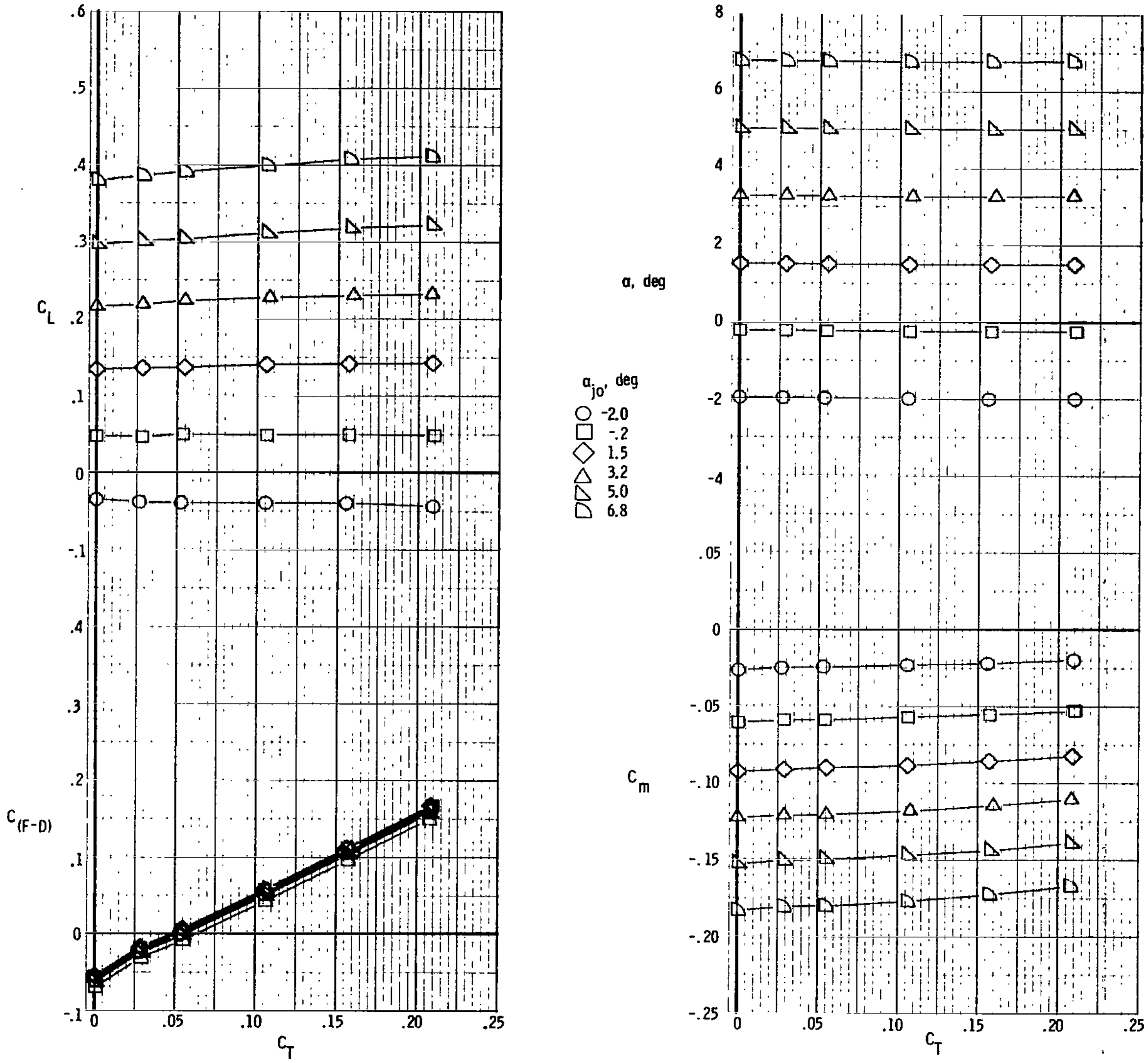

(f) M = 1.20.

Figure 11.- Concluded.

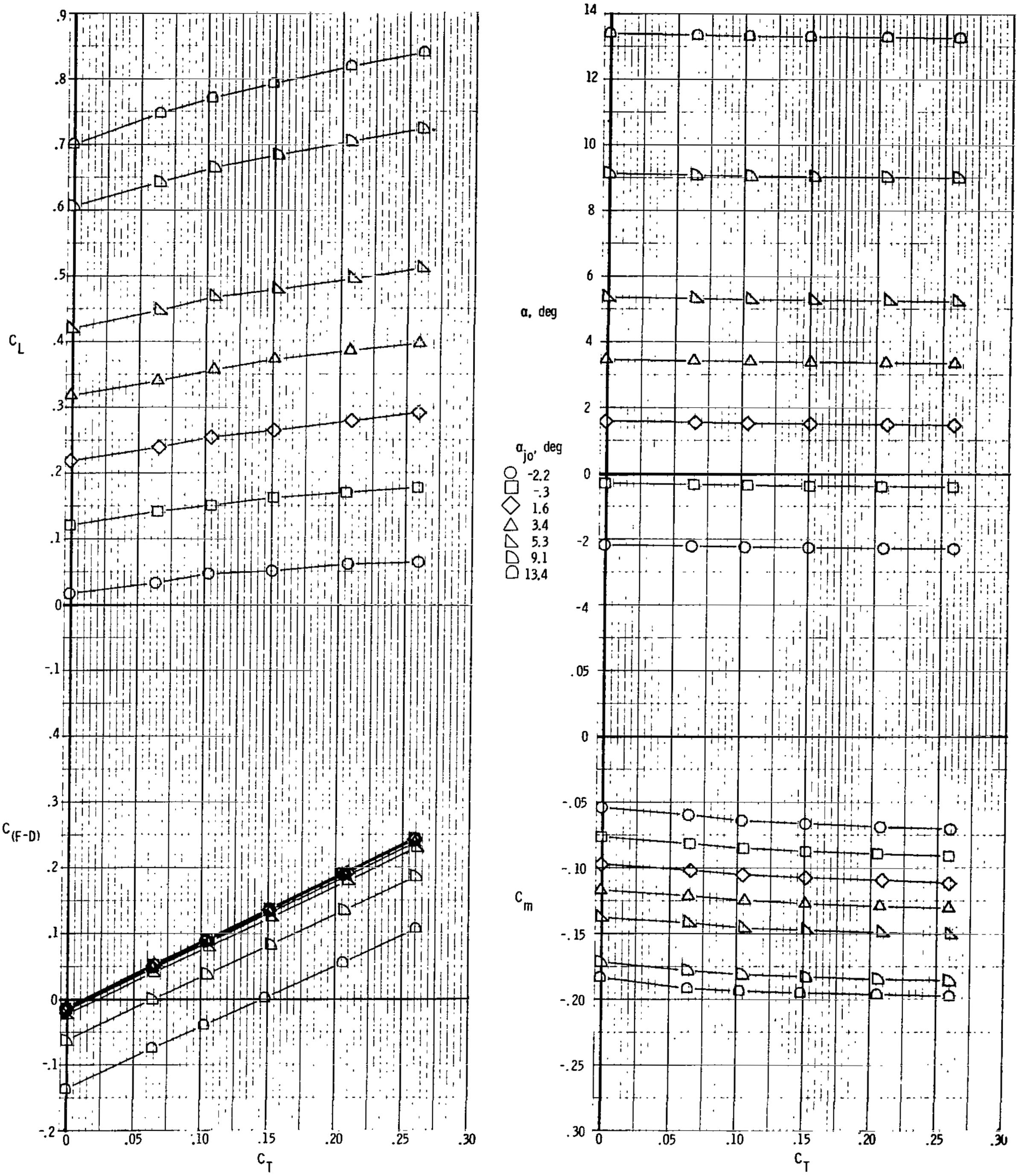

(a) M = 0.70.

Figure 12.- Basic aerodynamic characteristics. $\delta_d = 15^{\circ}$.

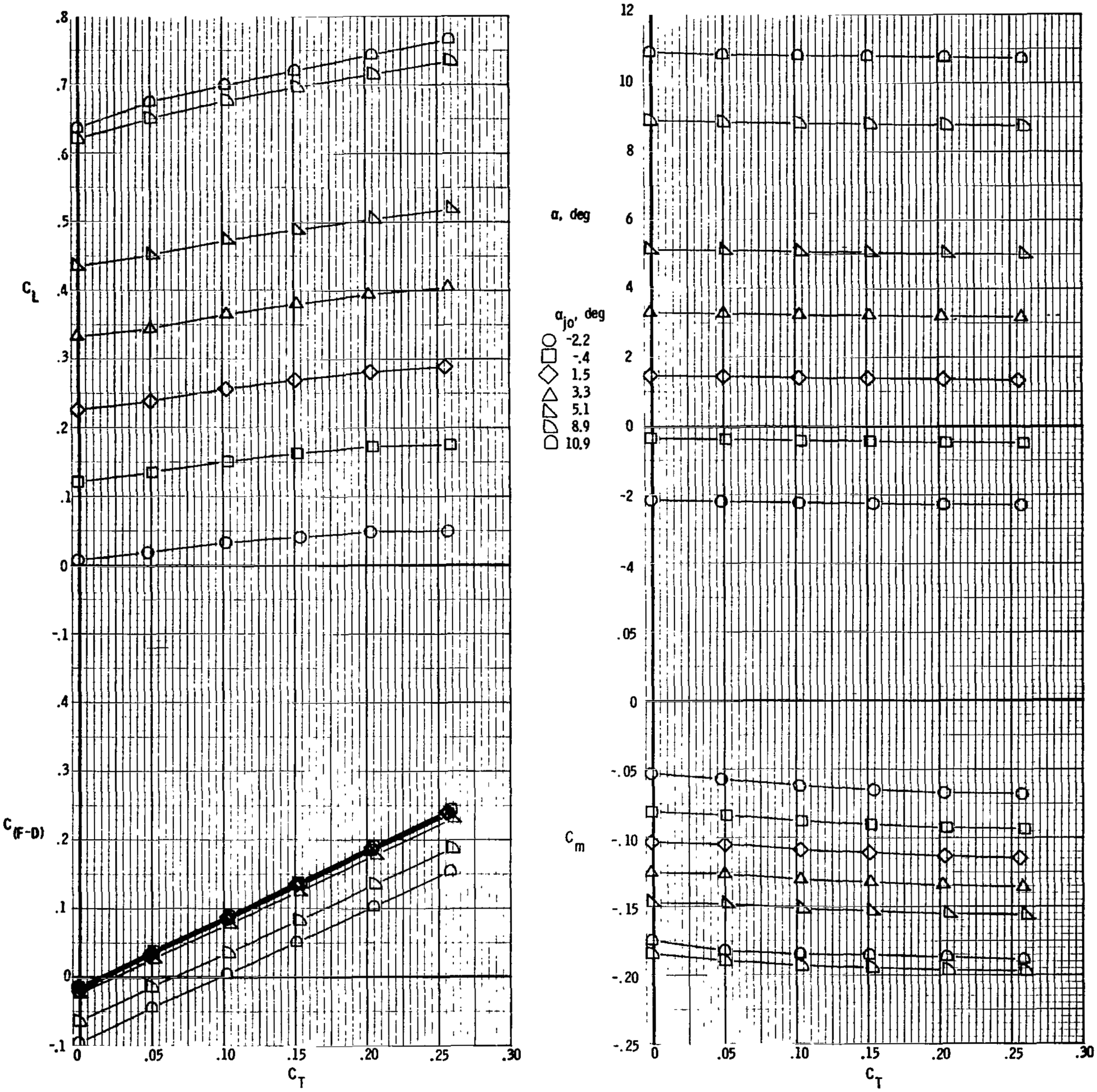

(b) M = 0.80.

Figure 12.- Continued.

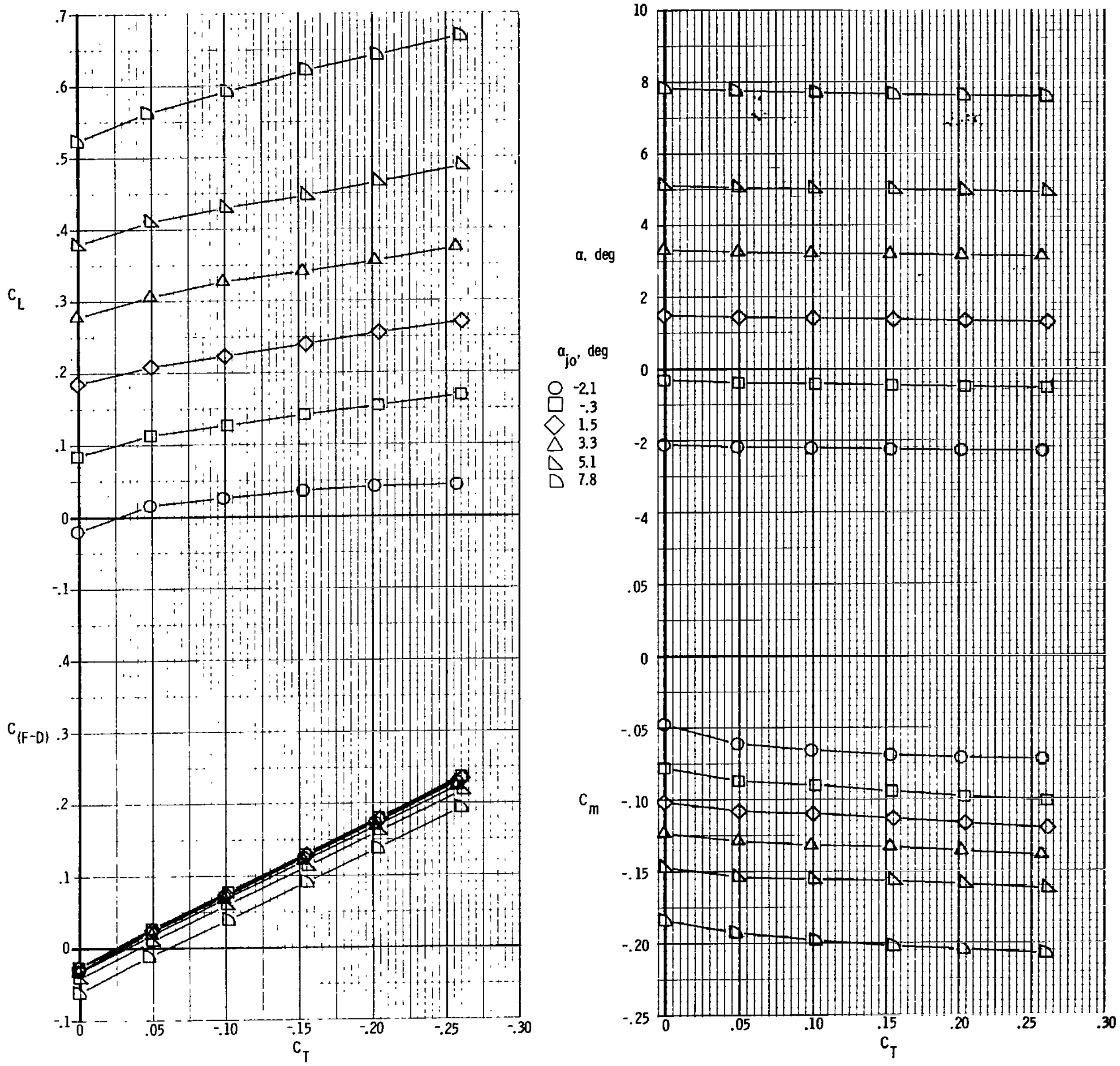

(c) M = 0.90.

Figure 12.- Continued.

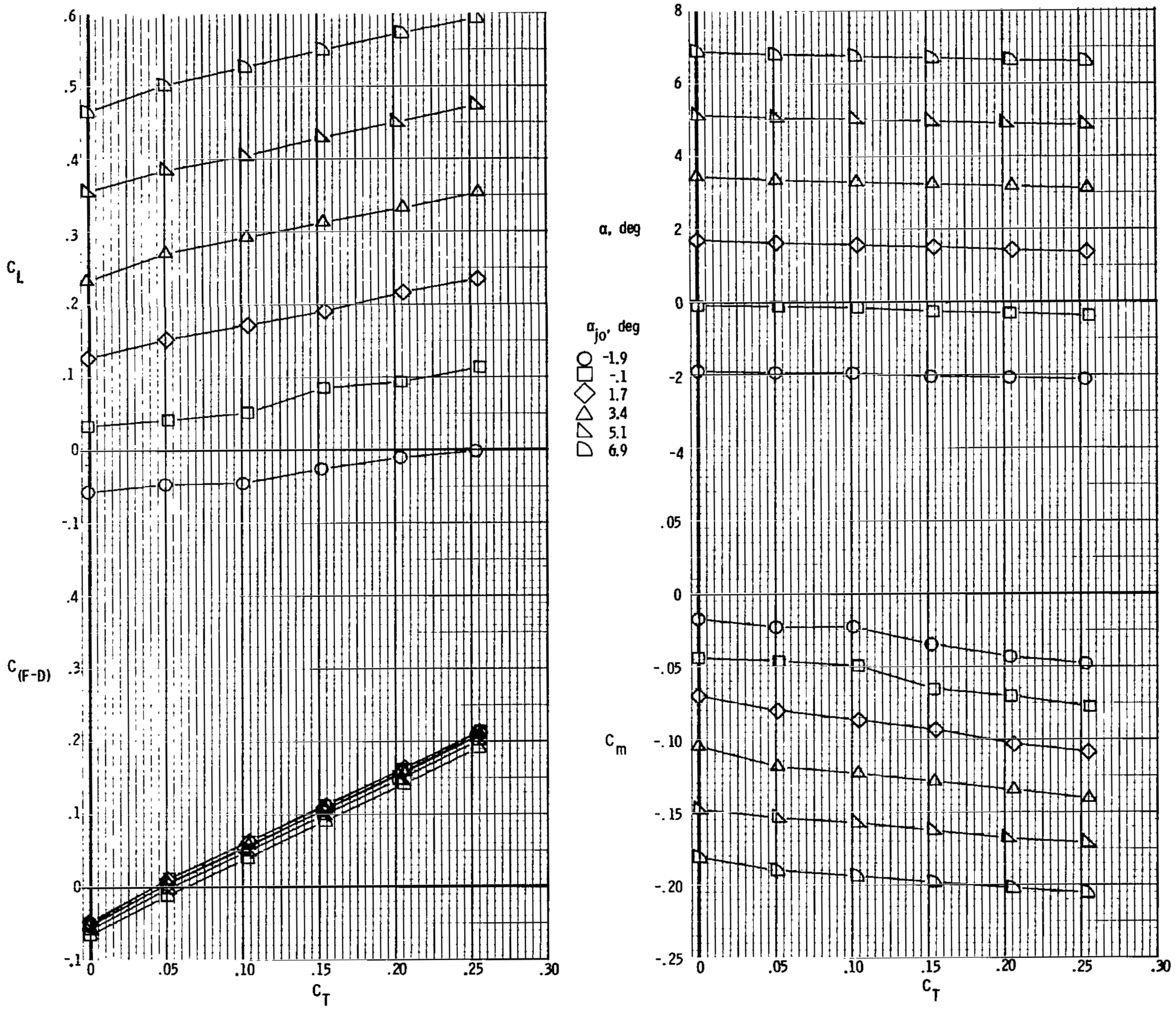

(d) M = 0.95.

Figure 12.- Concluded.

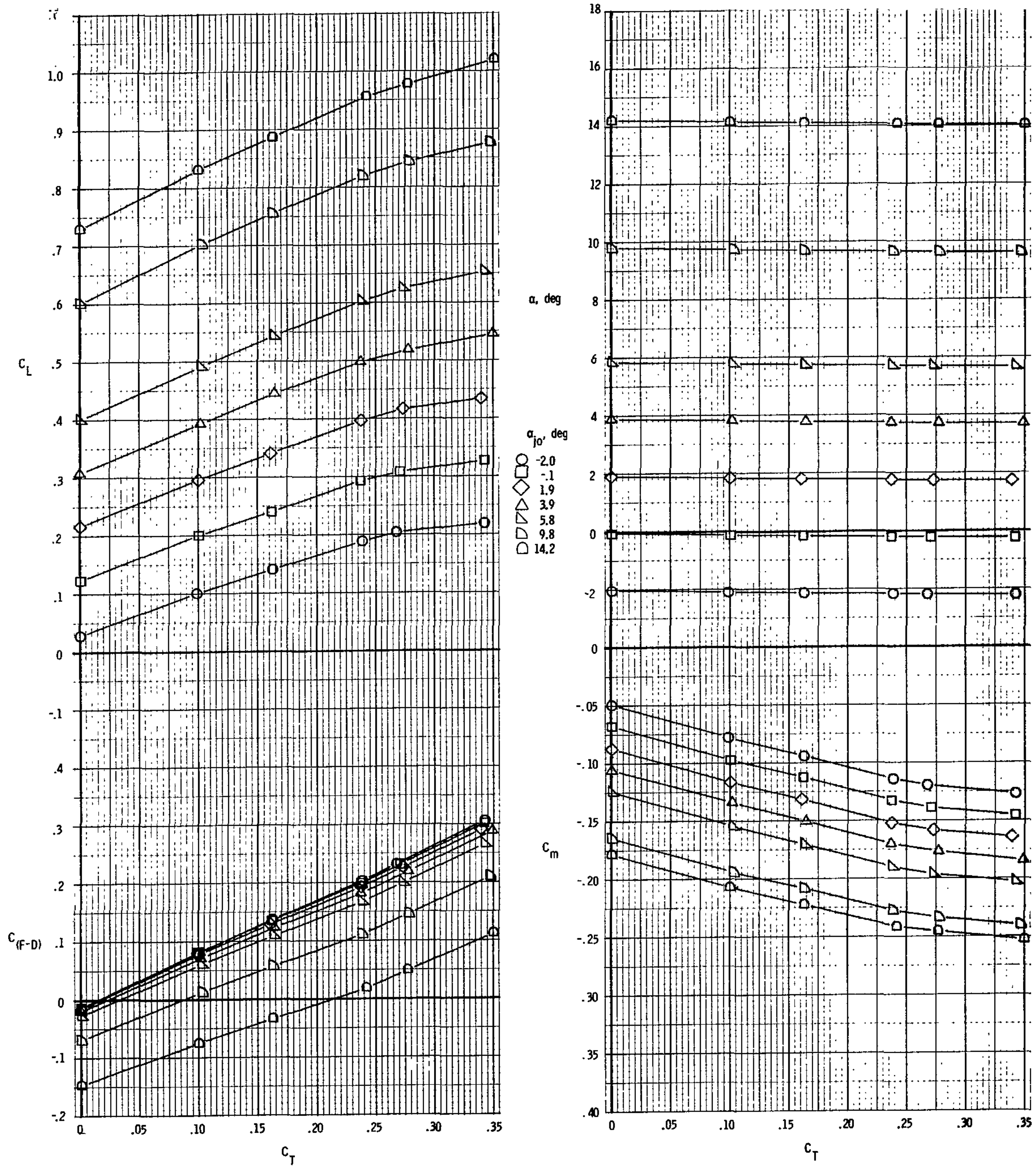

(a) M = 0.40.

Figure 13.- Basic aerodynamic characteristics. $\delta_d = 30^{\circ}$.

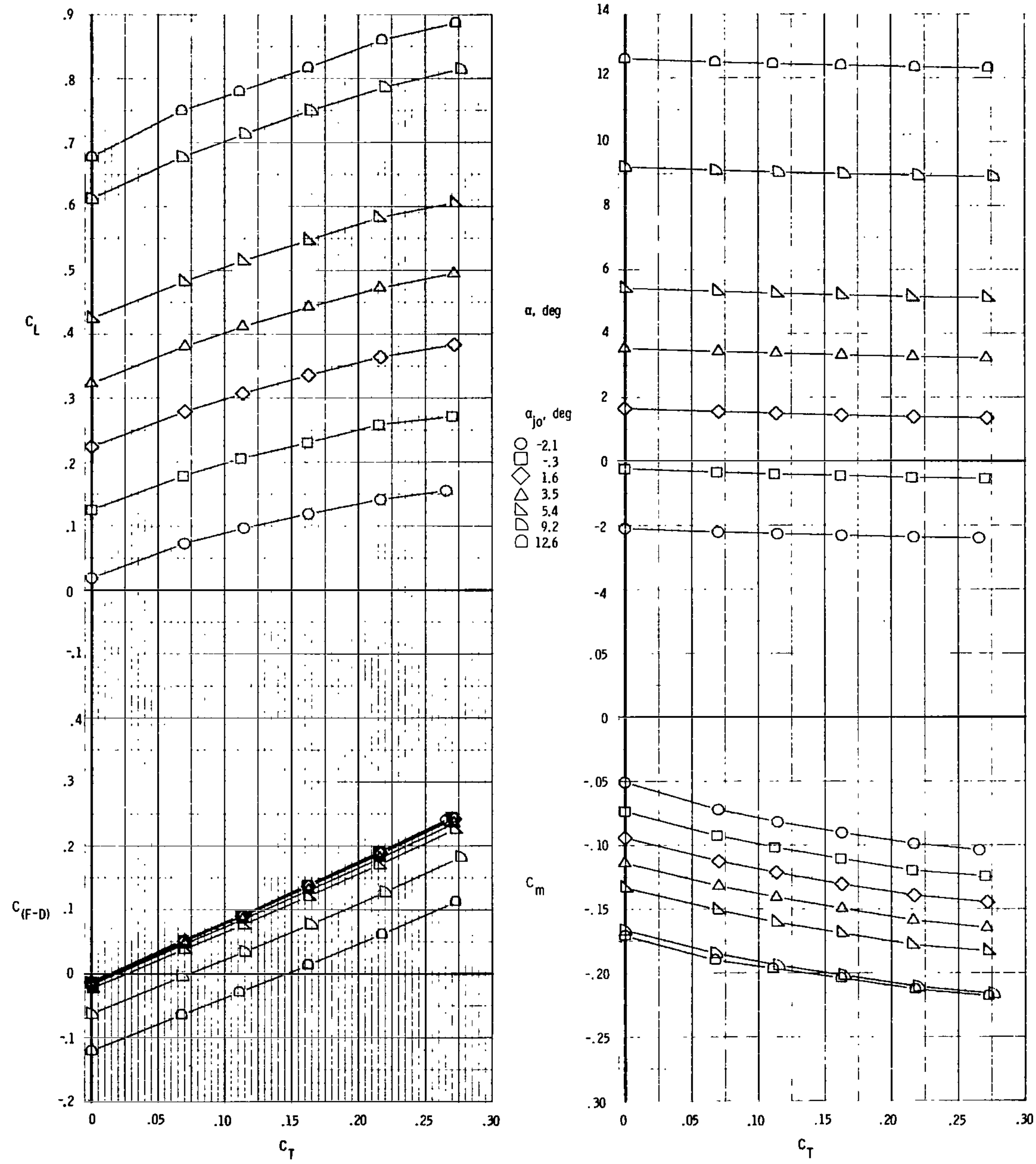

(b) M = 0.70.

Figure 13.- Continued.

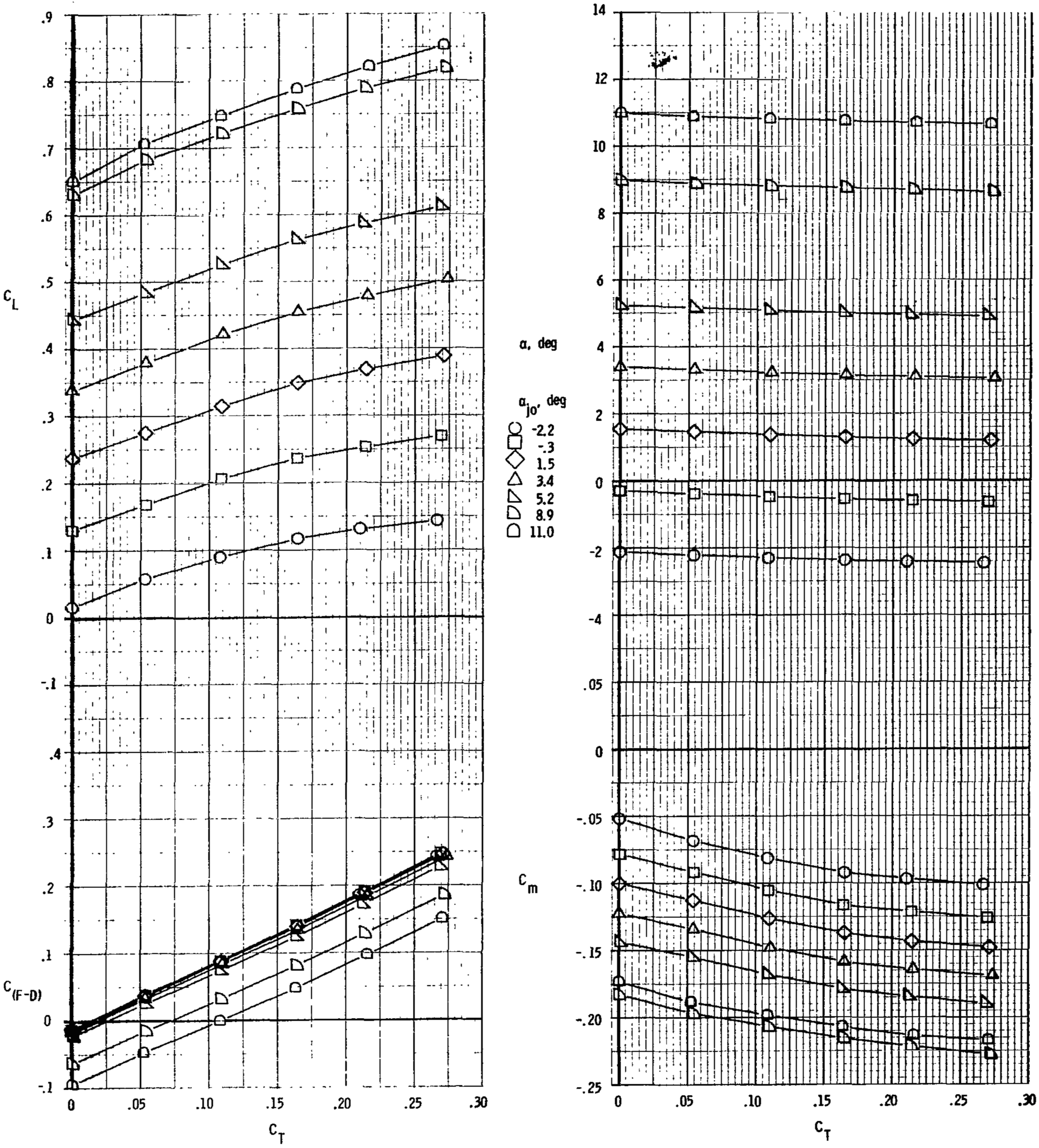

(c) M = 0.80.

Figure 13.- Continued.

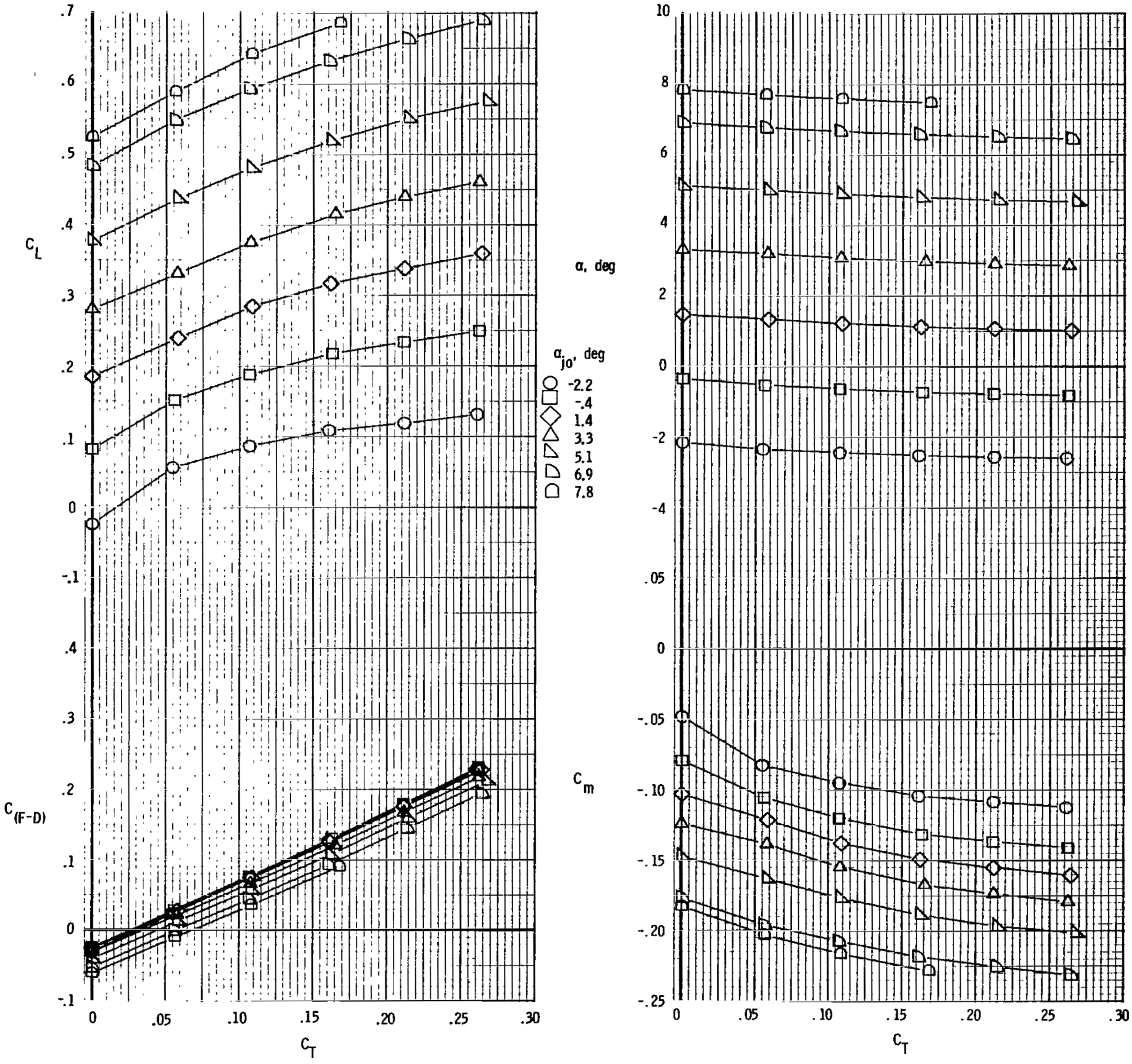

(d) M = 0.90.

Figure 13.- Continued.

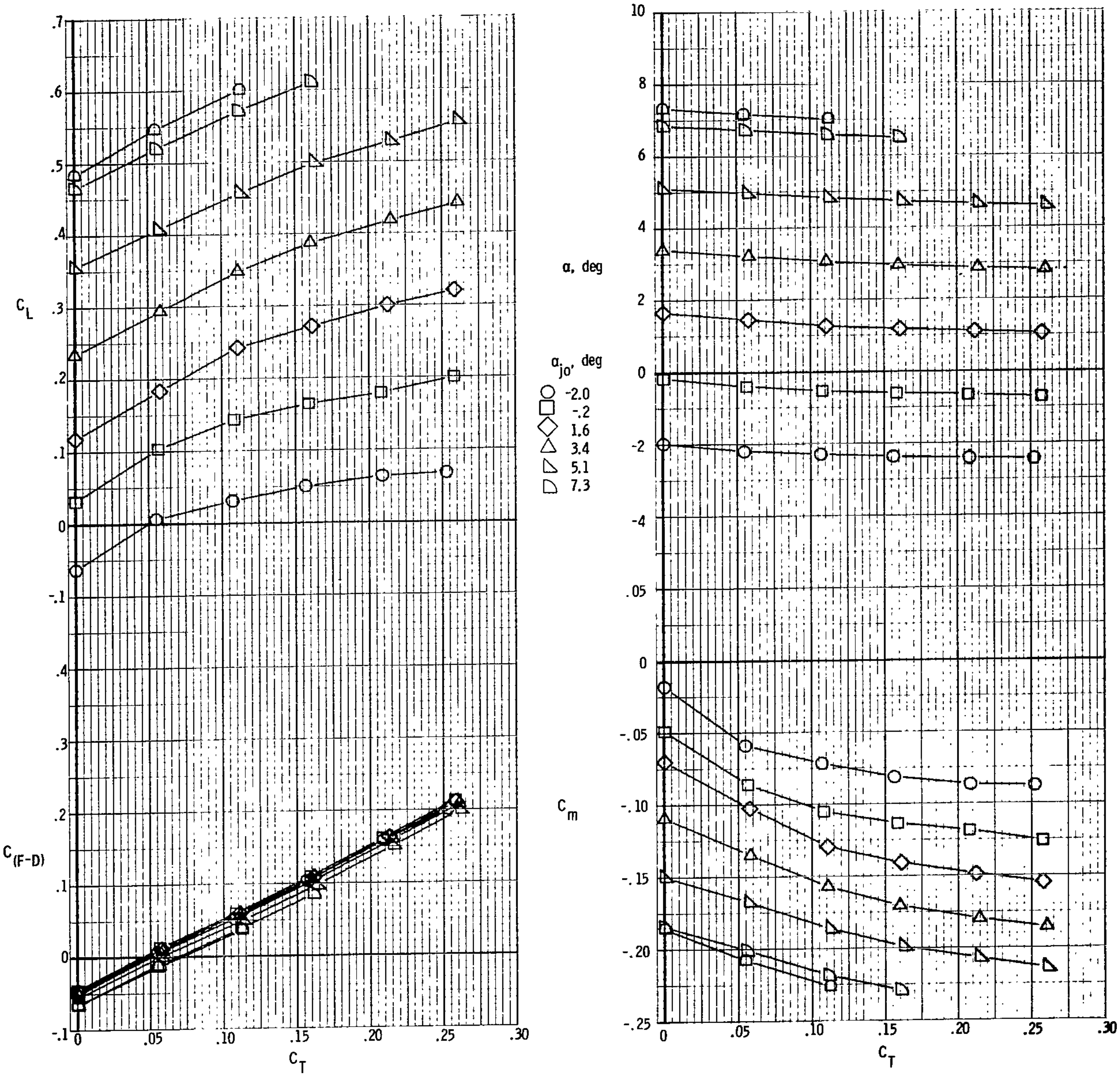

(e) M = 0.95.

Figure 13.- Continued.

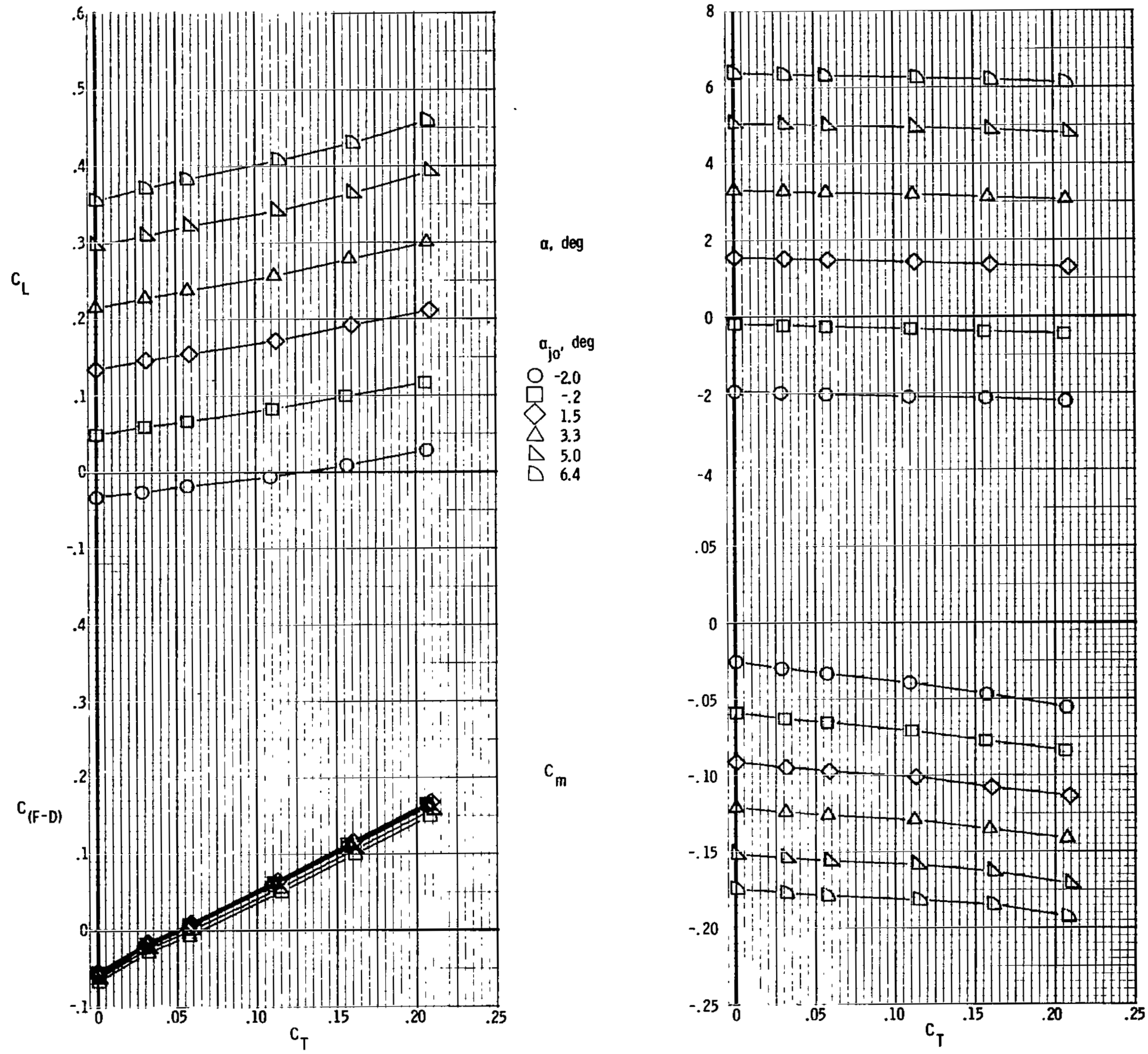

(f) M = 1.20.

Figure 13.- Concluded.

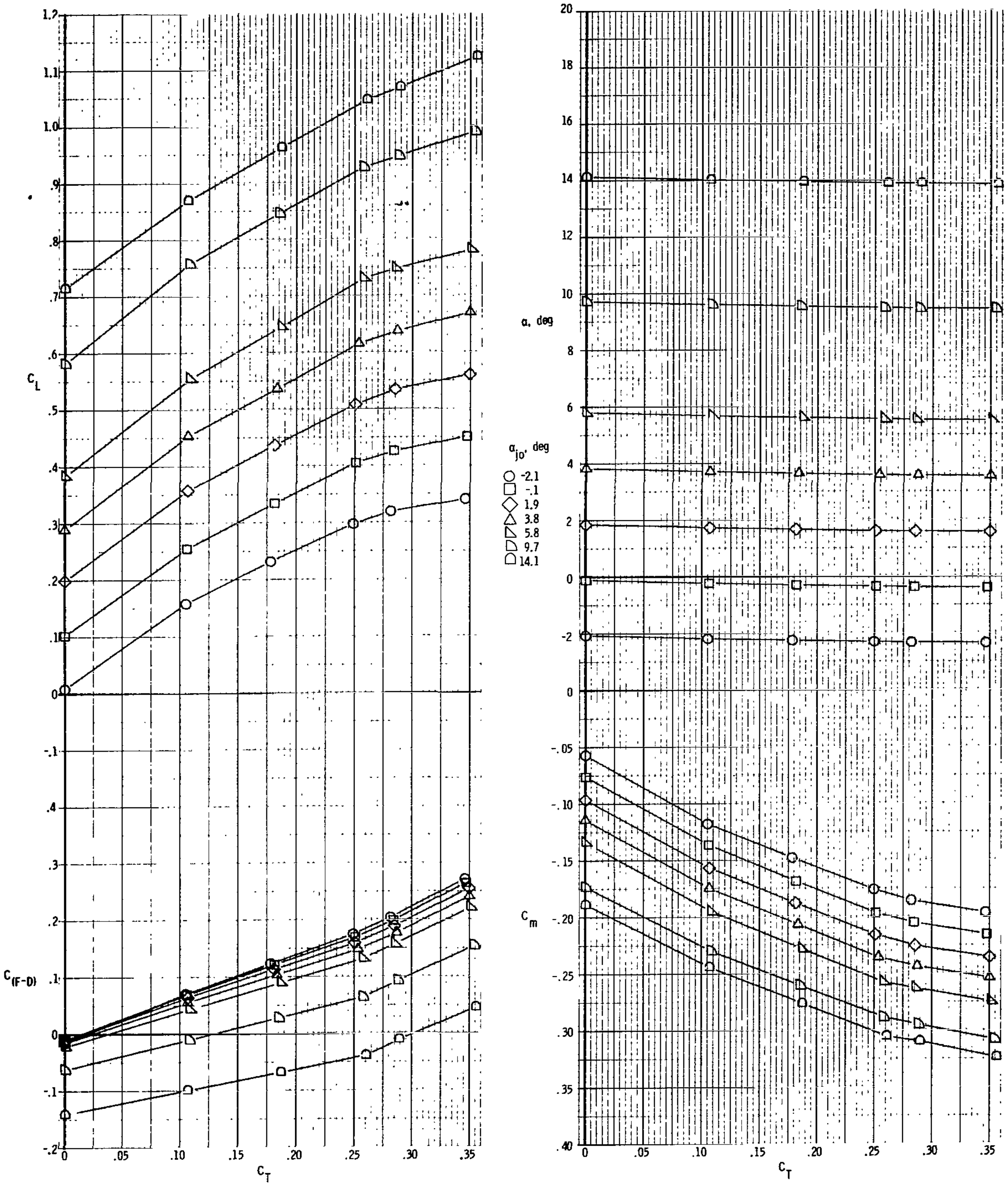

(a) M = 0.40.

Figure 14.- Basic aerodynamic characteristics. $\delta_d = 45^o$.

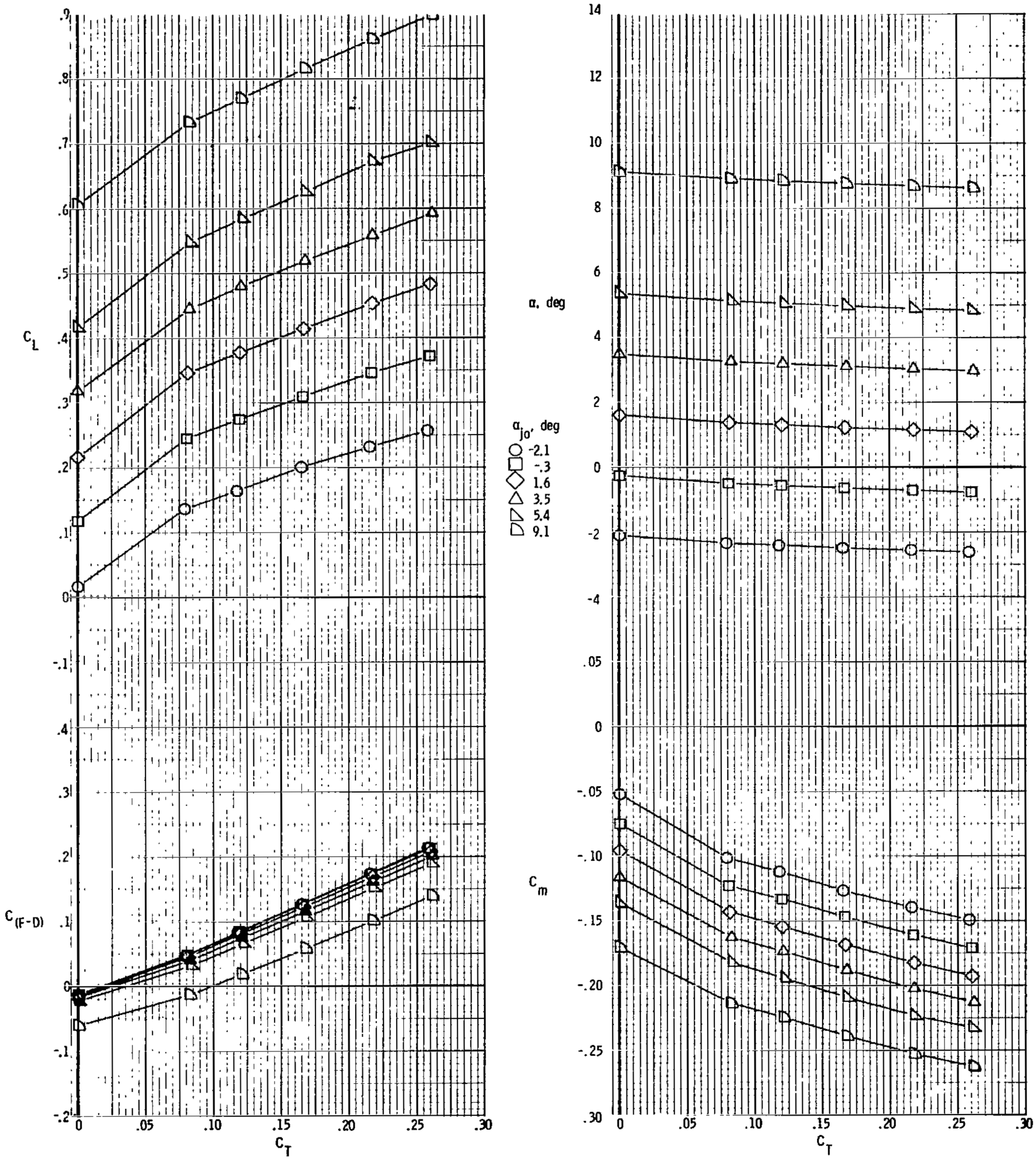

(b) M = 0.70.

Figure 14.- Continued.

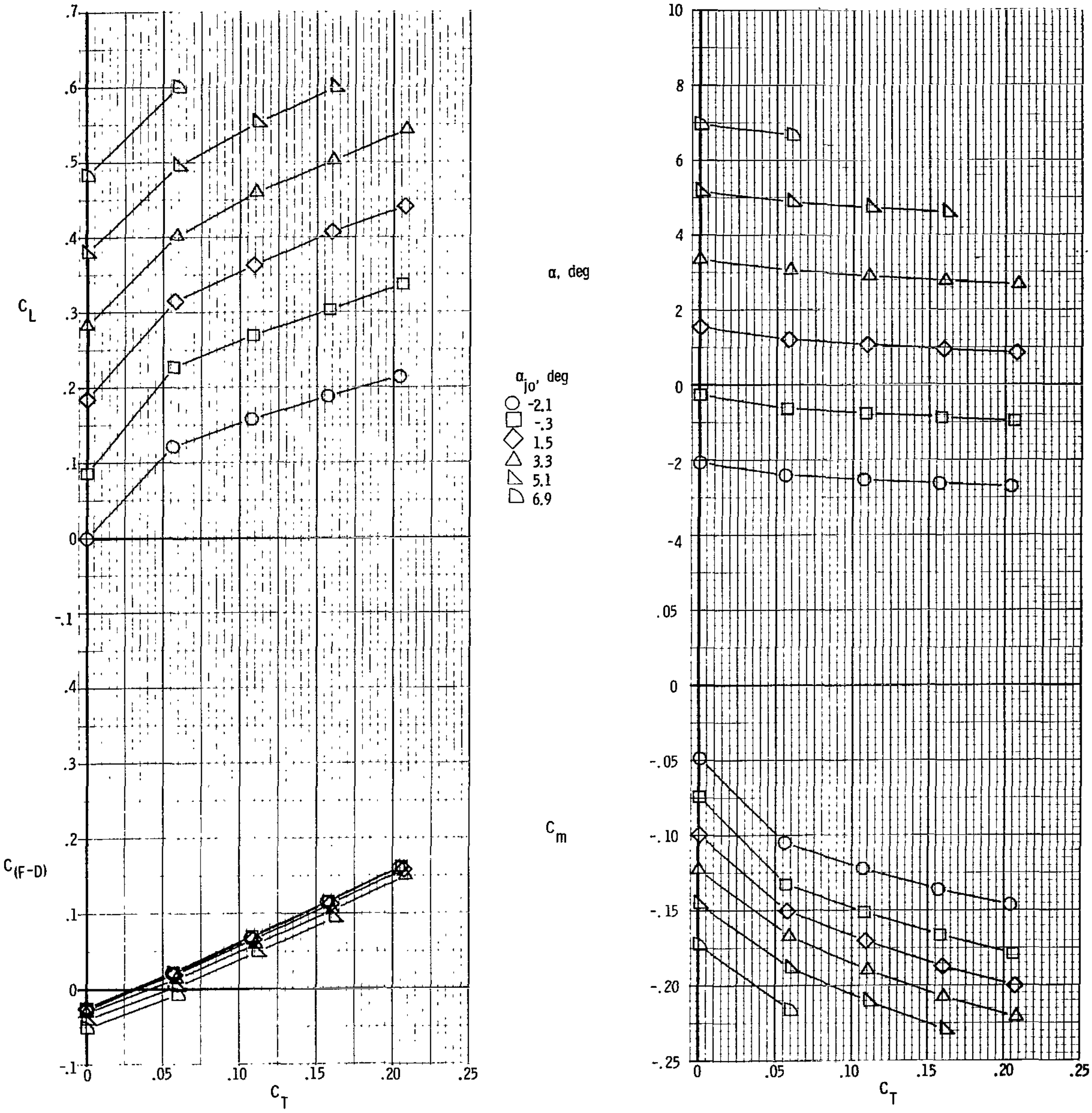

(c) M = 0.90.

Figure 14.- Concluded.

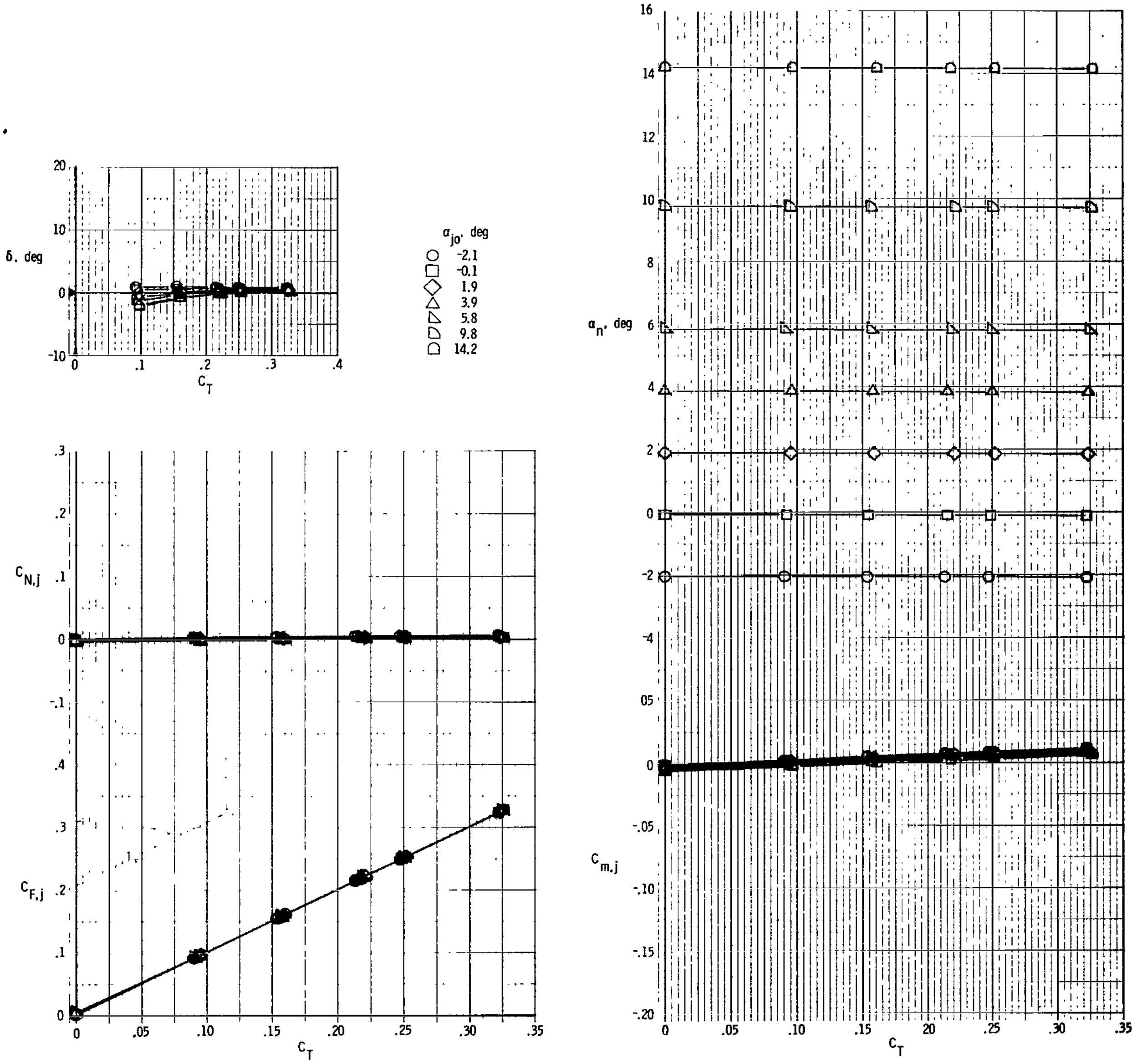

(a) M = 0.40.

Figure 15.- Basic nozzle thrust characteristics. $\delta_d = 0^o$.

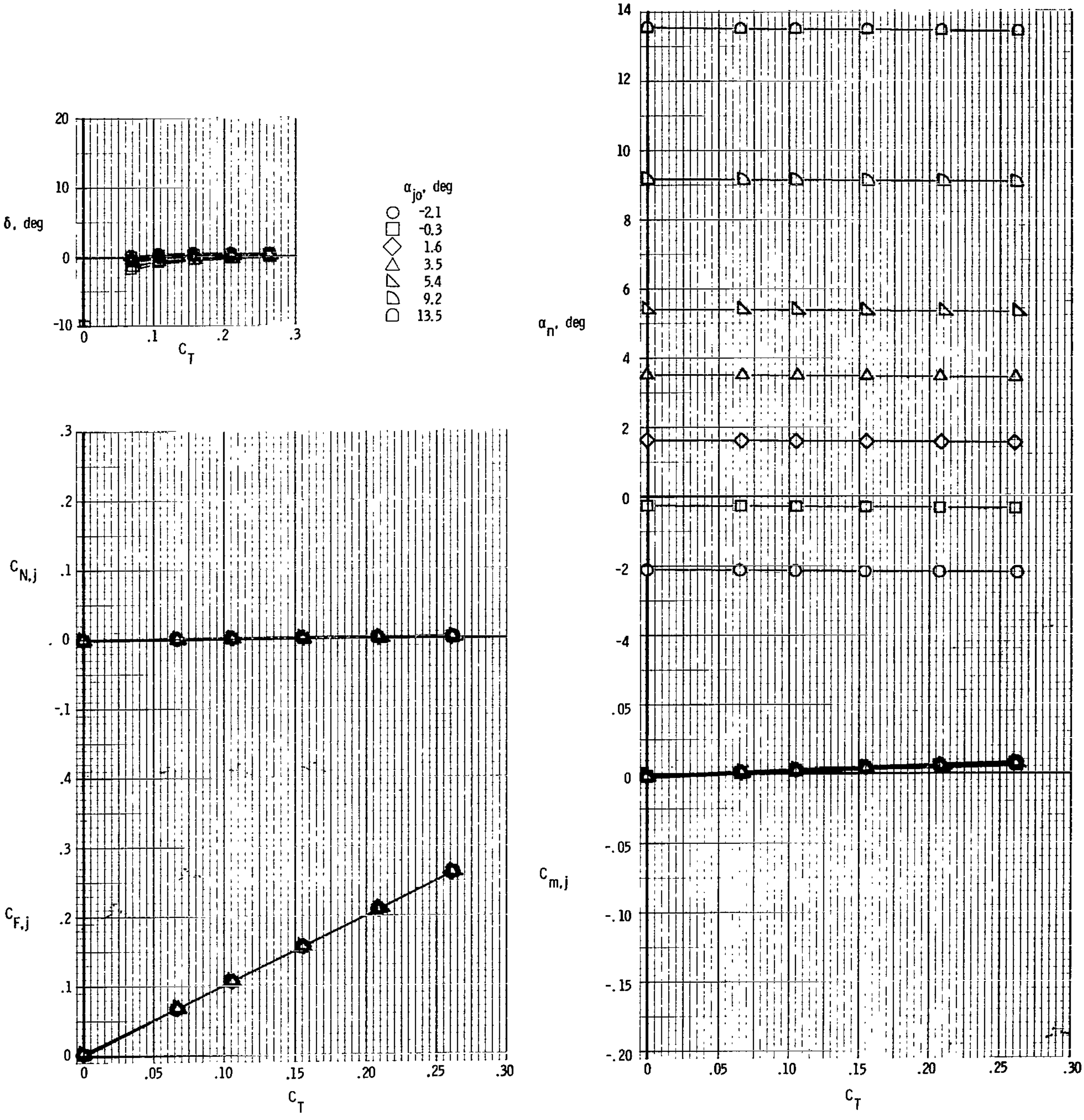

(b) M = 0.70.

Figure 15.- Continued.

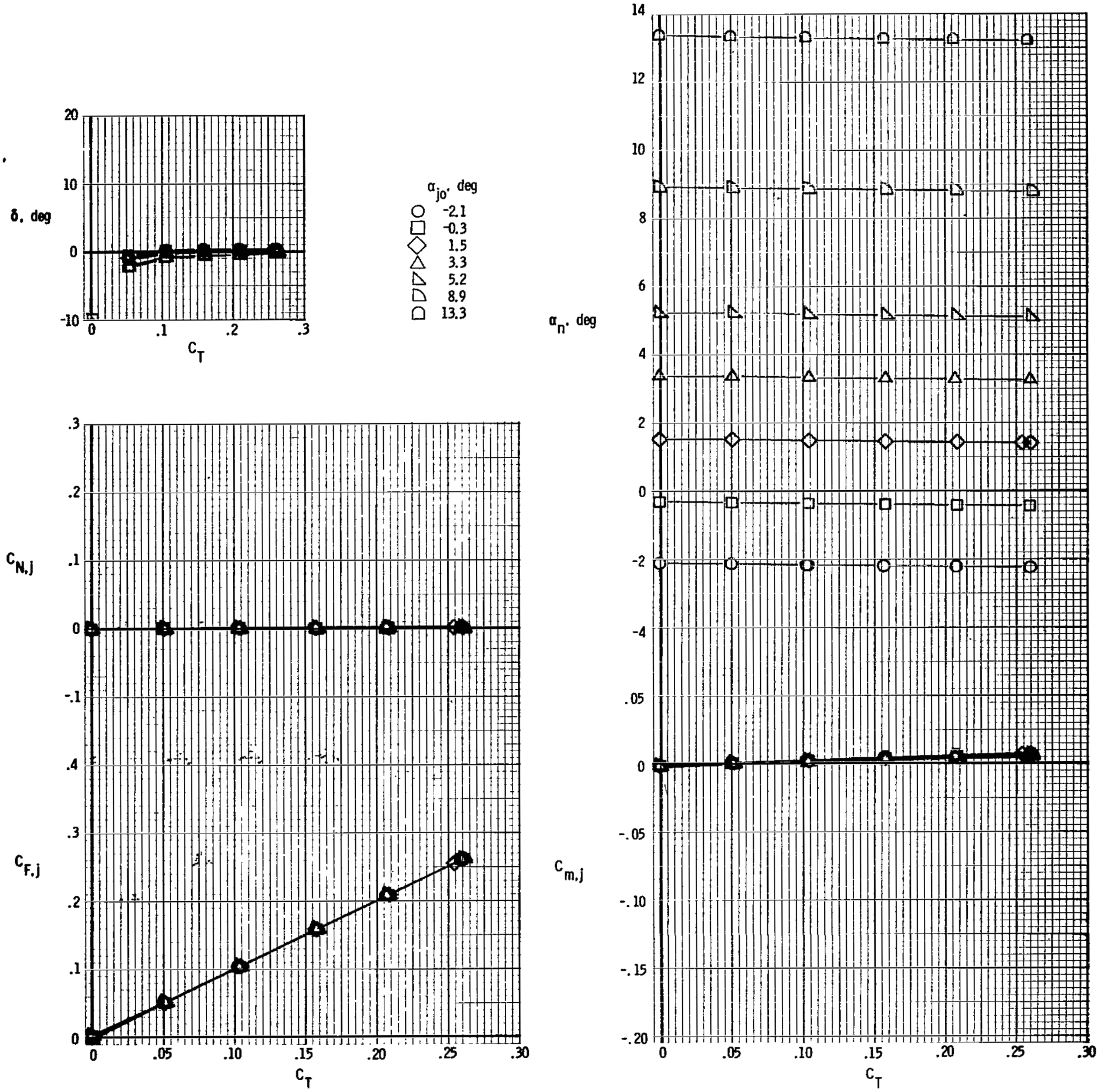

(c) M = 0.80.

Figure 15.- Continued.

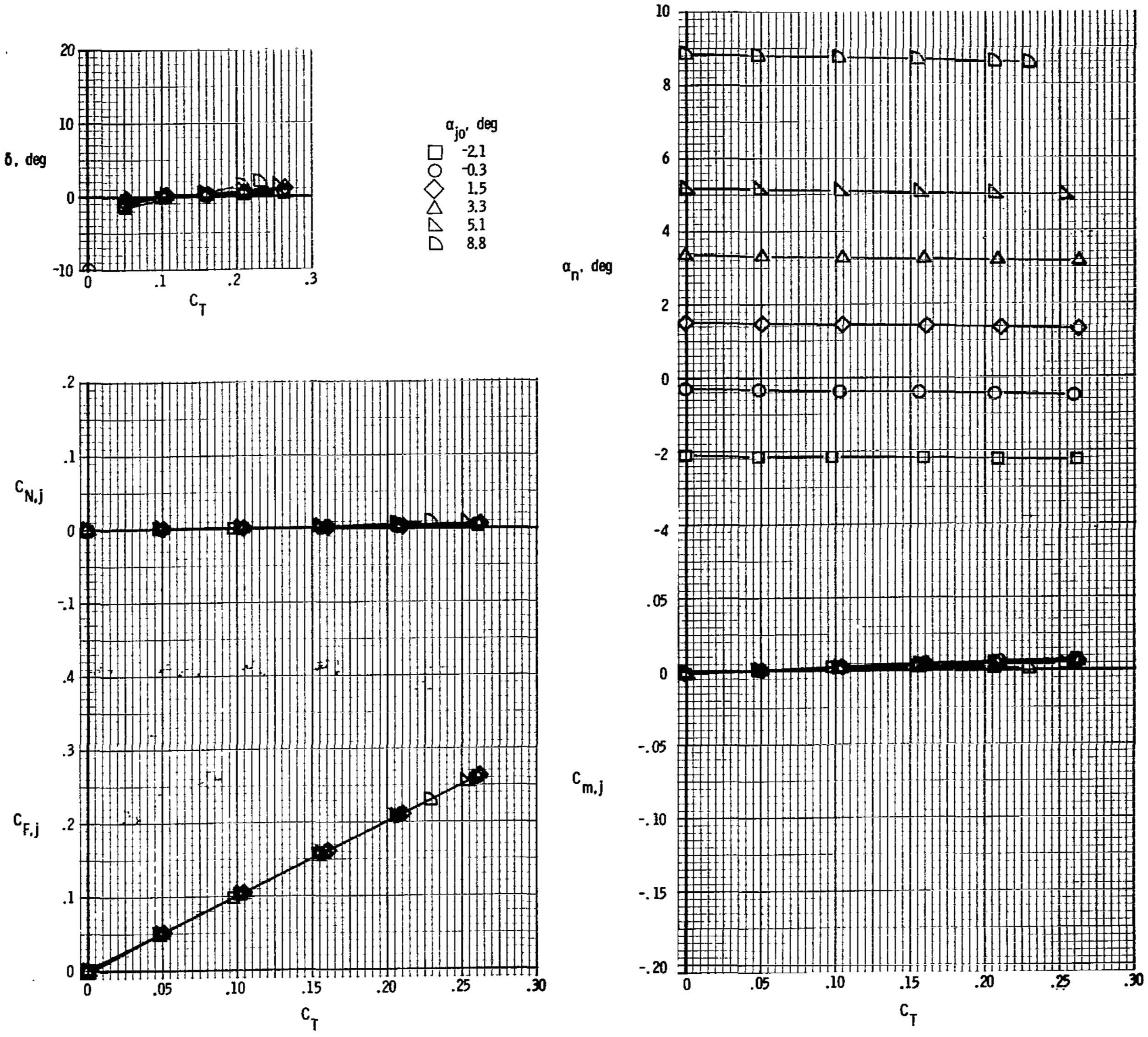

(d) M = 0.90.

Figure 15.- Continued.

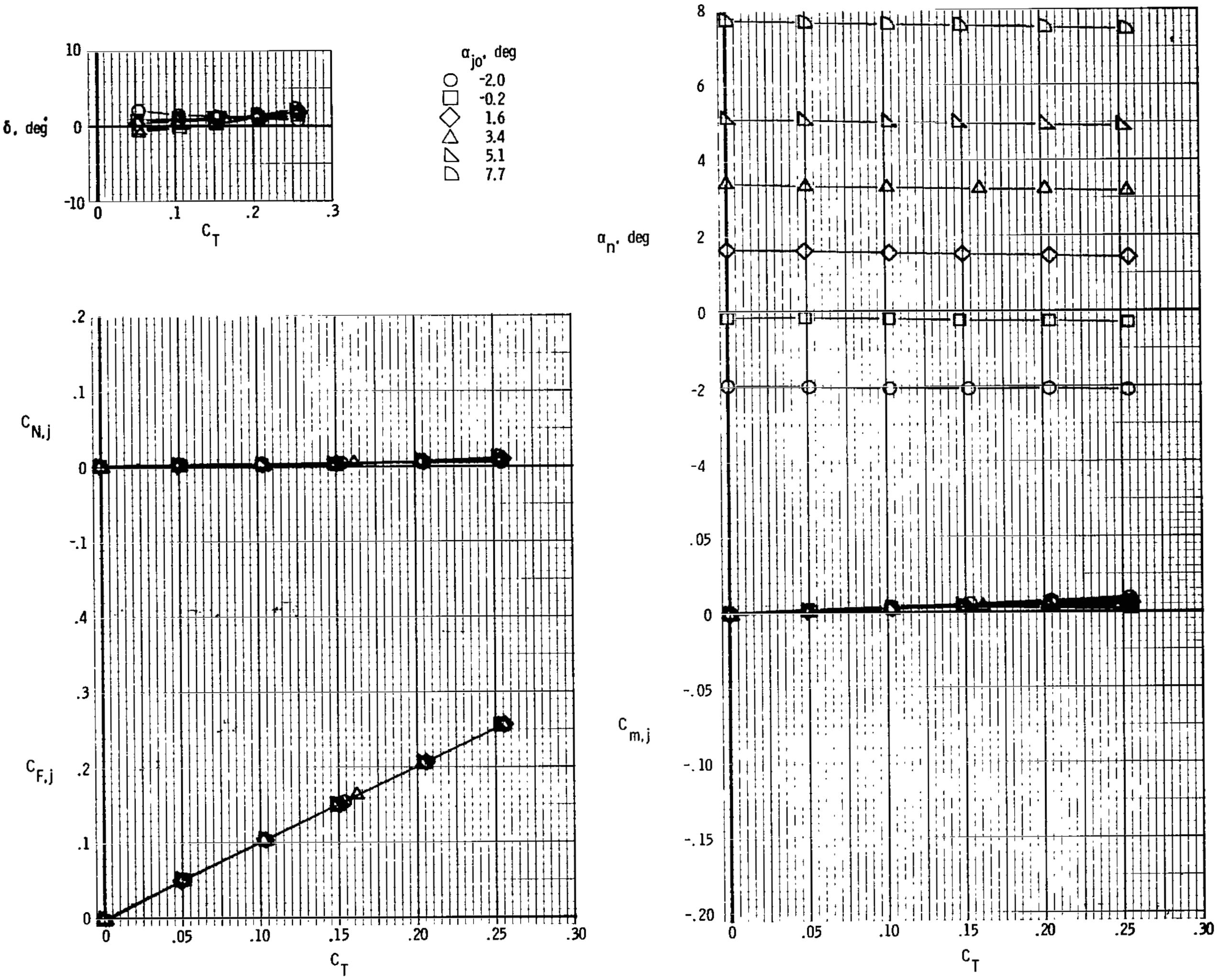

(e) M = 0.95.

Figure 15.- Continued.

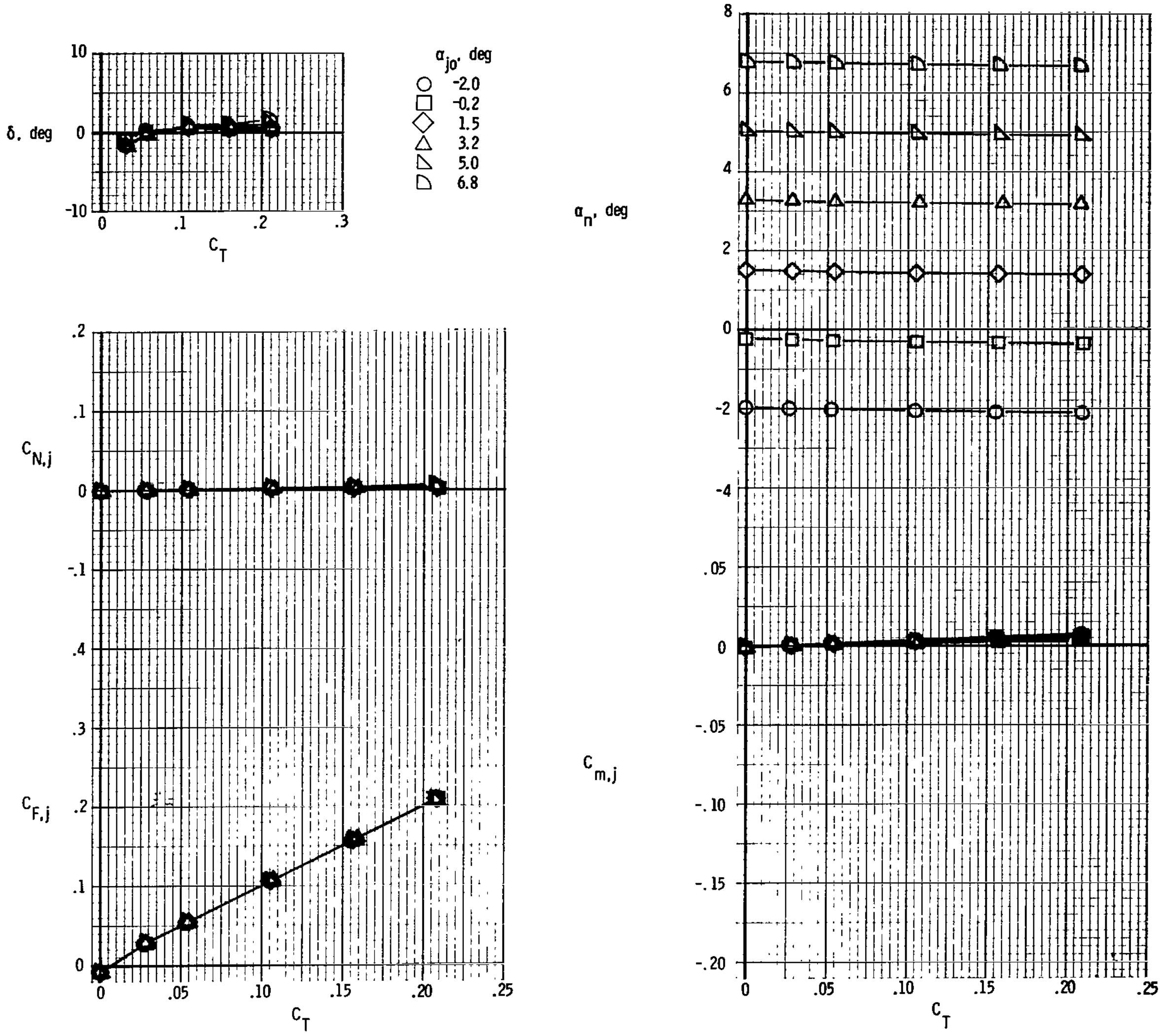

(f) M = 1.20.

Figure 15.- Concluded.

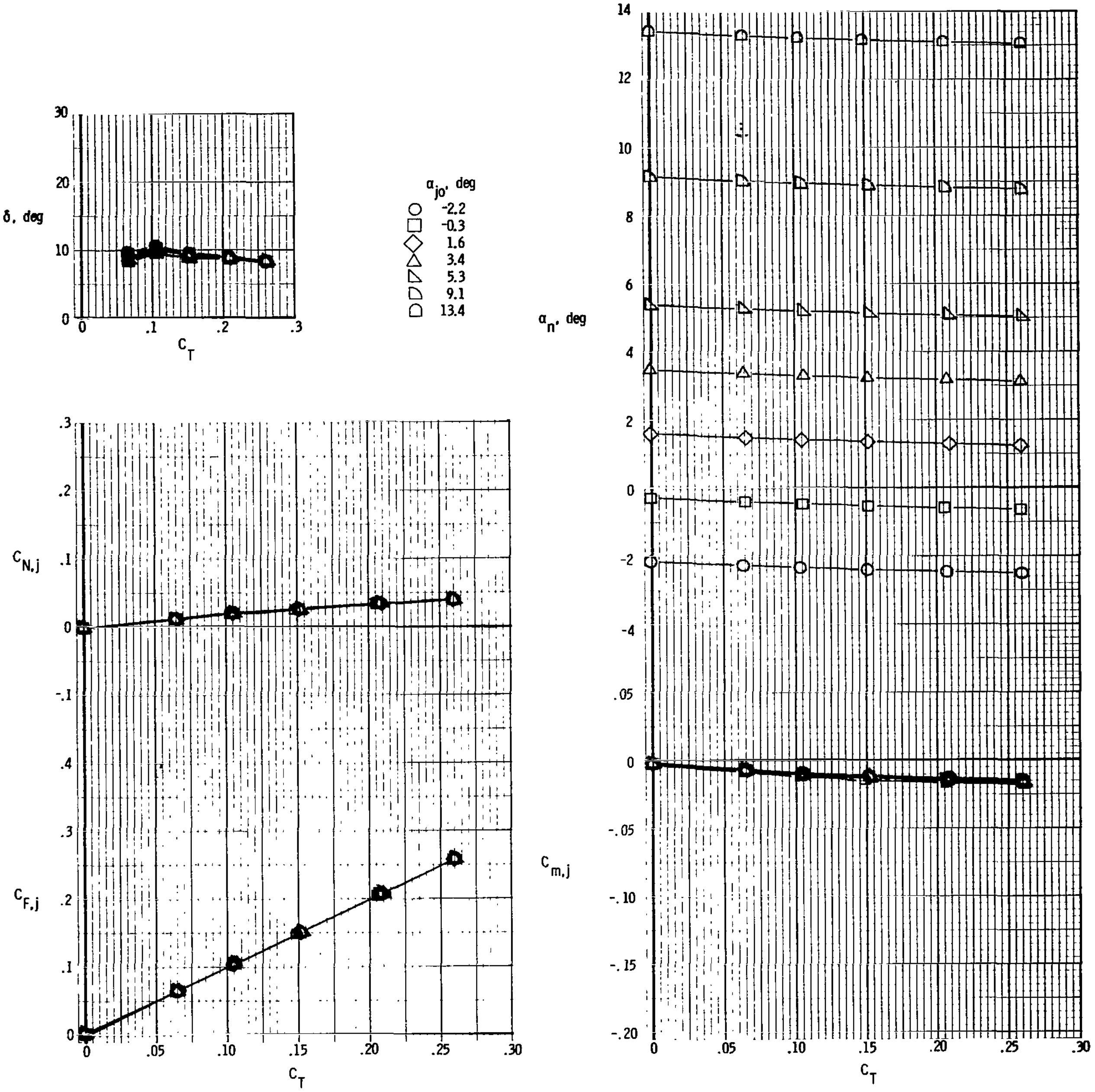

(a) M = 0.70.

Figure 16.- Basic nozzle thrust characteristics. $\delta_d = 15^\circ$.

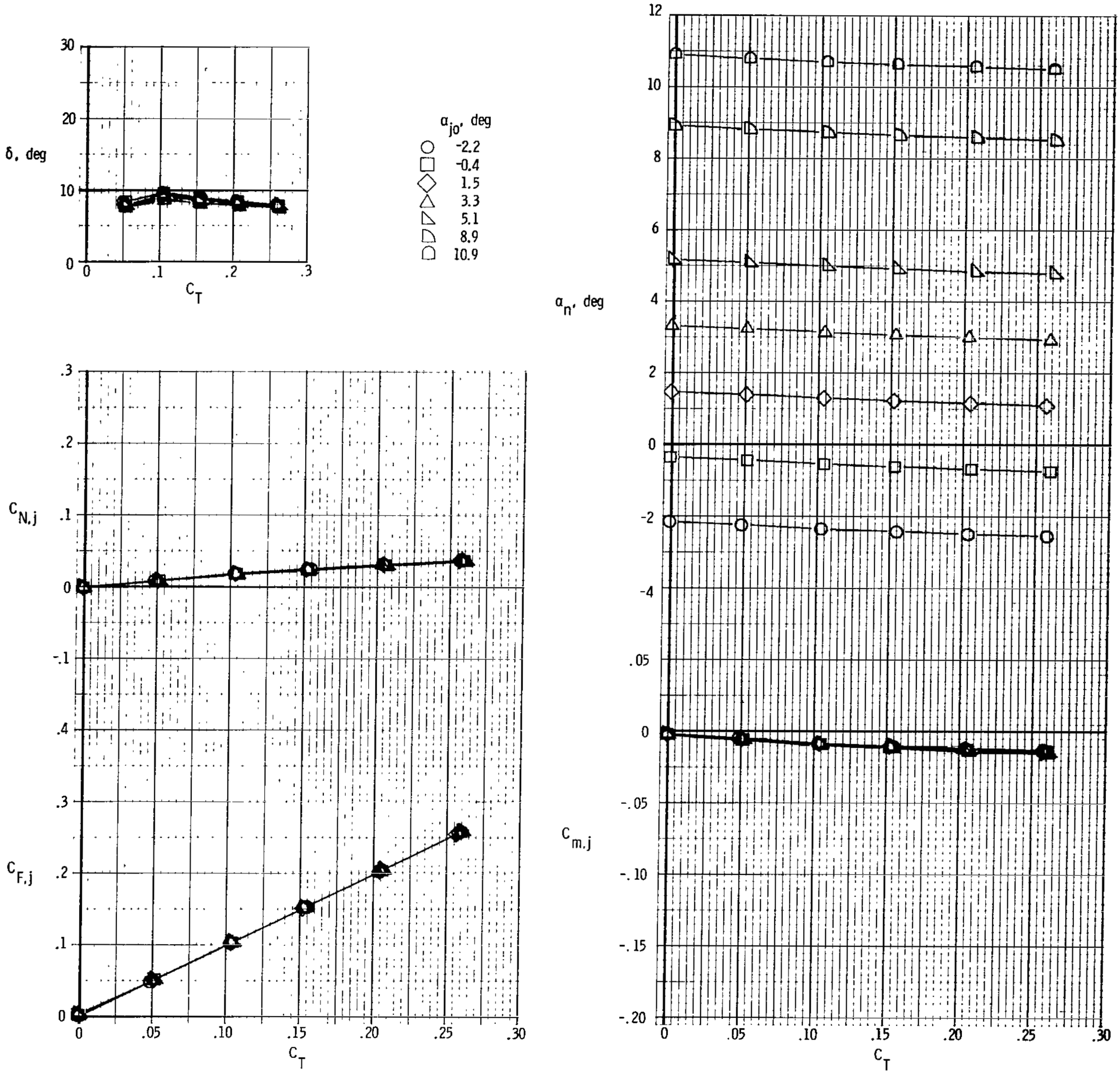

(b) M = 0.80.

Figure 16.- Continued.

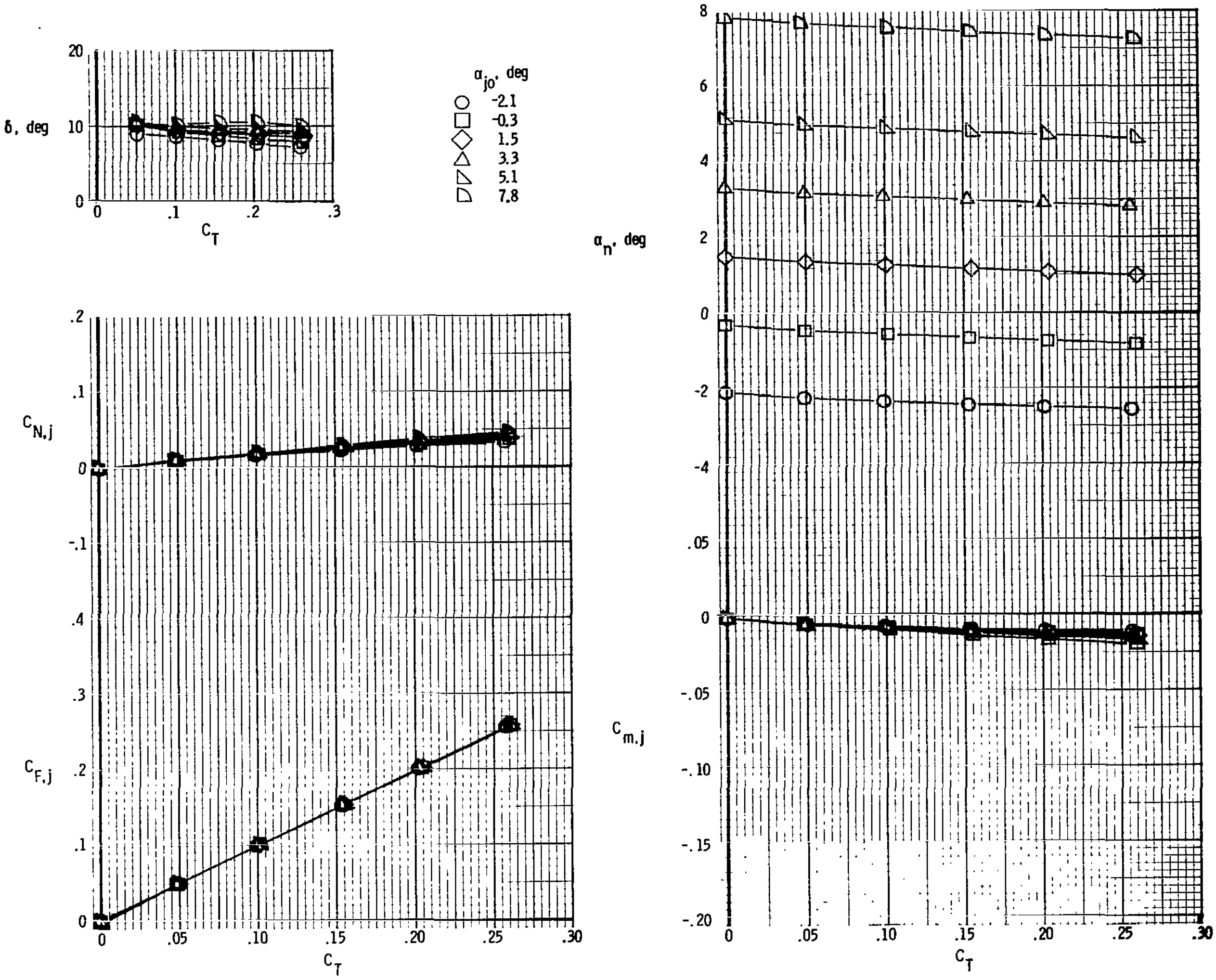

(c) M = 0.90.

Figure 16.- Continued.

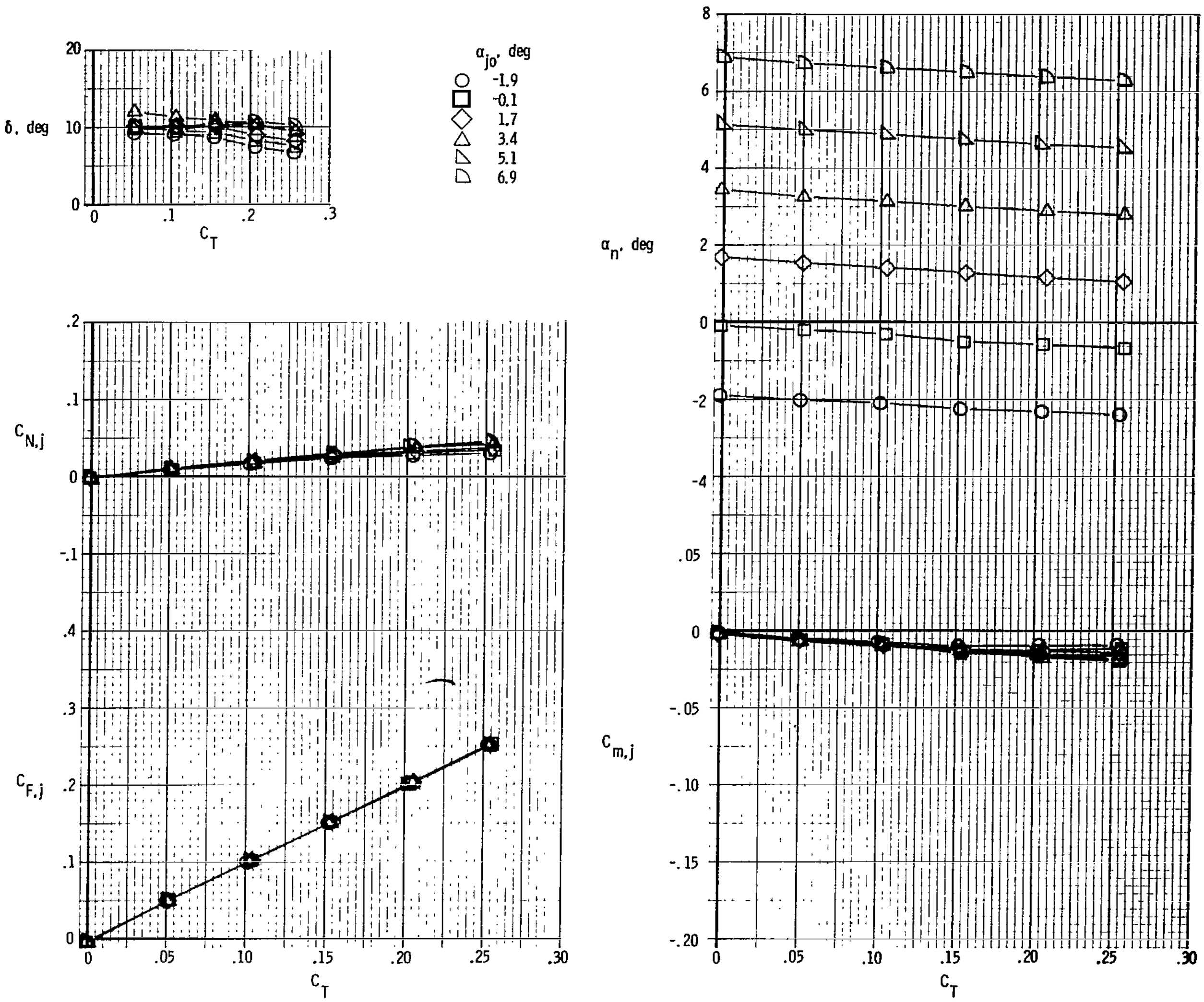

(d) M = 0.95.

Figure 16.- Concluded.

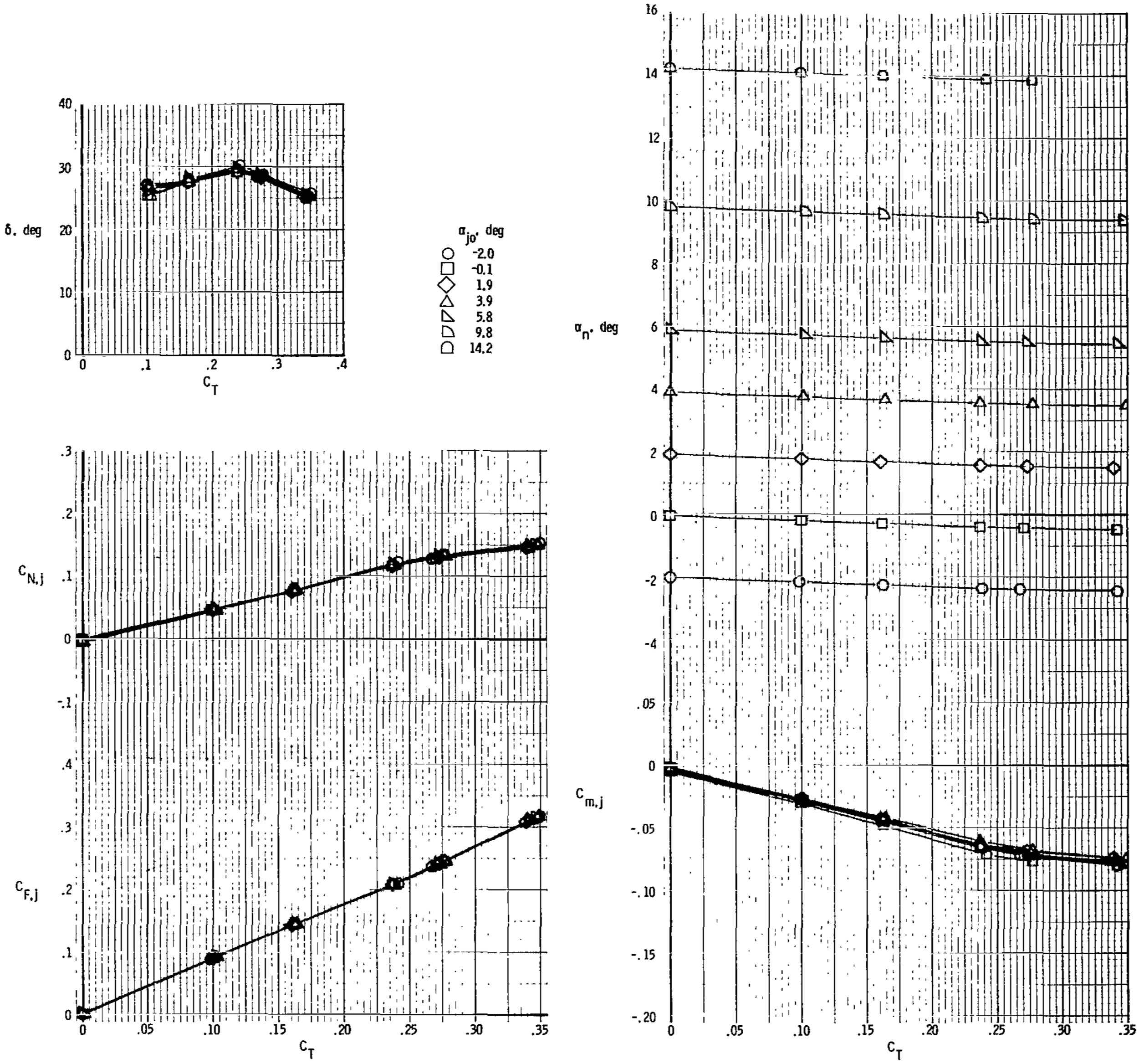

(a) M = 0.40.

Figure 17.- Basic nozzle thrust characteristics. $\delta_d = 30^{\circ}$.

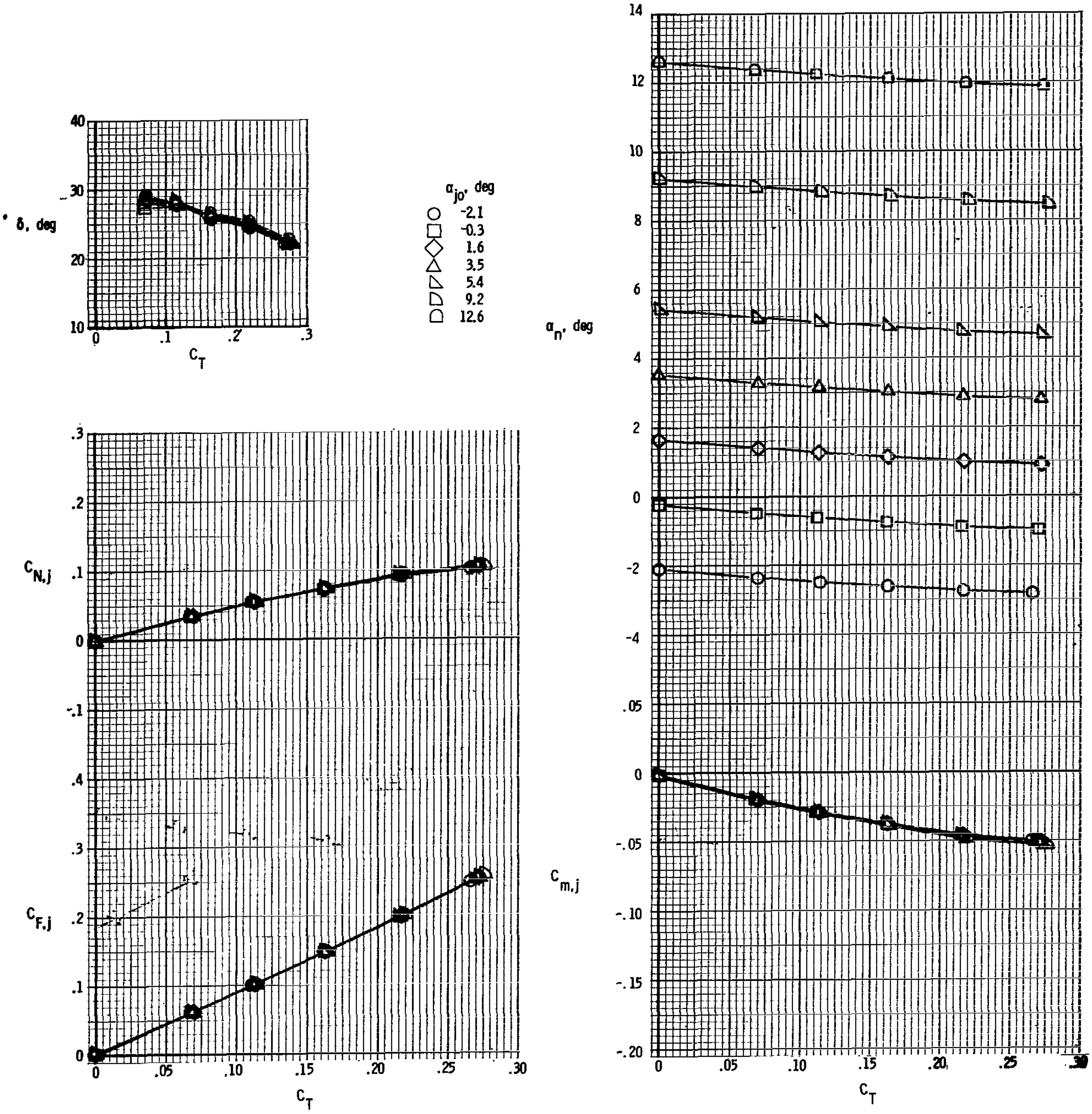

(b) M = 0.70.

Figure 17.- Continued.

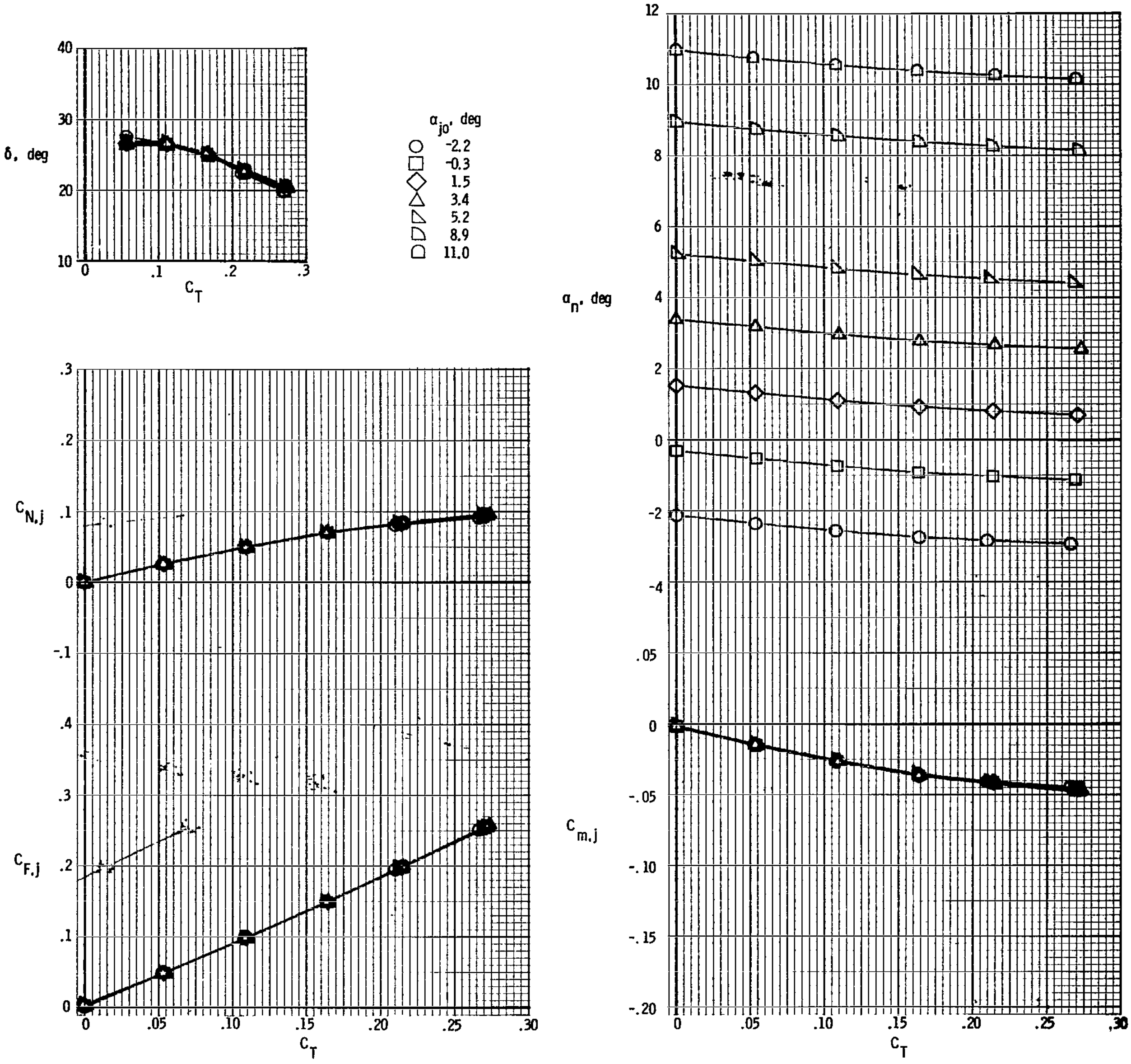

(c) M = 0.80.

Figure 17.- Continued.

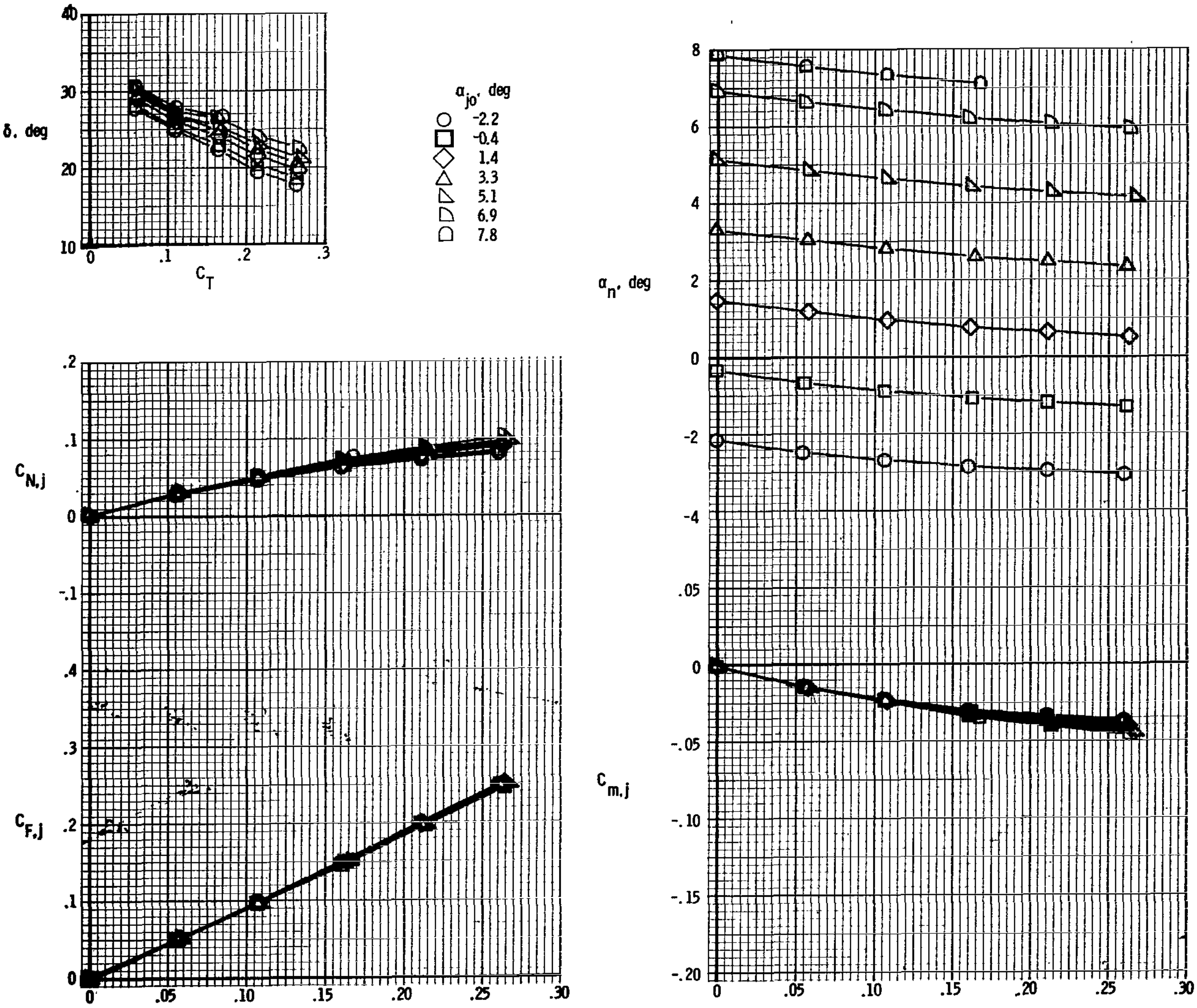

(d) M = 0.90.

Figure 17.- Continued.

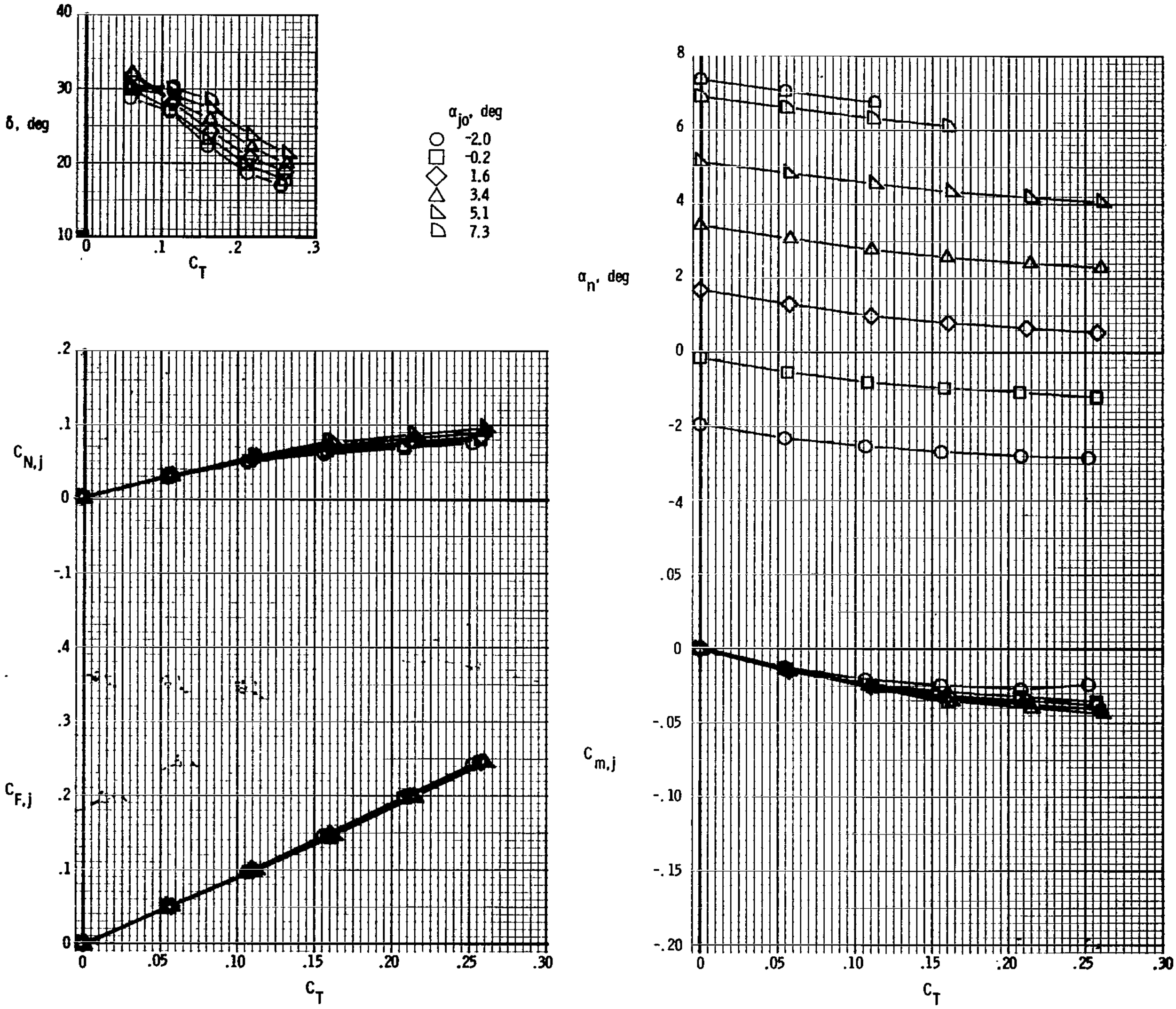

(e) M = 0.95.

Figure 17.- Continued.

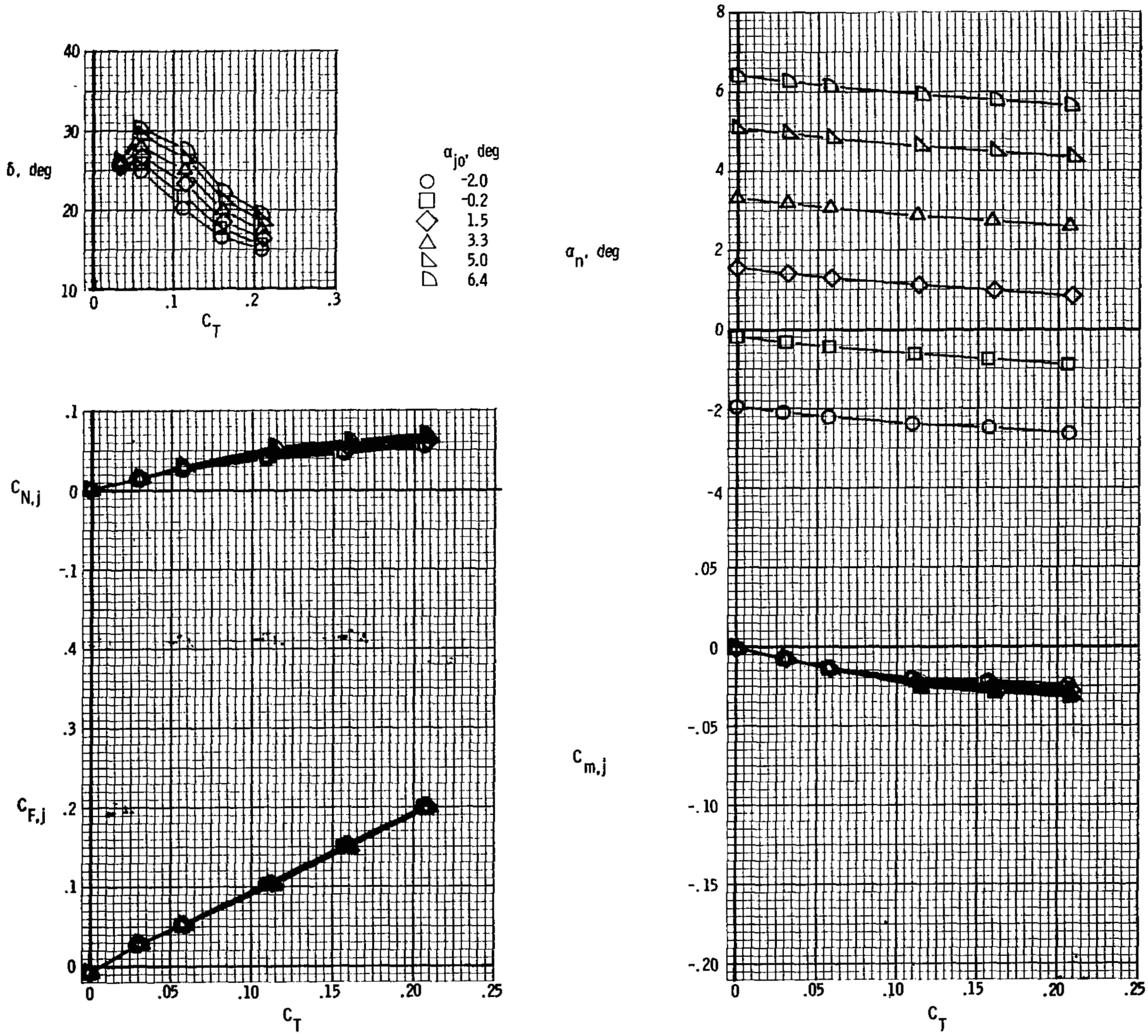

(f) M = 1.20.

Figure 17.- Concluded.

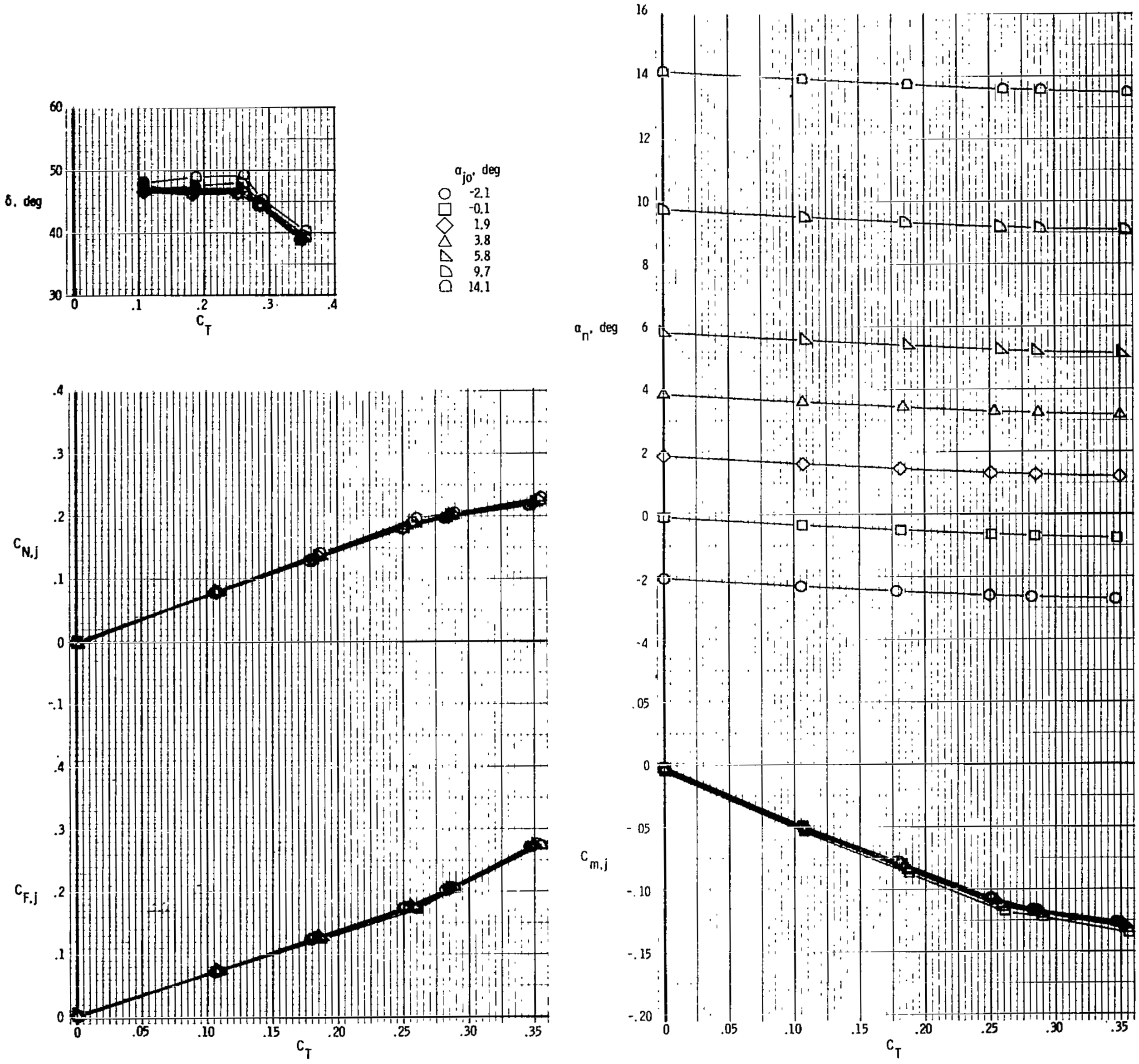

(a) M = 0.40.

Figure 18.- Basic nozzle thrust characteristics. $\delta_d = 45^o$.

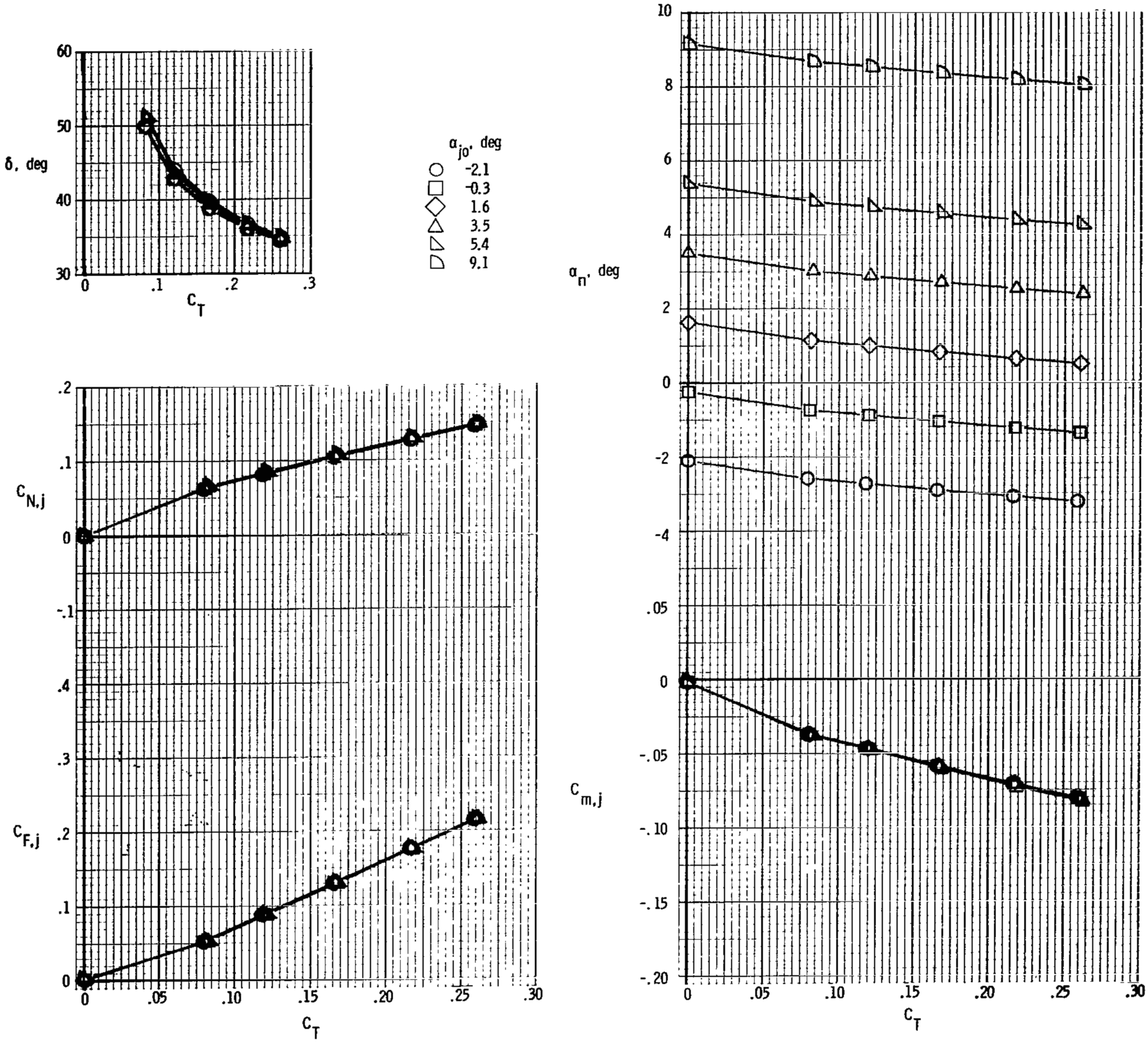

(b) M = 0.70.

Figure 18.- Continued.

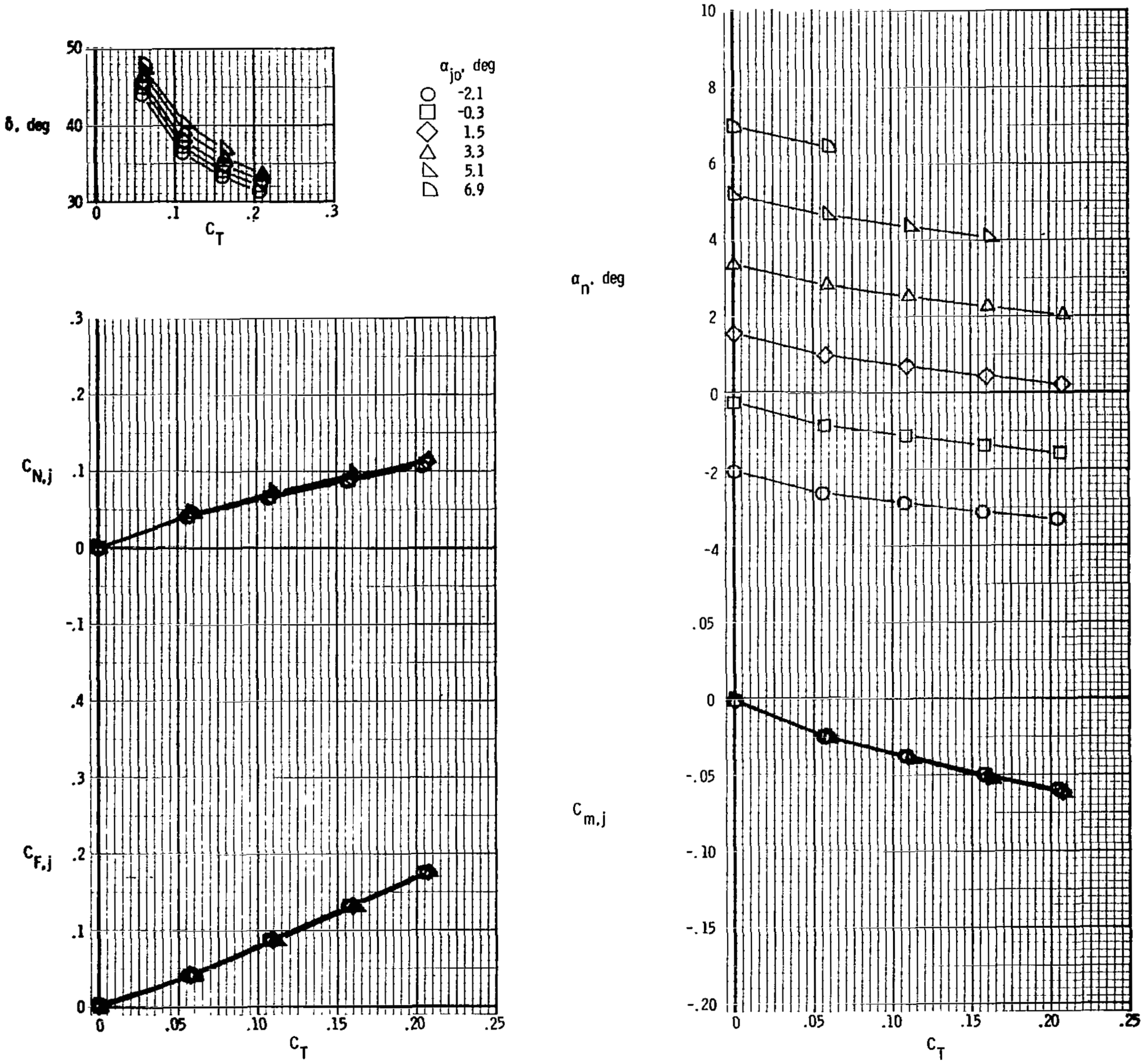

(c) M = 0.90.

Figure 18.- Concluded.

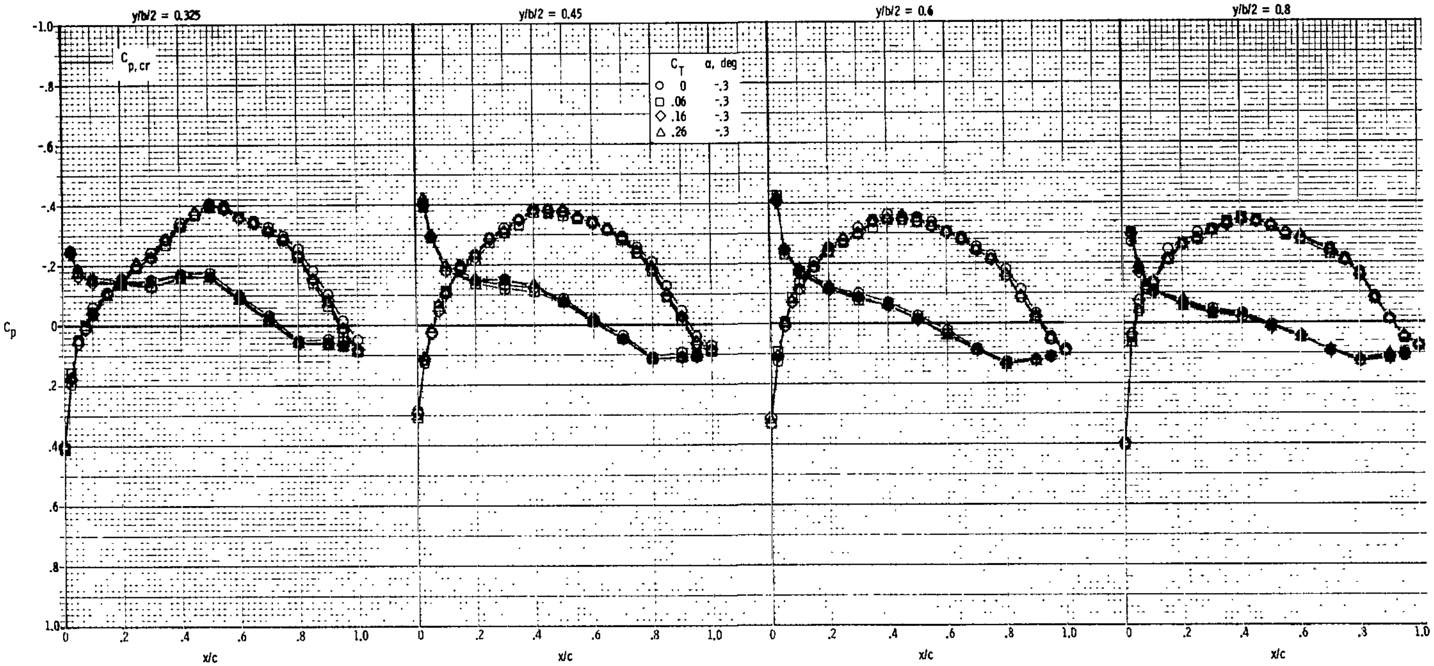

(a) M = 0.70; α = -0.3°.

Figure 19.- Wing chordwise pressure distributions. $\delta_d = 0^{\circ}$. Symbols with crosses denote airfoil lower surface.

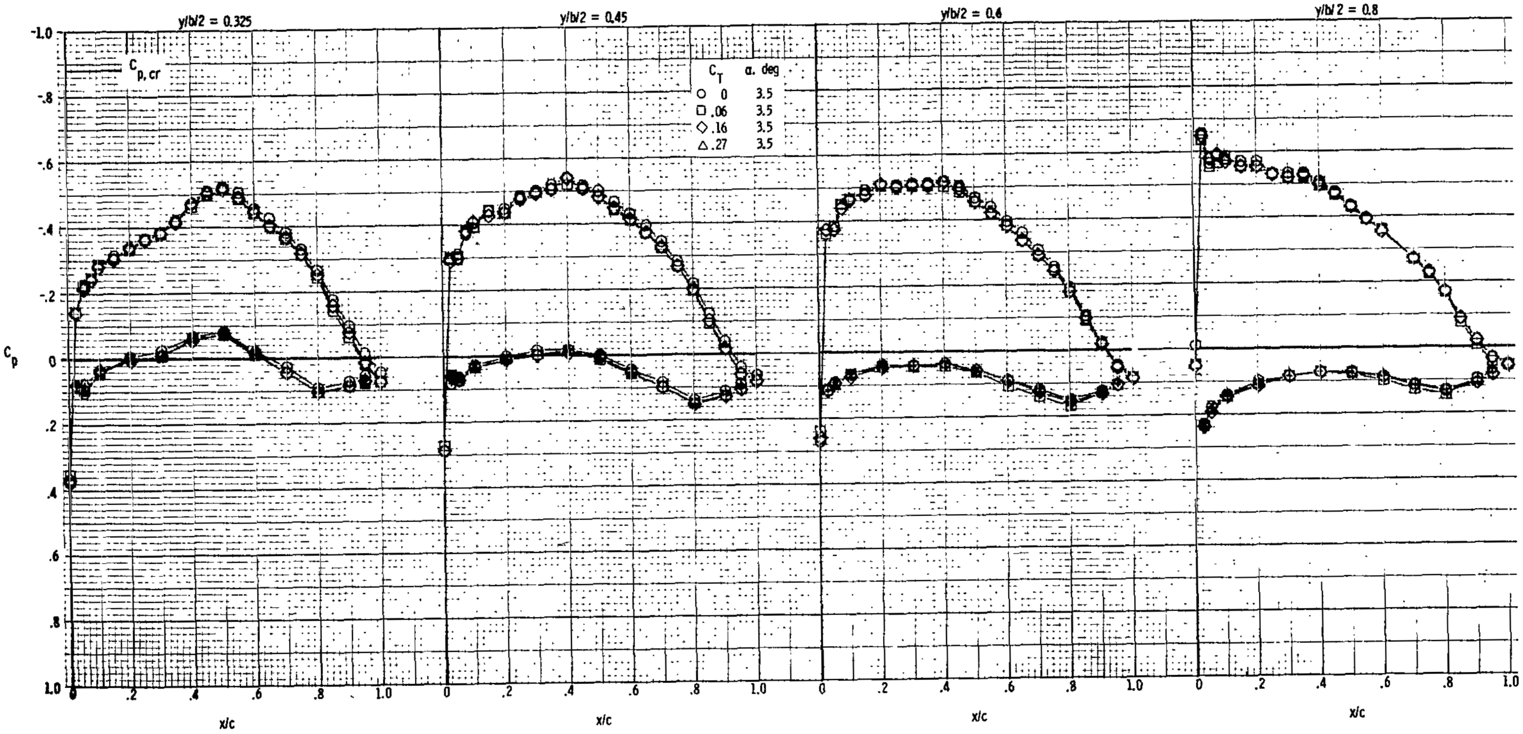

(b) M = 0.70; α = 3.5°.

Figure 19.- Continued.

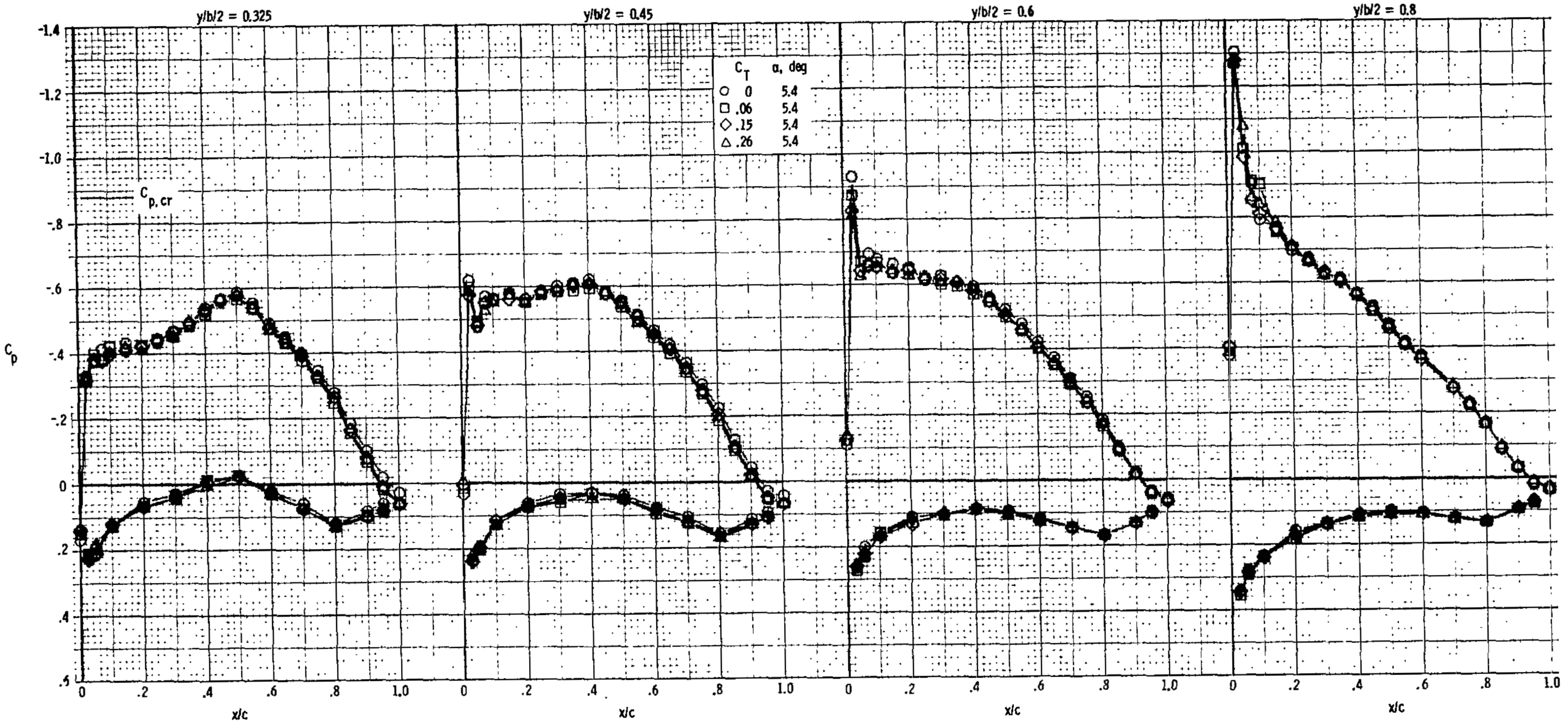

(c) M = 0.70; α = 5.4°.

Figure 19.- Continued.

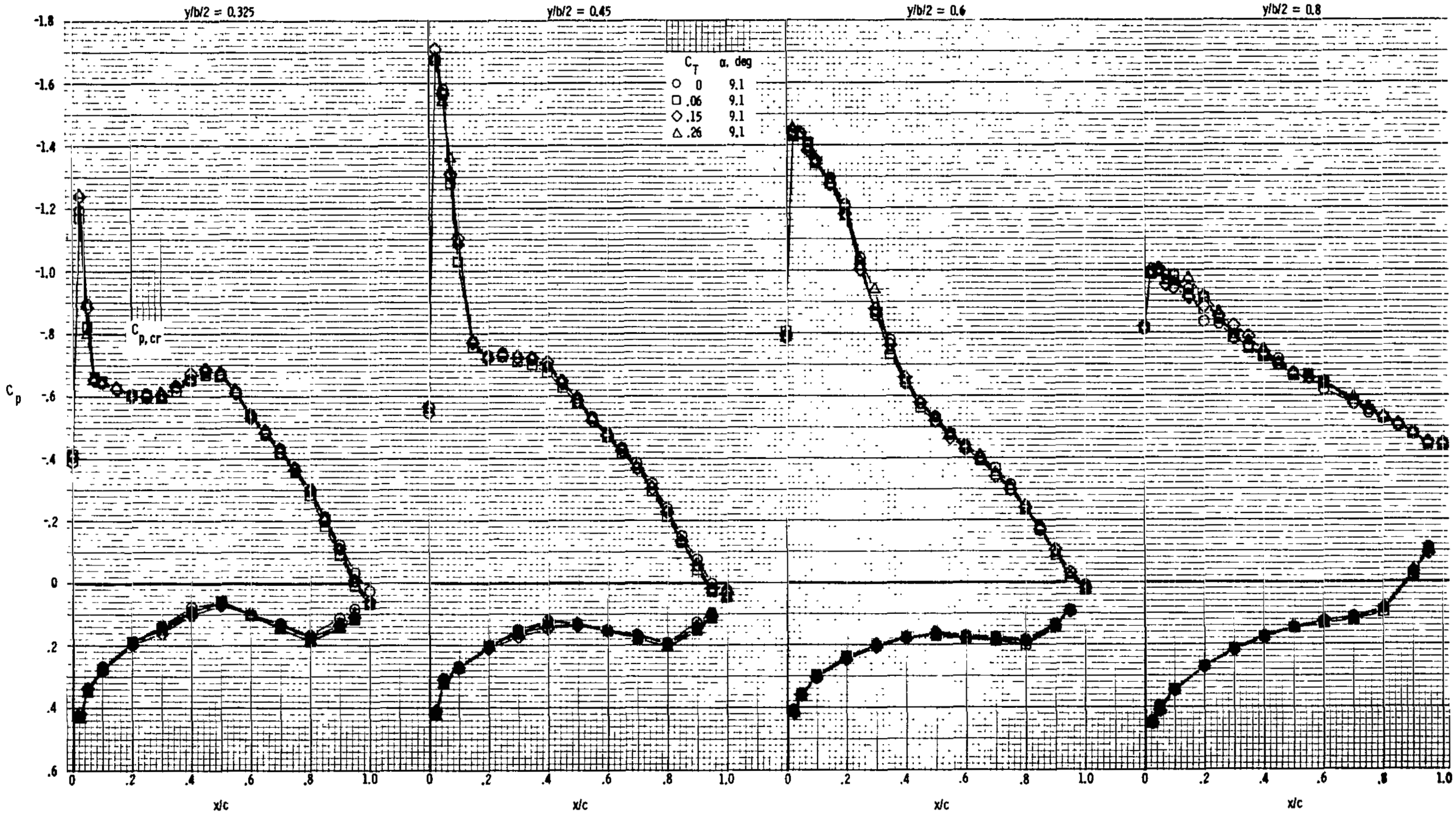

(d) M = 0.70; $\alpha = 9.1^{\circ}$.

Figure 19.- Continued.

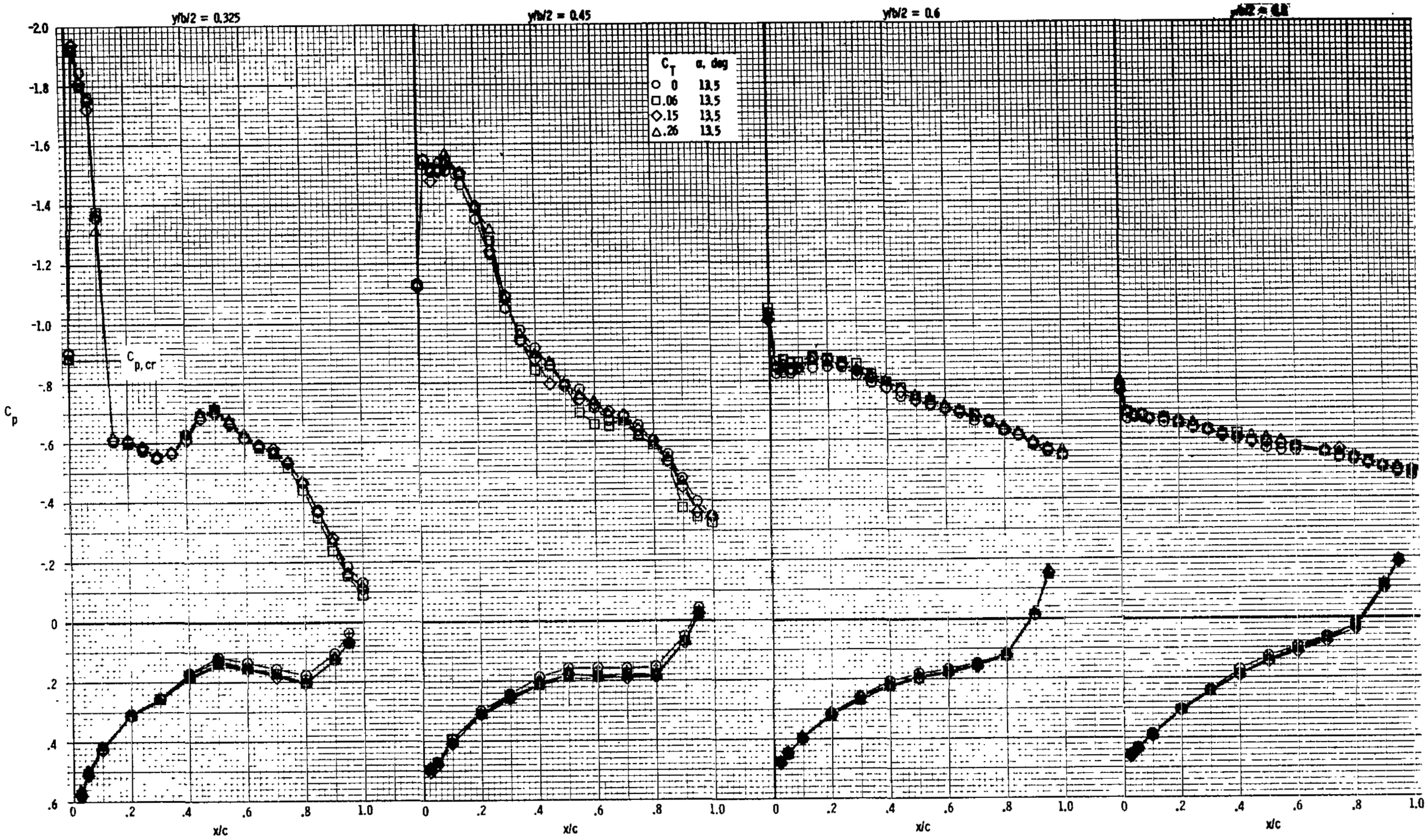

(e) M = 0.70; α = 13.5°.

Figure 19.- Continued.

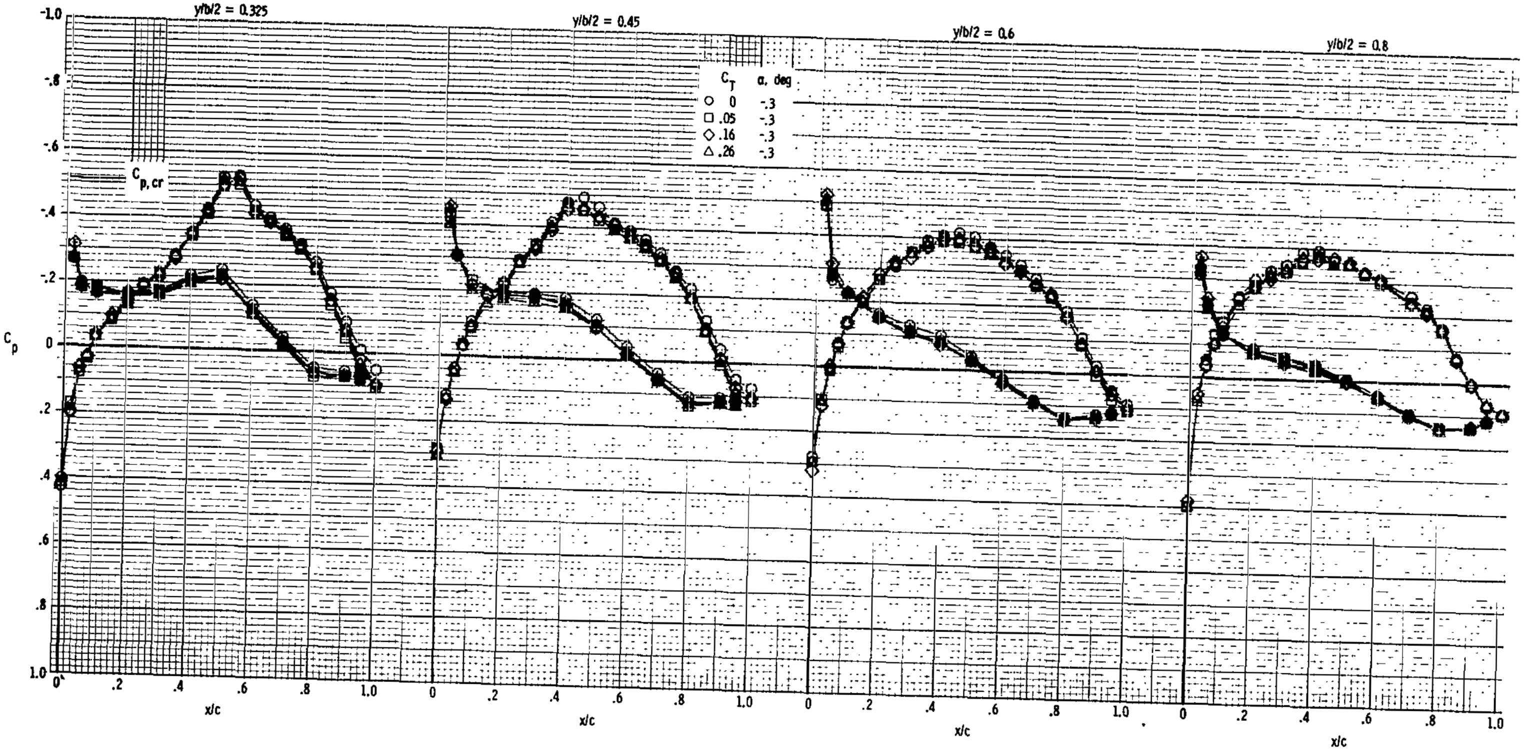

(f) M = 0.80; α = -0.3°.

Figure 19.- Continued.

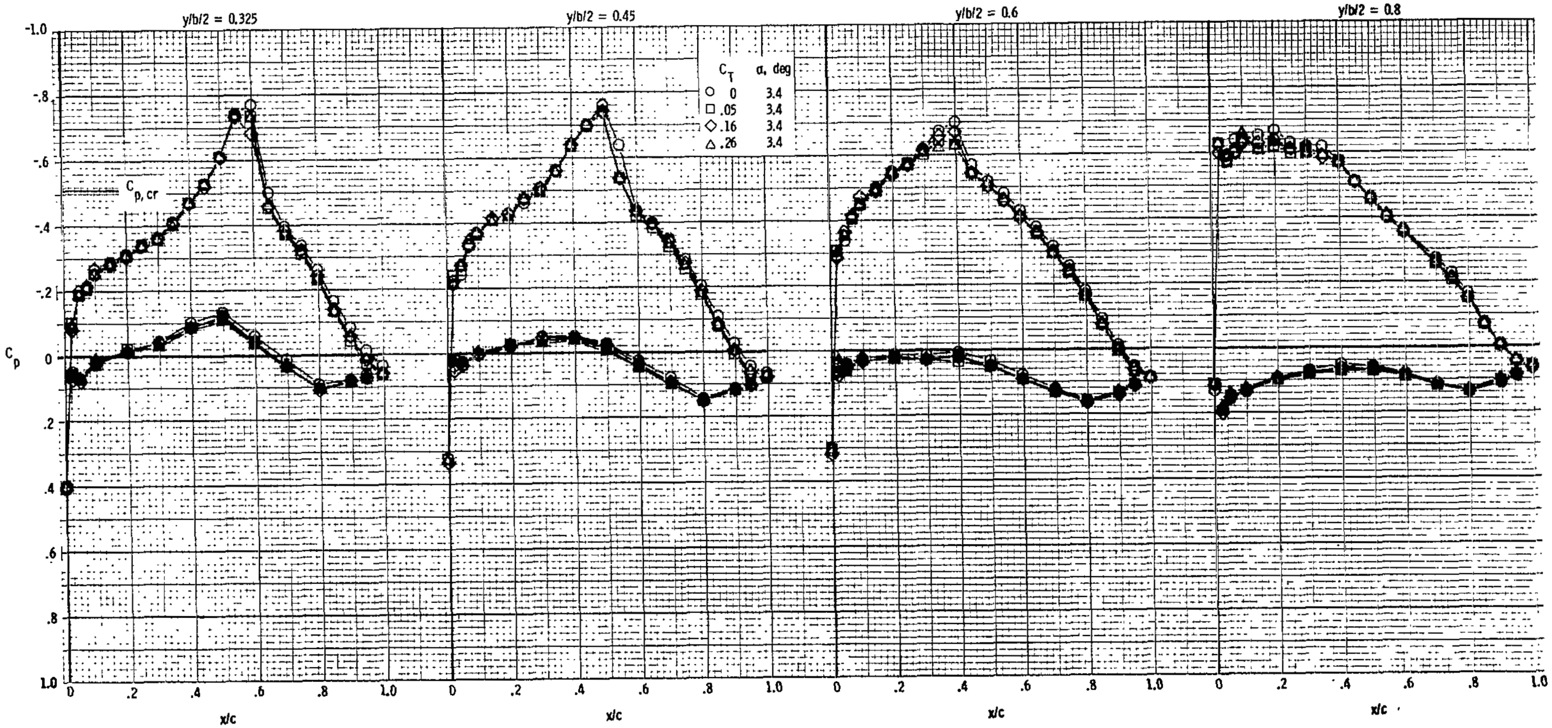

(g) M = 0.80; α = 3.4°.

Figure 19.- Continued.

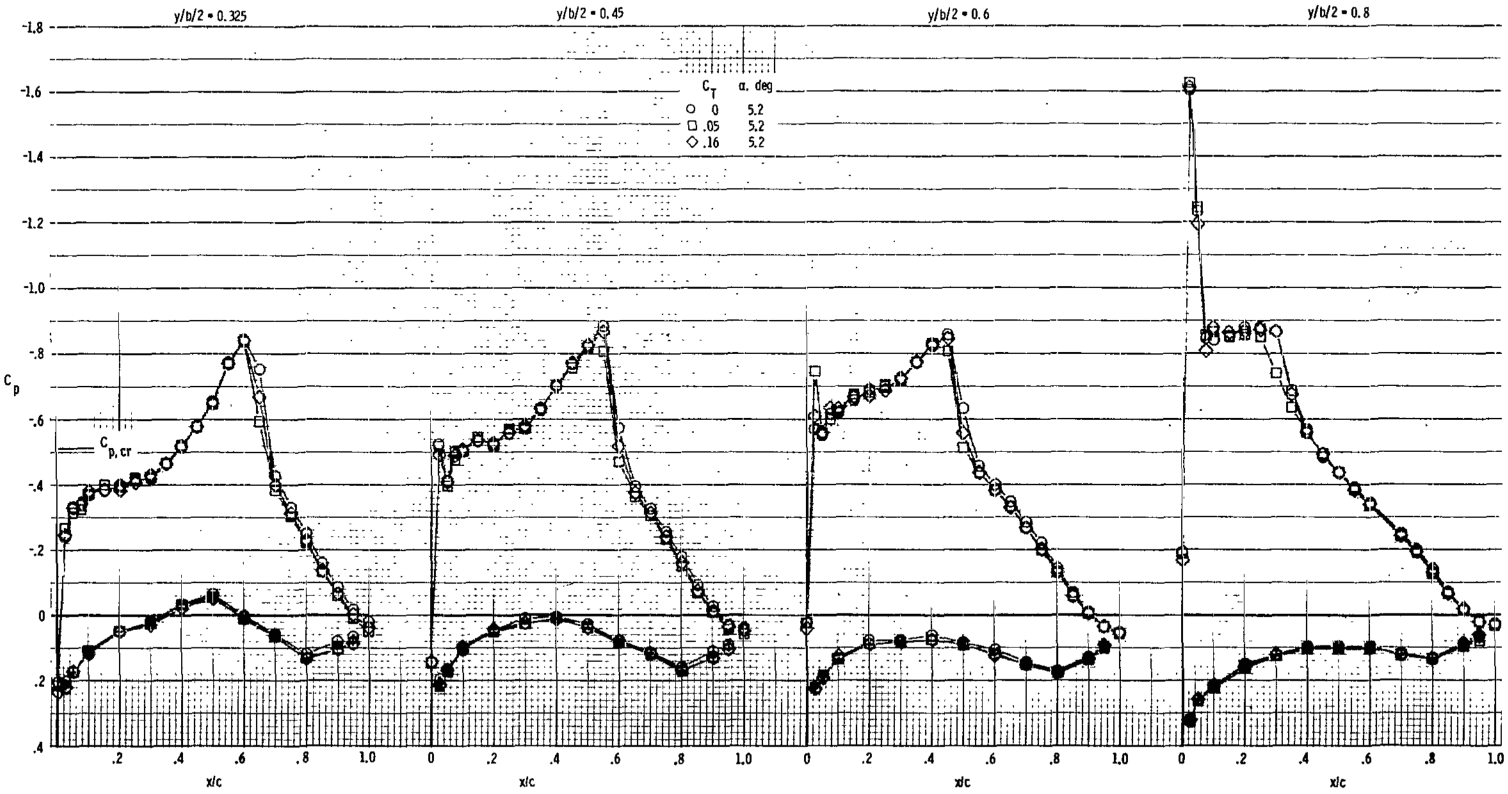

(h) M = 0.80; α = 5.2°.

Figure 19.- Continued.

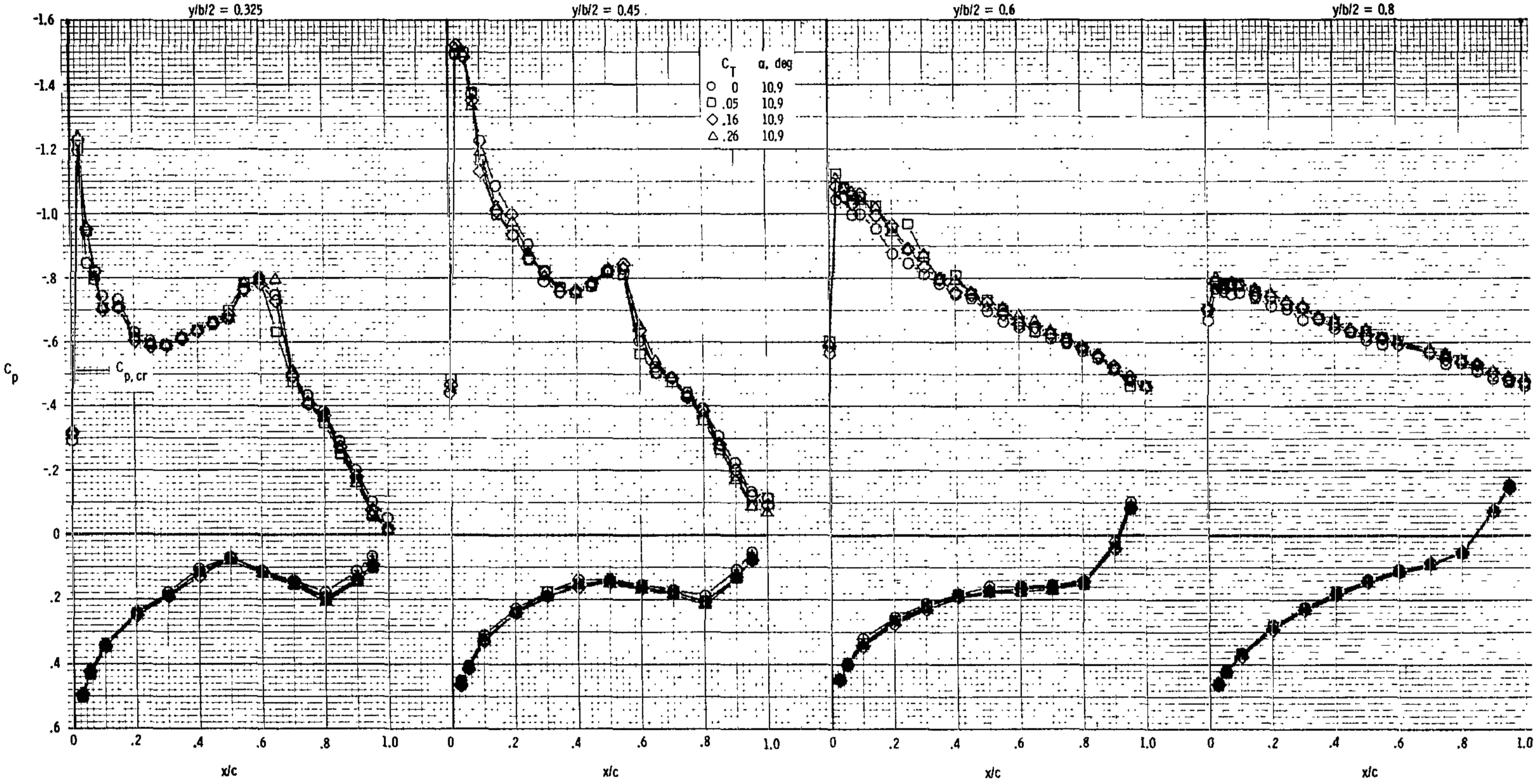

(i) M = 0.80; α = 10.9°.

Figure 19.- Continued.

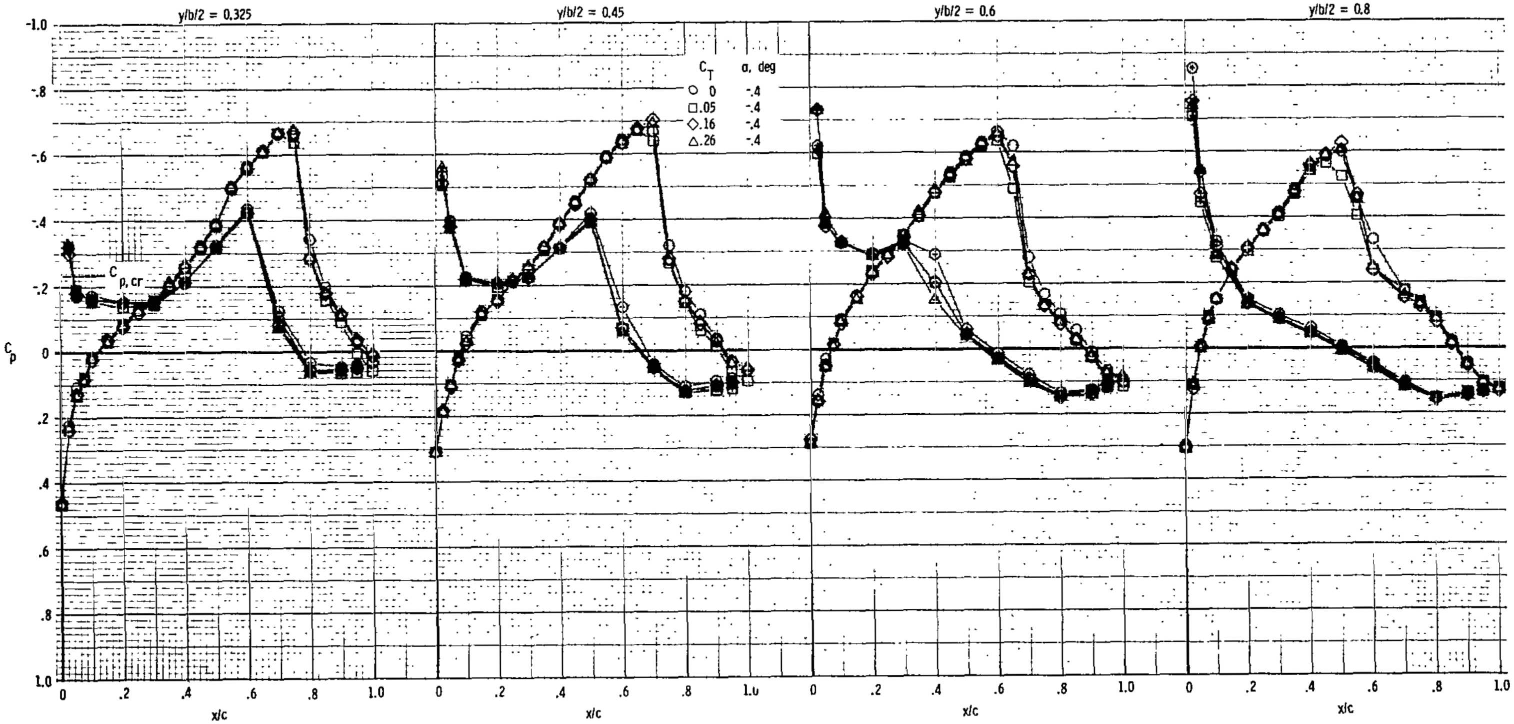

(j) M = 0.90; α = -0.4°.

Figure 19.- Continued.

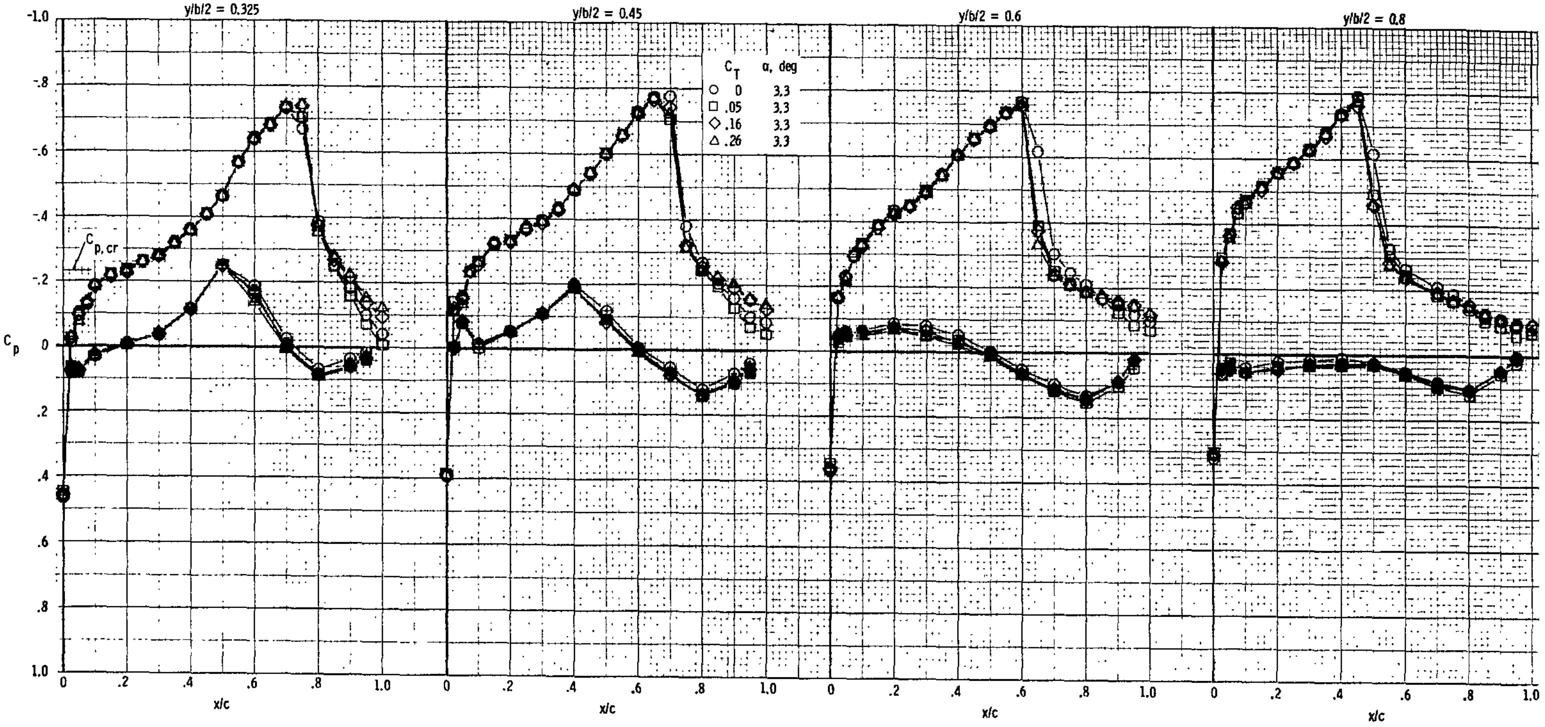

(k) M = 0.90; $\alpha = 3.3^{\circ}$.

Figure 19.- Continued.

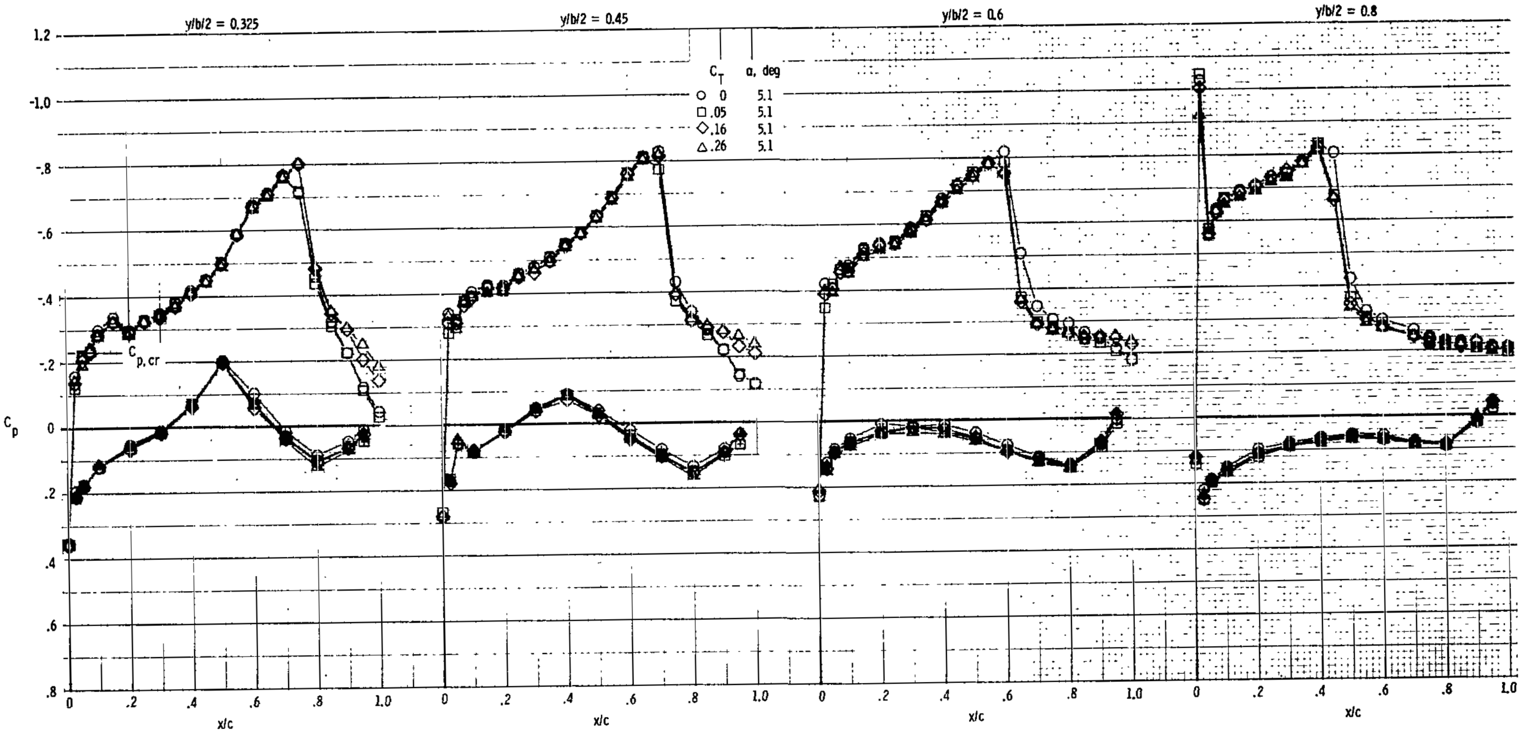

(l) M = 0.90; α = 5.1°.

Figure 19.- Continued.

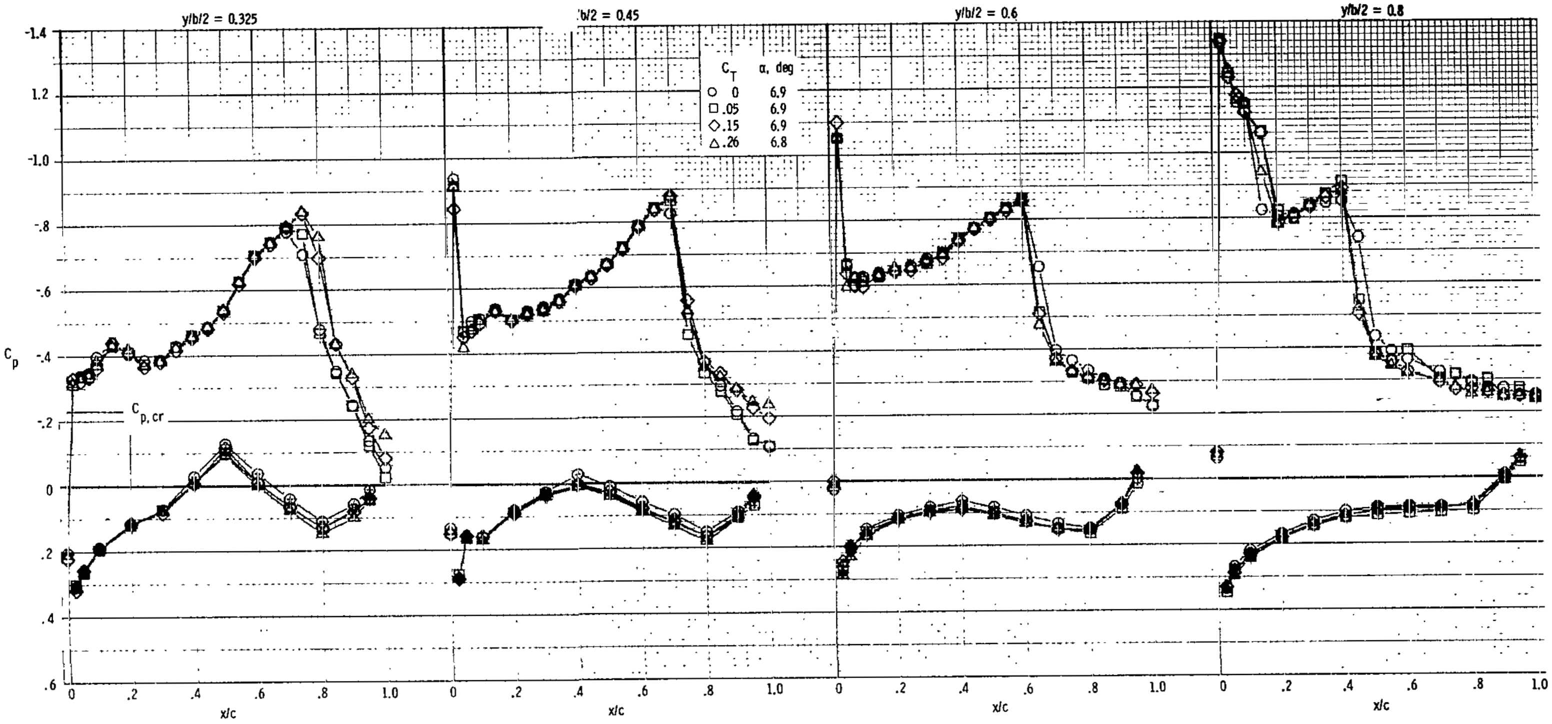

(m) M = 0.90; $\alpha = 6.9^{\circ}$.

Figure 19.- Continued.

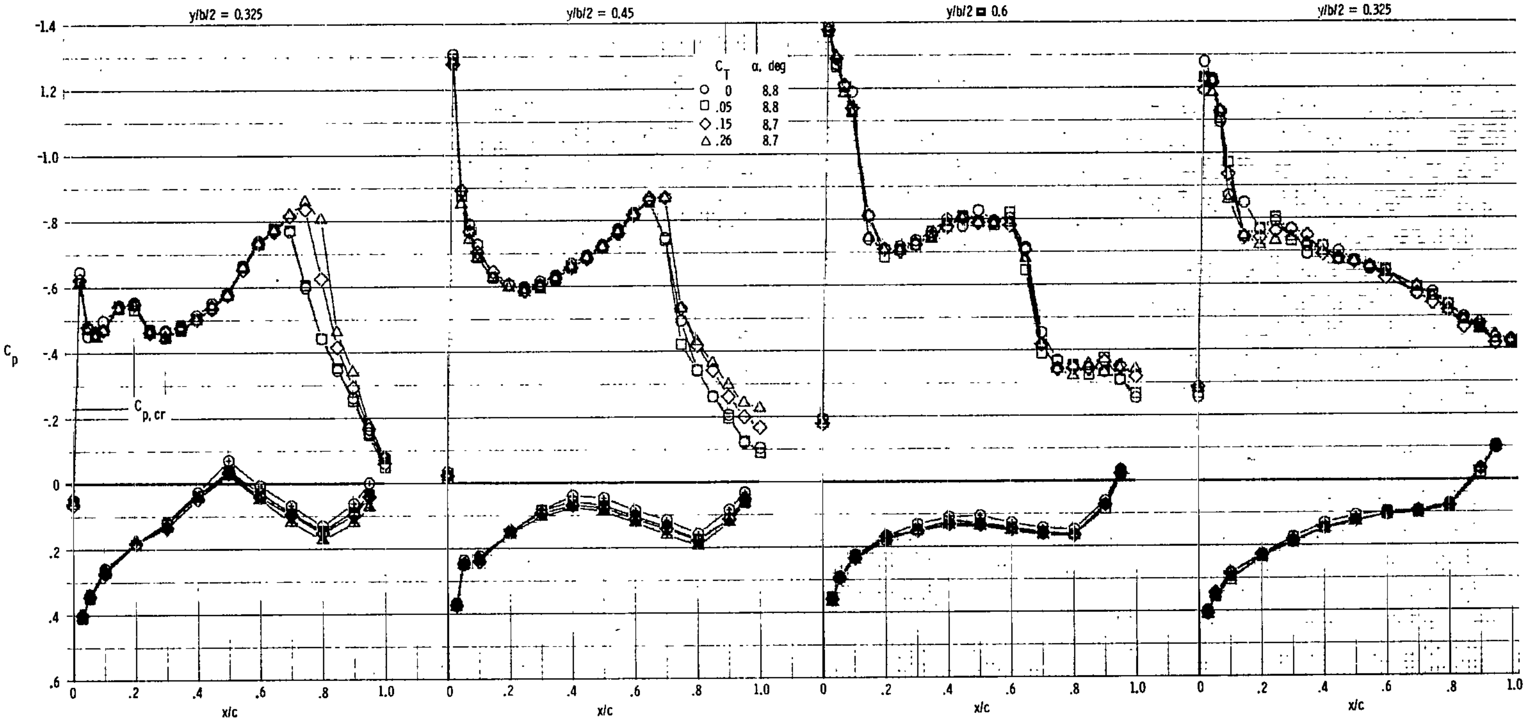

(n) M = 0.90; $\alpha = 8.8^{\circ}$.

Figure 19.- Continued.

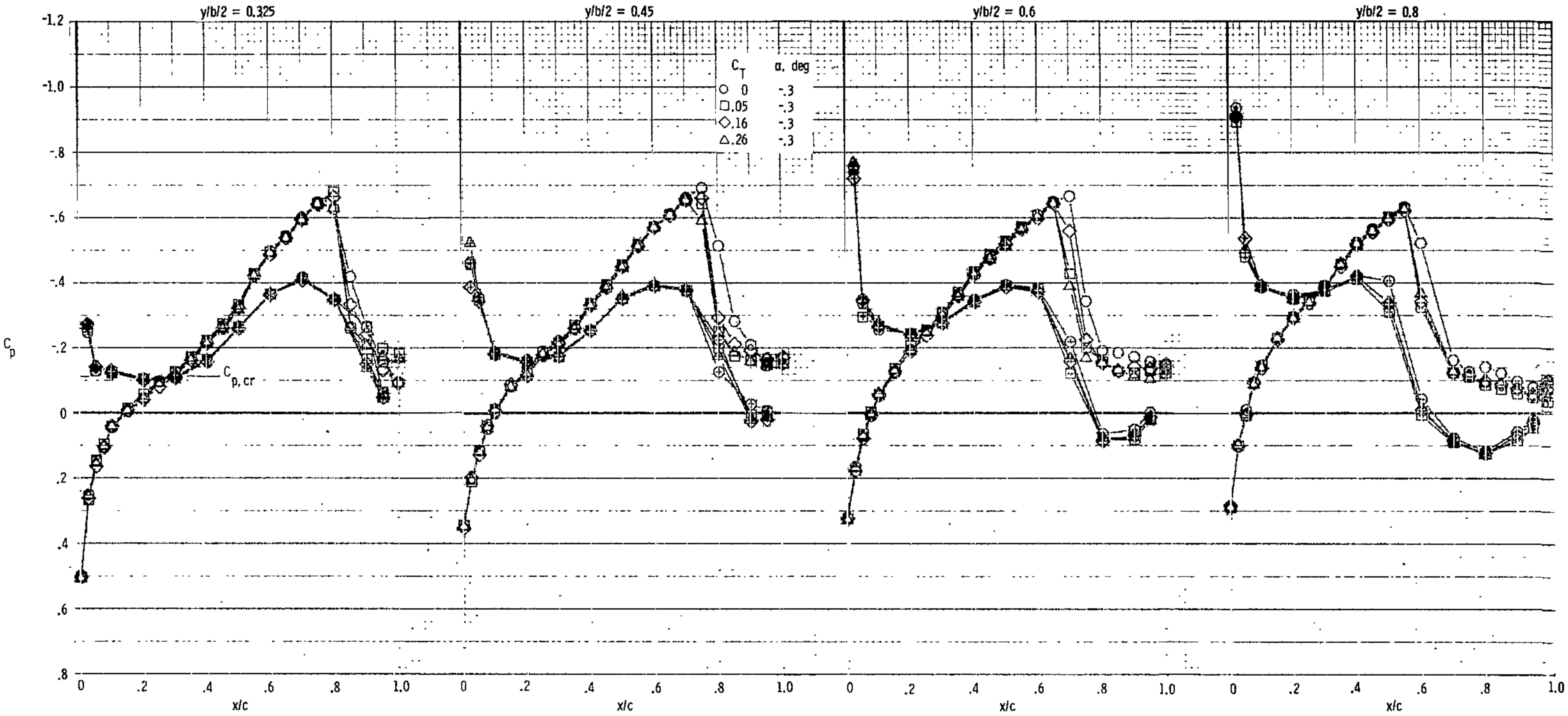

(o) M = 0.95; α = -0.3°.

Figure 19.- Continued.

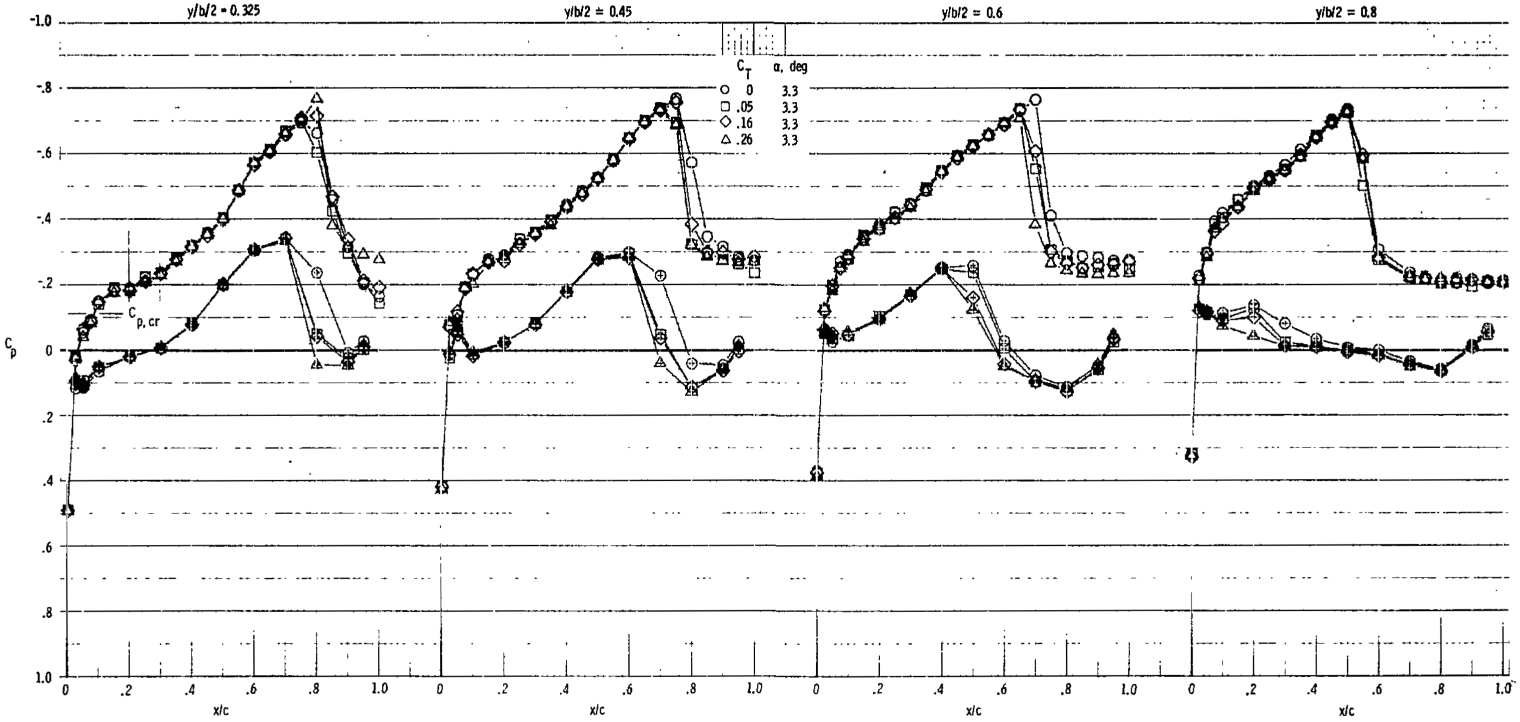

(p) M = 0.95; α = 3.3°.

Figure 19.- Continued.

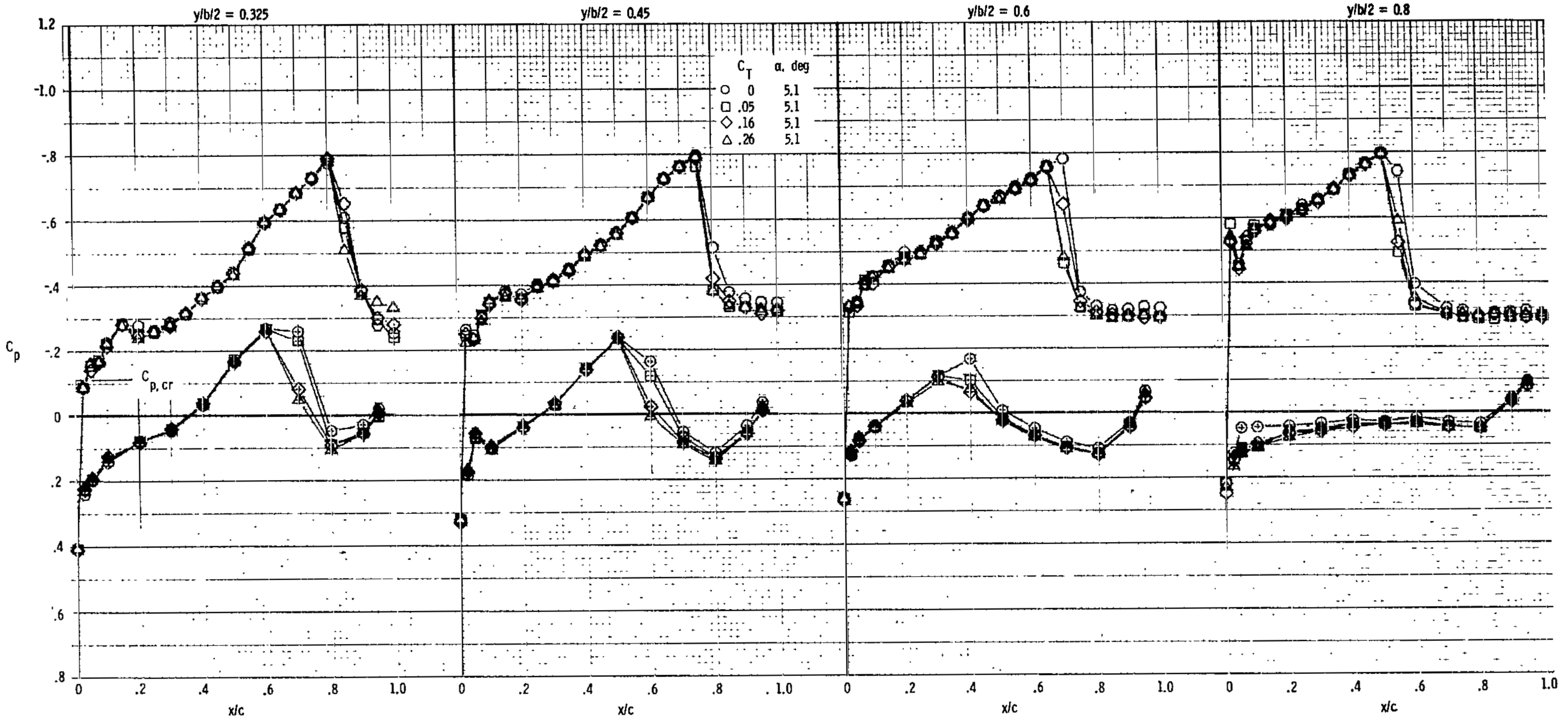

(q) M = 0.95; α = 5.1°.

Figure 19.- Continued.

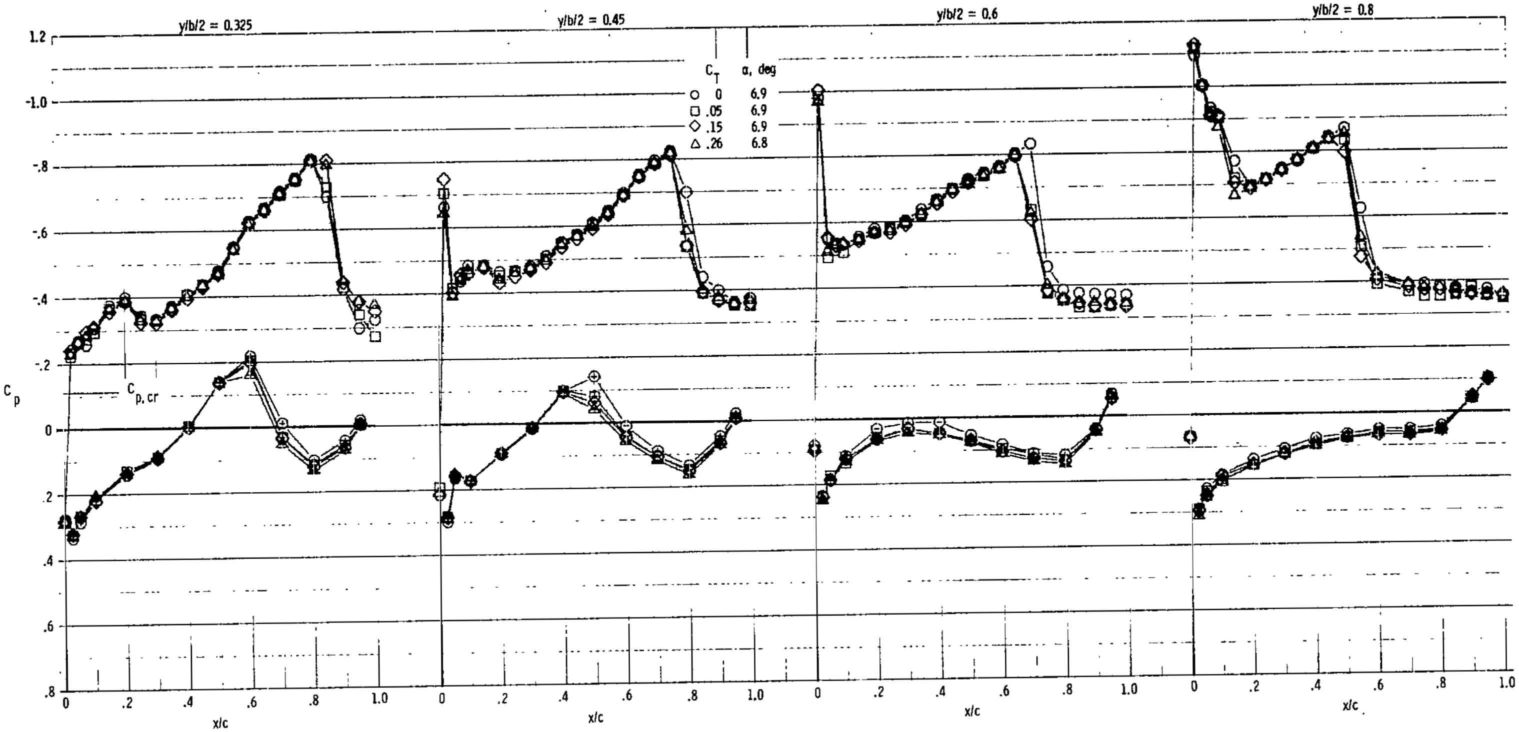

(r) M = 0.95; α = 6.9°.

Figure 19.- Continued.

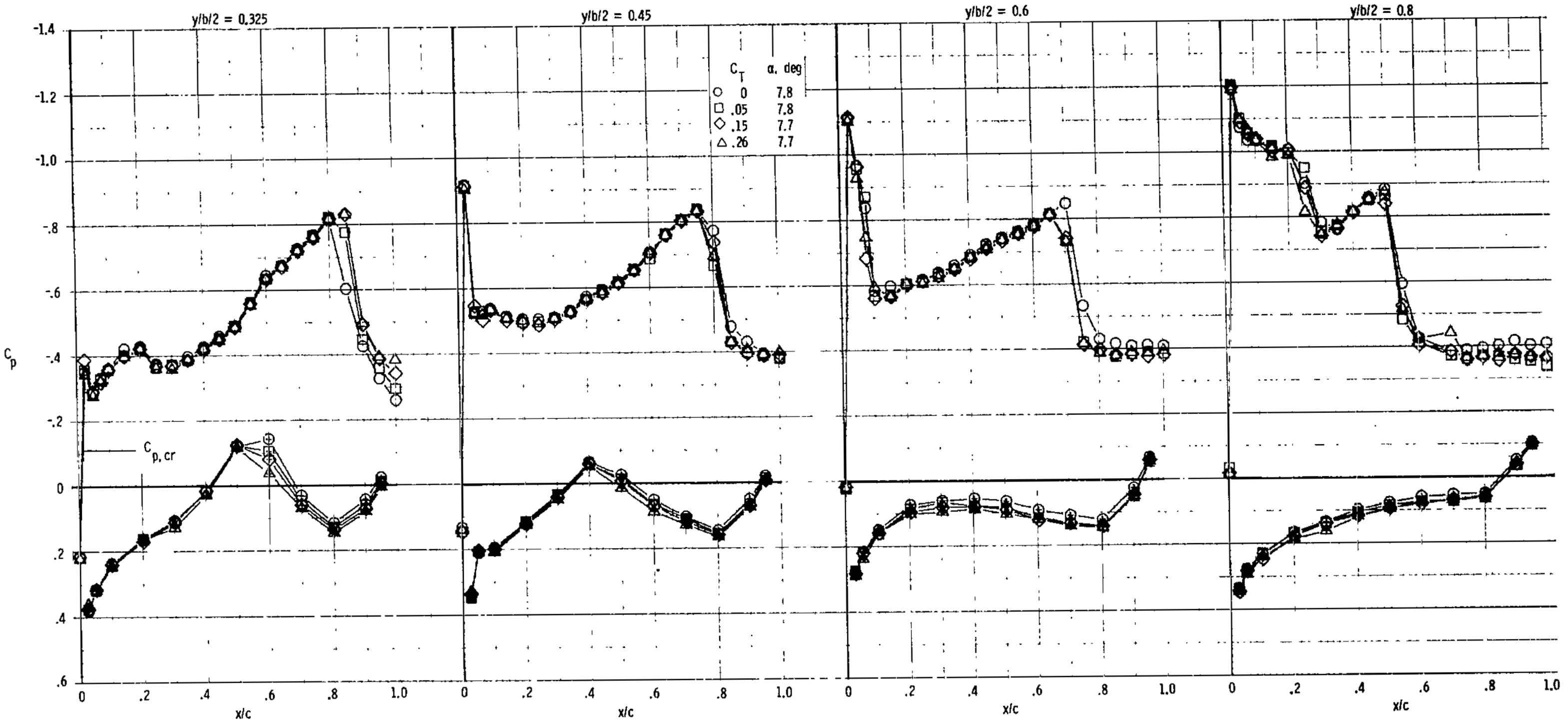

(s) M = 0.95; $\alpha = 7.8^{\circ}$.

Figure 19.- Concluded.

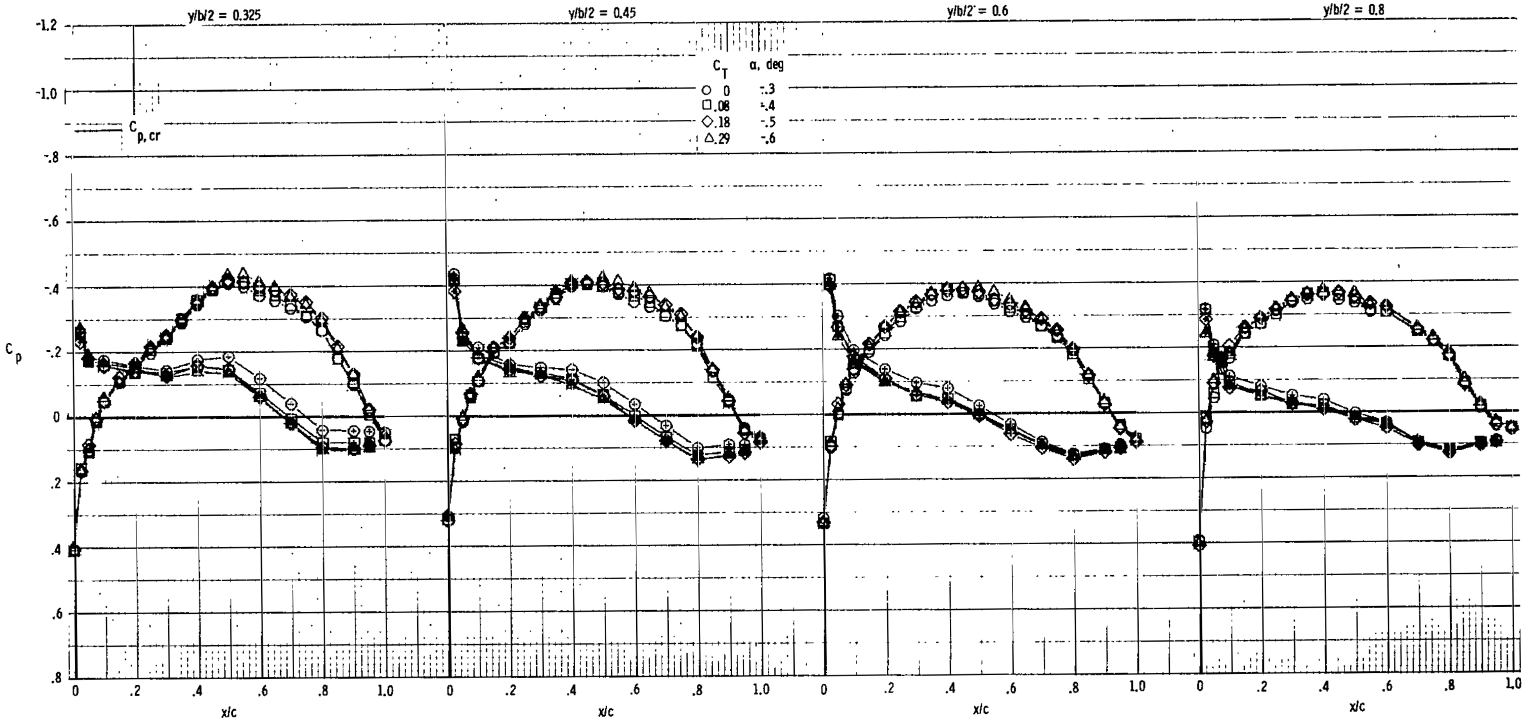

(a) M = 0.70; $\alpha \approx -0.5^\circ$.

Figure 20.- Chordwise pressure distributions. $\delta_d = 30^\circ$. Symbols with crosses denote airfoil lower surface.

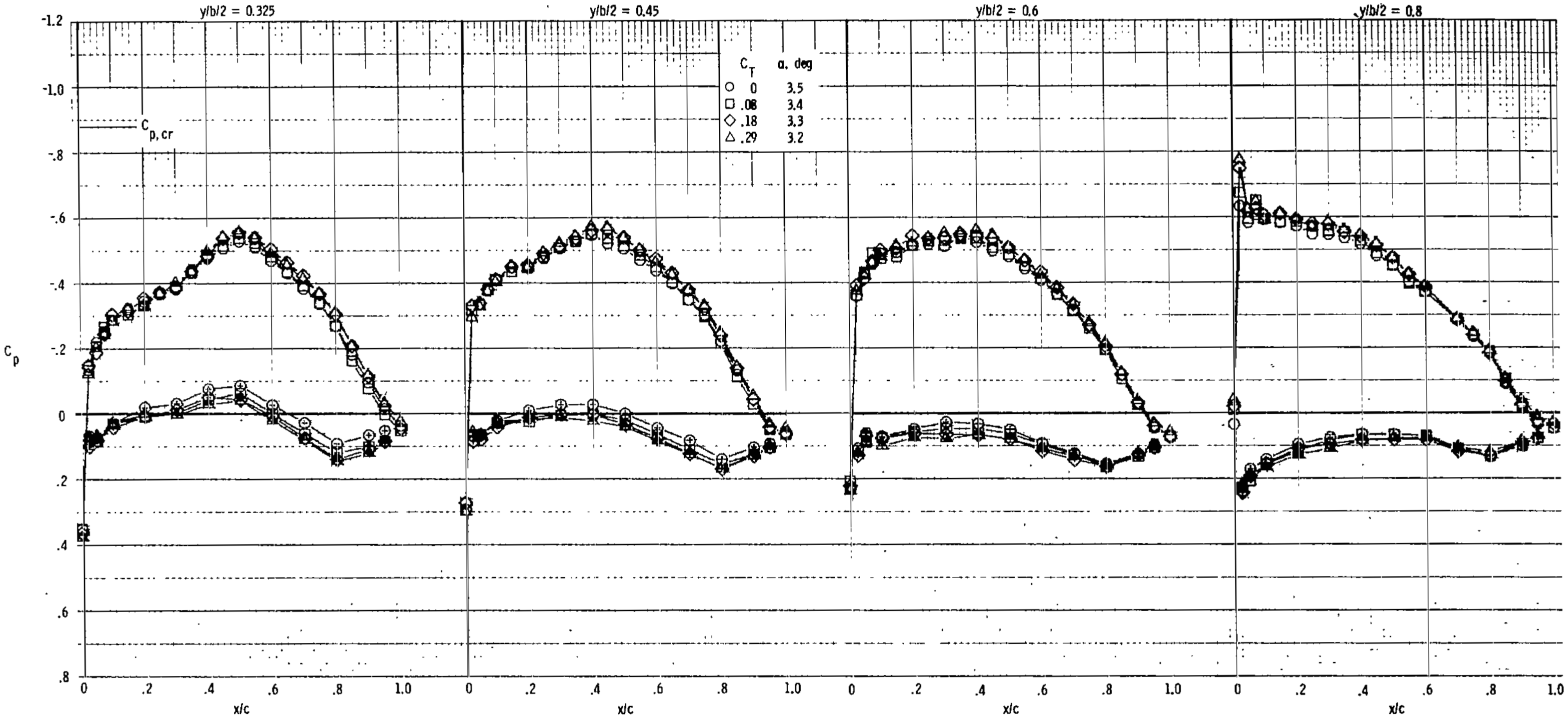

(b) M = 0.70; $\alpha \approx 3.4^{\circ}$.

Figure 20.- Continued.

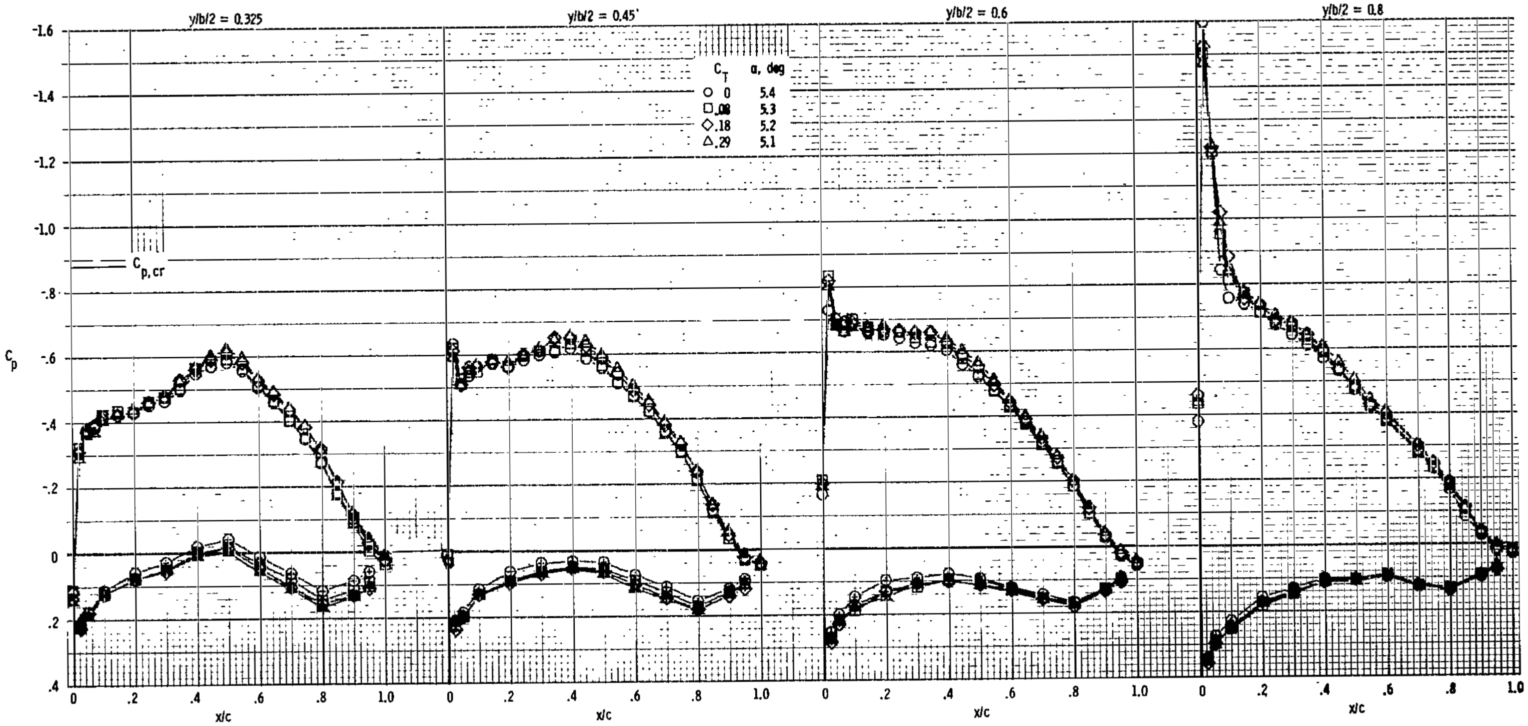

(c) M = 0.70; $\alpha \approx 5.3^{\circ}$.

Figure 20.- Continued.

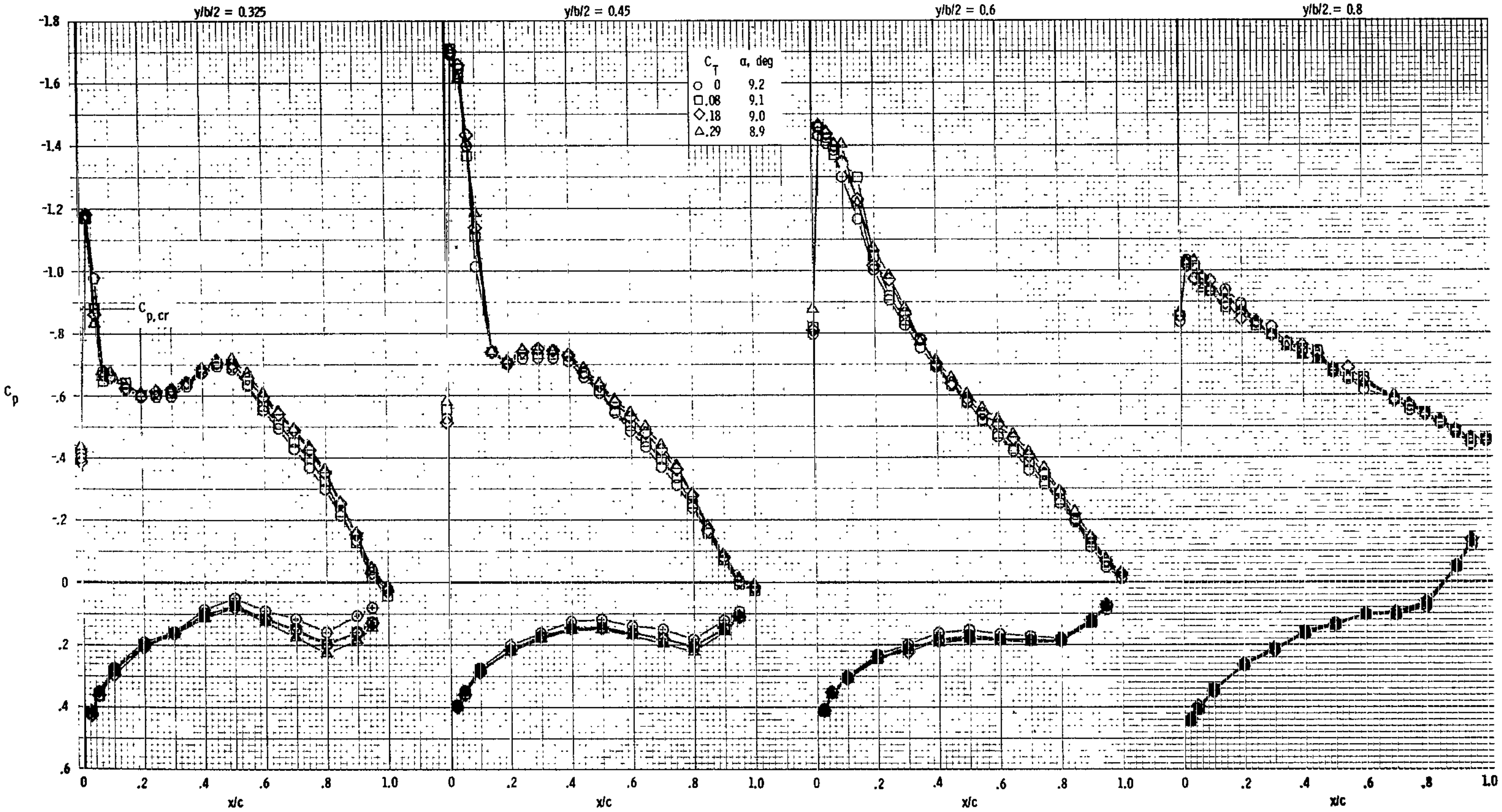

(d) M = 0.70; $\alpha \approx 9.1^{\circ}$.

Figure 20.- Continued.

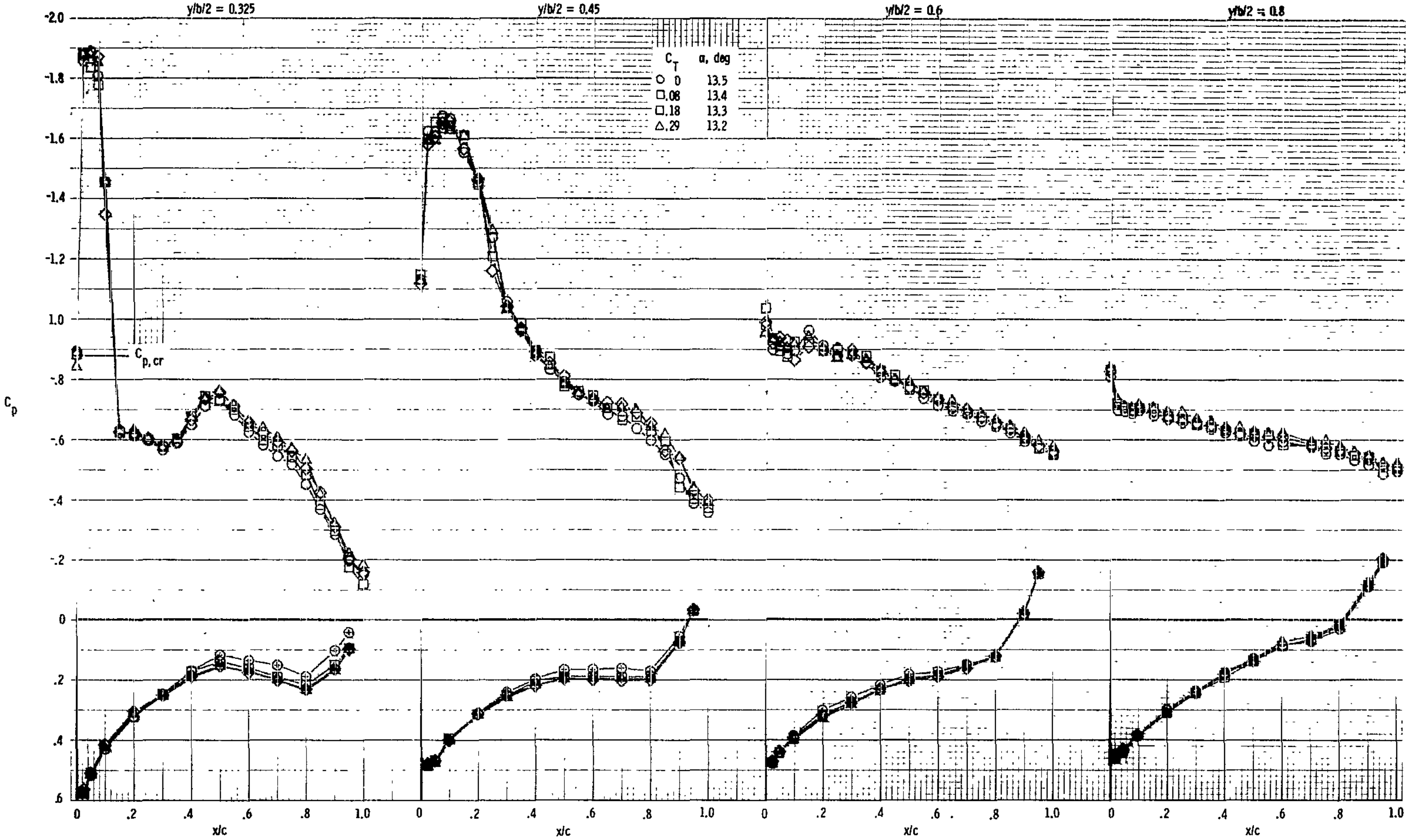

(e) M = 0.70; $\alpha \approx 13.4^{\circ}$.

Figure 20.- Continued.

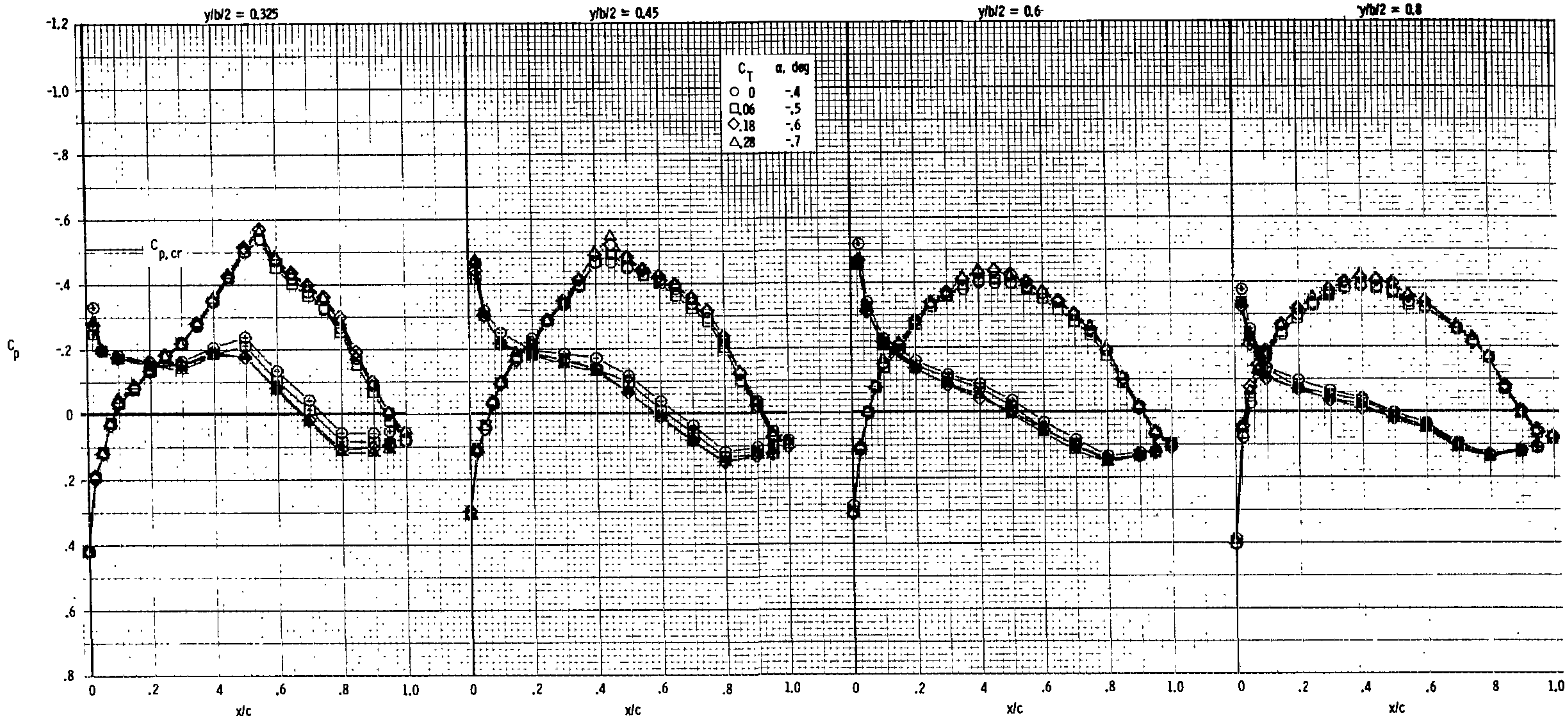

(f) M = 0.80; $\alpha \approx -0.5^{\circ}$.

Figure 20.- Continued.

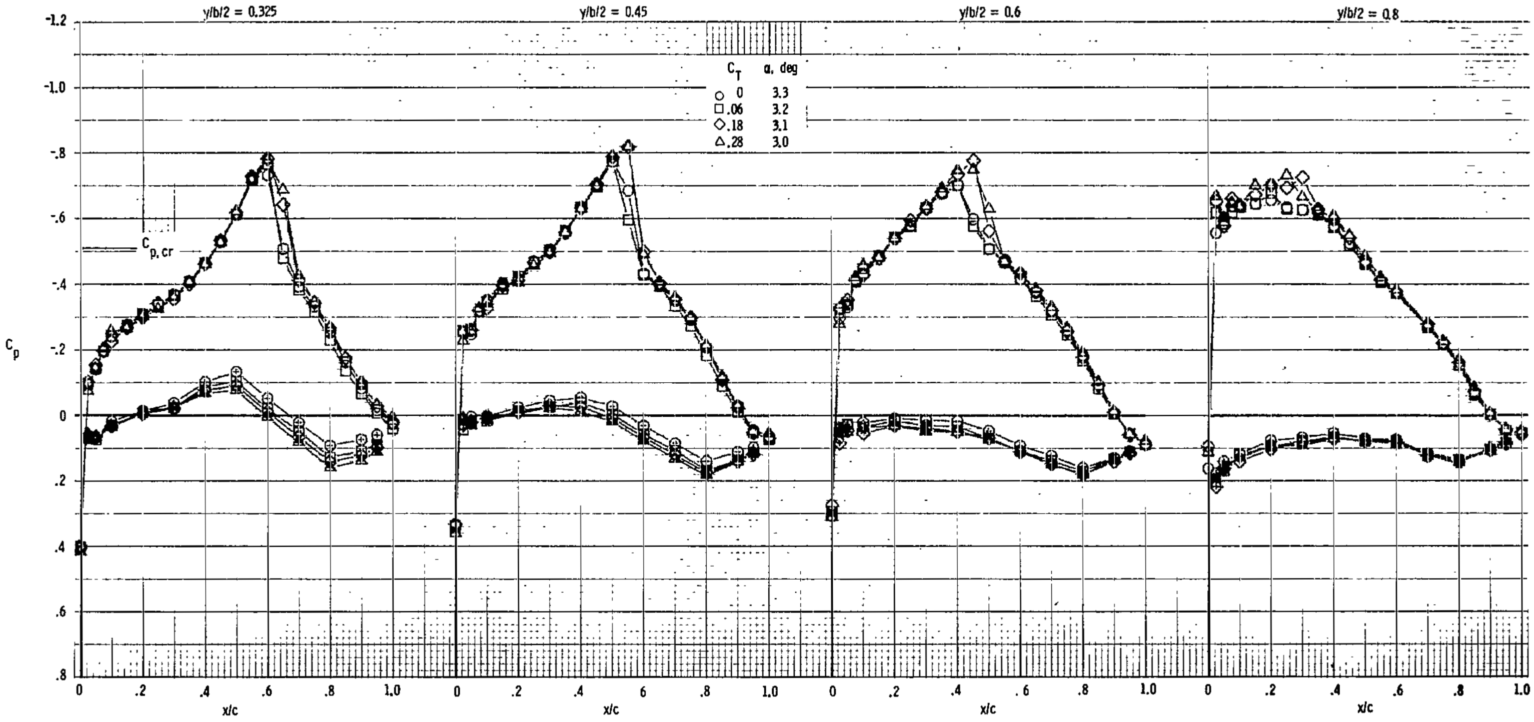

(g) M = 0.80; $\alpha \approx 3.2^{o}$.

Figure 20.- Continued.

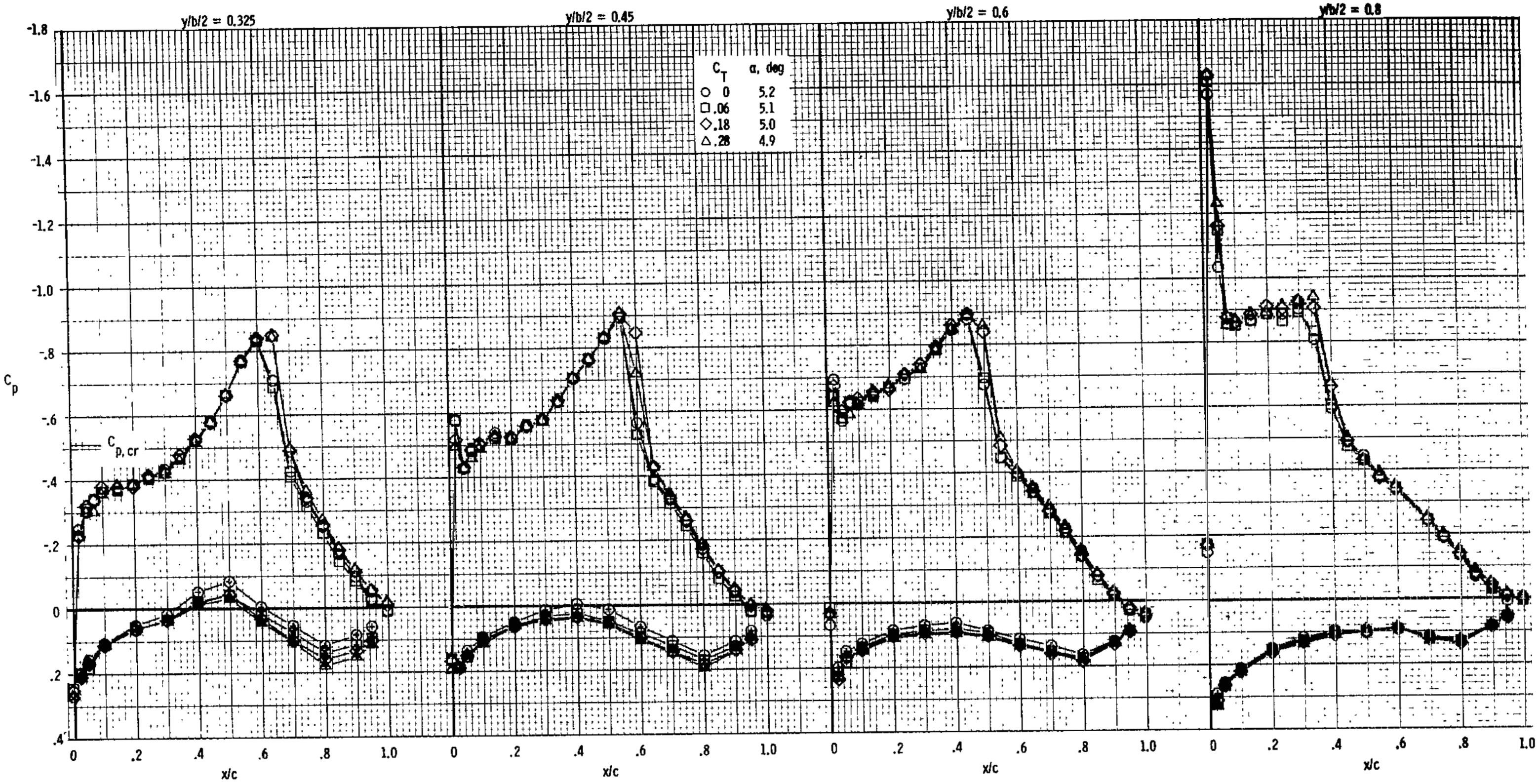

(h) M = 0.80; $\alpha \approx 5.1^{\circ}$.

Figure 20.- Continued.

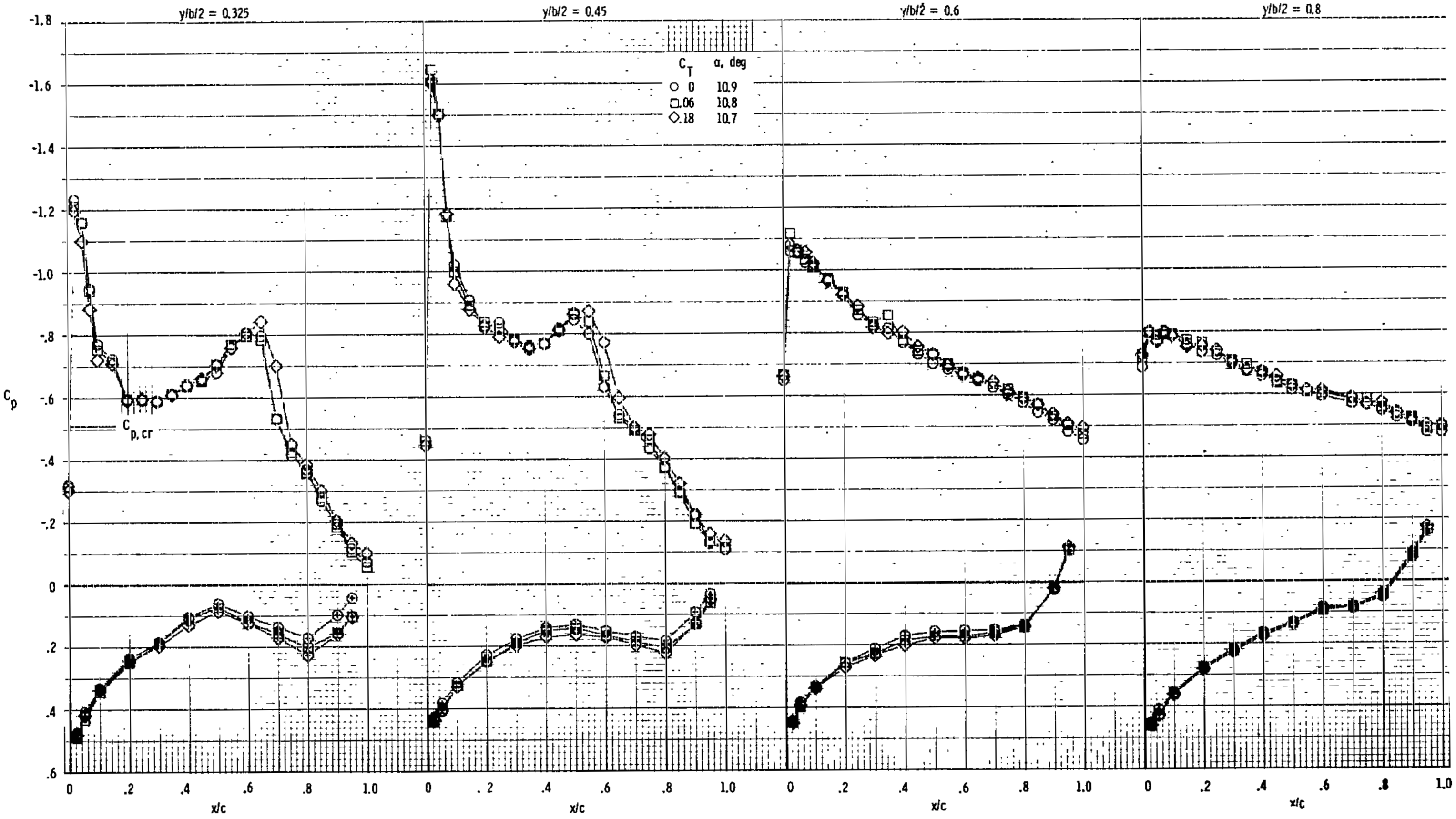

(i) M = 0.80; $\alpha \approx 10.8^{\circ}$.

Figure 20.- Continued.

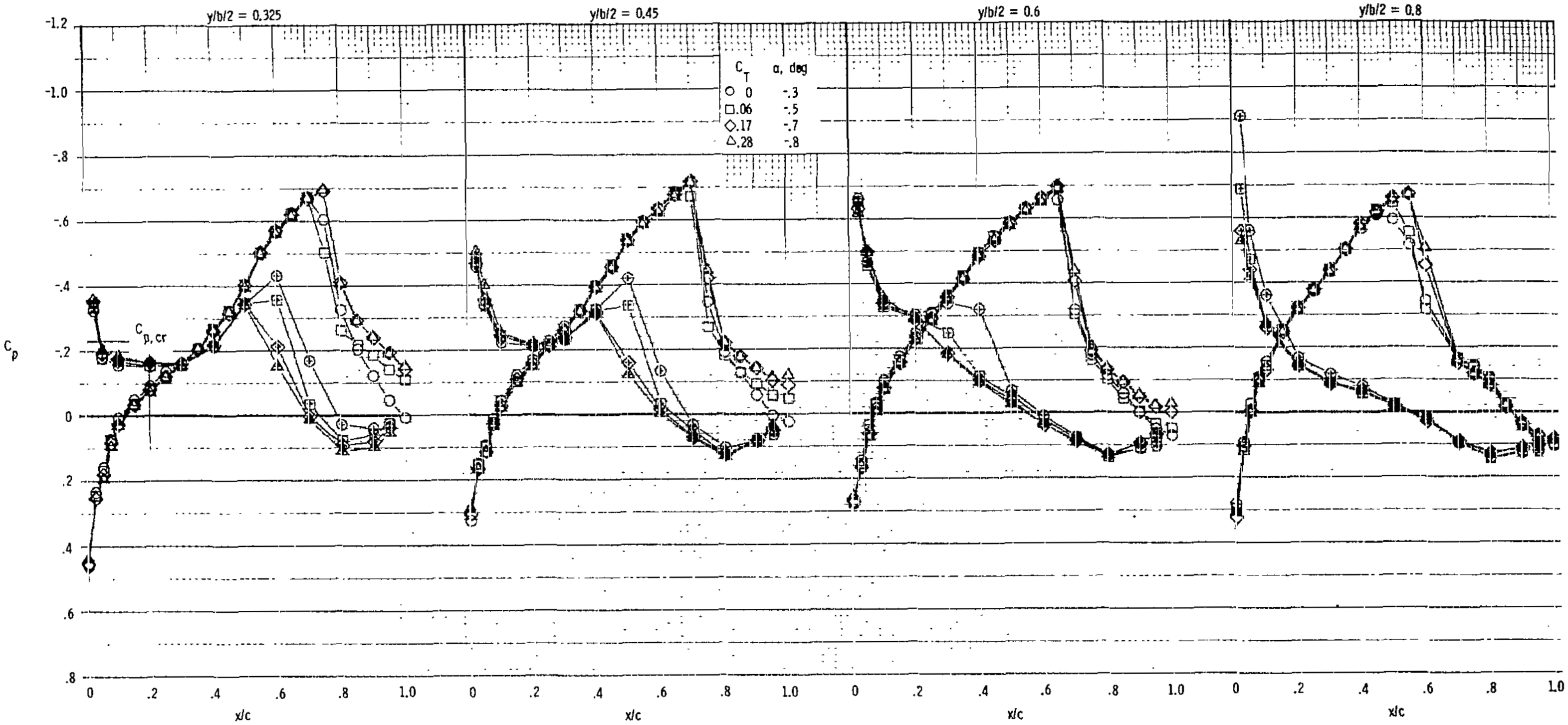

(j) M = 0.90; $\alpha \approx -0.5^{\circ}$.

Figure 20.- Continued.

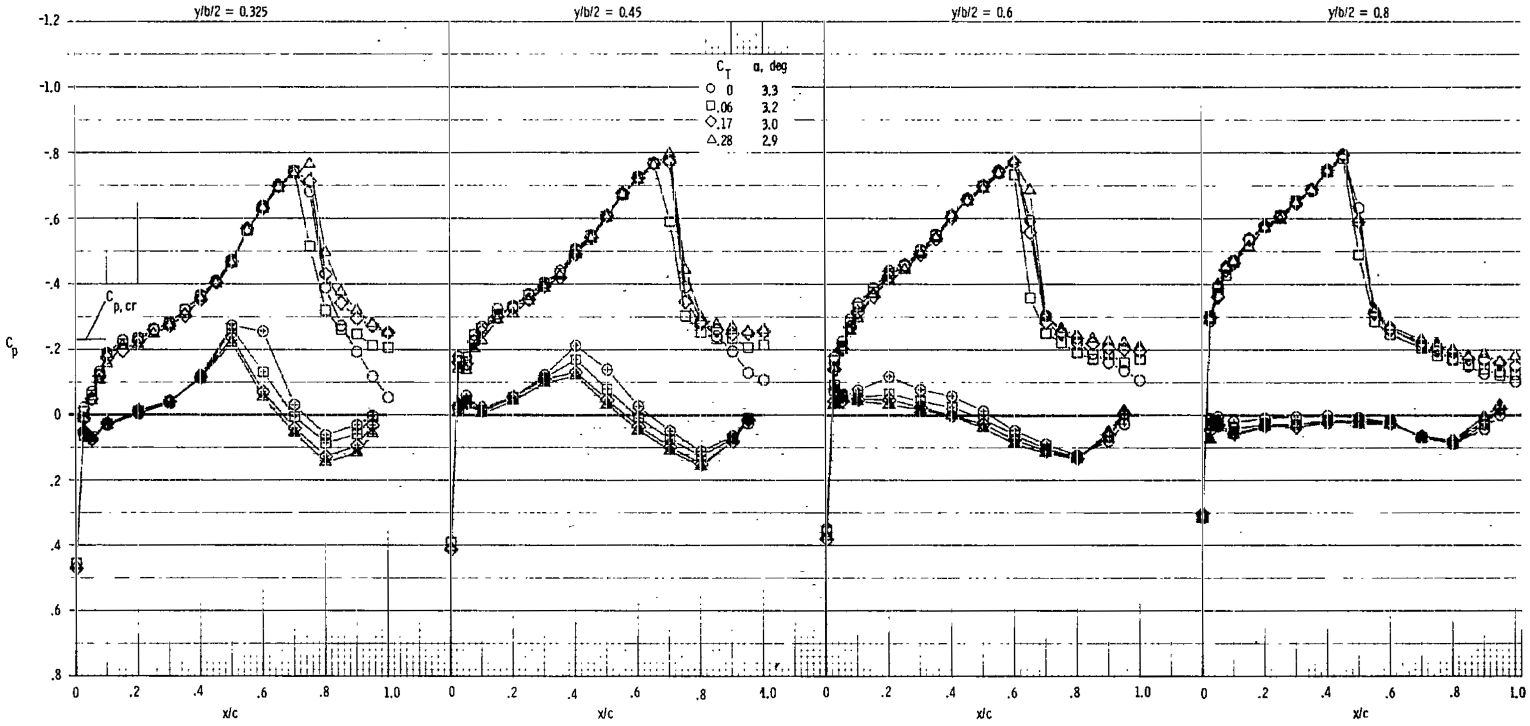

(k) M = 0.90; $\alpha \approx 3.2^{\circ}$.

Figure 20.- Continued.

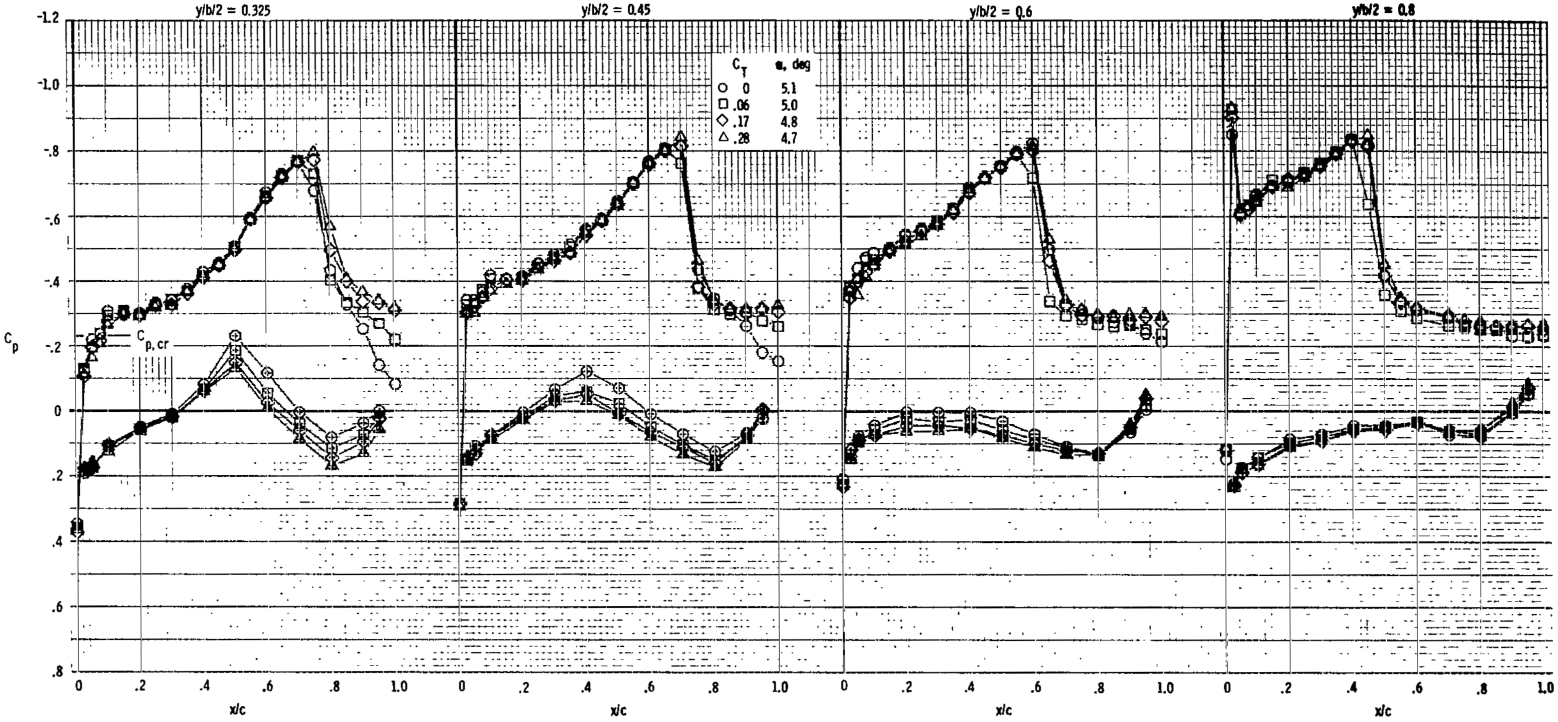

(l) M = 0.90; $\alpha \approx 5.0^{\circ}$.

Figure 20.- Continued.

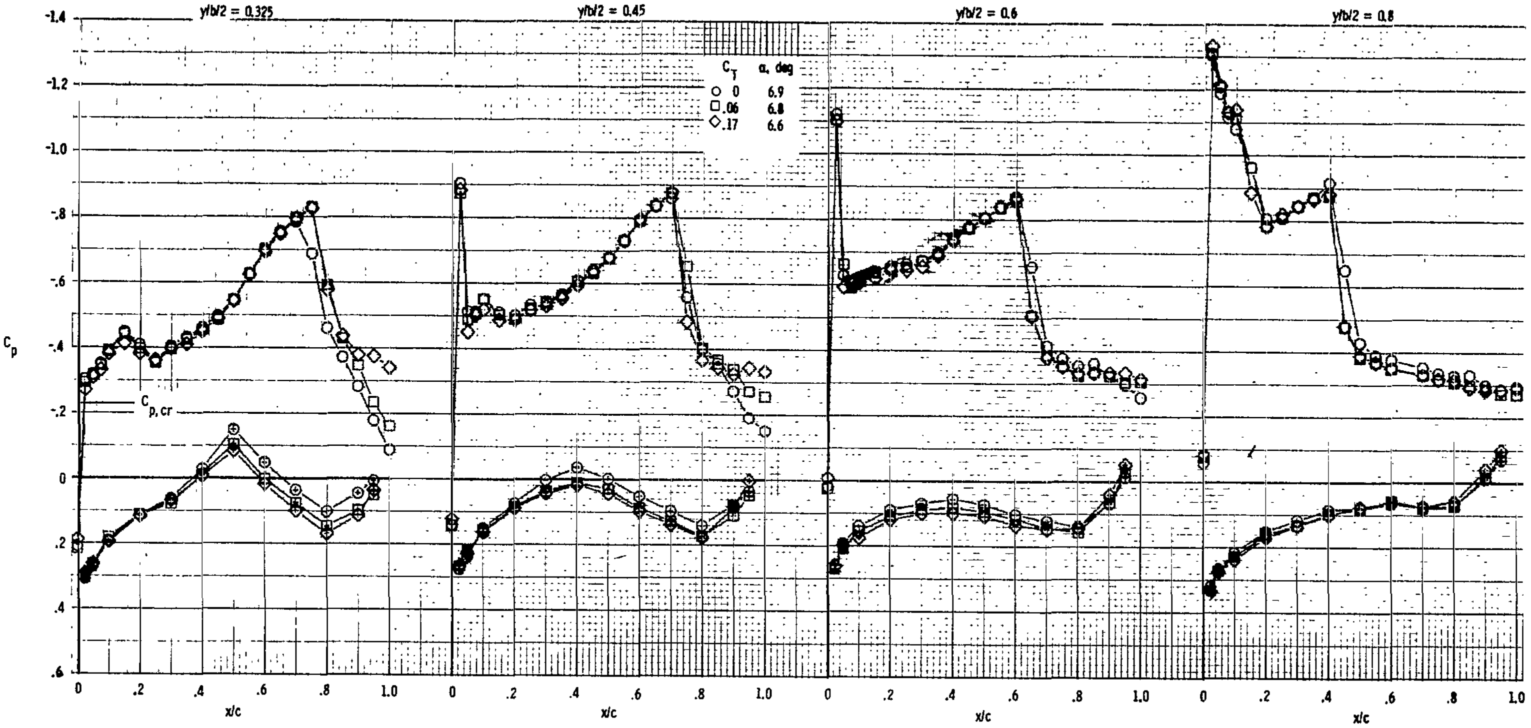

(m) M = 0.90; α ≈ 6.8°.

Figure 20.- Continued.

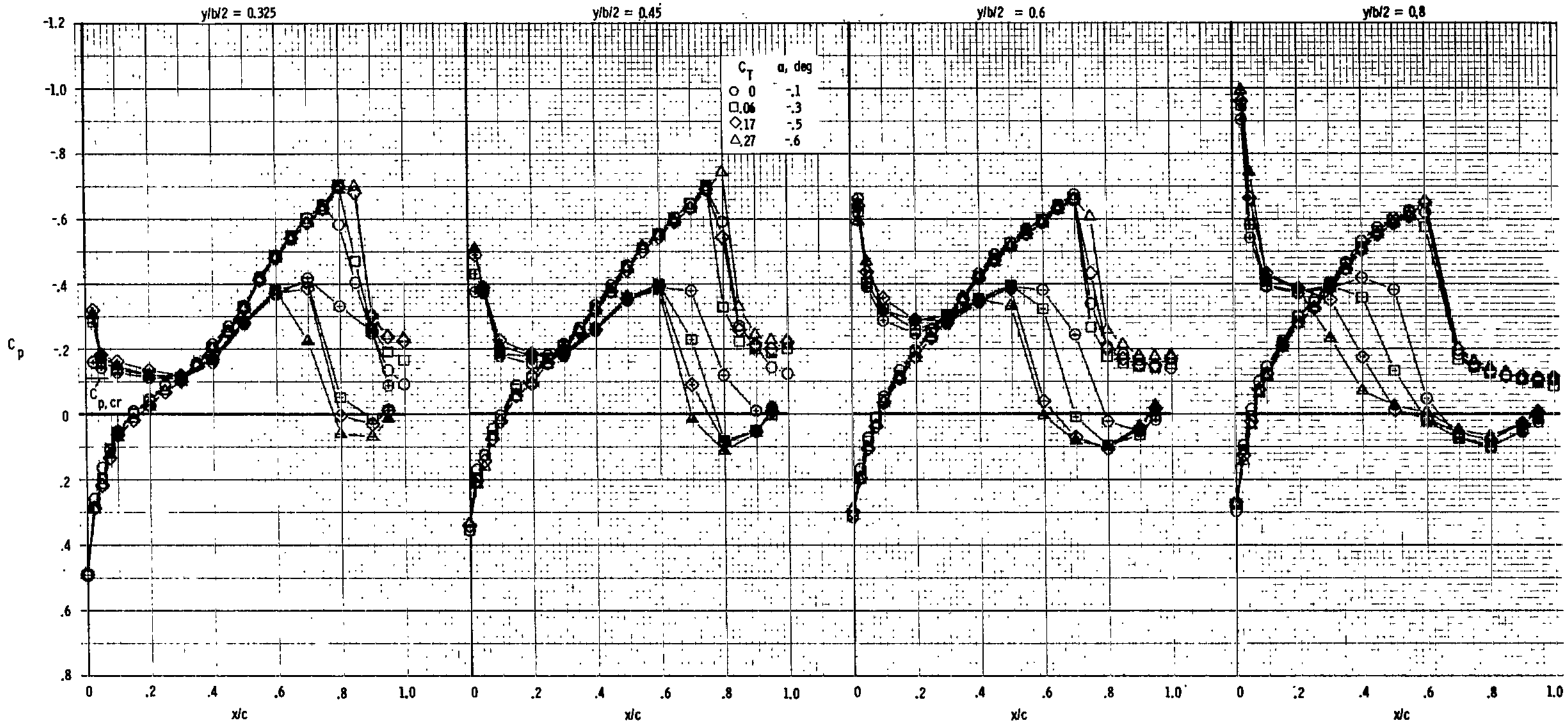

(n) M = 0.95; $\alpha \approx -0.3^{\circ}$.

Figure 20.- Continued.

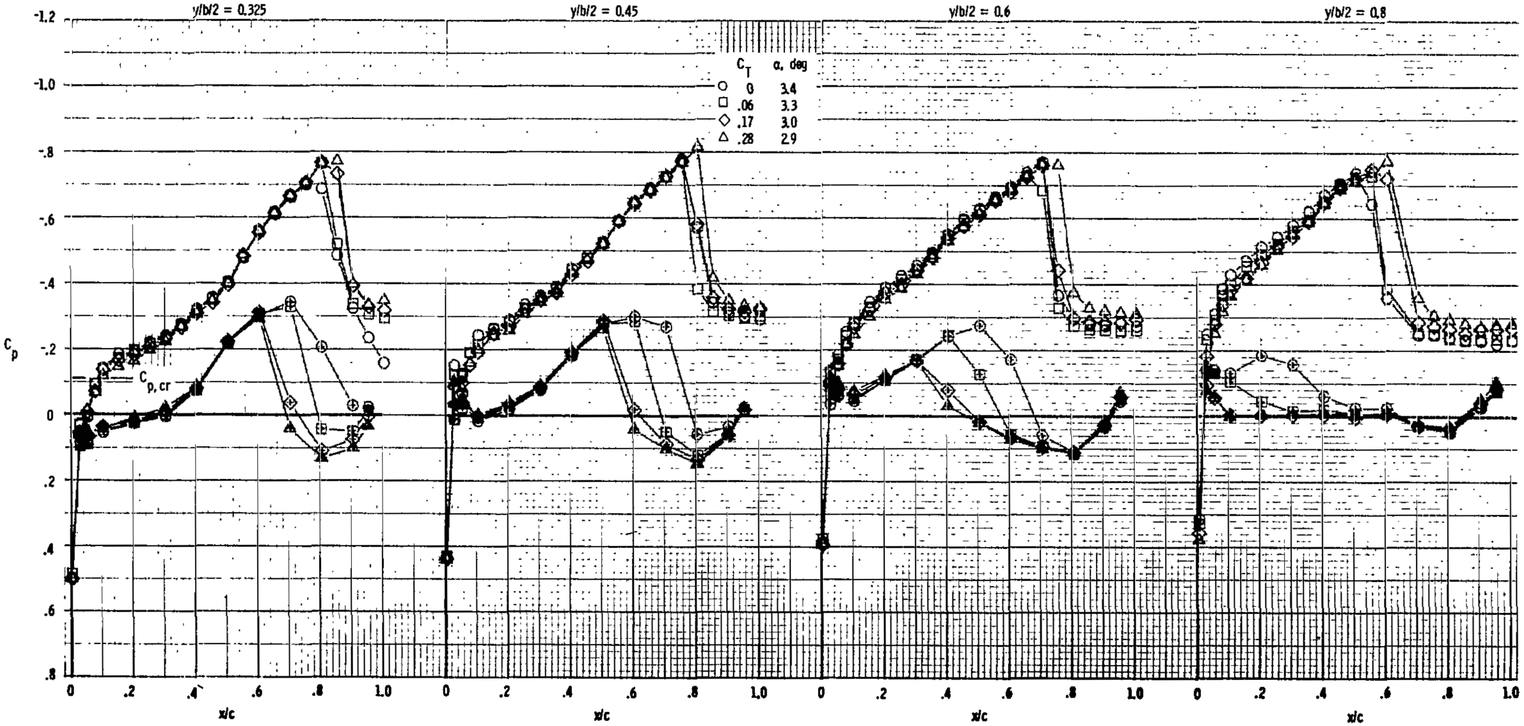

(o) M = 0.95; α ≈ 3.3°.

Figure 20.- Continued.

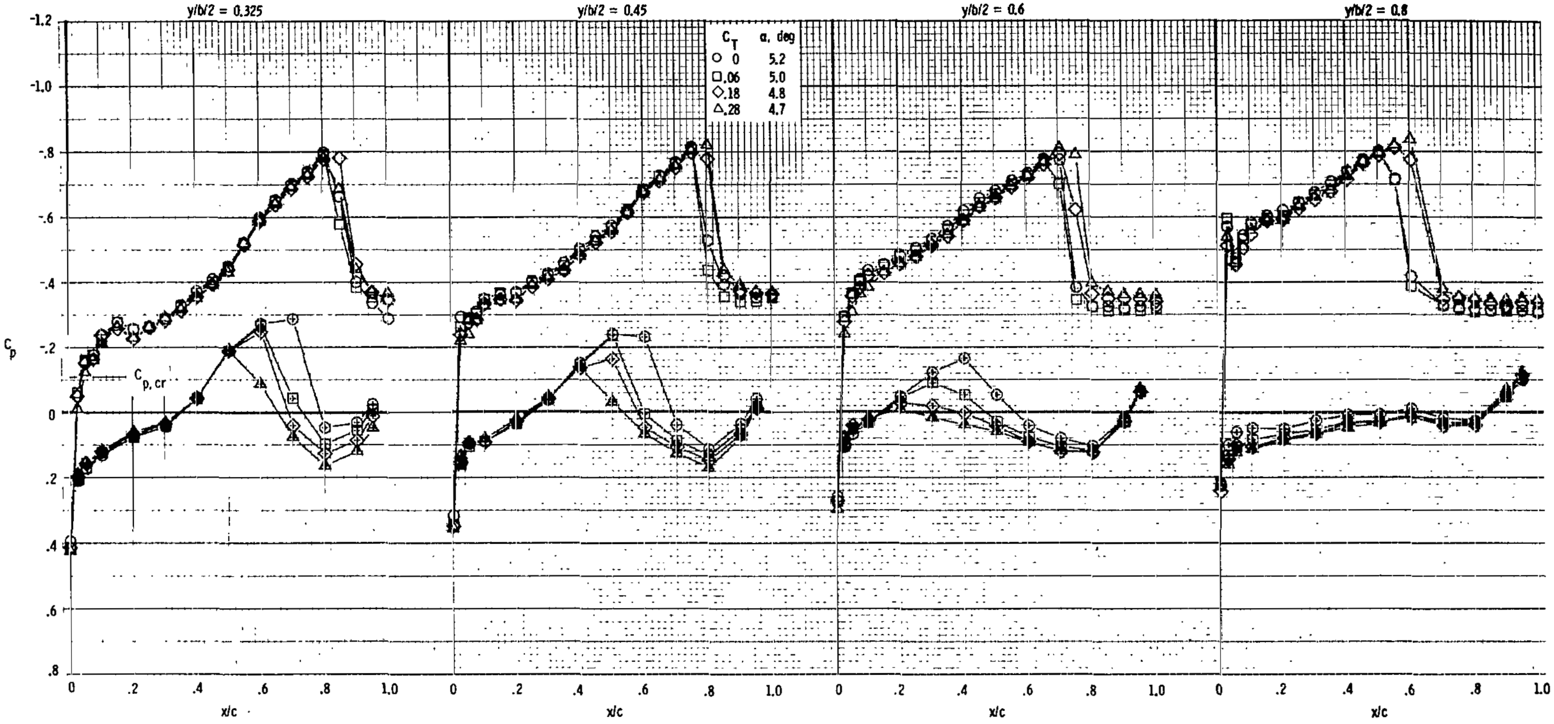

(p) M = 0.95; α ≈ 5.0°.

Figure 20.- Continued.

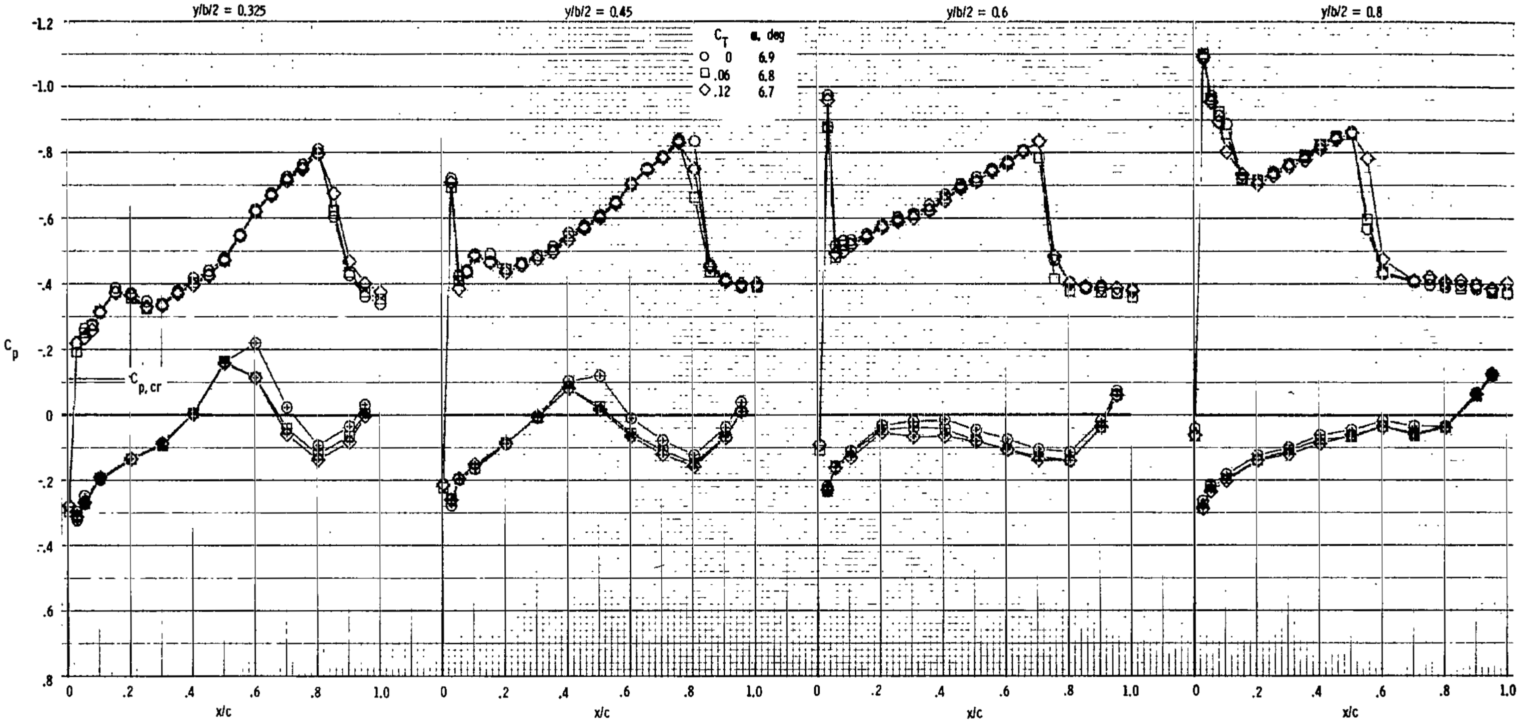

(q) M = 0.95; $\alpha \approx 6.8^{\circ}$.

Figure 20. - Concluded.

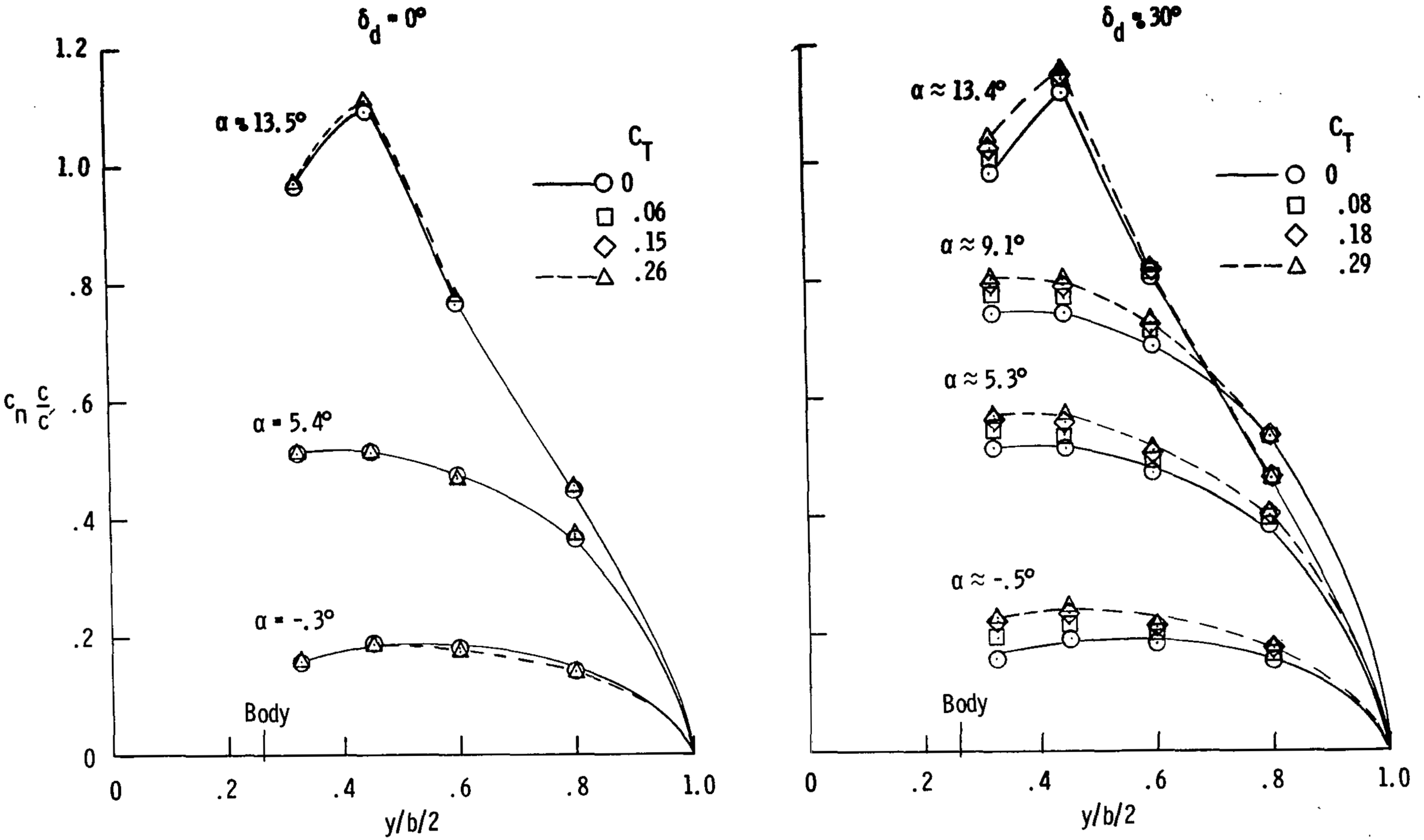

(a) M = 0.70.

Figure 21.- Typical spanwise variation of section normal-force parameter.

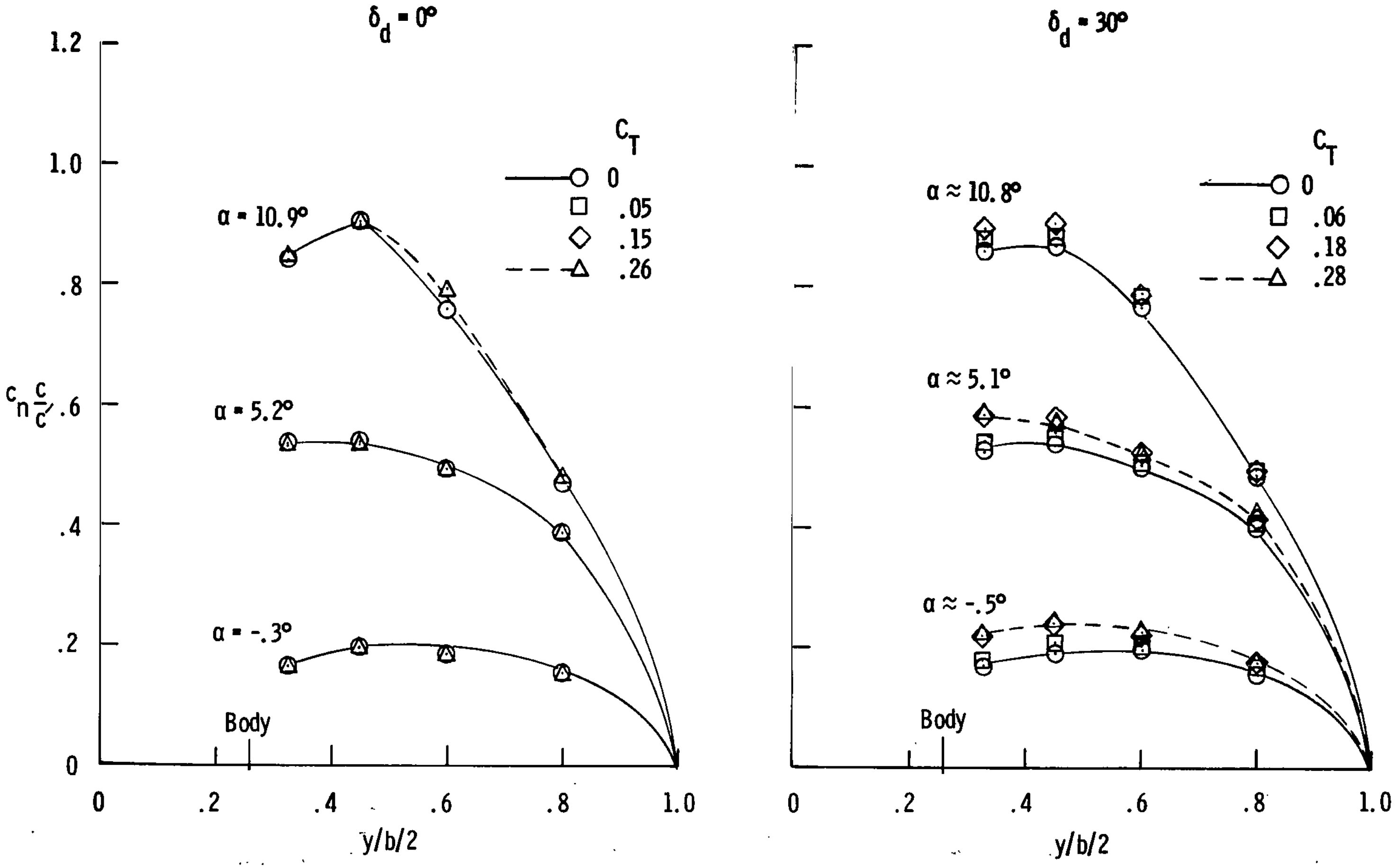

(b) M = 0.80.

Figure 21.- Continued.

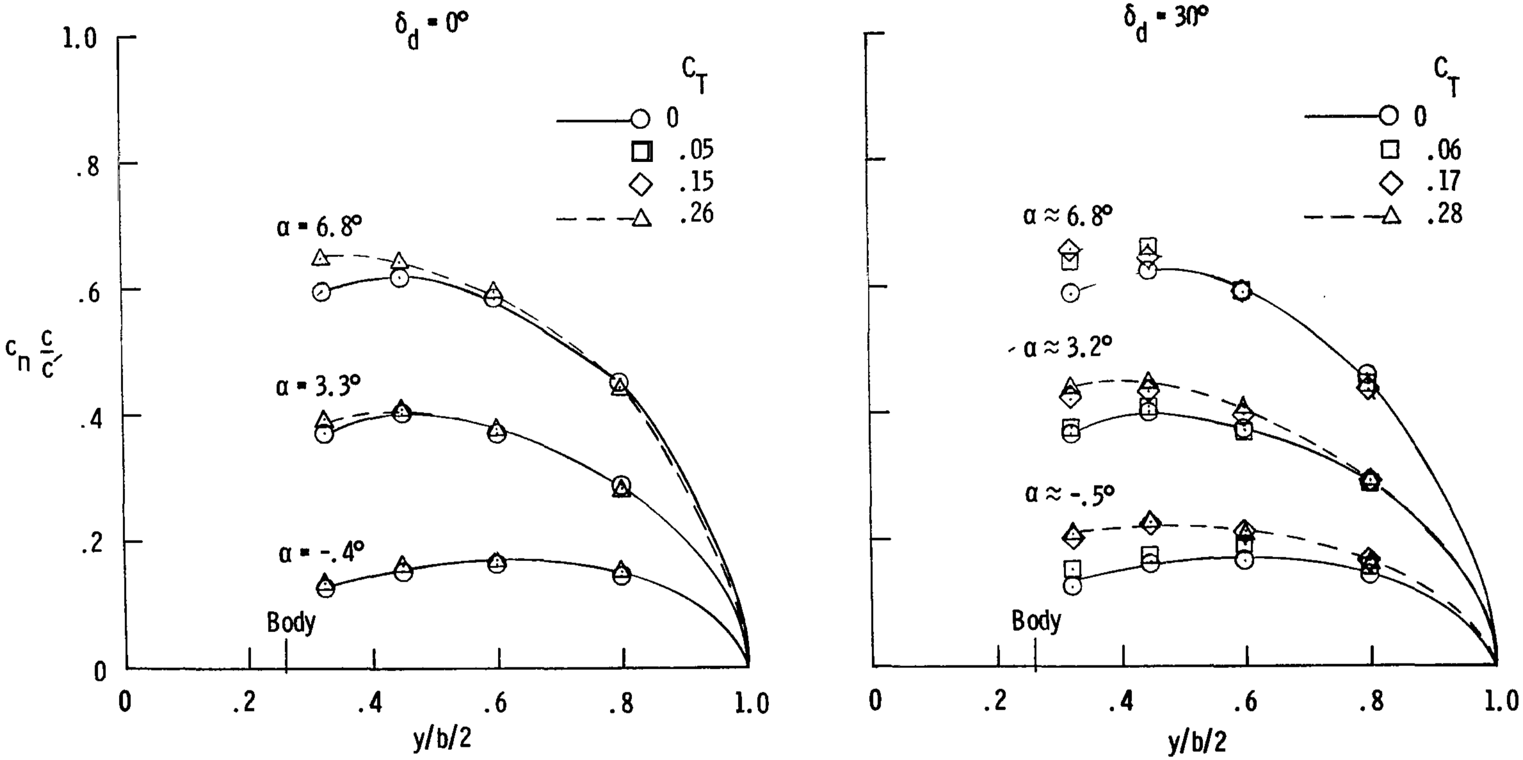

(c) M = 0.90.

Figure 21.- Continued.

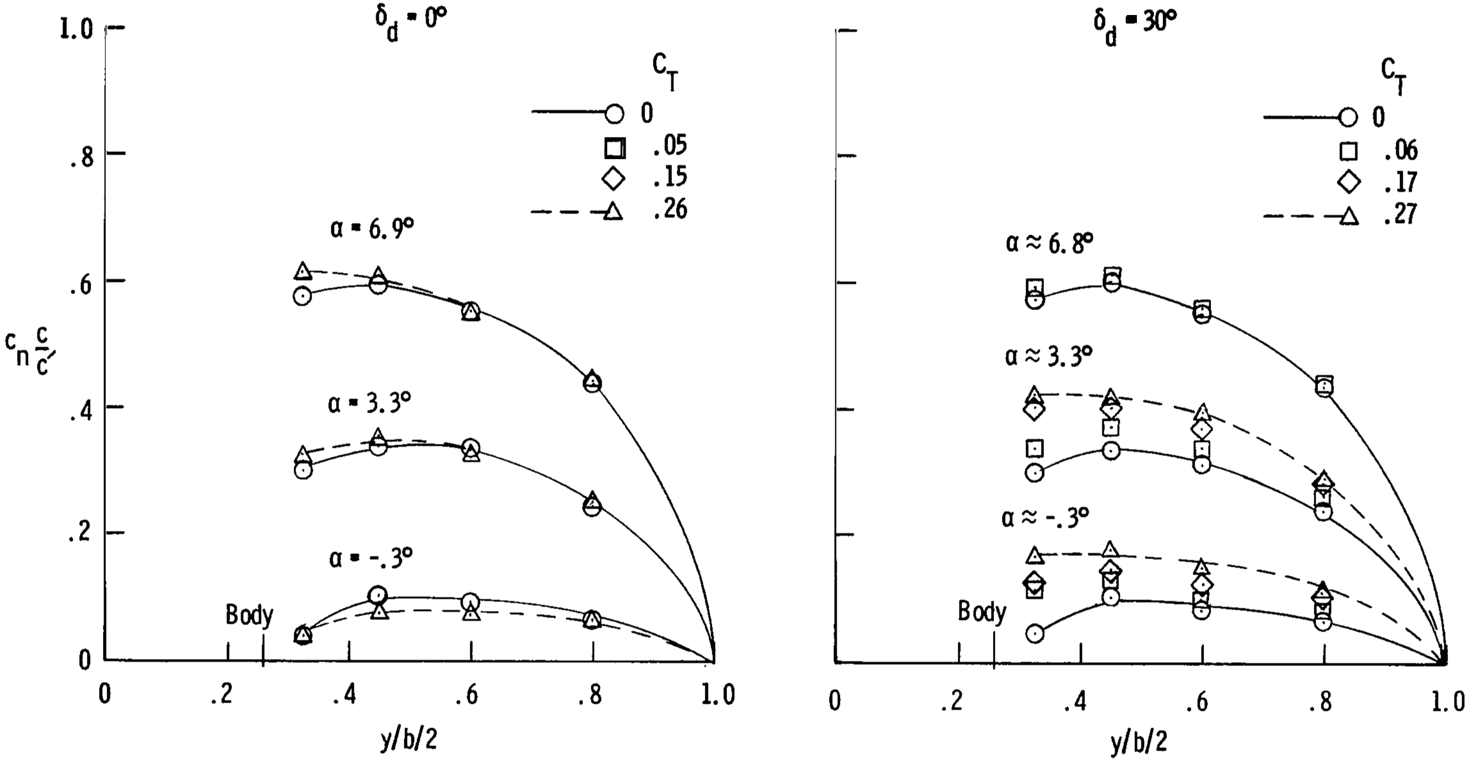

(d) M = 0.95.

Figure 21.- Concluded.

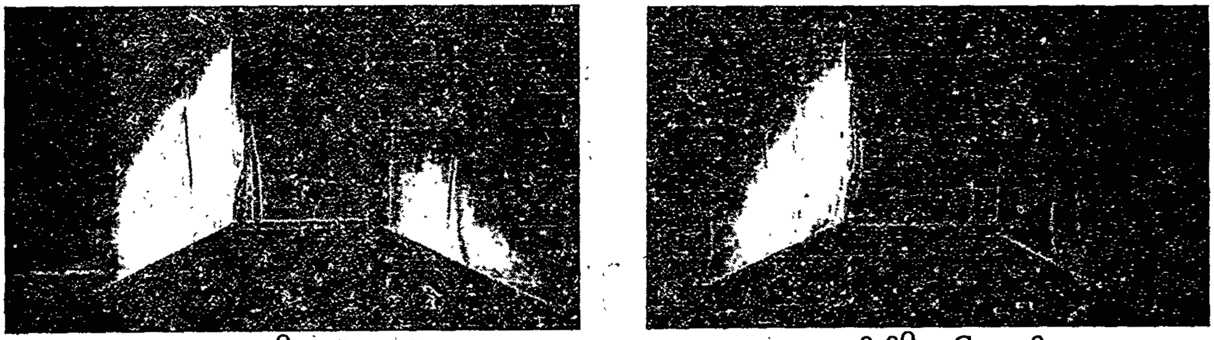

$\alpha = -0.3^{\circ}$; $C_T = 0$ $\alpha = 8.8^{\circ}$; $C_T = 0$

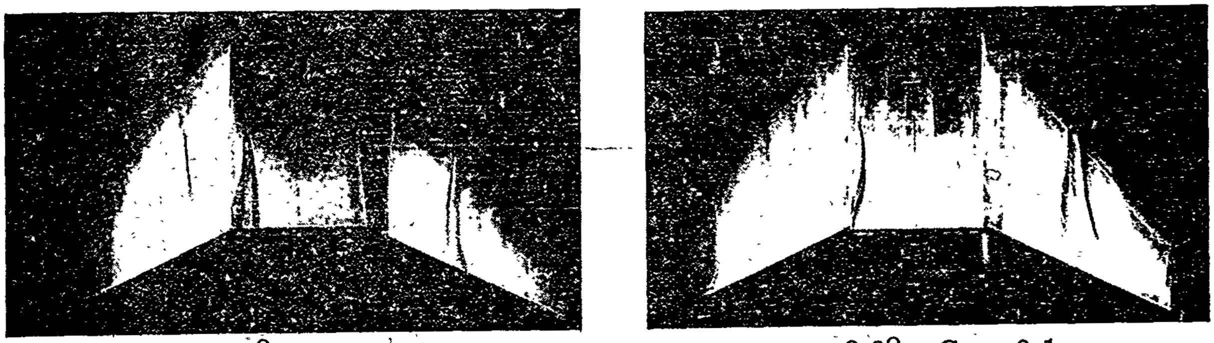

$\alpha = -0.5^{\circ}$; $C_T = 0.1$ $\alpha = 8.6^{\circ}$; $C_T = 0.1$

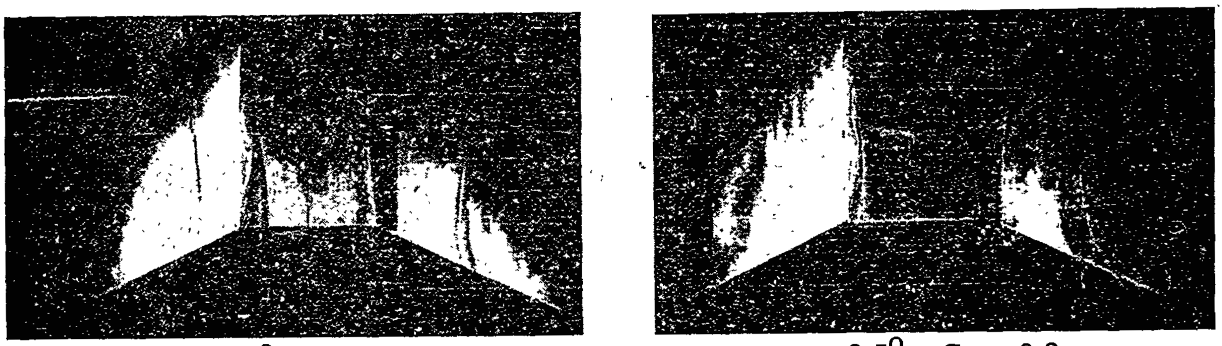

$\alpha = -0.7^{\circ}$; $C_T = 0.2$ $\alpha = 8.5^{\circ}$; $C_T = 0.2$

(a) $M = 0.70$. L-75-207

Figure 22.- Photographs of oil-flow characteristics. $\delta_d = 30^{\circ}$.

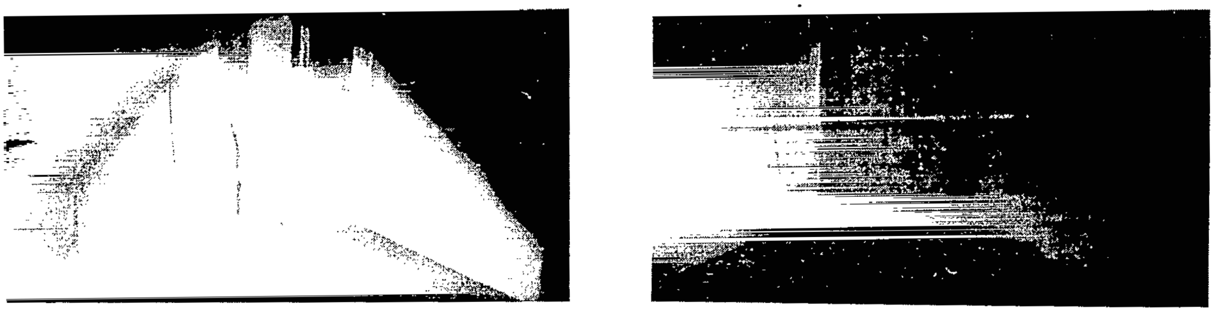

$\alpha = -0.4^\circ$; $C_T = 0$

$\alpha = 3.1^\circ$; $C_T = 0$

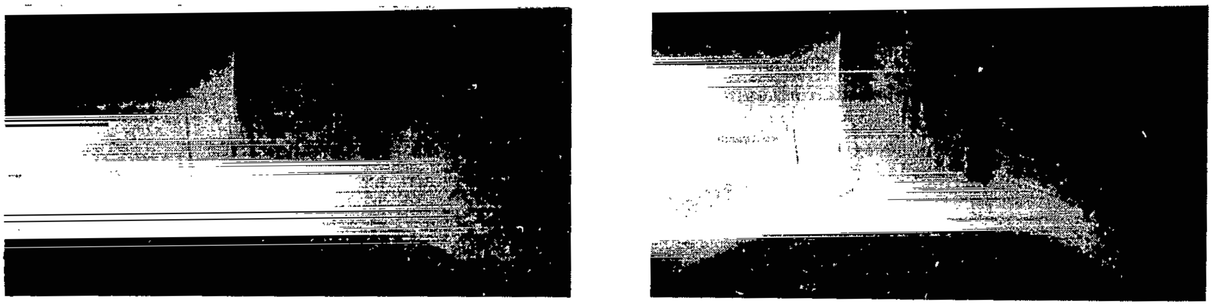

$\alpha = -0.7^\circ$; $C_T = 0.1$

$\alpha = 2.8^\circ$; $C_T = 0.1$

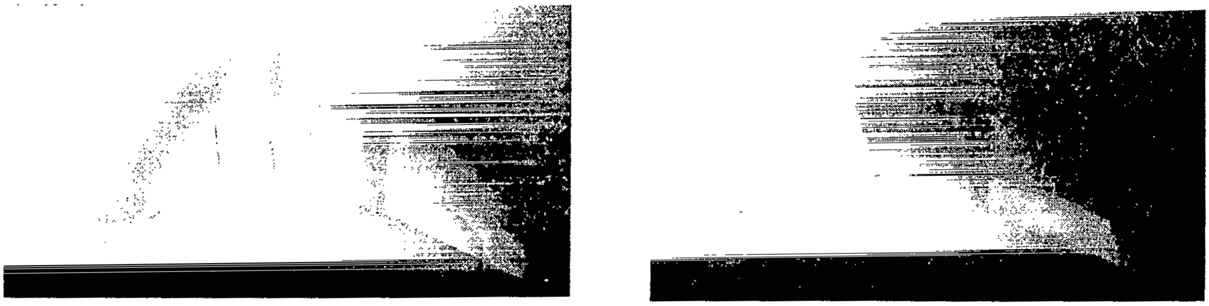

$\alpha = -0.9^\circ$; $C_T = 0.2$

$\alpha = 2.6^\circ$; $C_T = 0.2$

(b) M = 0.90.

L-75-208

Figure 22.- Continued.

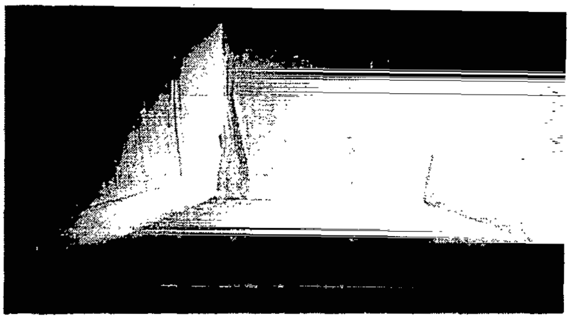

$\alpha = 3.2^{\circ}$; $C_T = 0$

$\alpha = -0.6^{\circ}$; $C_T = 0.1$ $\alpha = 2.8^{\circ}$; $C_T = 0.1$

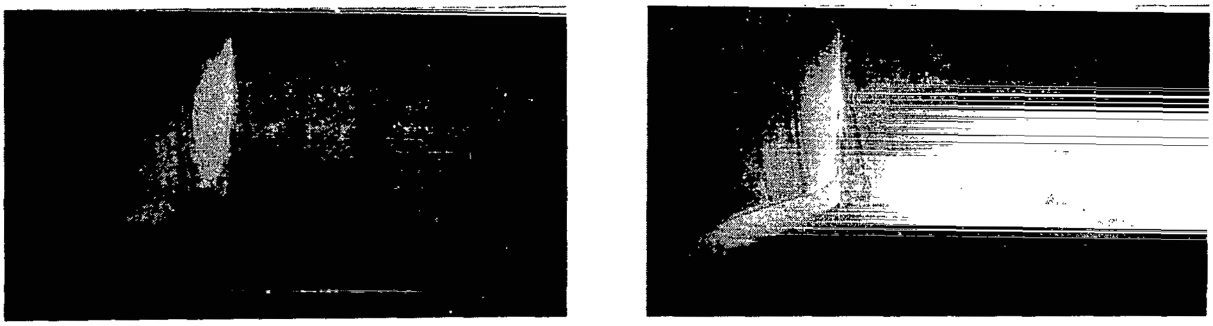

$\alpha = -0.8^{\circ}$; $C_T = 0.2$ $\alpha = 2.6^{\circ}$; $C_T = 0.2$

(c) M = 0.95. L-75-209

Figure 22.- Concluded.

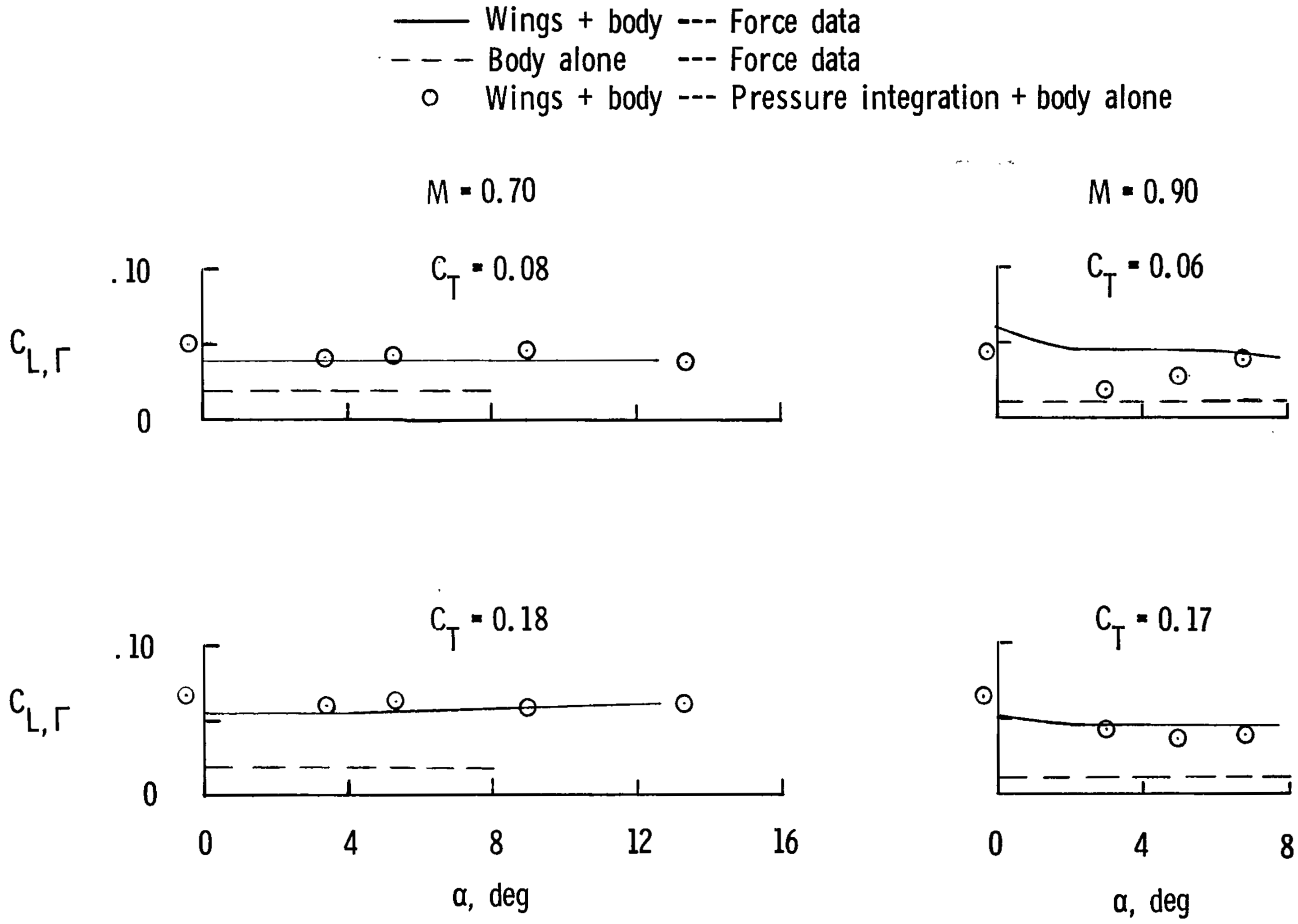

Figure 23.- Comparison of measured and integrated jet-induced supercirculation lift. $\delta_d = 30^\circ$.

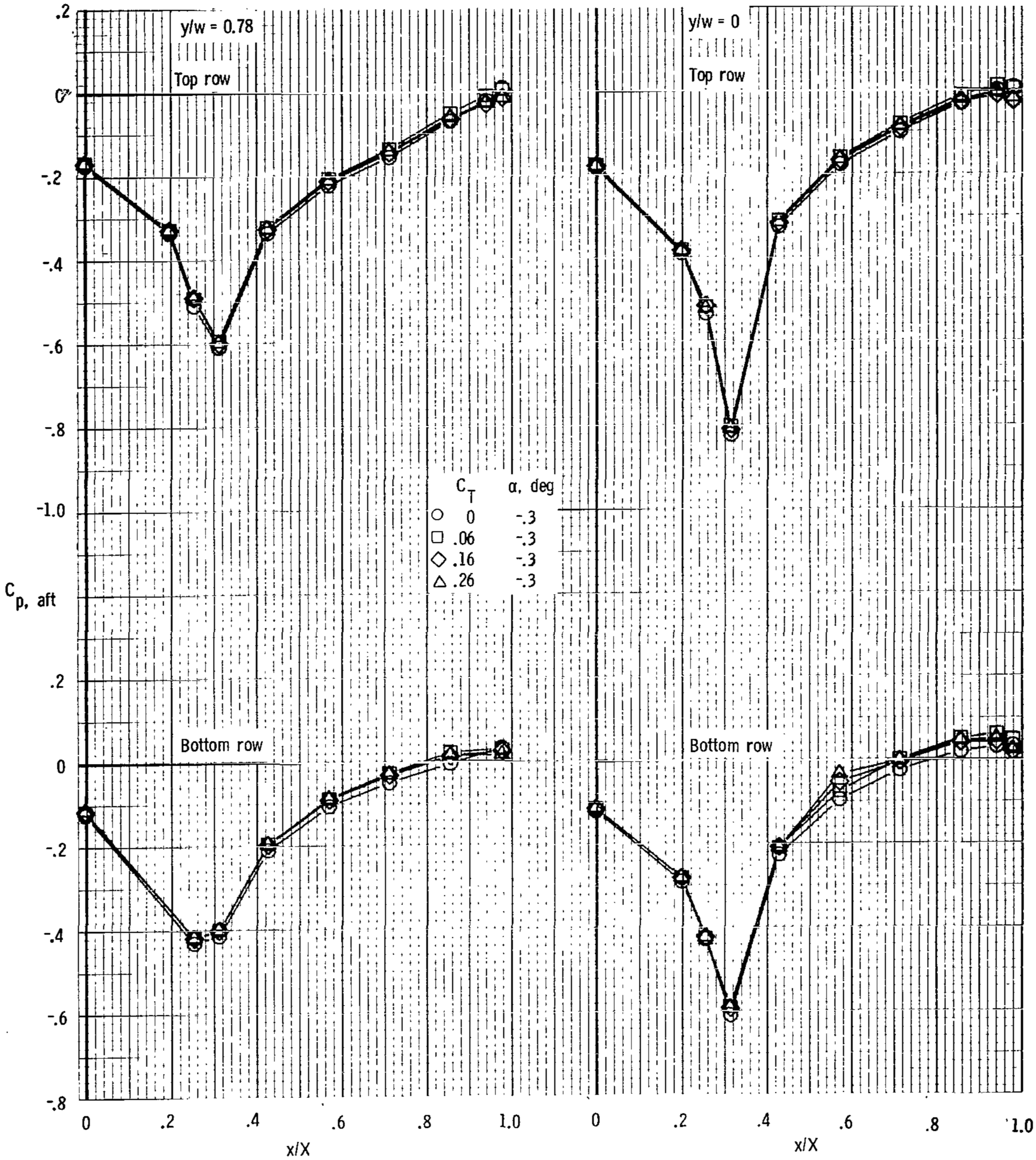

(a) M = 0.70; α = -0.3°.

Figure 24.- Afterbody pressure distributions. $\delta_d = 0^{\circ}$.

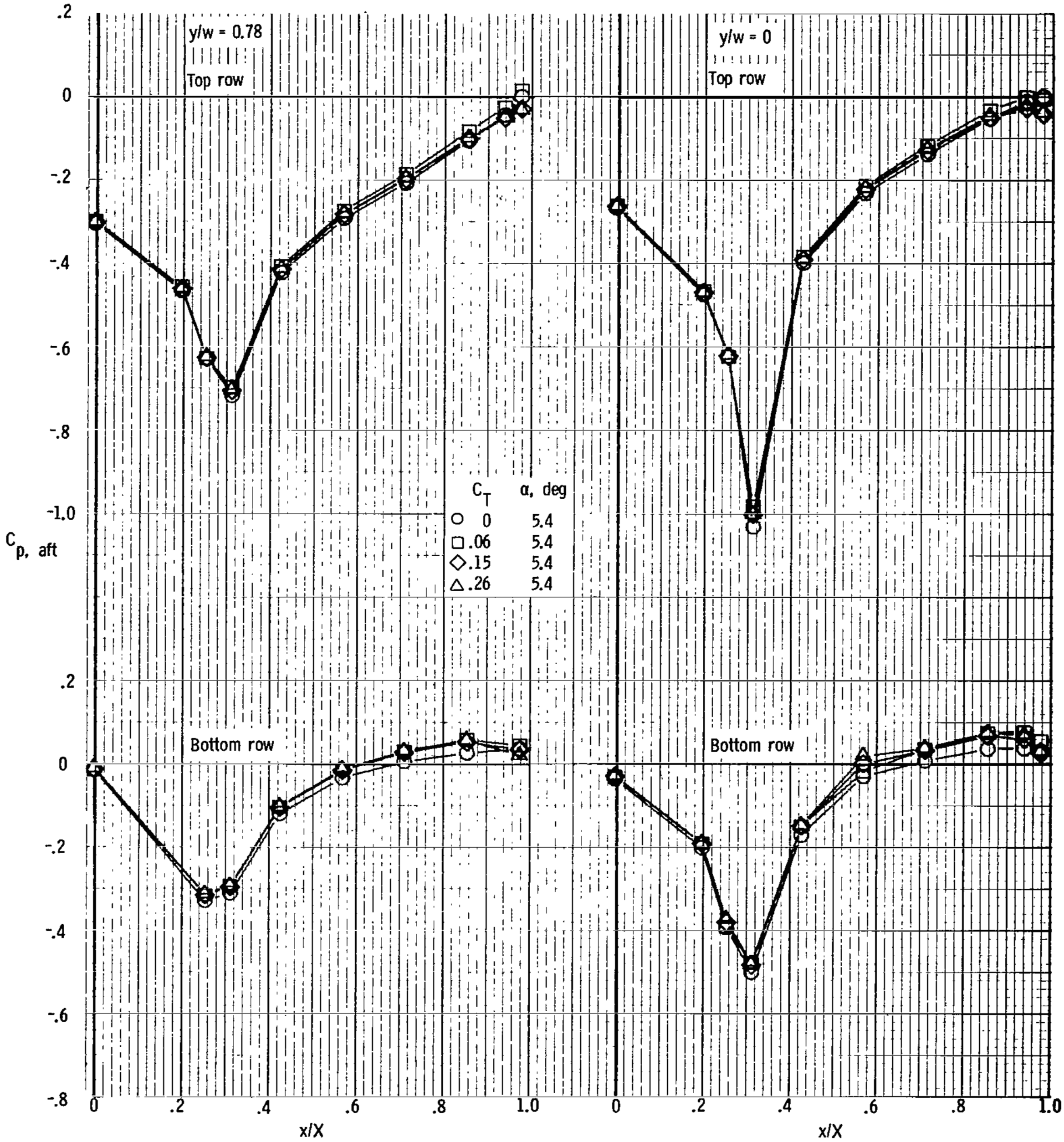

(b) M = 0.70; α = 5.4°.

Figure 24. - Continued.

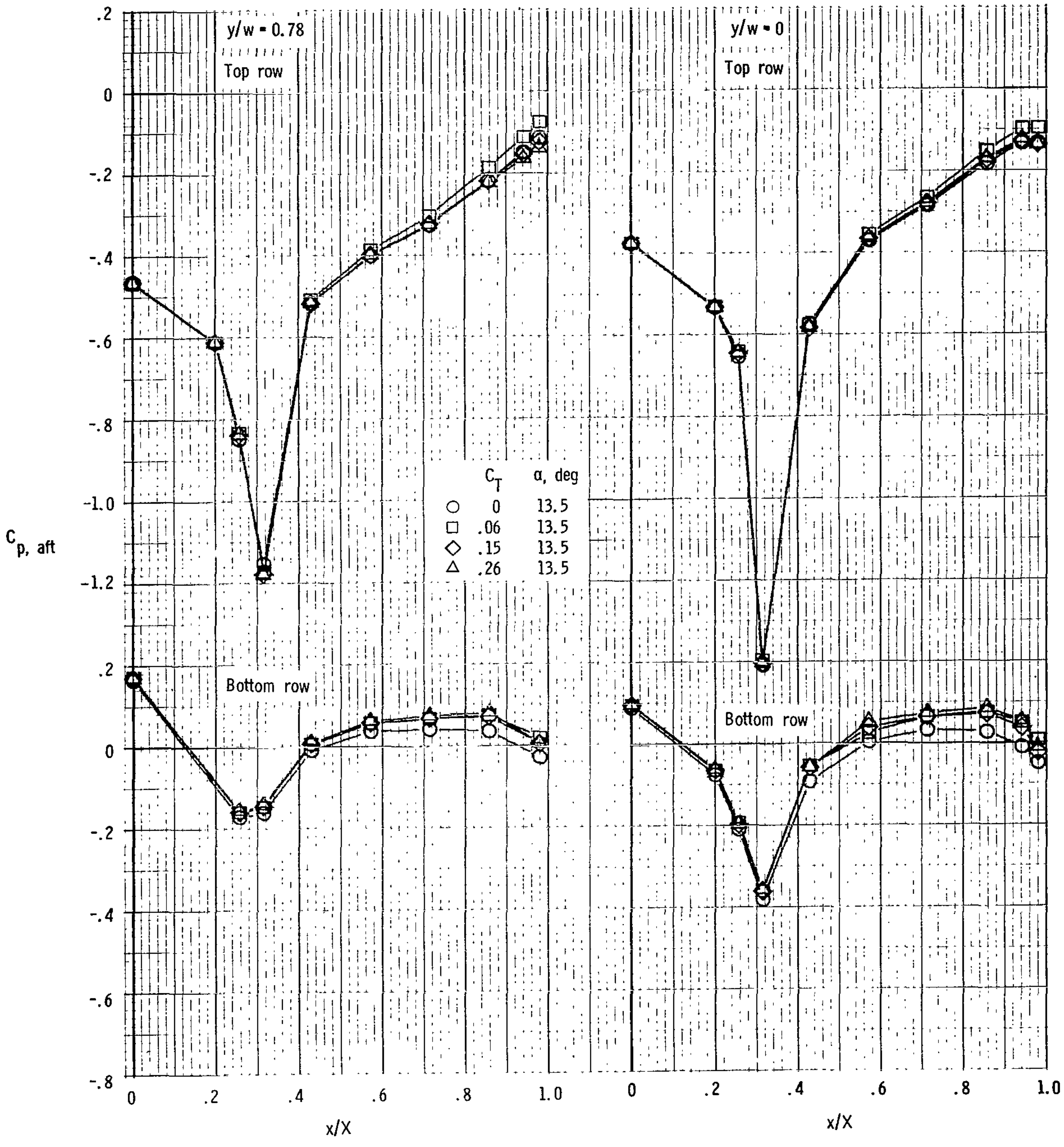

(c) M = 0.70; α = 13.5°.

Figure 24.- Continued.

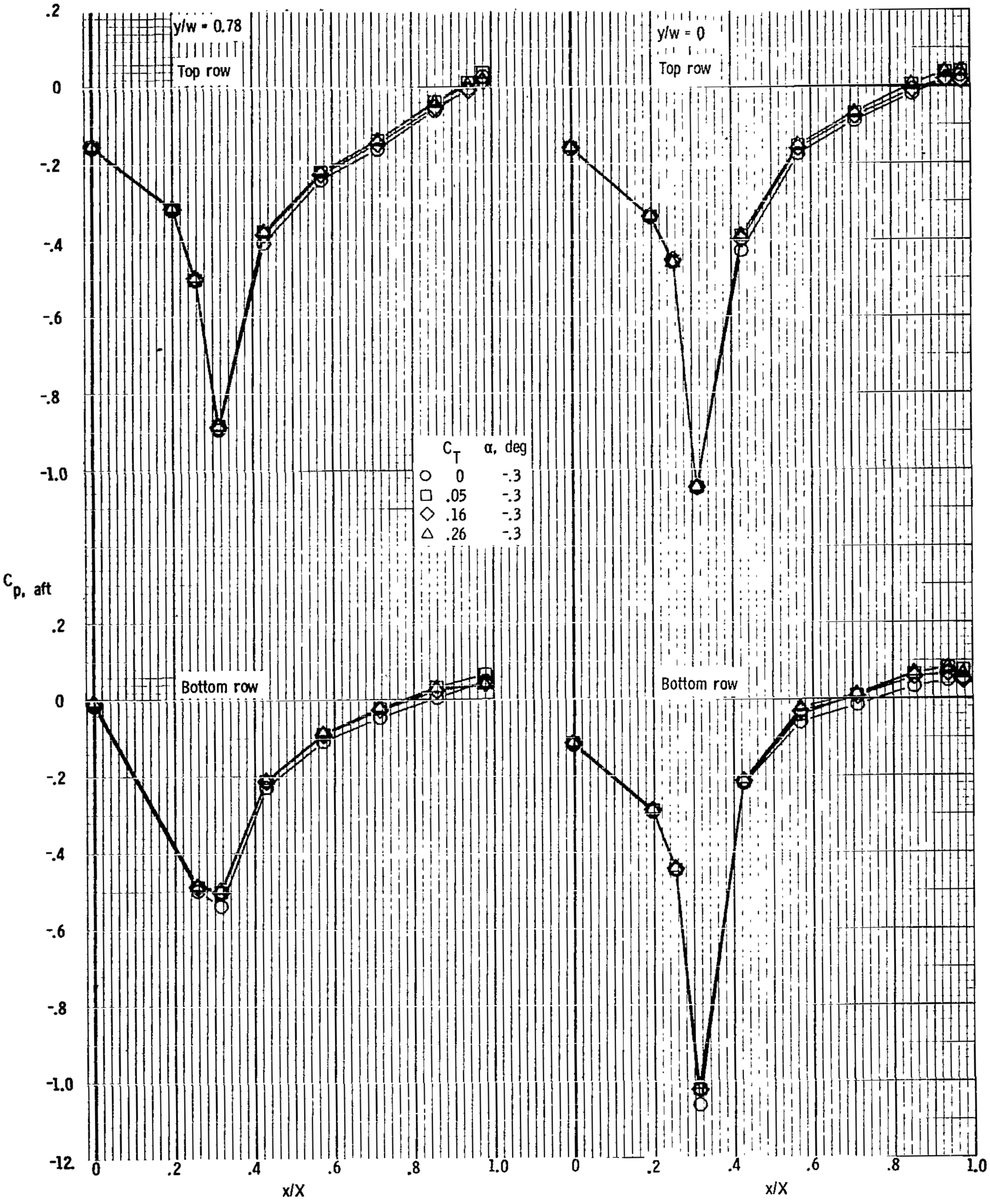

(d) M = 0.80; α = -0.3°.

Figure 24.- Continued.

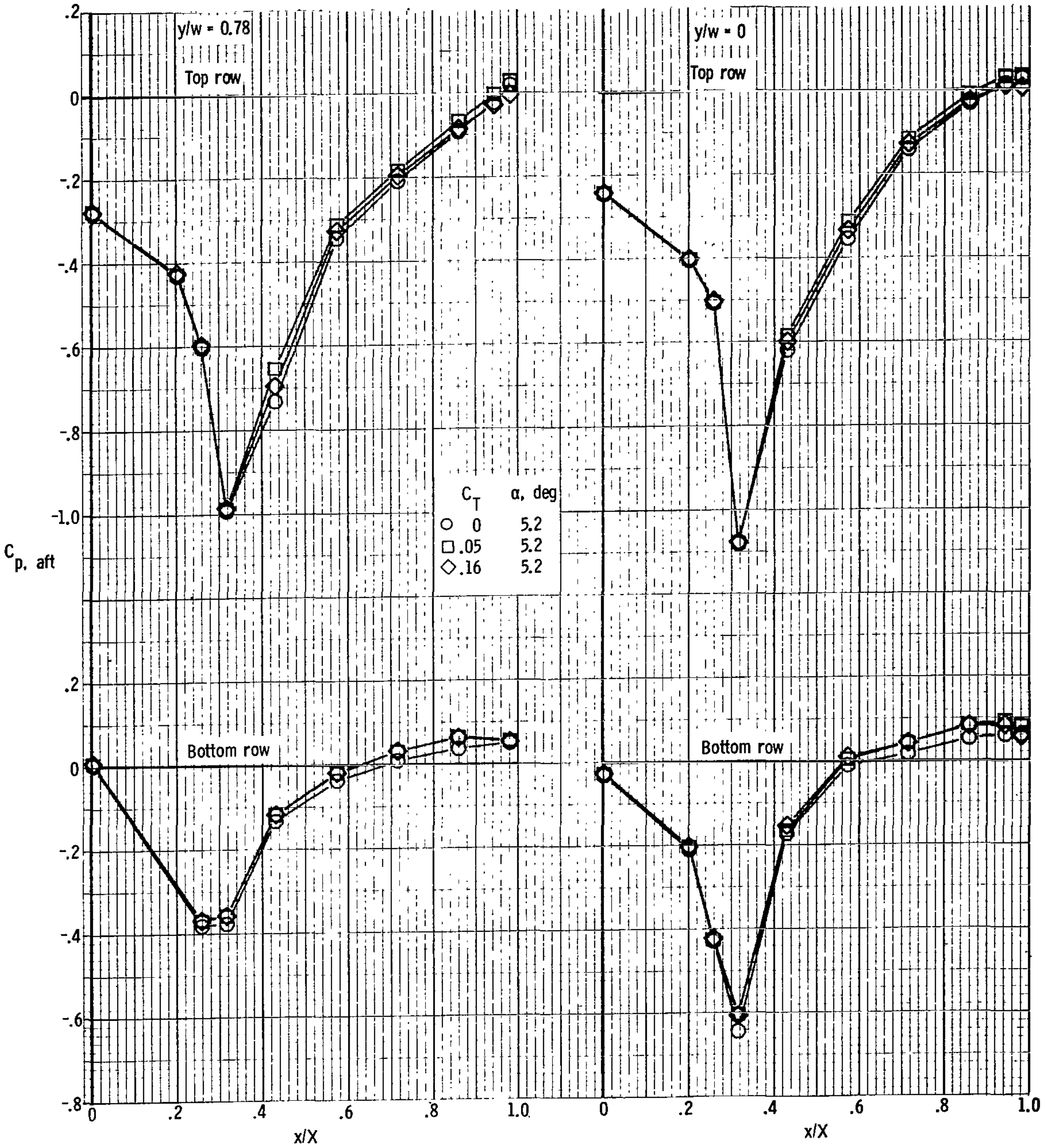

(e) M = 0.80; α = 5.2°.

Figure 24.- Continued.

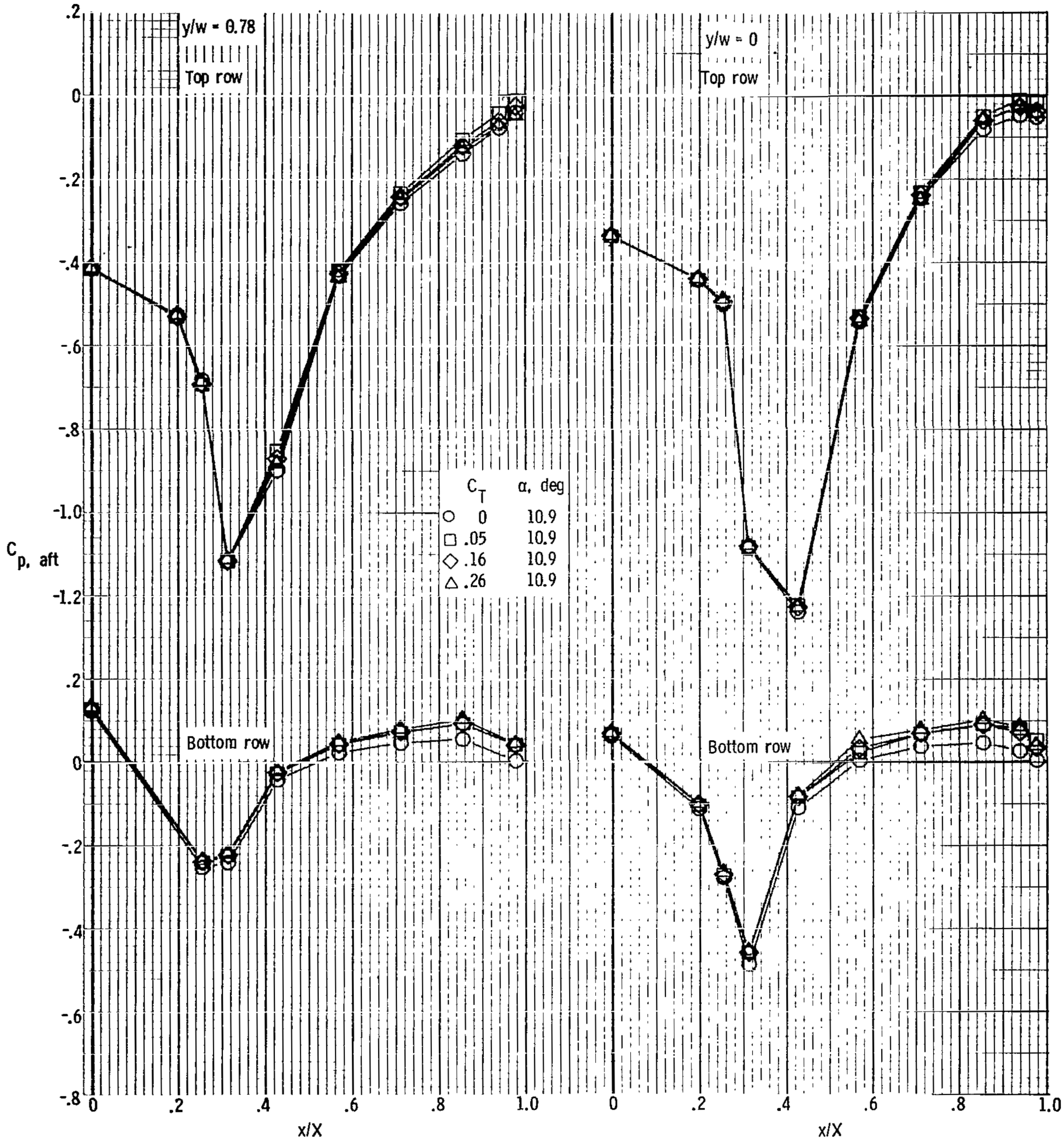

(f) M = 0.80; α = 10.9°.

Figure 24.- Continued.

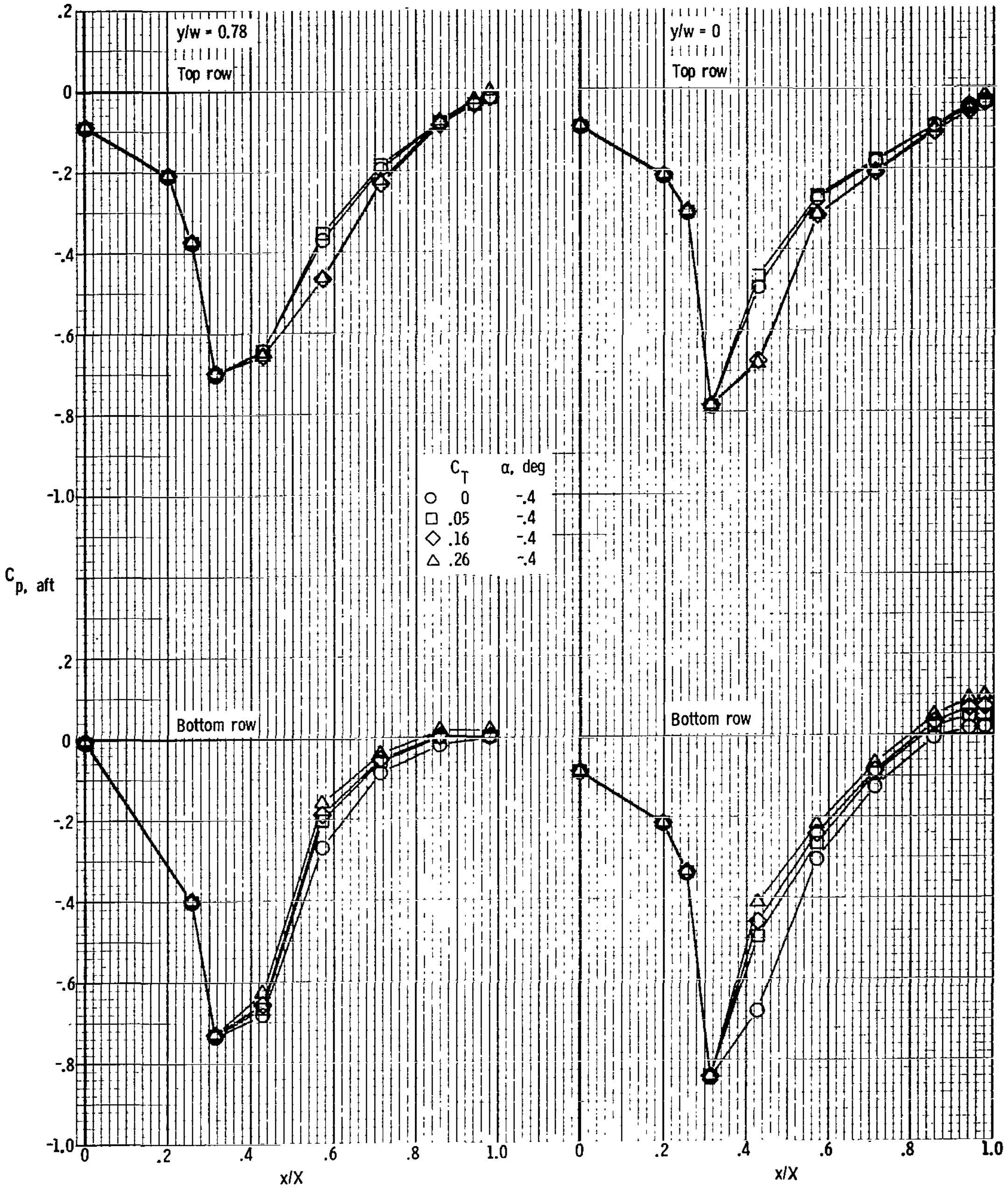

(g) M = 0.90; α = -0.4°.

Figure 24.- Continued.

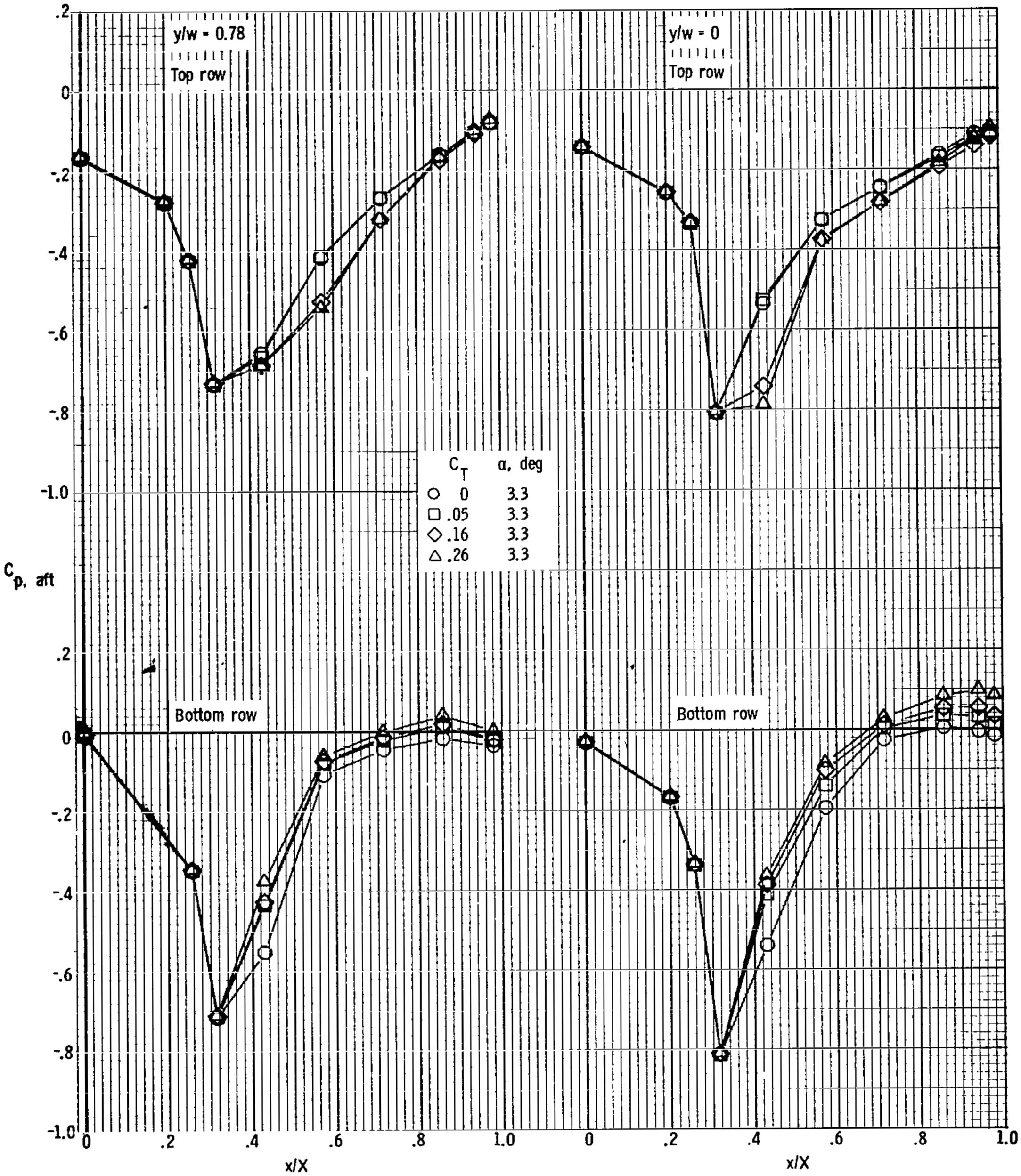

(h) M = 0.90; α = 3.3°.

Figure 24.- Continued.

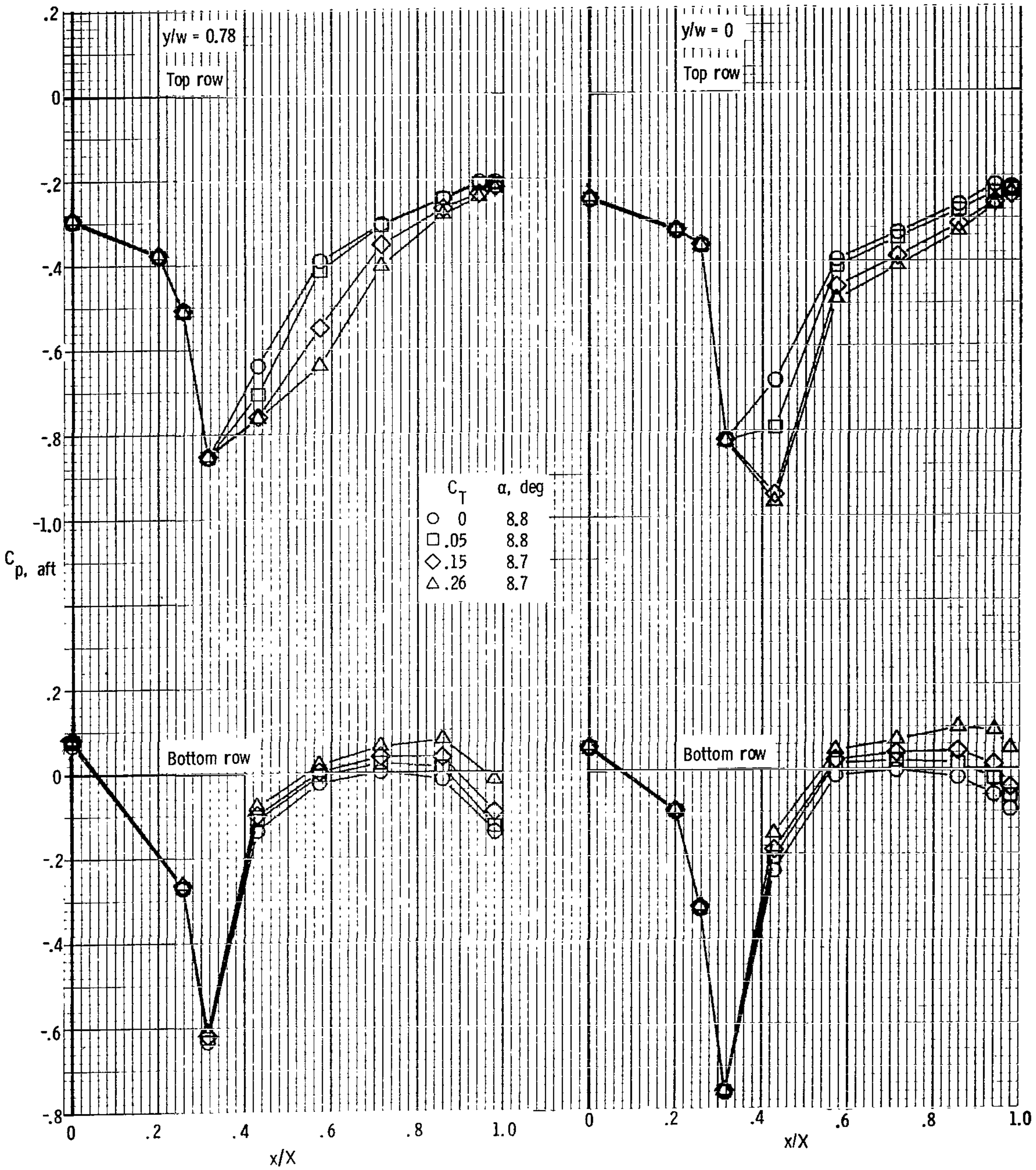

(i) M = 0.90; $\alpha \approx 8.8^{\circ}$.

Figure 24.- Continued.

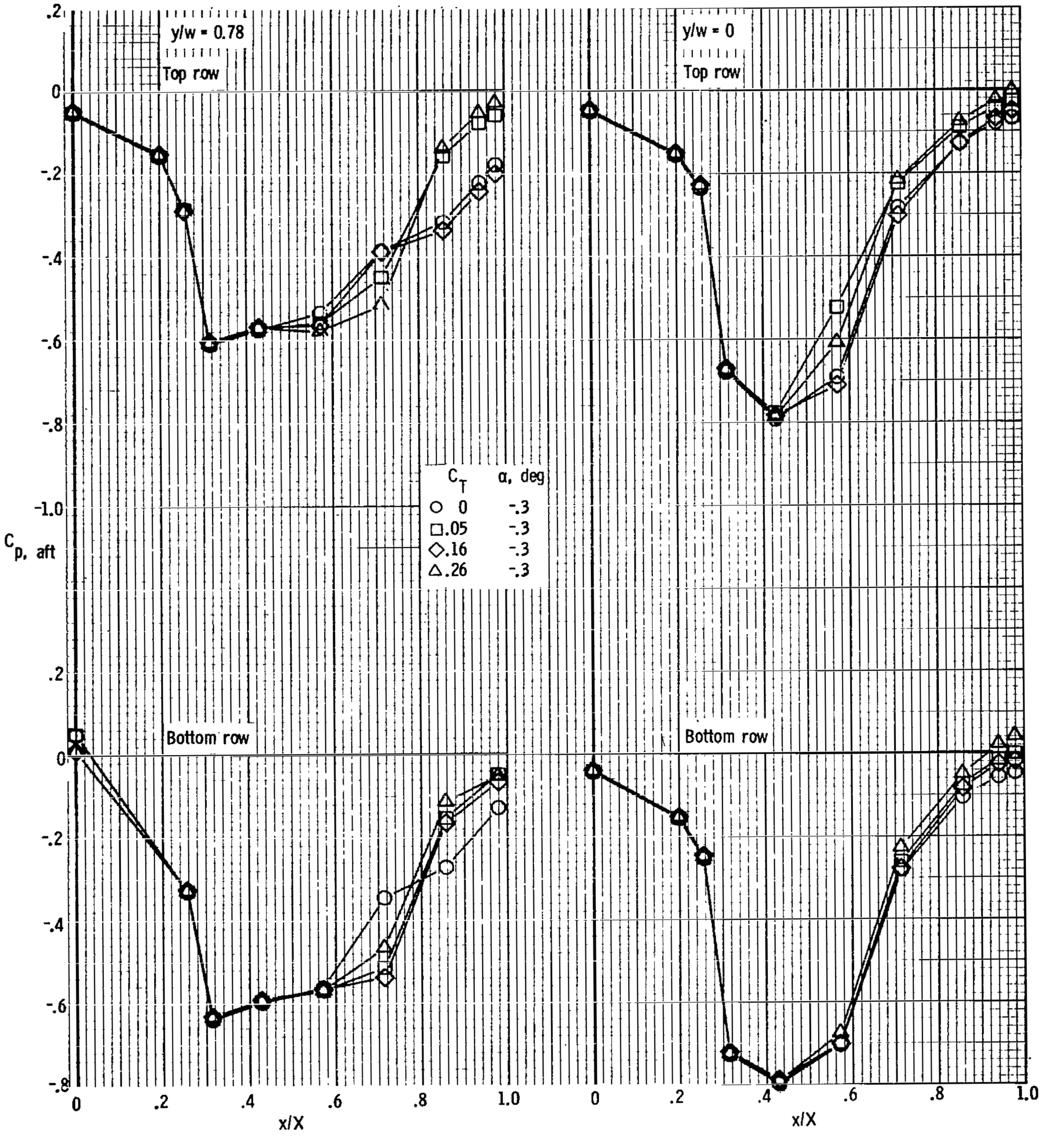

(j) M = 0.95; α = -0.3°.

Figure 24.- Continued.

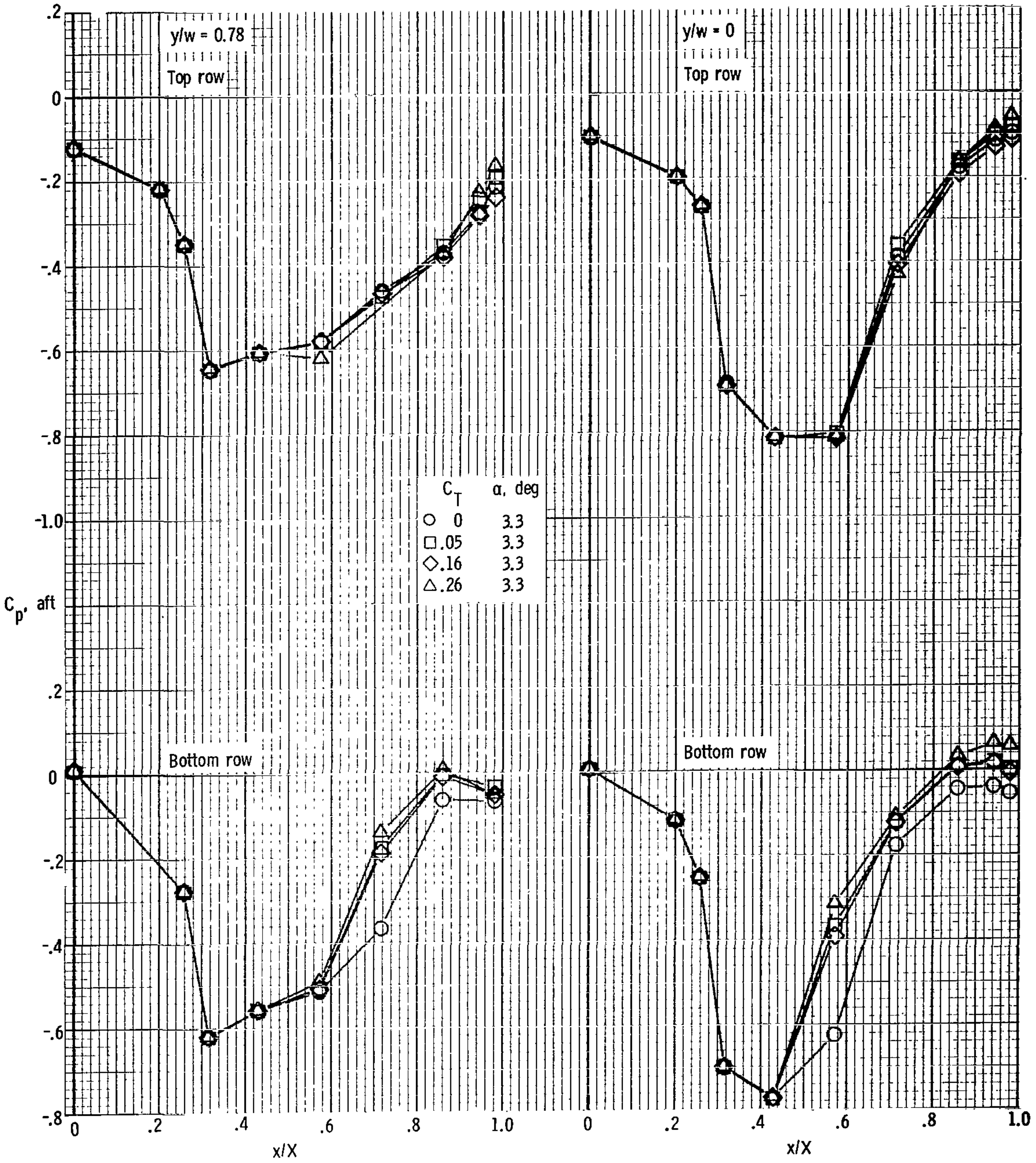

(k) M = 0.95; $\alpha = 3.3^{\circ}$.

Figure 24.- Continued.

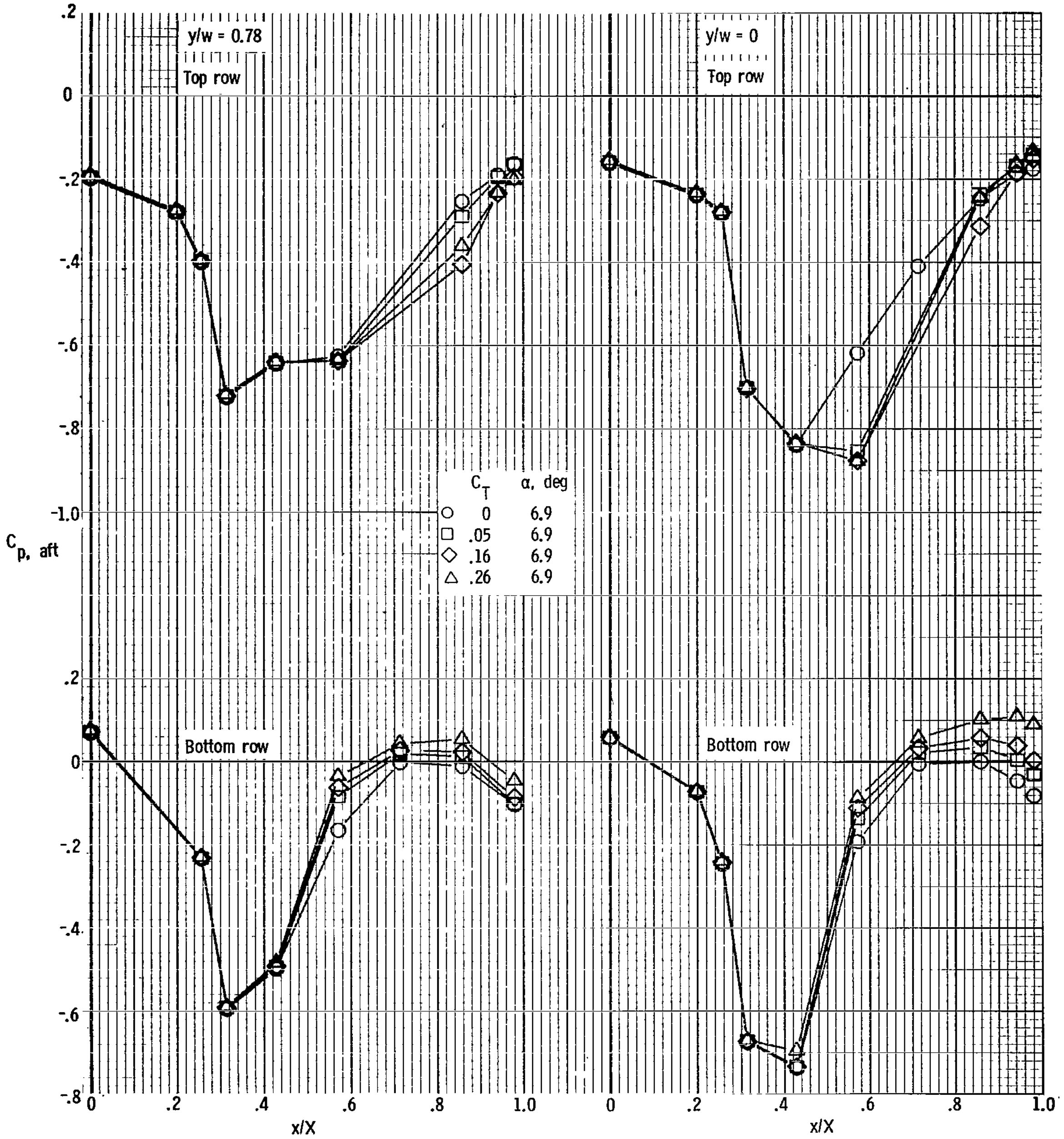

C_T	α, deg
○ 0	6.9
□ .05	6.9
◇ .16	6.9
△ .26	6.9

(l) M = 0.95; α = 6.9°.

Figure 24.- Concluded.

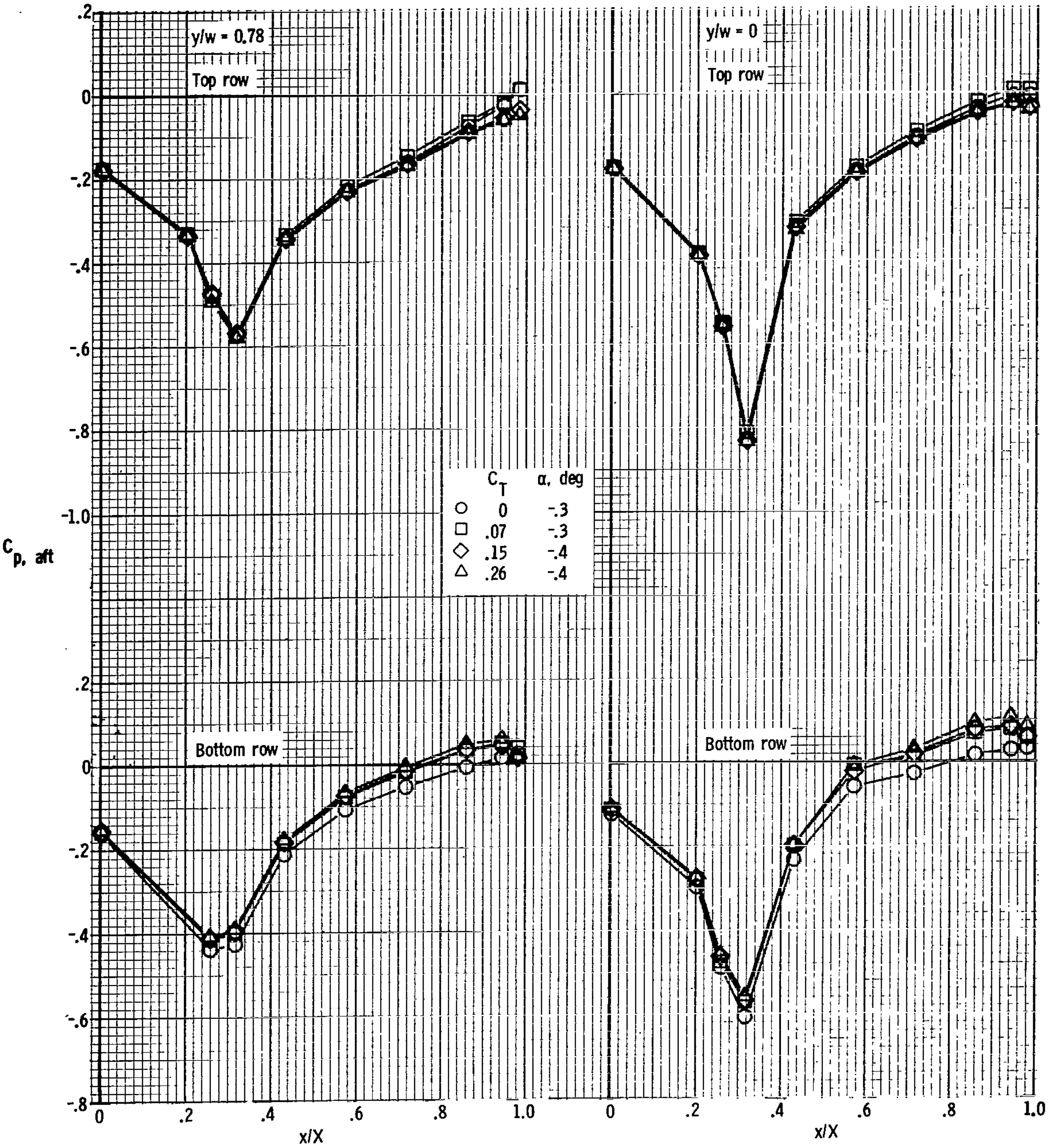

(a) M = 0.70; $\alpha \approx -0.3^{\circ}$.

Figure 25.- Afterbody pressure distributions. $\delta_d = 15^{\circ}$.

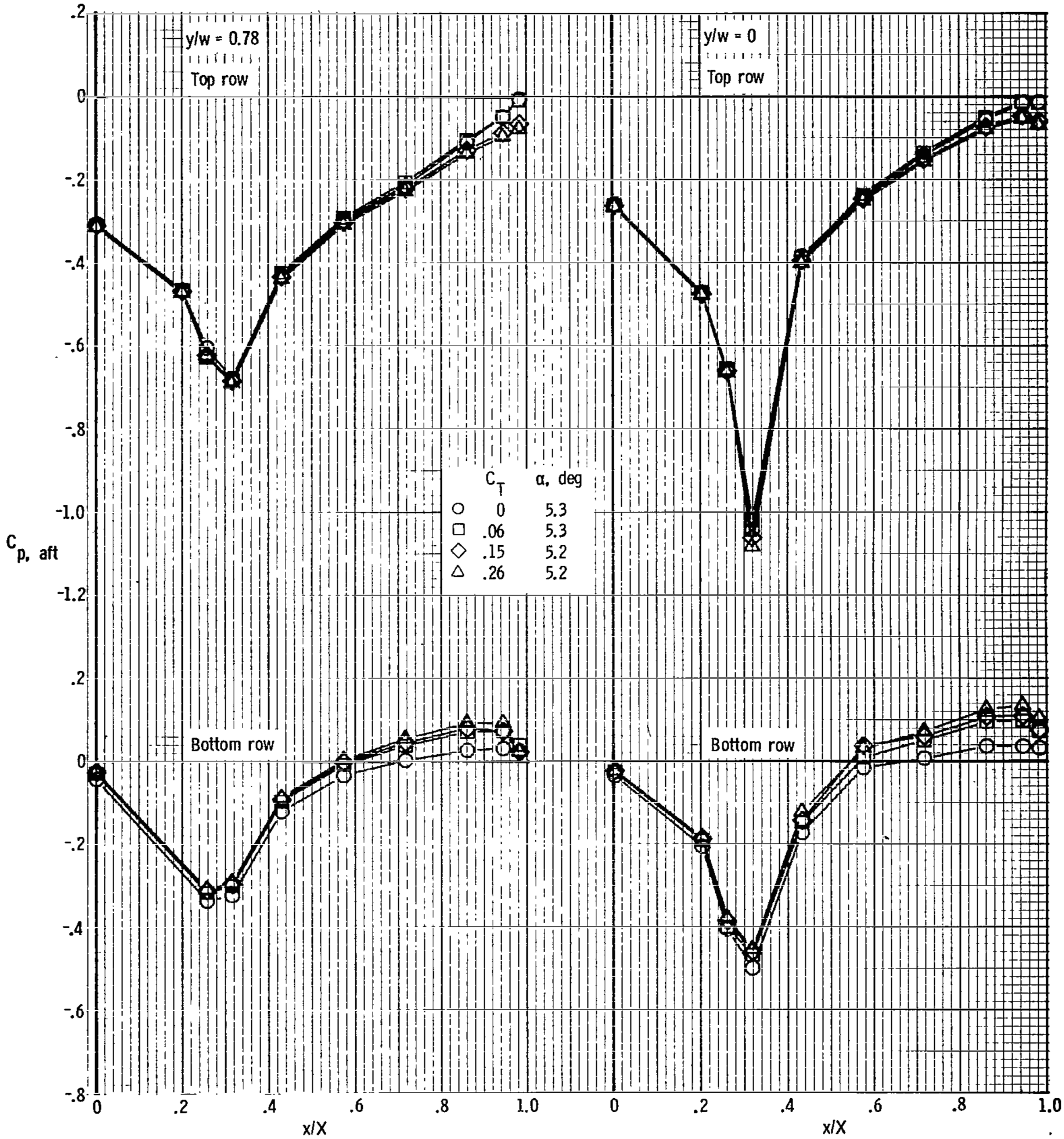

(b) M = 0.70; $\alpha \approx 5.3^{\circ}$.

Figure 25.- Continued.

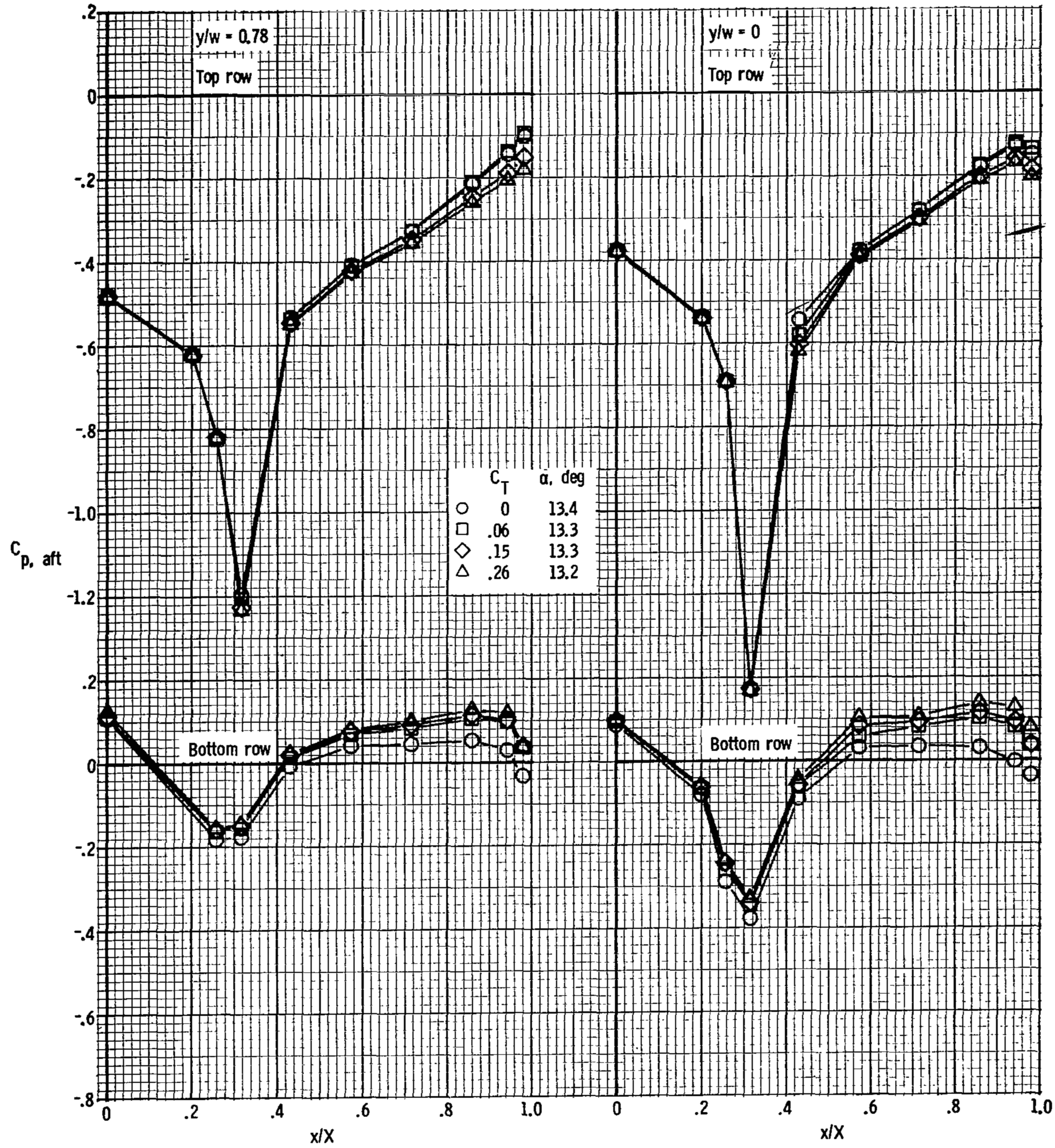

(c) M = 0.70; $\alpha \approx 13.3^{\circ}$.

Figure 25.- Continued.

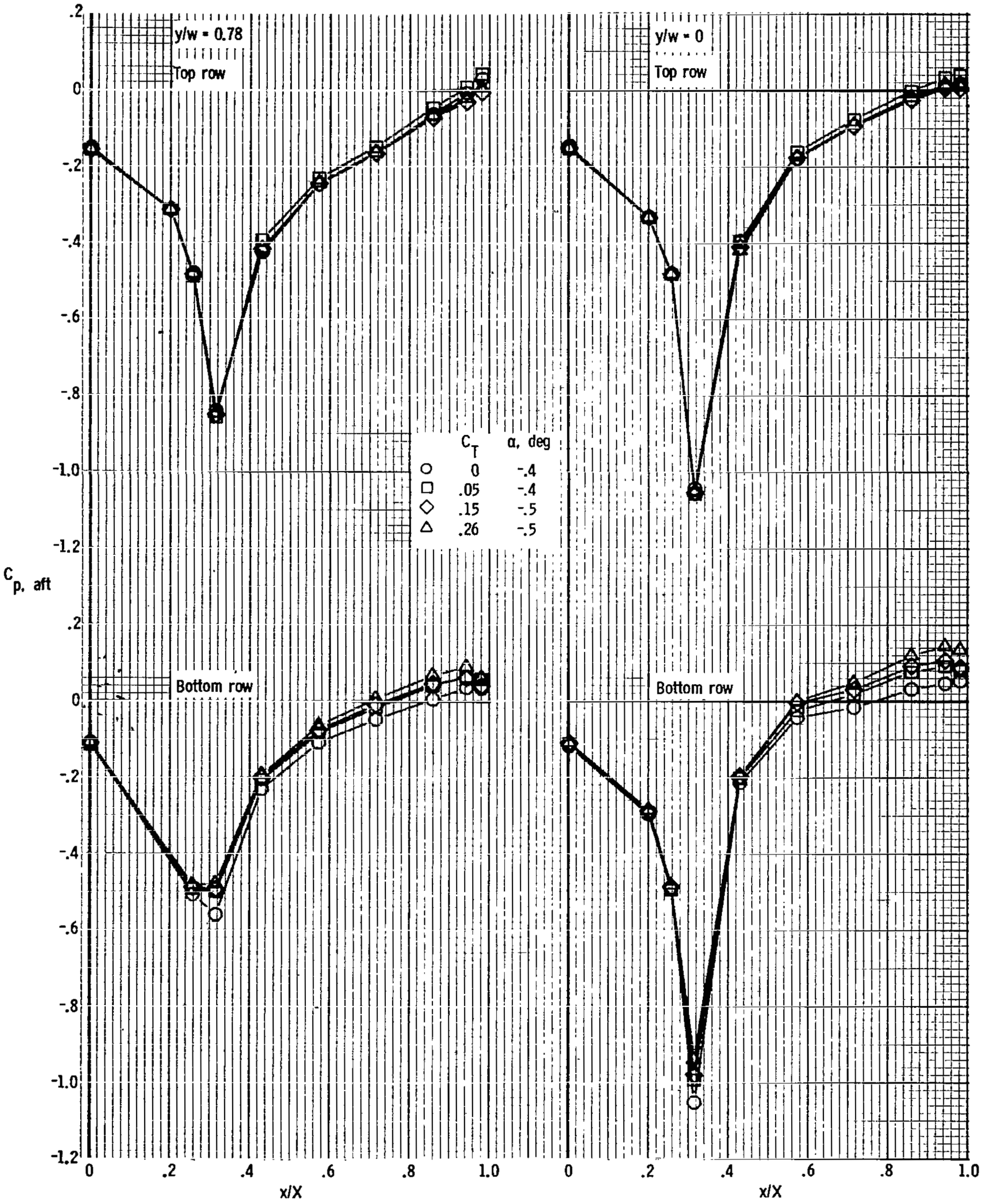

(d) M = 0.80; α ≈ -0.4°.

Figure 25.- Continued.

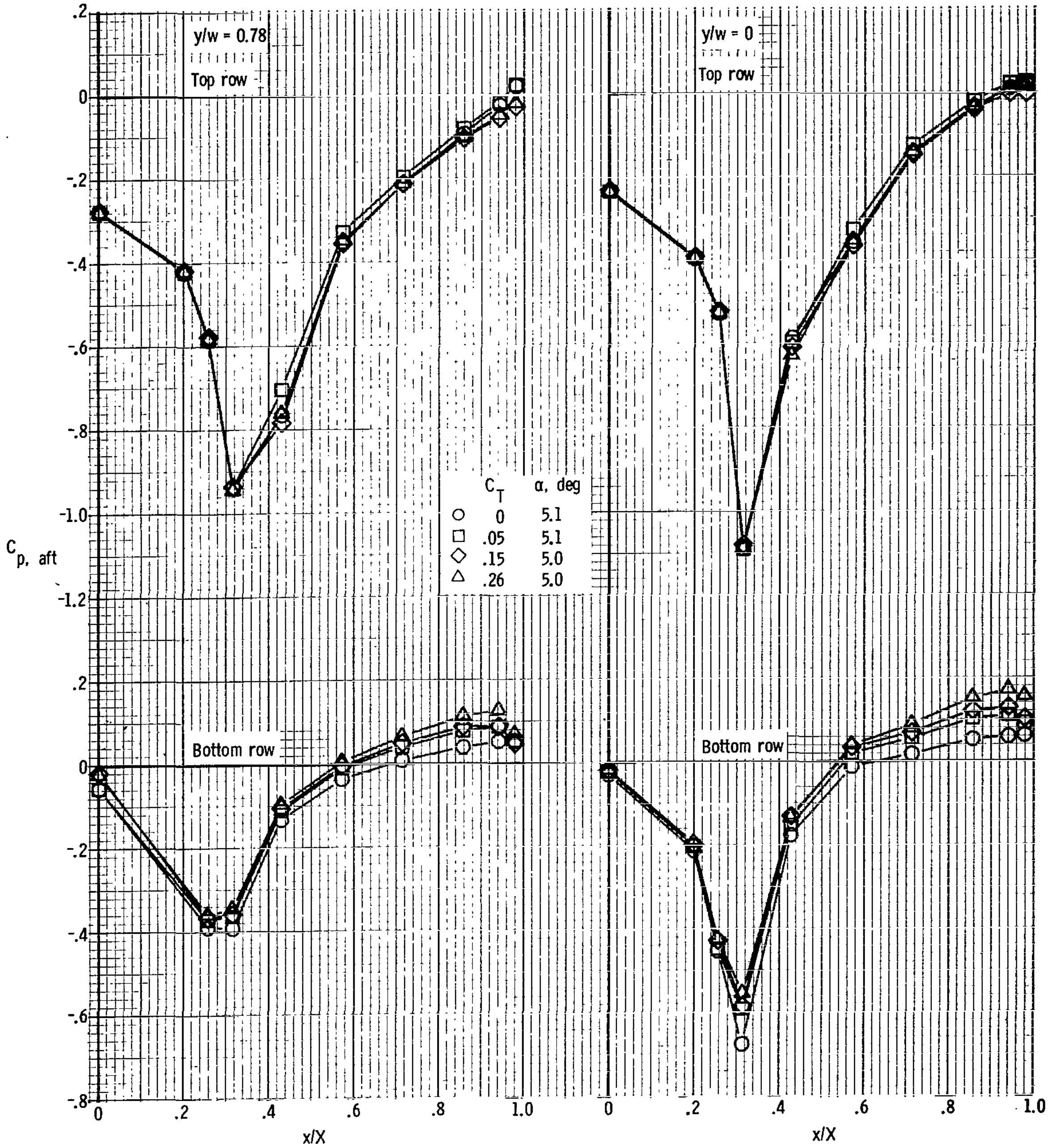

(e) M = 0.80; $\alpha \approx 5.1^{\circ}$.

Figure 25.- Continued.

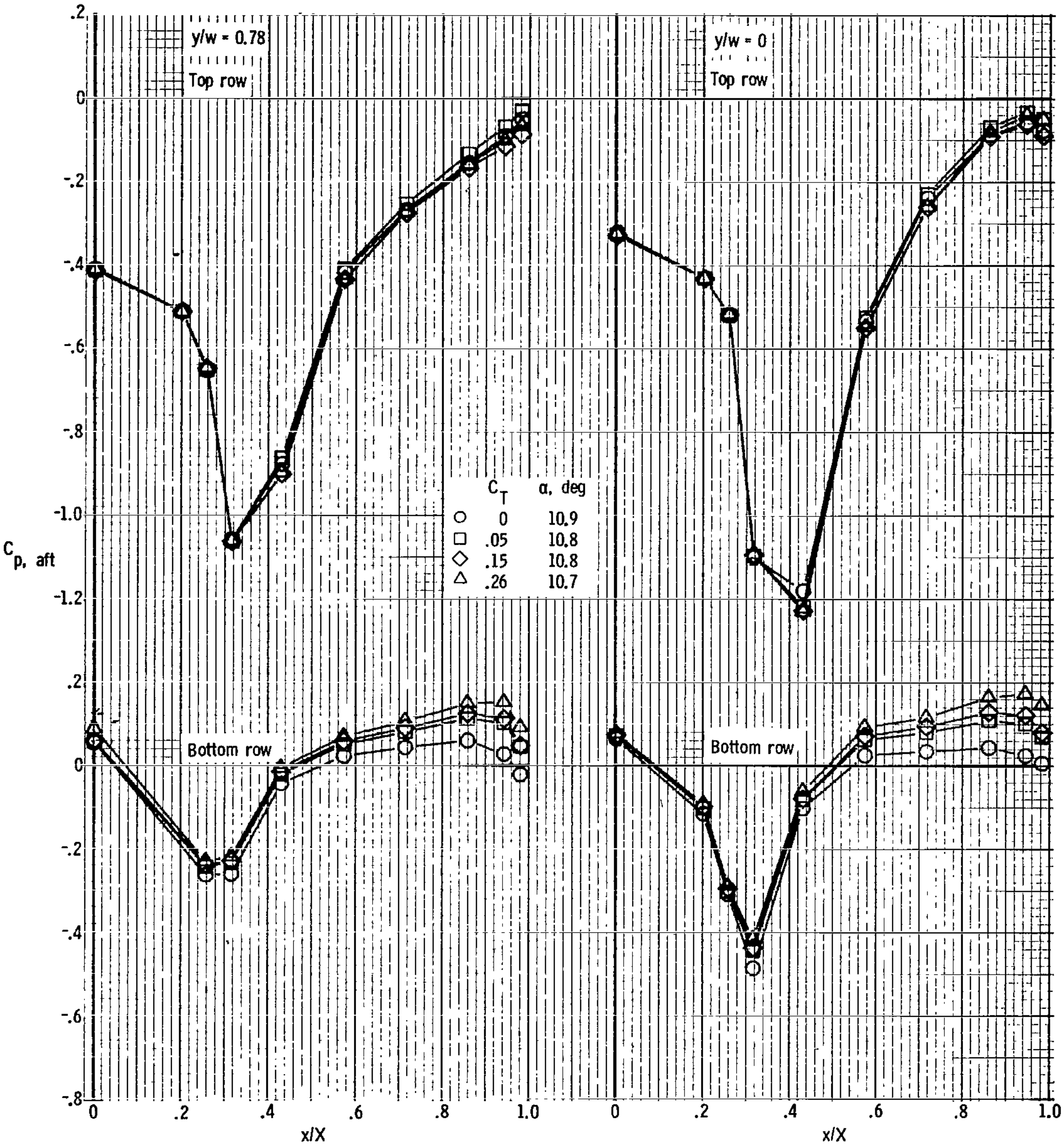

(f) M = 0.80; $\alpha \approx 10.8^{\circ}$.

Figure 25.- Continued.

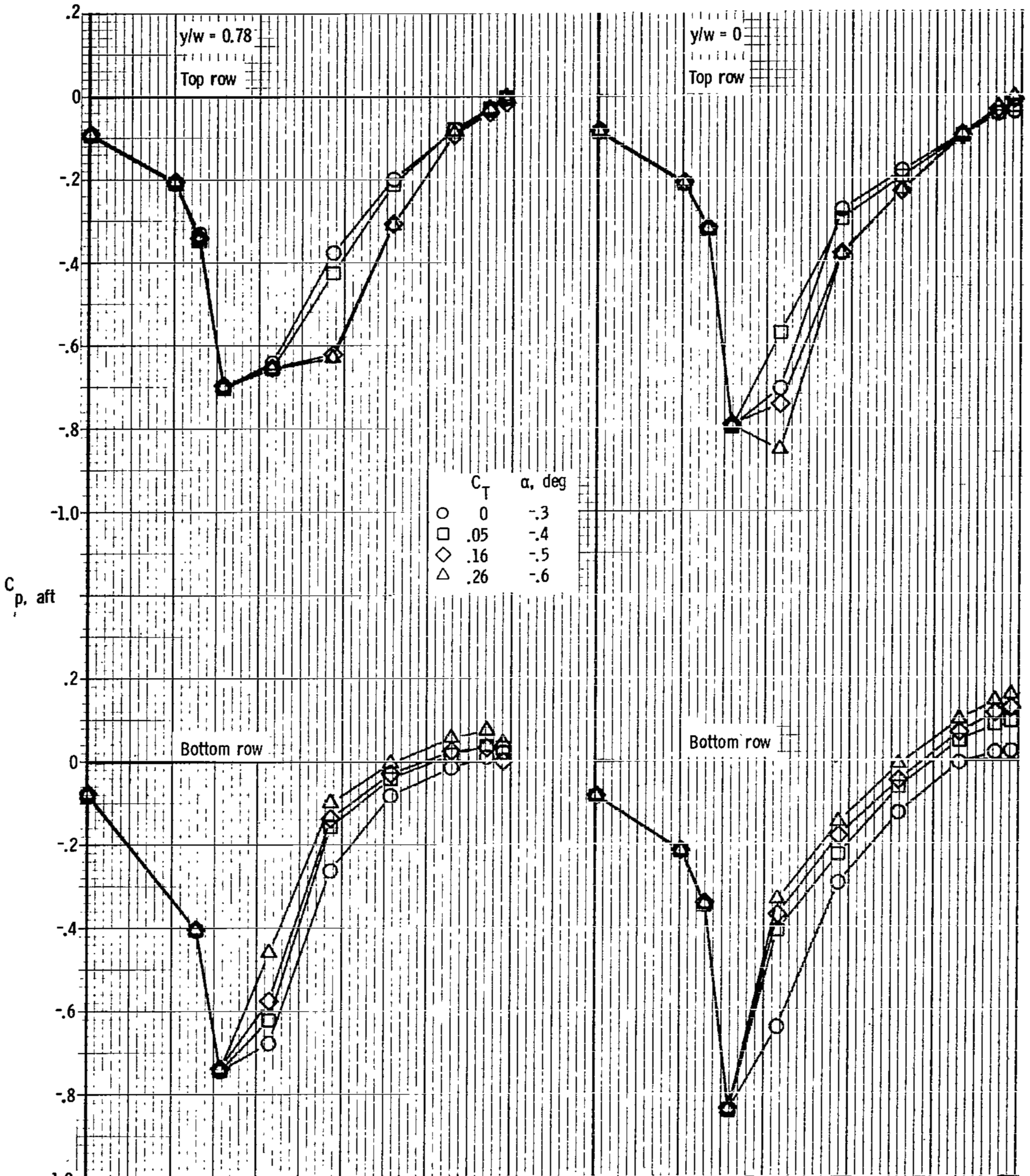

(g) M = 0.90; $\alpha \approx -0.4^{\circ}$.

Figure 25.- Continued.

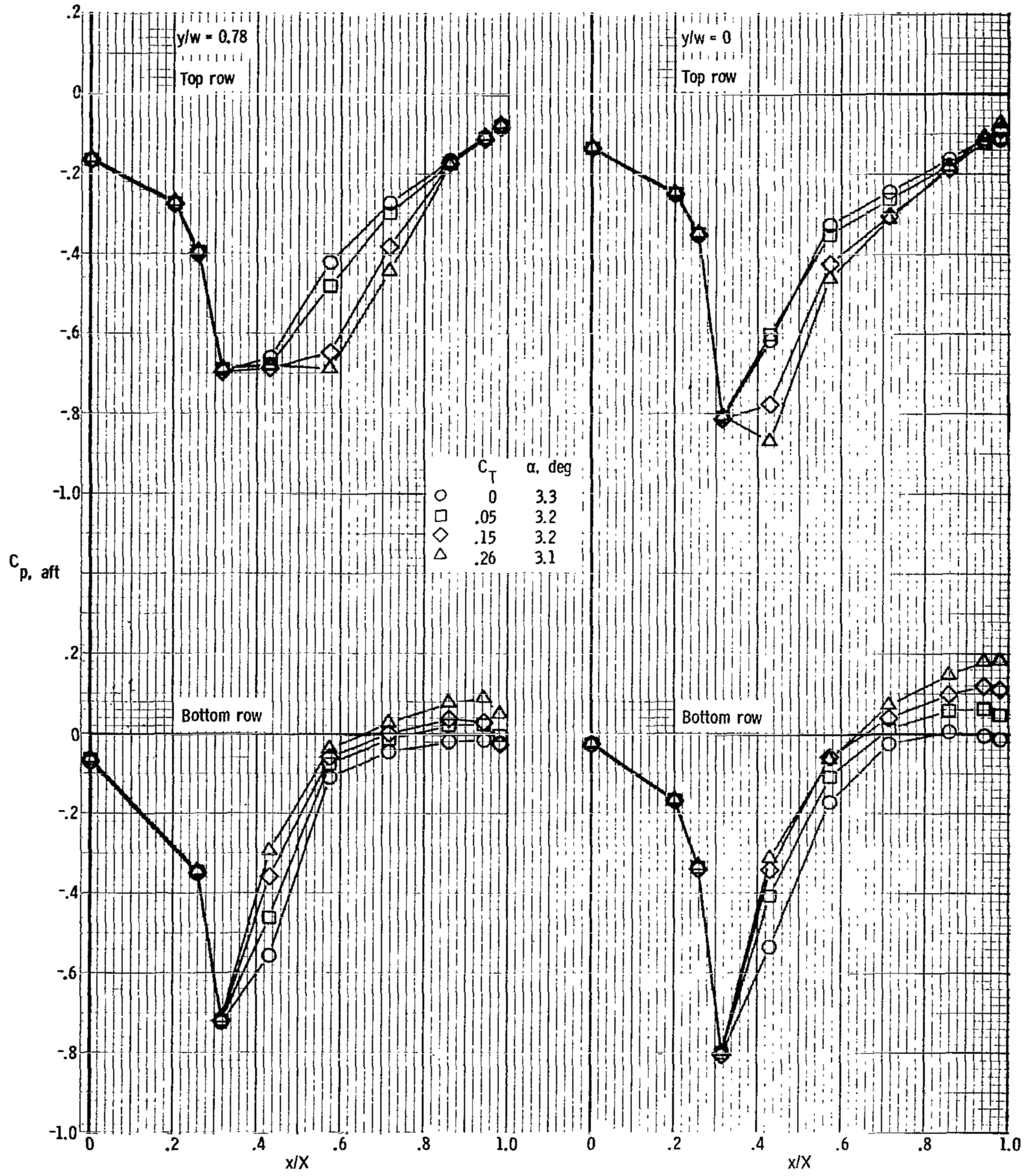

(h) M = 0.90; $\alpha \approx 3.2^{\circ}$.

Figure 25.- Continued.

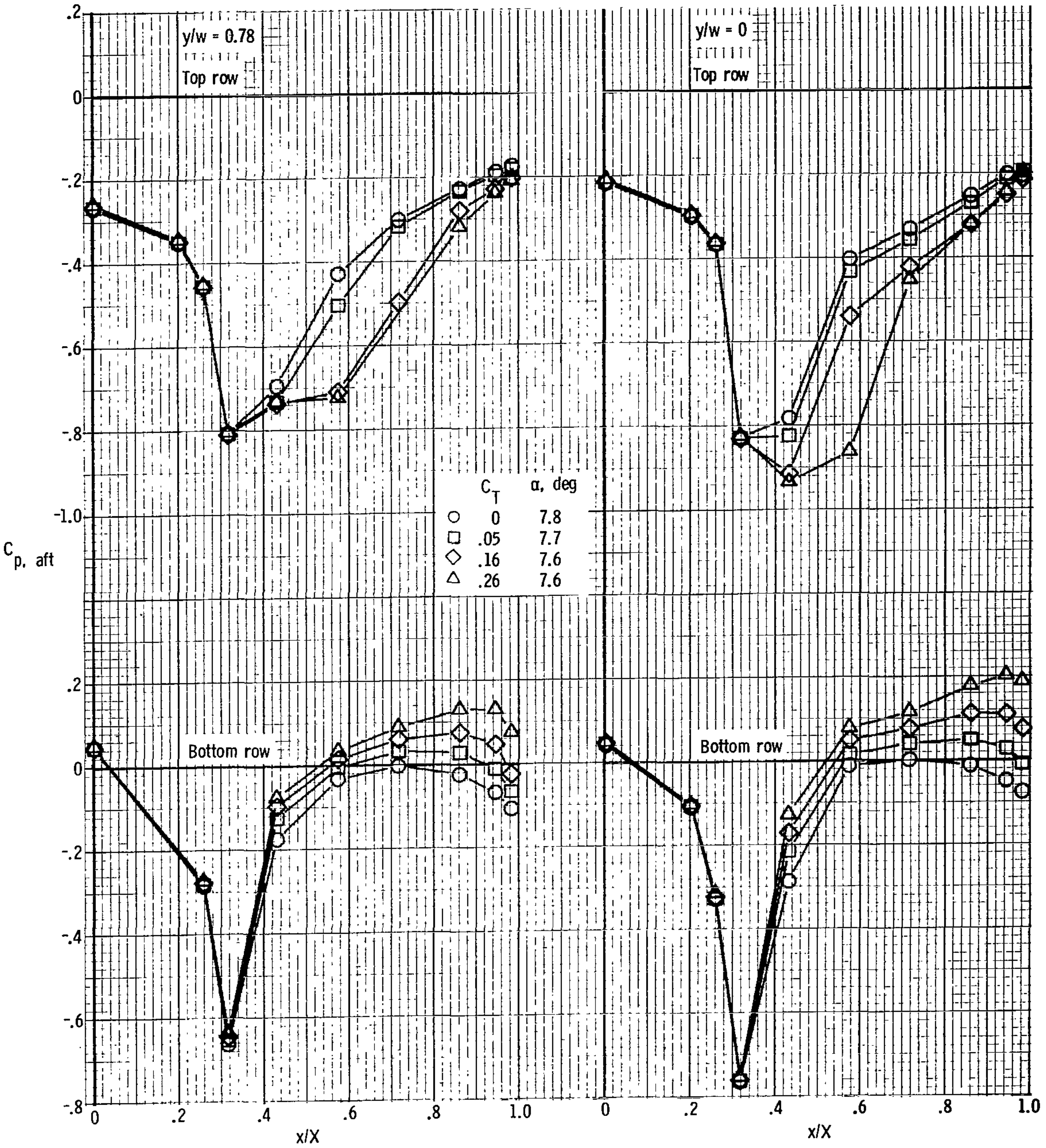

(i) M = 0.90; $\alpha \approx 7.7^{\circ}$.

Figure 25.- Continued.

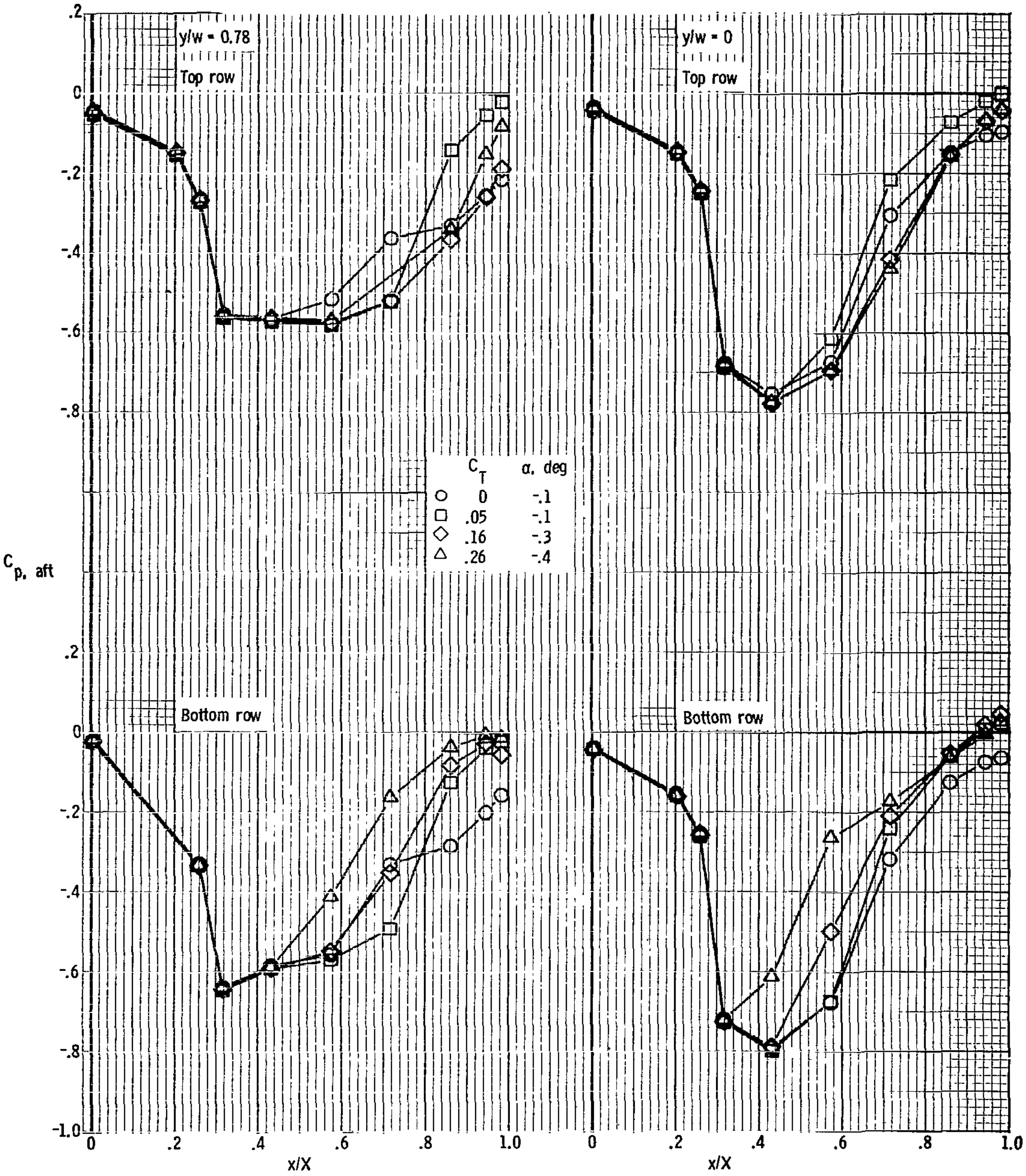

(j) M = 0.95; $\alpha \approx -0.1^{\circ}$.

Figure 25.- Continued.

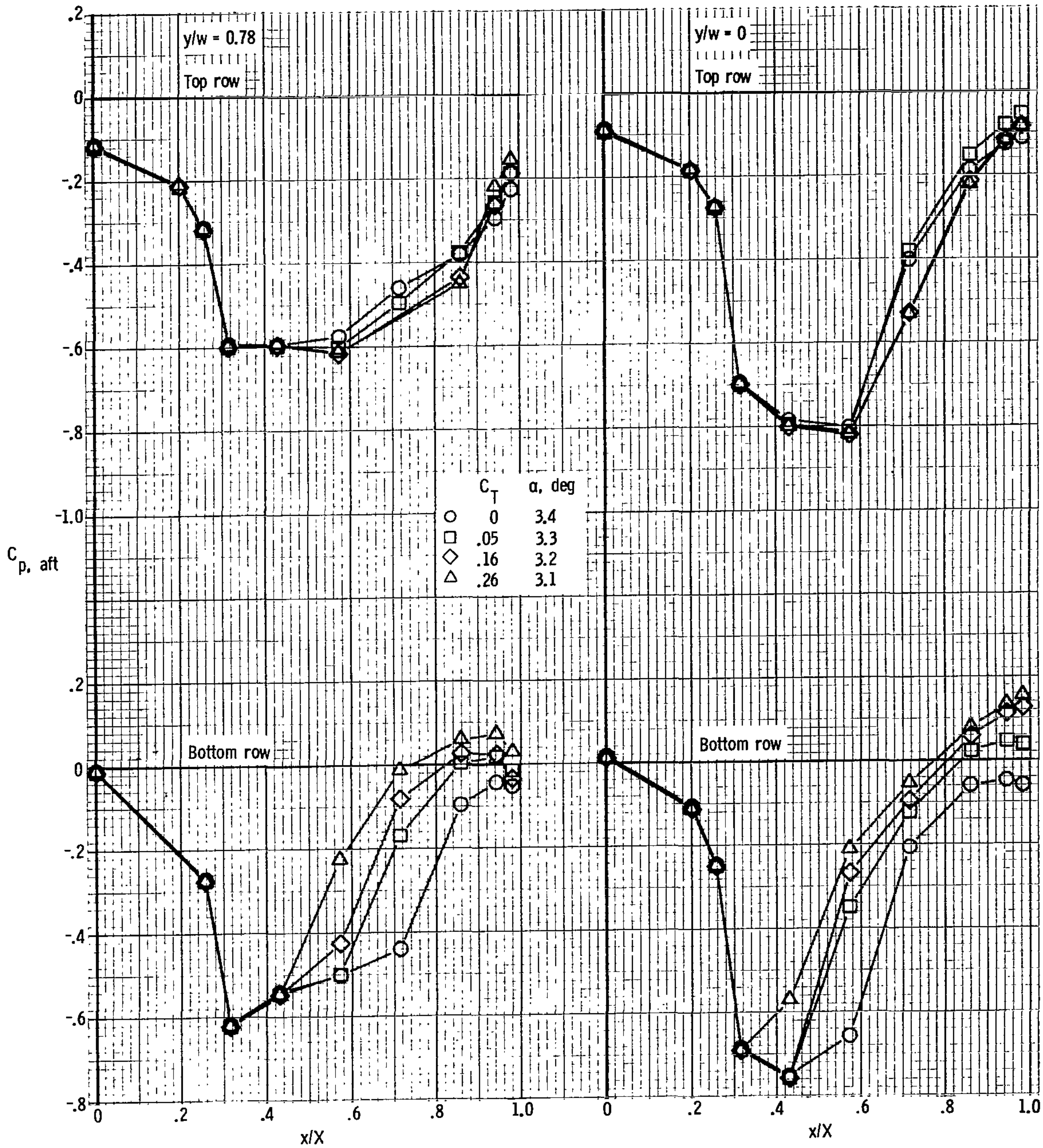

(k) M = 0.95; $\alpha \approx 3.3^\circ$.

Figure 25.- Continued.

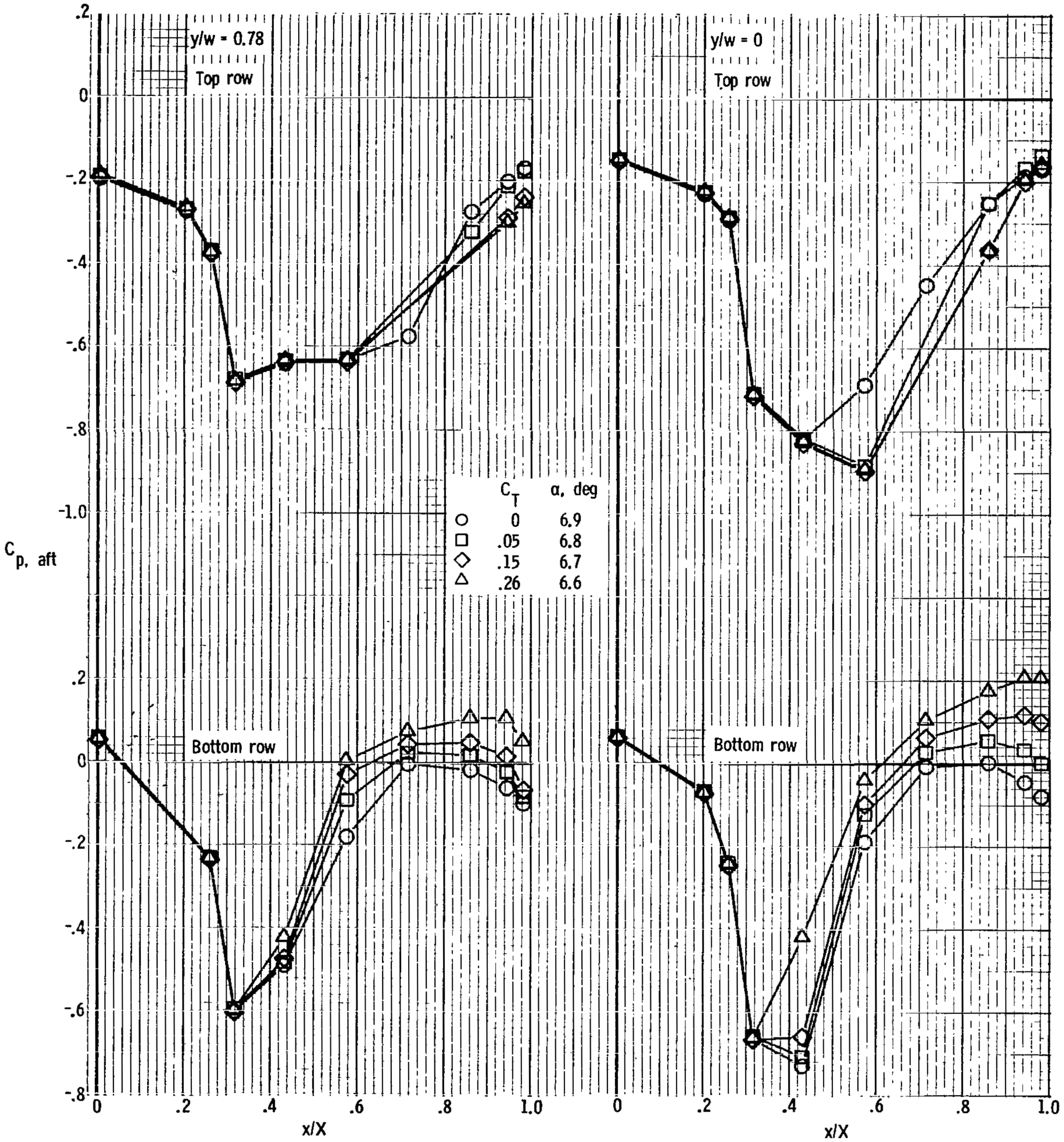

(l) M = 0.95; $\alpha \approx 6.8^{\circ}$.

Figure 25.- Concluded.

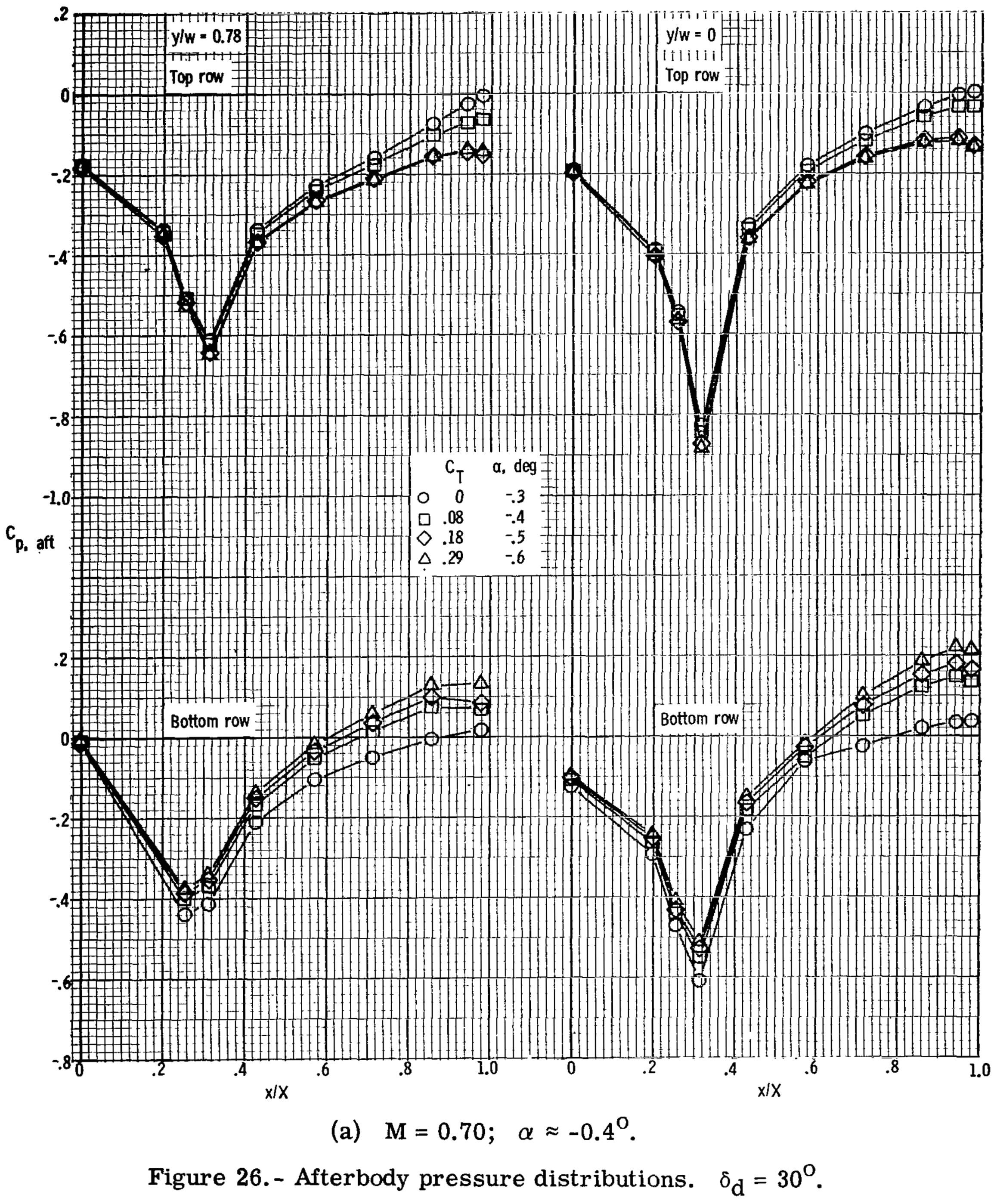

(a) M = 0.70; $\alpha \approx -0.4^{\circ}$.

Figure 26.- Afterbody pressure distributions. $\delta_d = 30^{\circ}$.

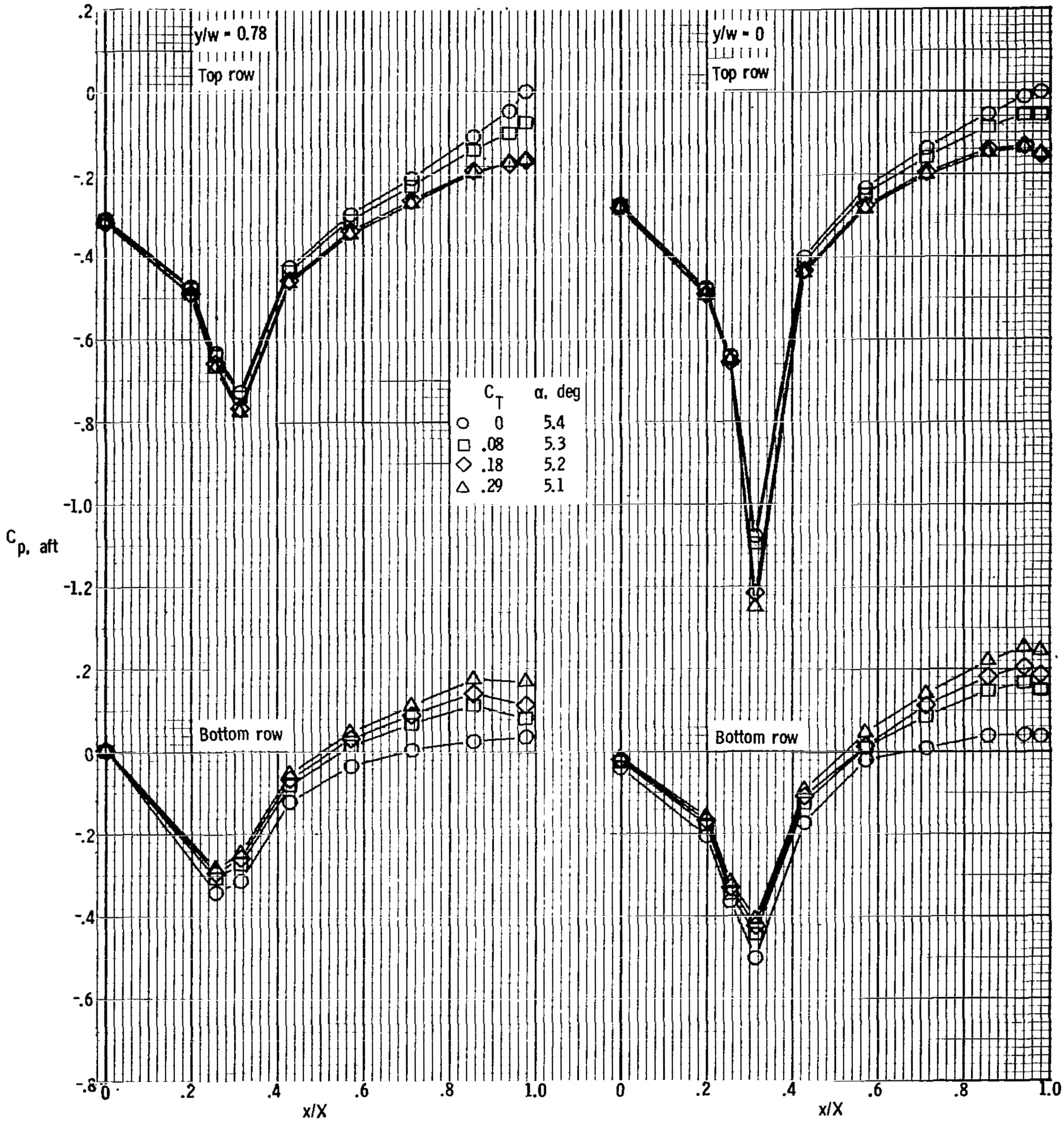

(b) M = 0.70; $\alpha \approx 5.3^{\circ}$.

Figure 26.- Continued.

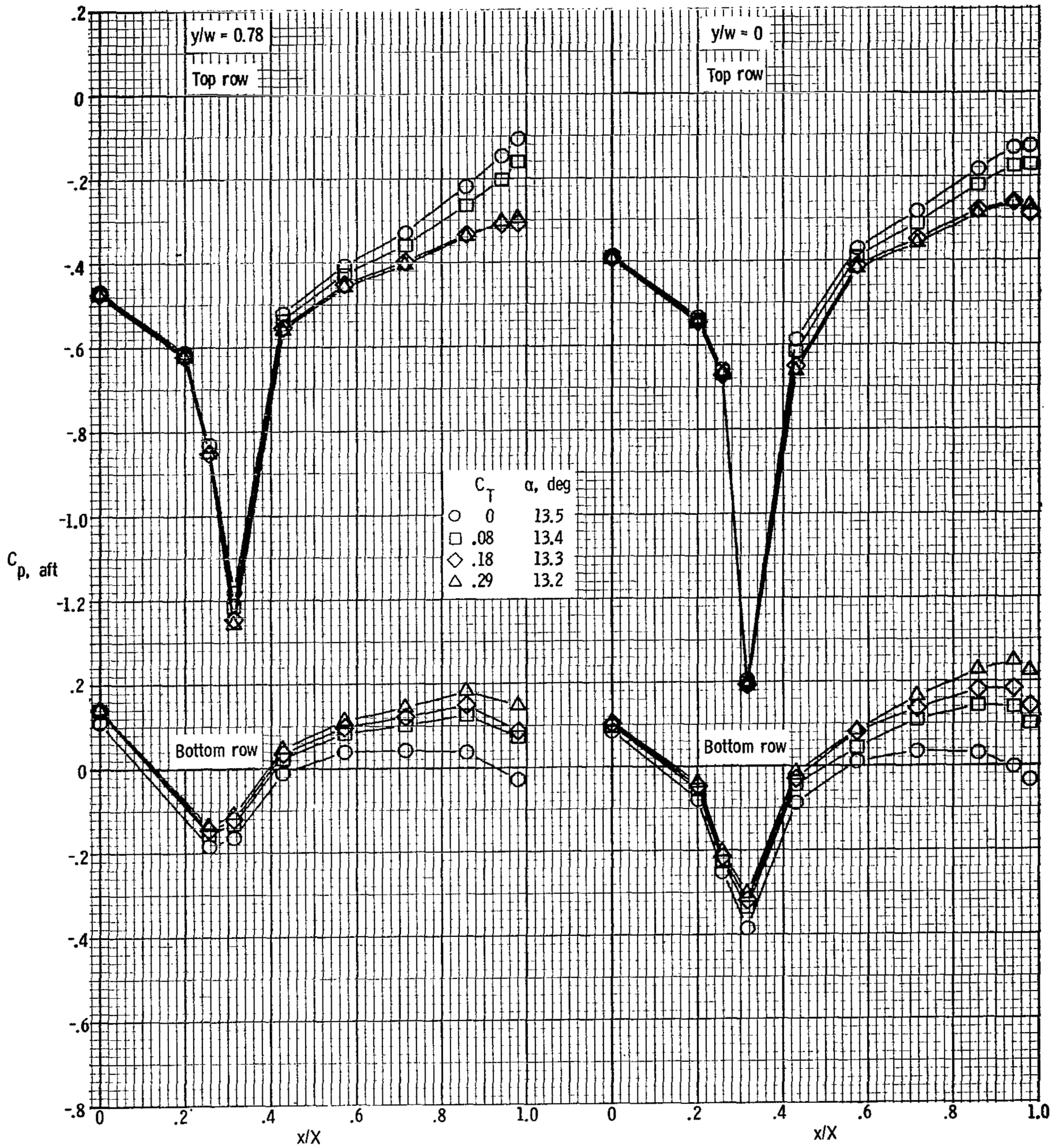

(c) M = 0.70; $\alpha \approx 13.4^{\circ}$.

Figure 26.- Continued.

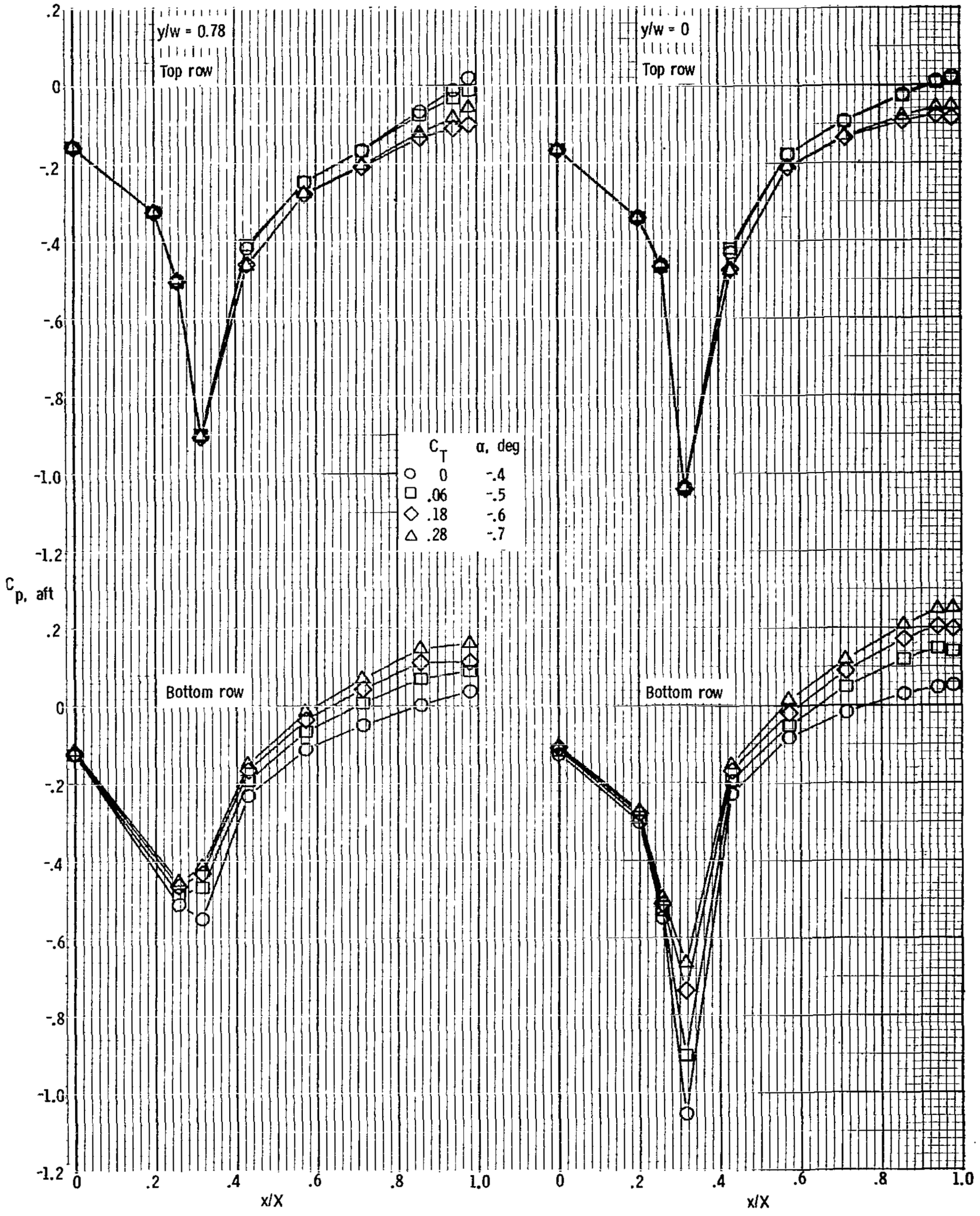

(d) M = 0.80; $\alpha \approx -0.5^{\circ}$.

Figure 26.- Continued.

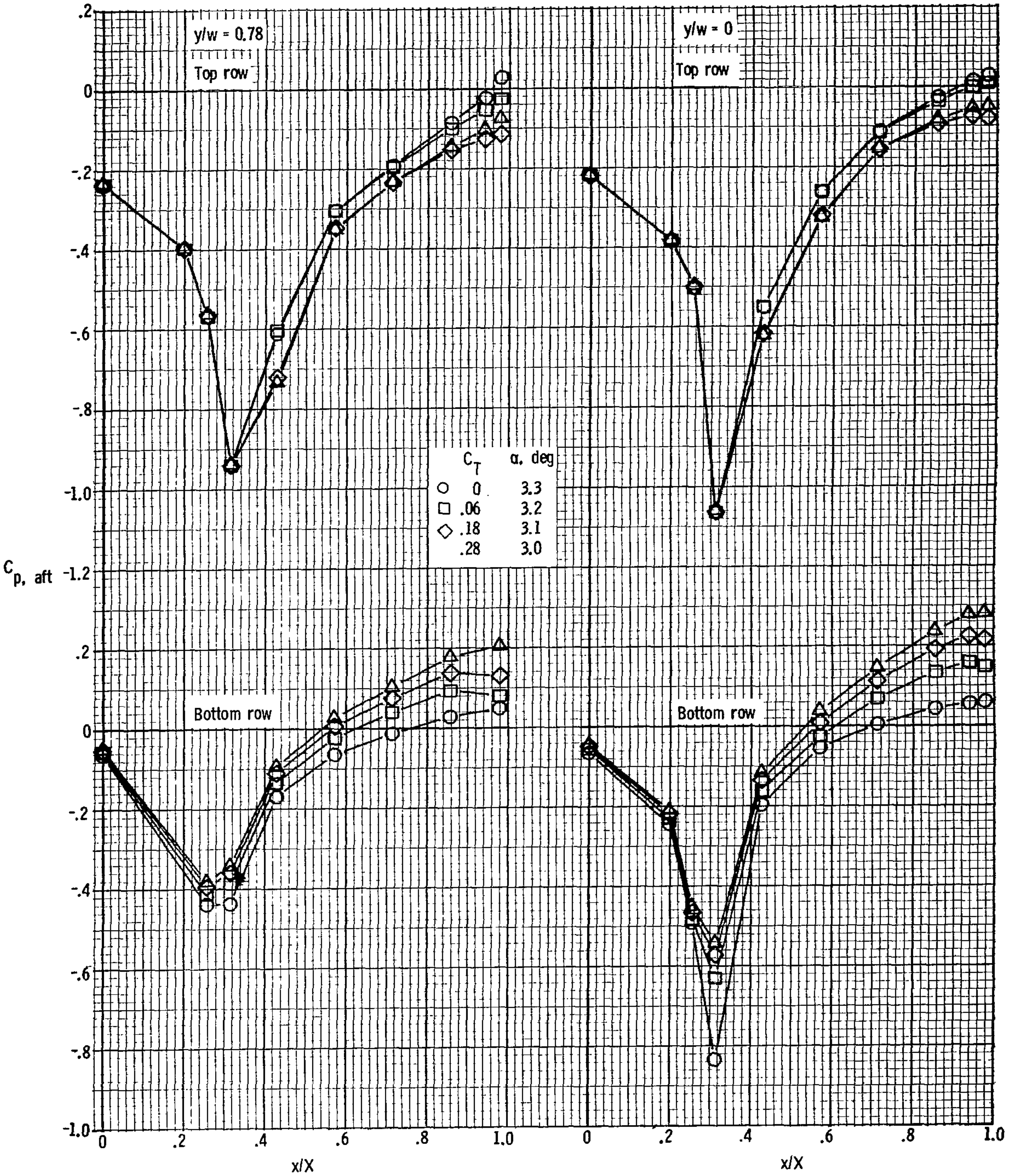

(e) M = 0.80; $\alpha \approx 3.2^{\circ}$.

Figure 26.- Continued.

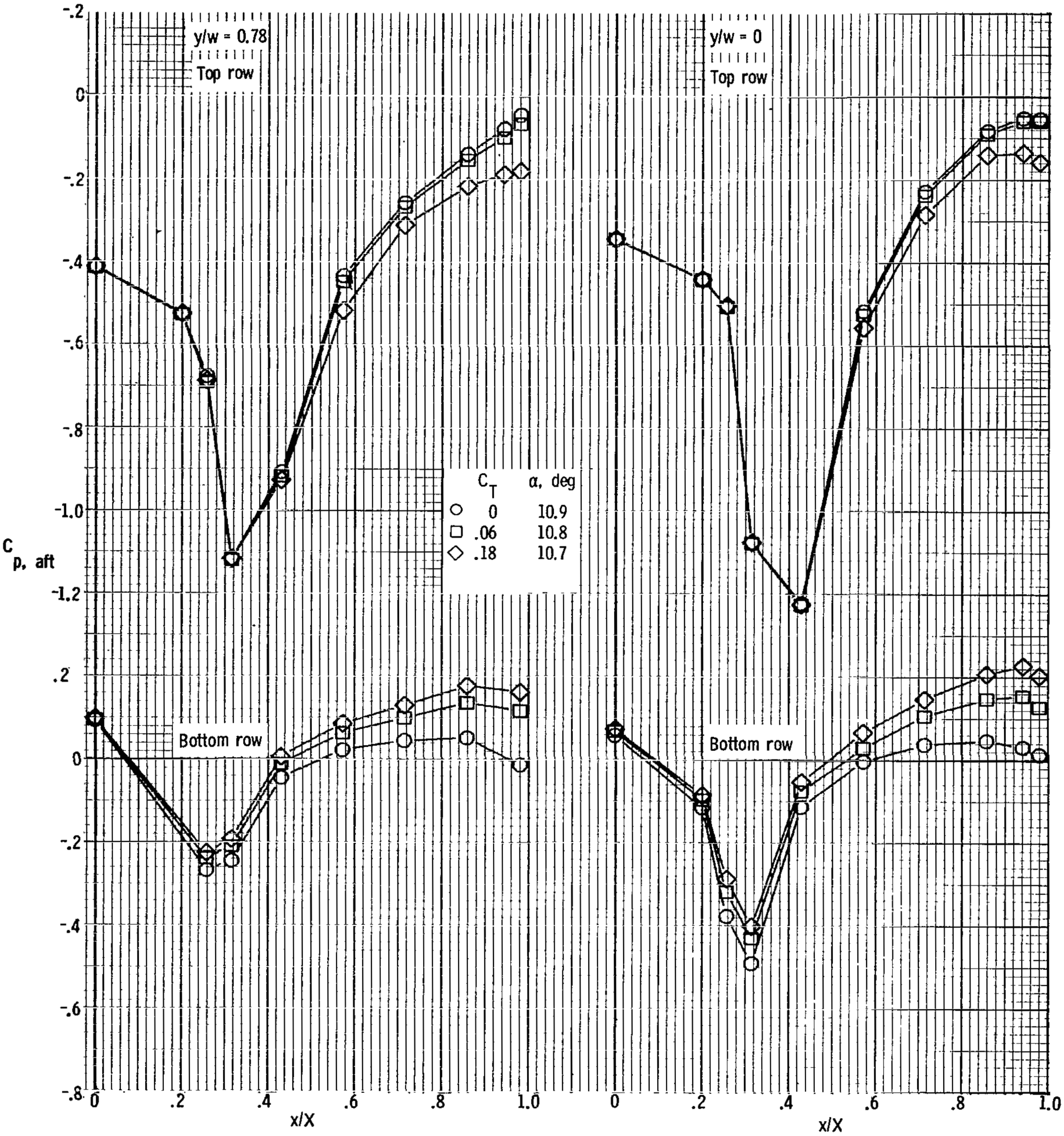

(f) M = 0.80; $\alpha \approx 10.8^{\circ}$.

Figure 26.- Continued.

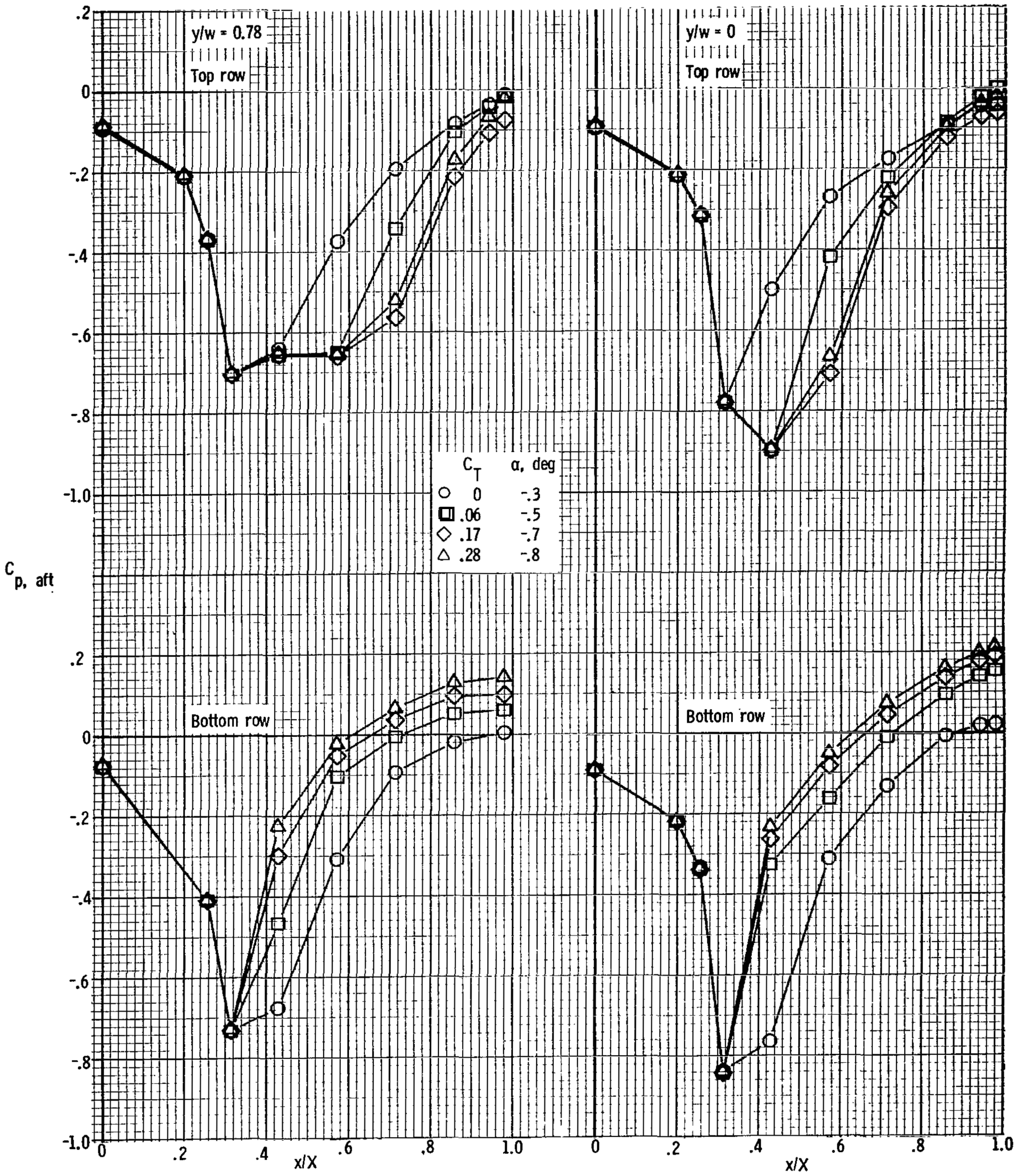

(g) M = 0.90; $\alpha \approx -0.5^{\circ}$.

Figure 26.- Continued.

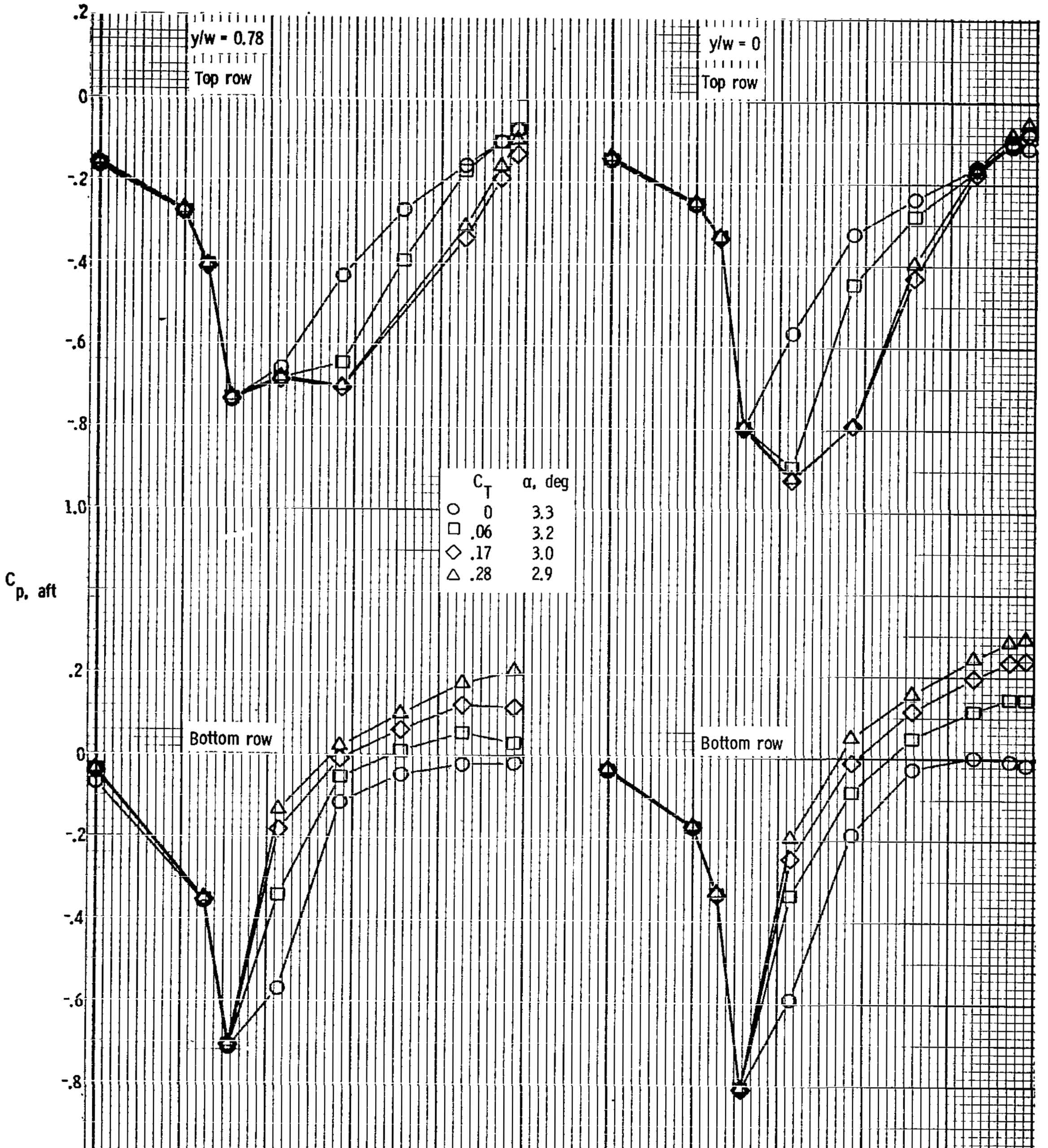

(h) M = 0.90; $\alpha \approx 3.2^{\circ}$.

Figure 26.- Continued.

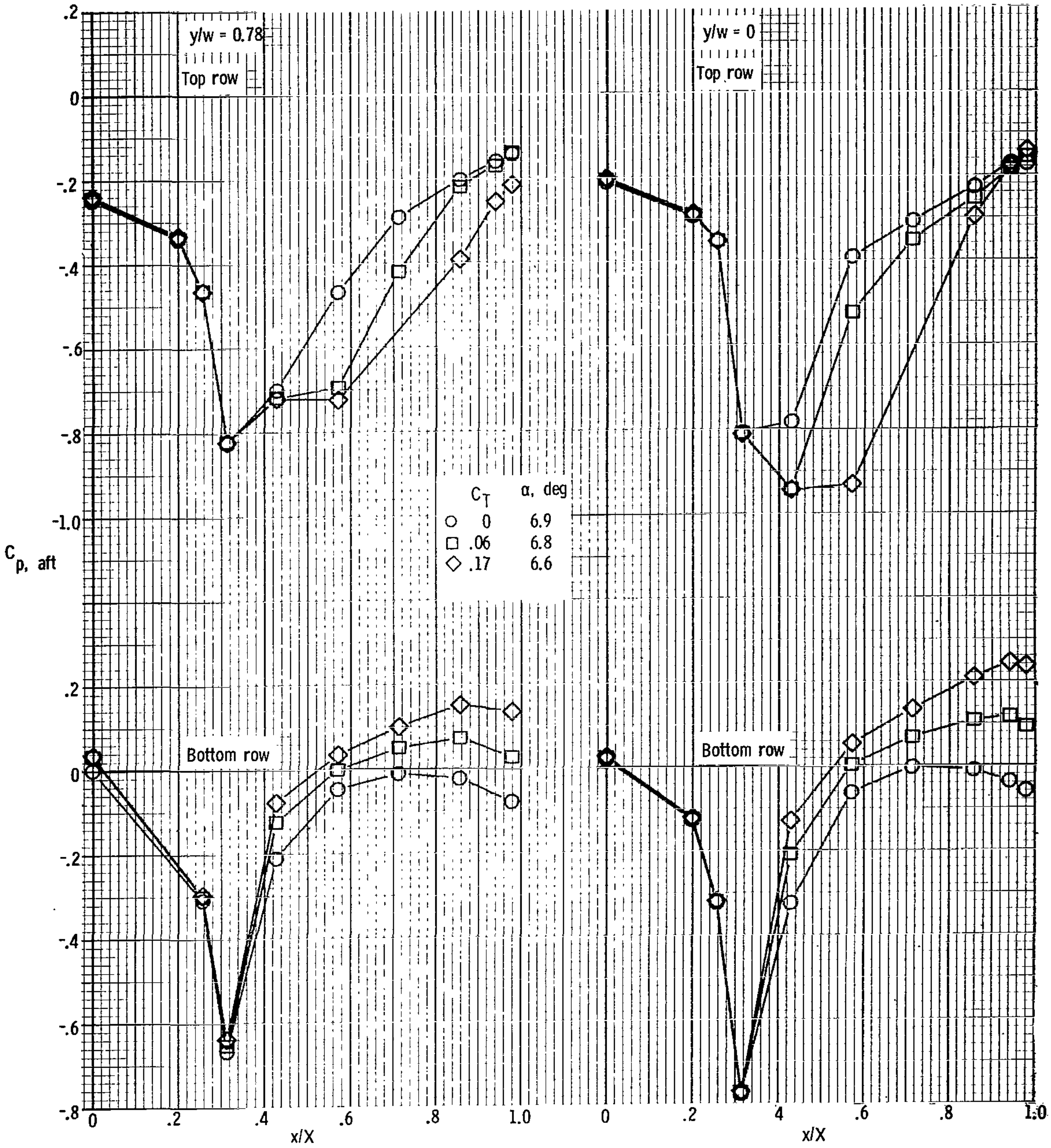

(i) M = 0.90; $\alpha \approx 6.8^{\circ}$.

Figure 26.- Continued.

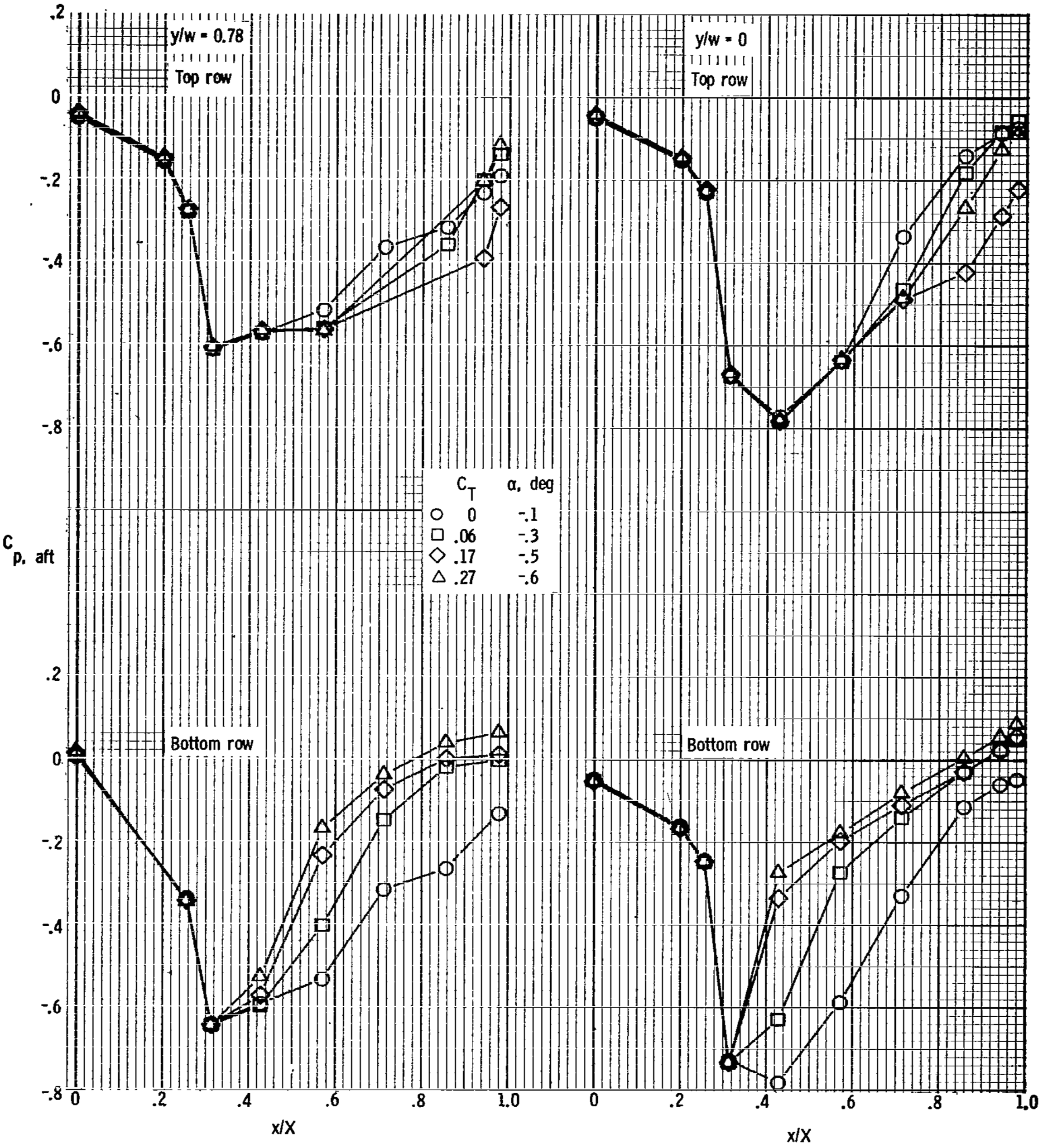

(j) M = 0.95; $\alpha \approx -0.3^{\circ}$.

Figure 26.- Continued.

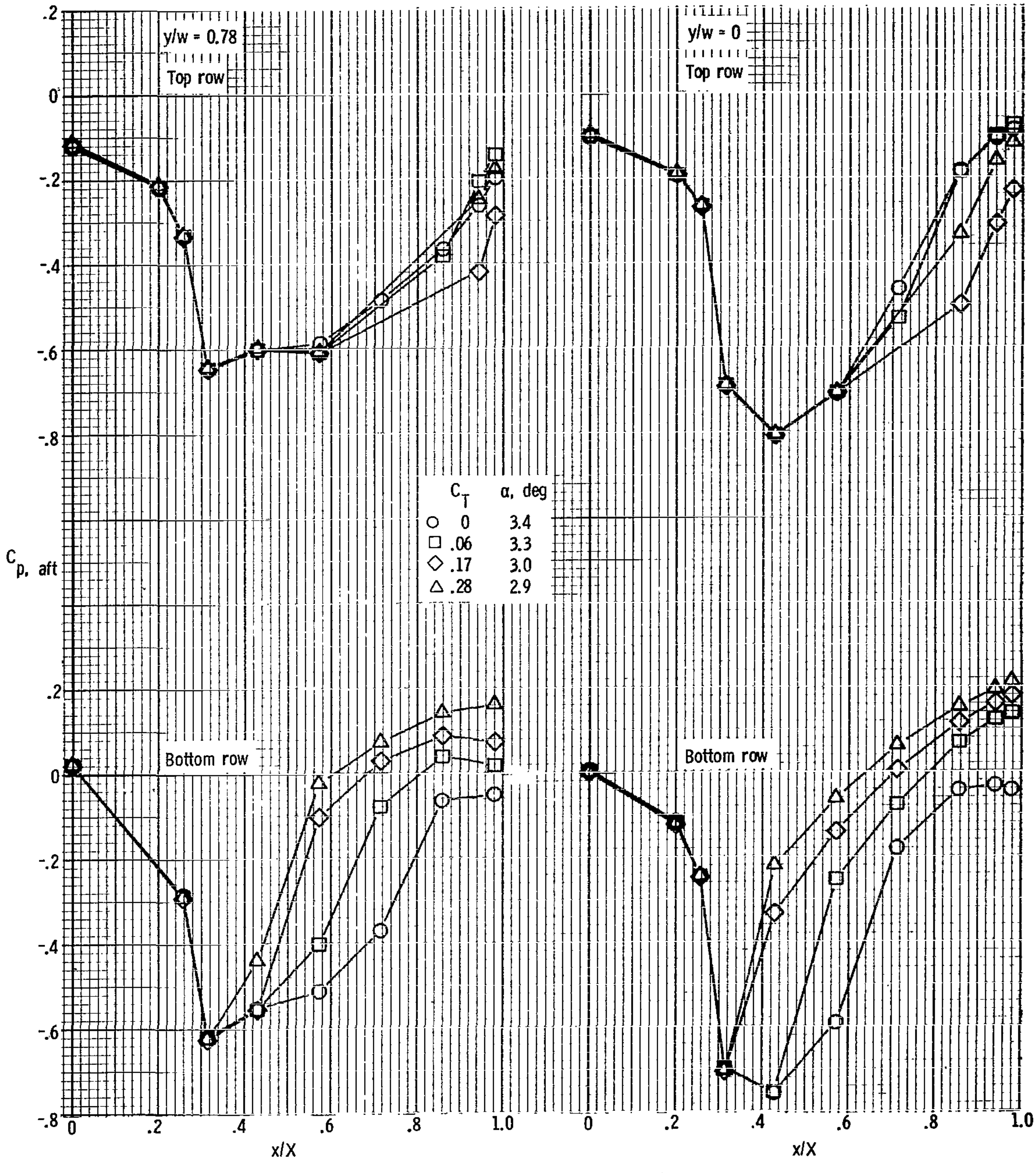

(k) M = 0.95; $\alpha \approx 3.3^{\circ}$.

Figure 26.- Continued.

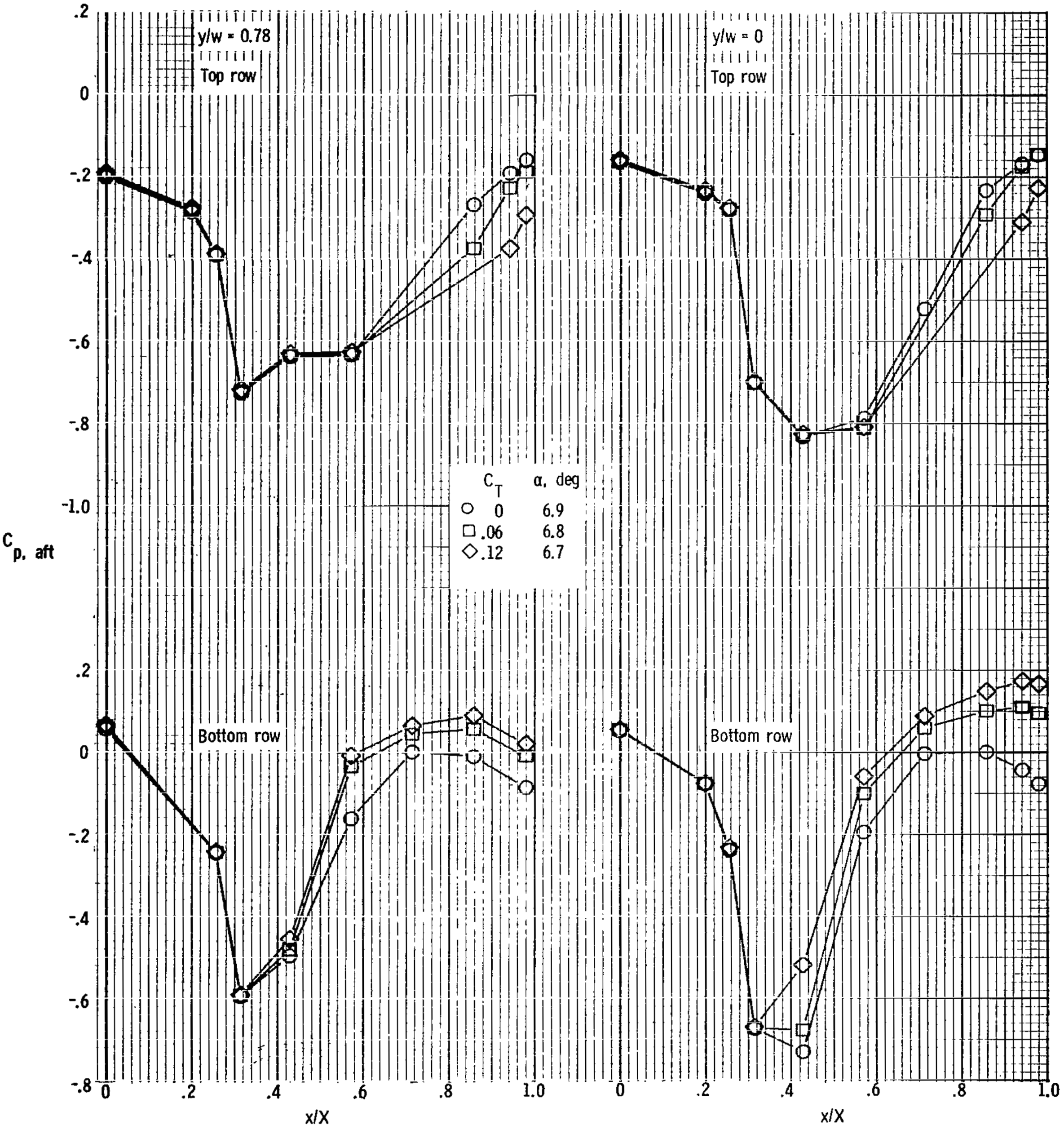

(l) M = 0.95; $\alpha \approx 6.8^{\circ}$.

Figure 26.- Concluded.

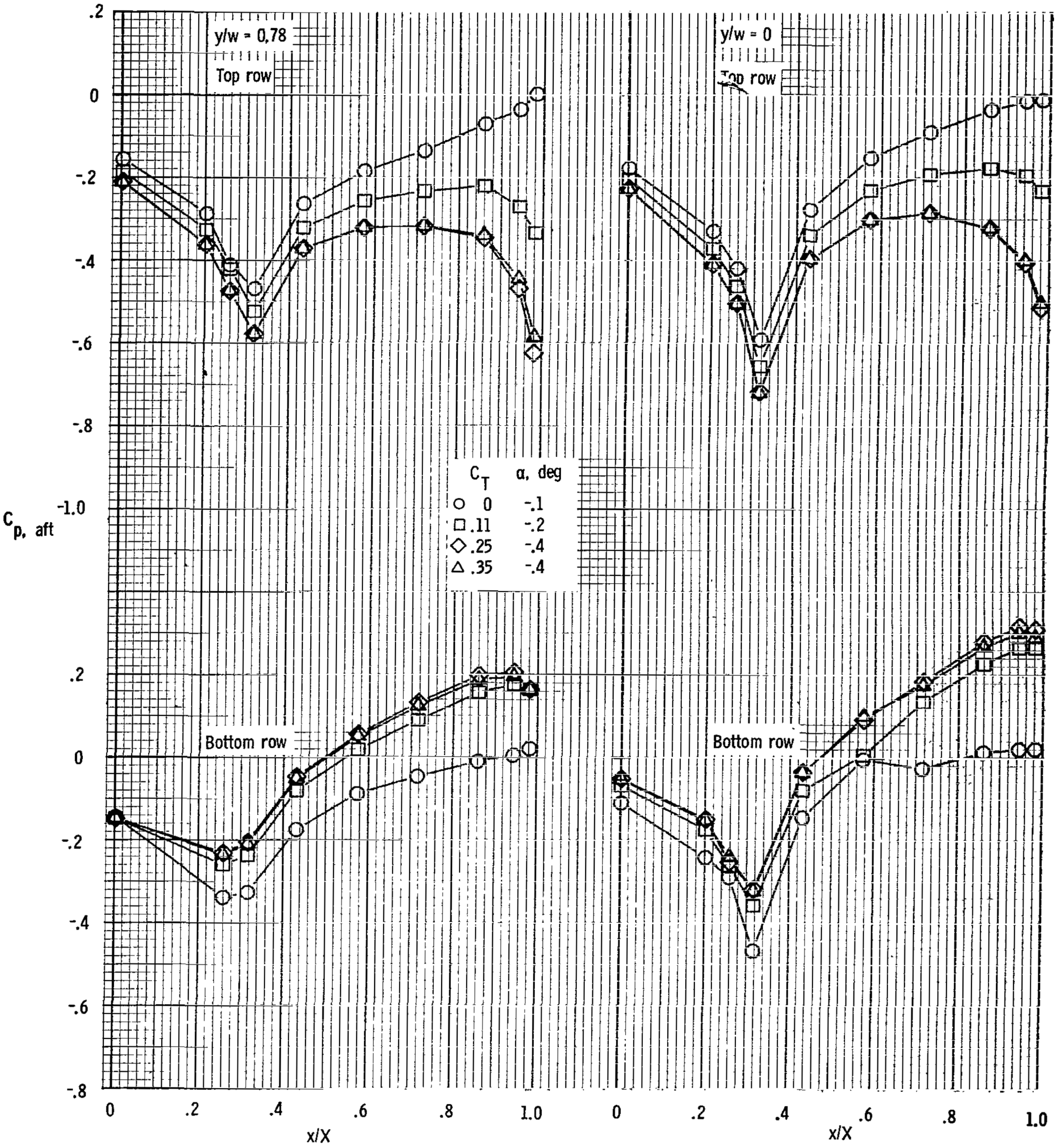

(a) M = 0.40; $\alpha \approx -0.2^{\circ}$.

Figure 27.- Afterbody pressure distributions. $\delta_d = 45^{\circ}$.

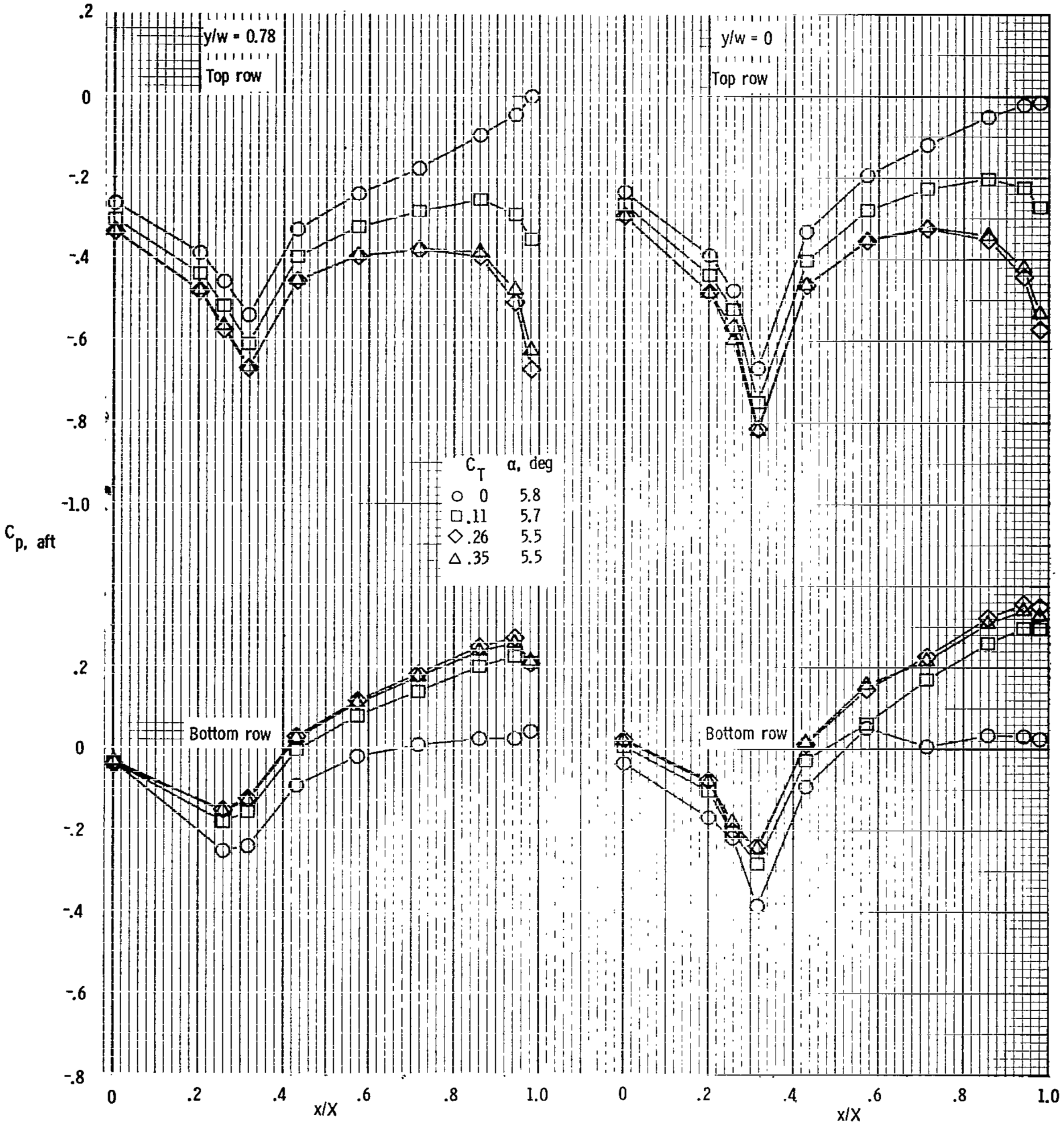

(b) M = 0.40; $\alpha \approx 5.7^{\circ}$.

Figure 27.- Continued.

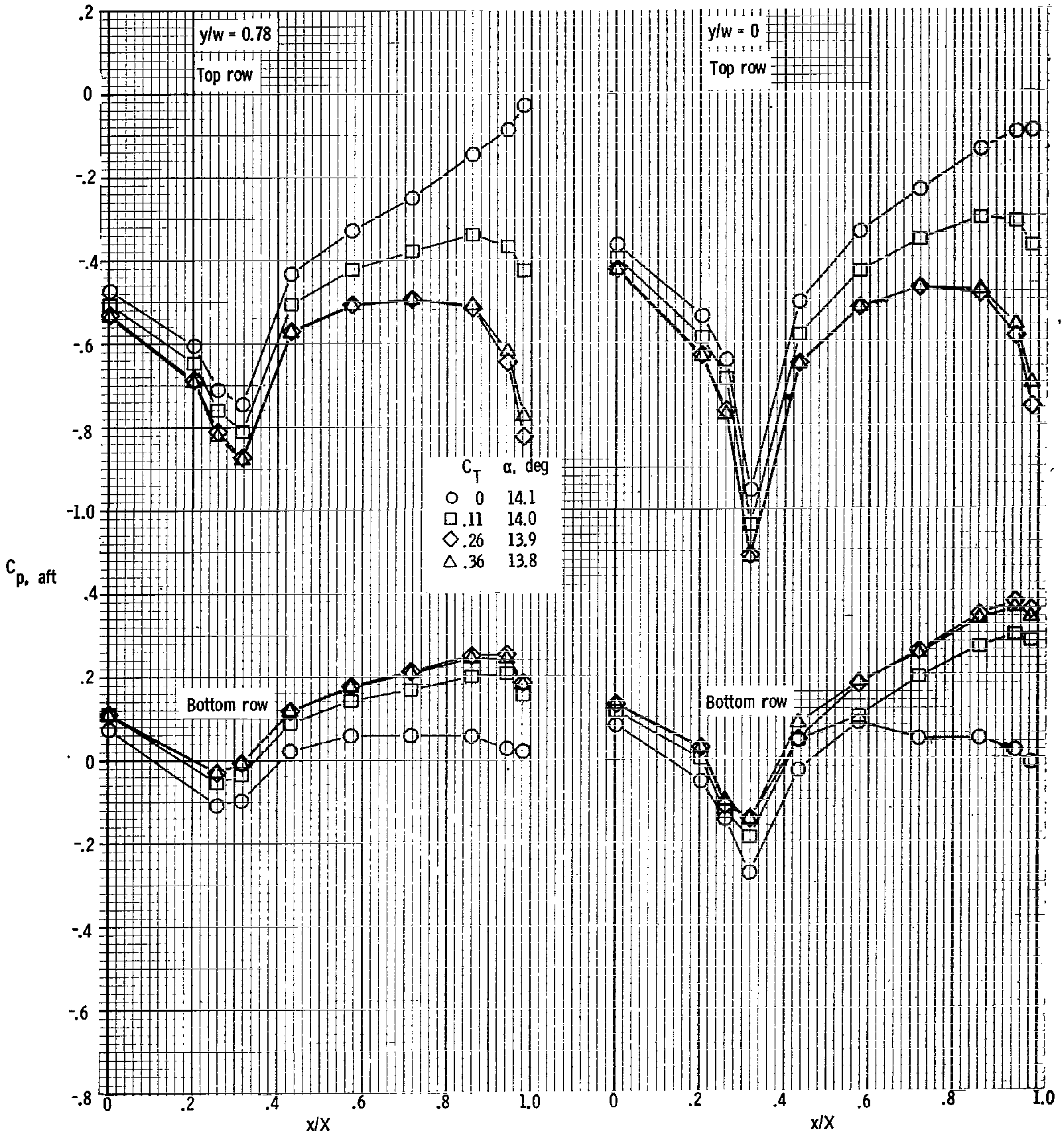

(c) $M = 0.40$; $\alpha \approx 14.8^{\circ}$.

Figure 27.- Continued.

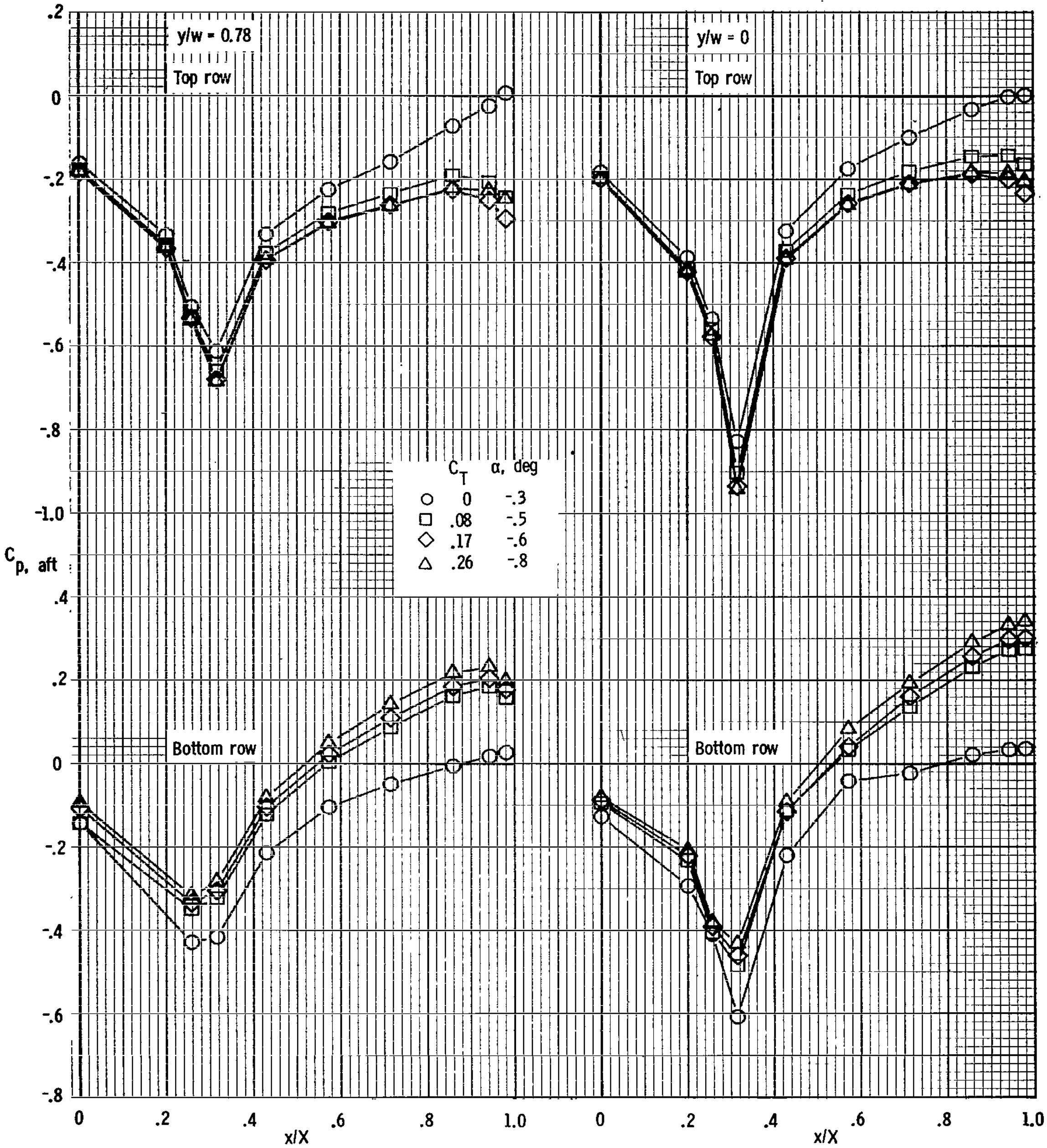

(d) M = 0.70; $\alpha \approx -0.5^{\circ}$.

Figure 27.- Continued.

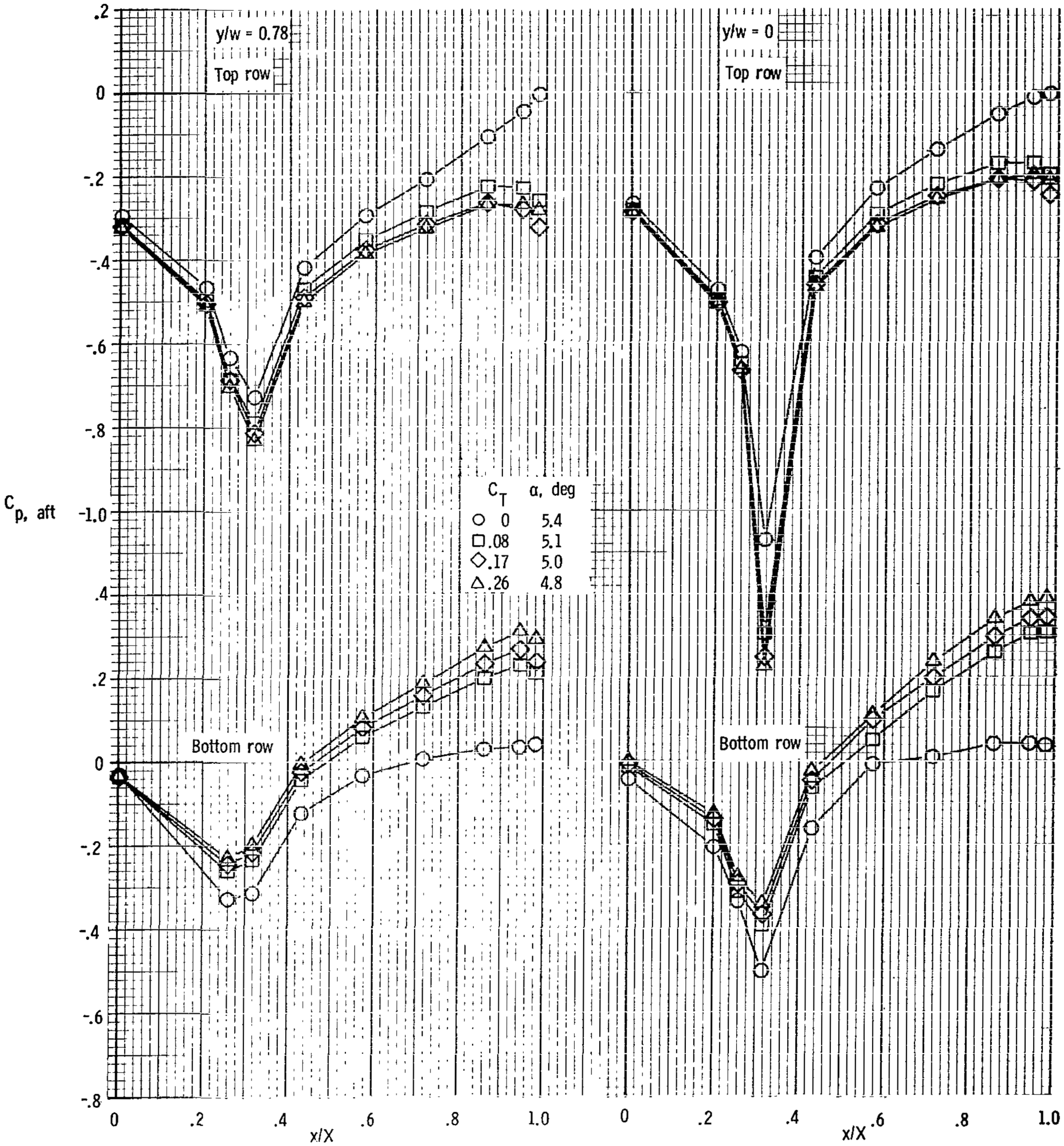

(e) M = 0.70; $\alpha \approx 5.1^{\circ}$.

Figure 27.- Continued.

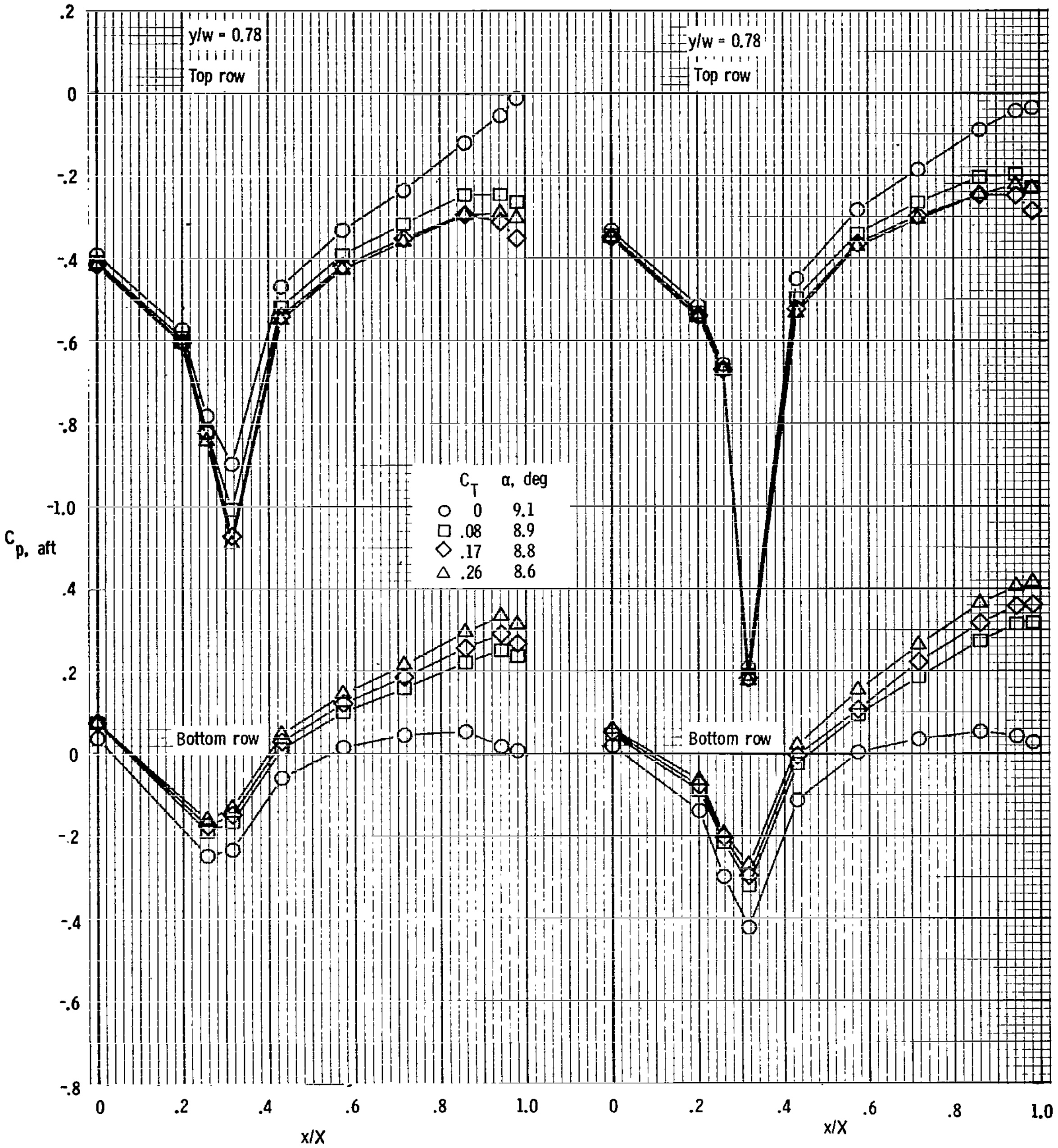

(f) M = 0.70; $\alpha \approx 8.9^{\circ}$.

Figure 27.- Continued.

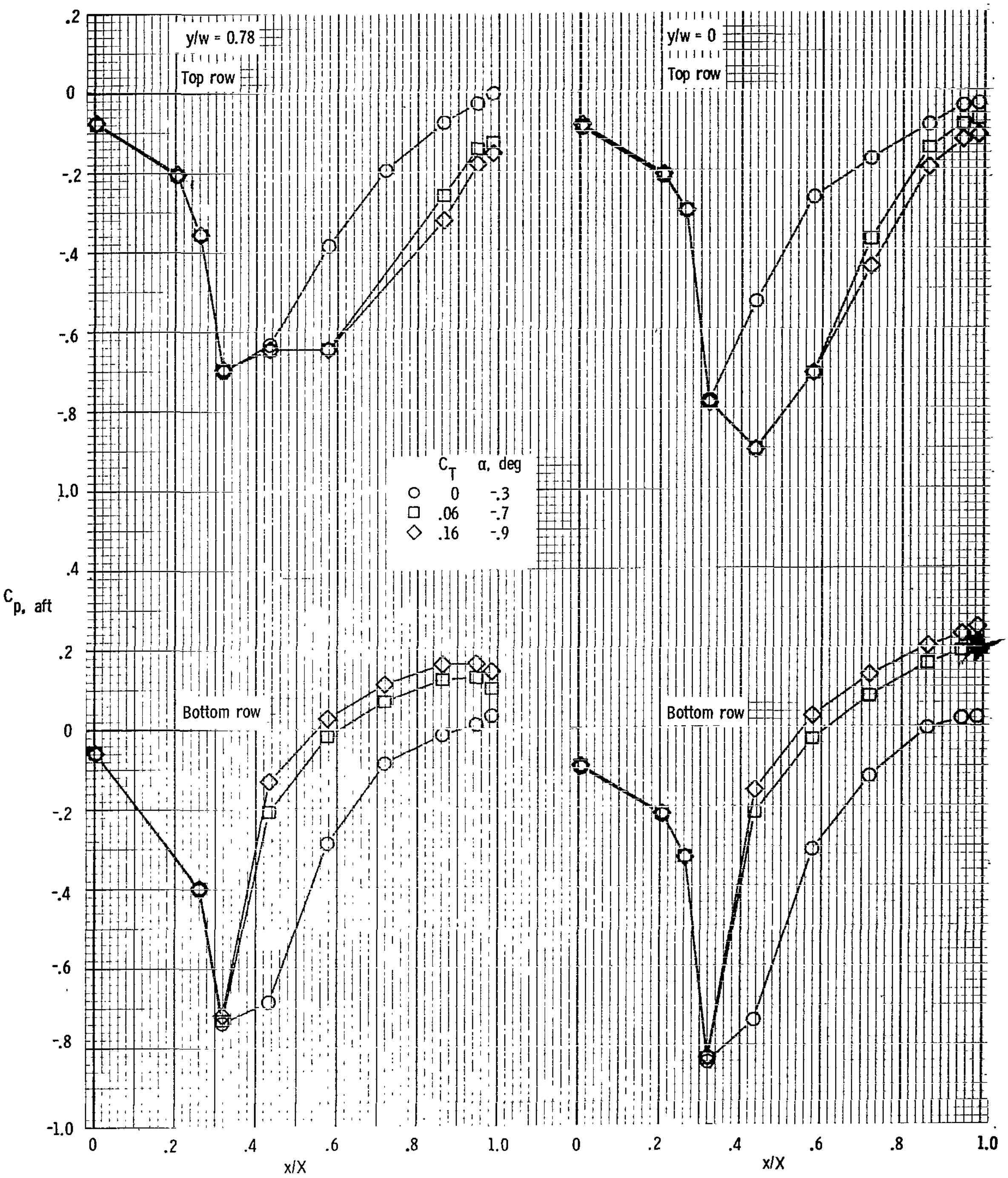

(g) M = 0.90; $\alpha \approx -0.7^{\circ}$.

Figure 27.- Continued.

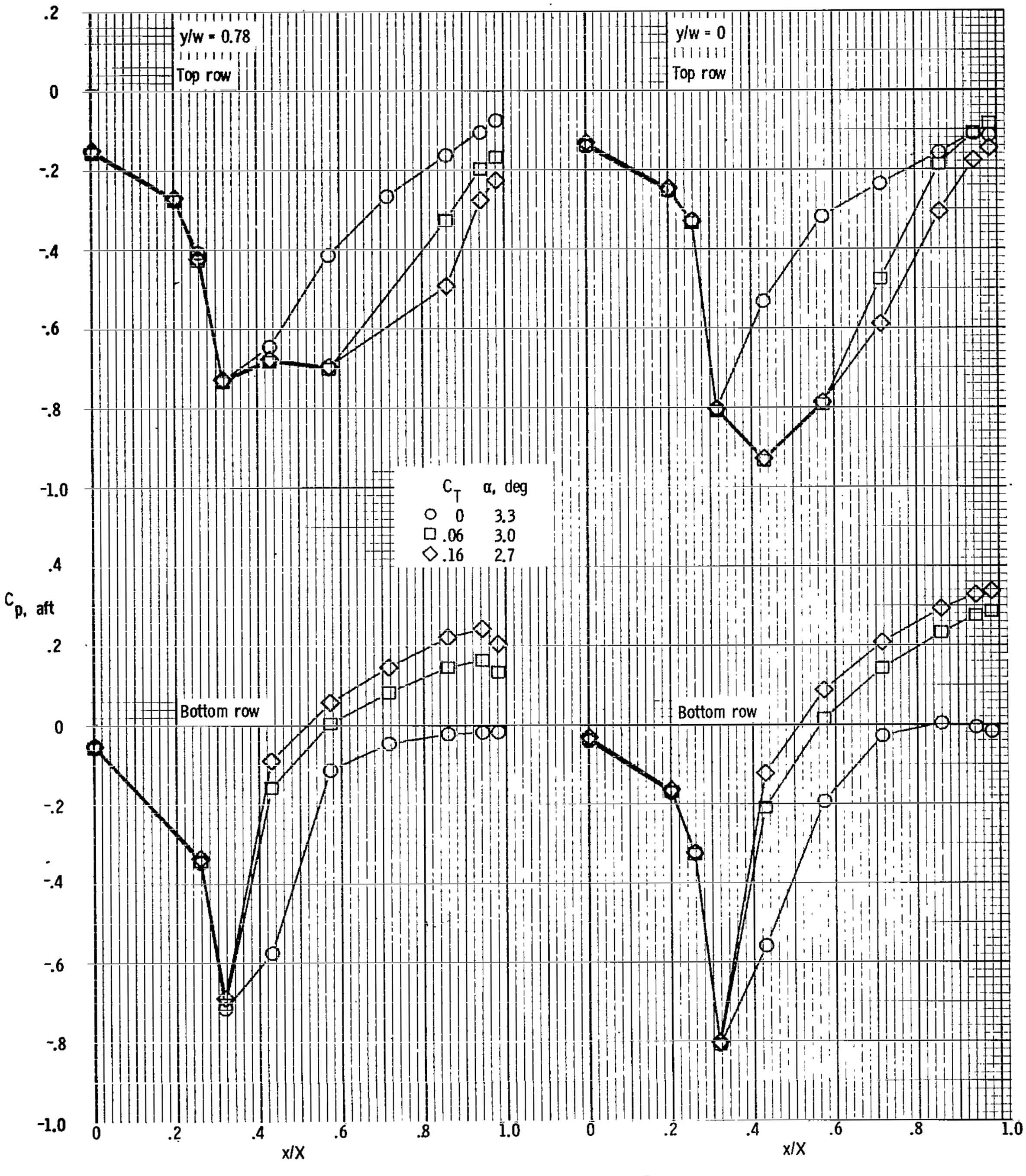

(h) M = 0.90; $\alpha \approx 3.0^{\circ}$.

Figure 27.- Continued.

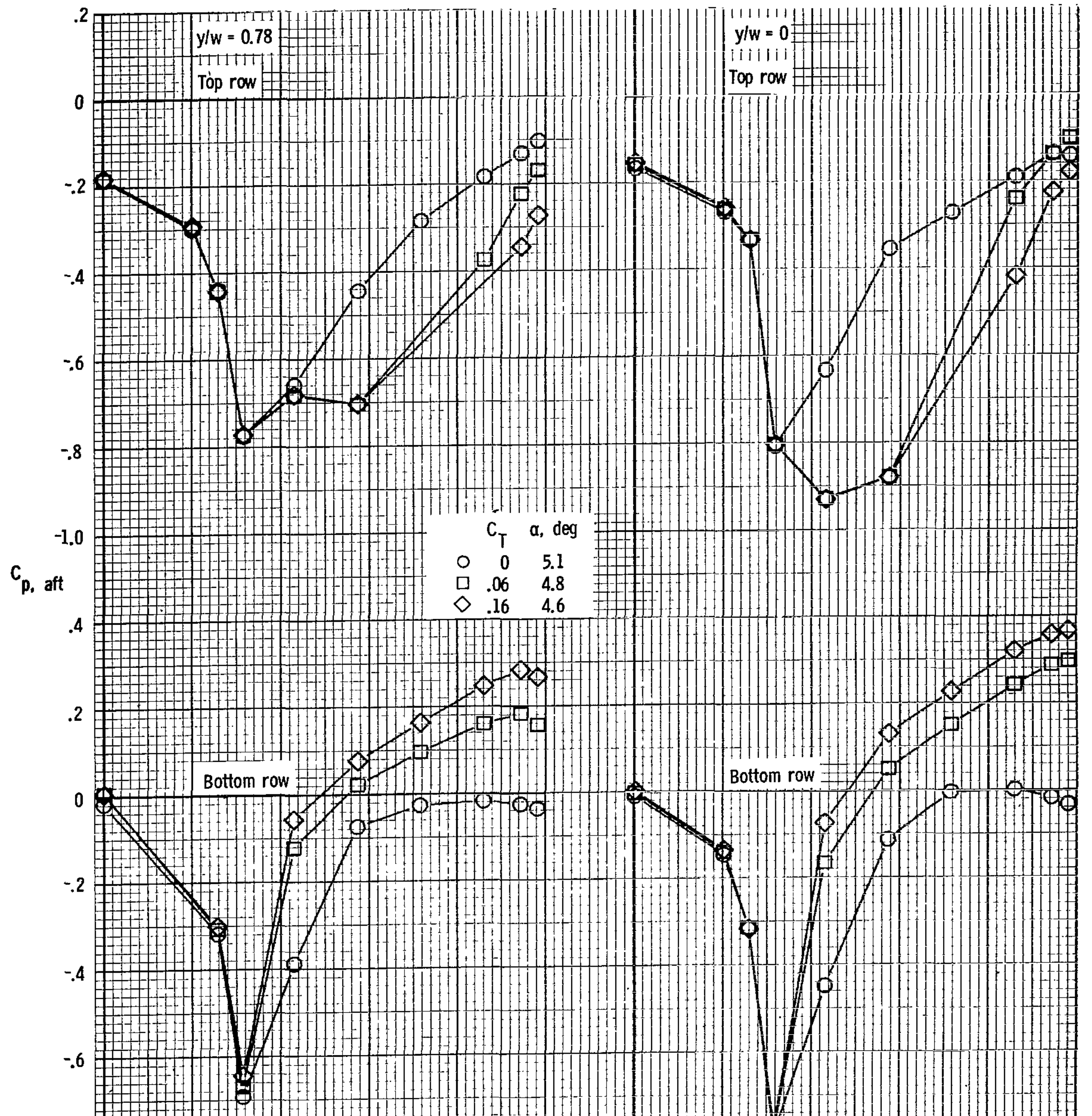

(i) M = 0.90; $\alpha \approx 4.8^{\circ}$.

Figure 27.- Concluded.

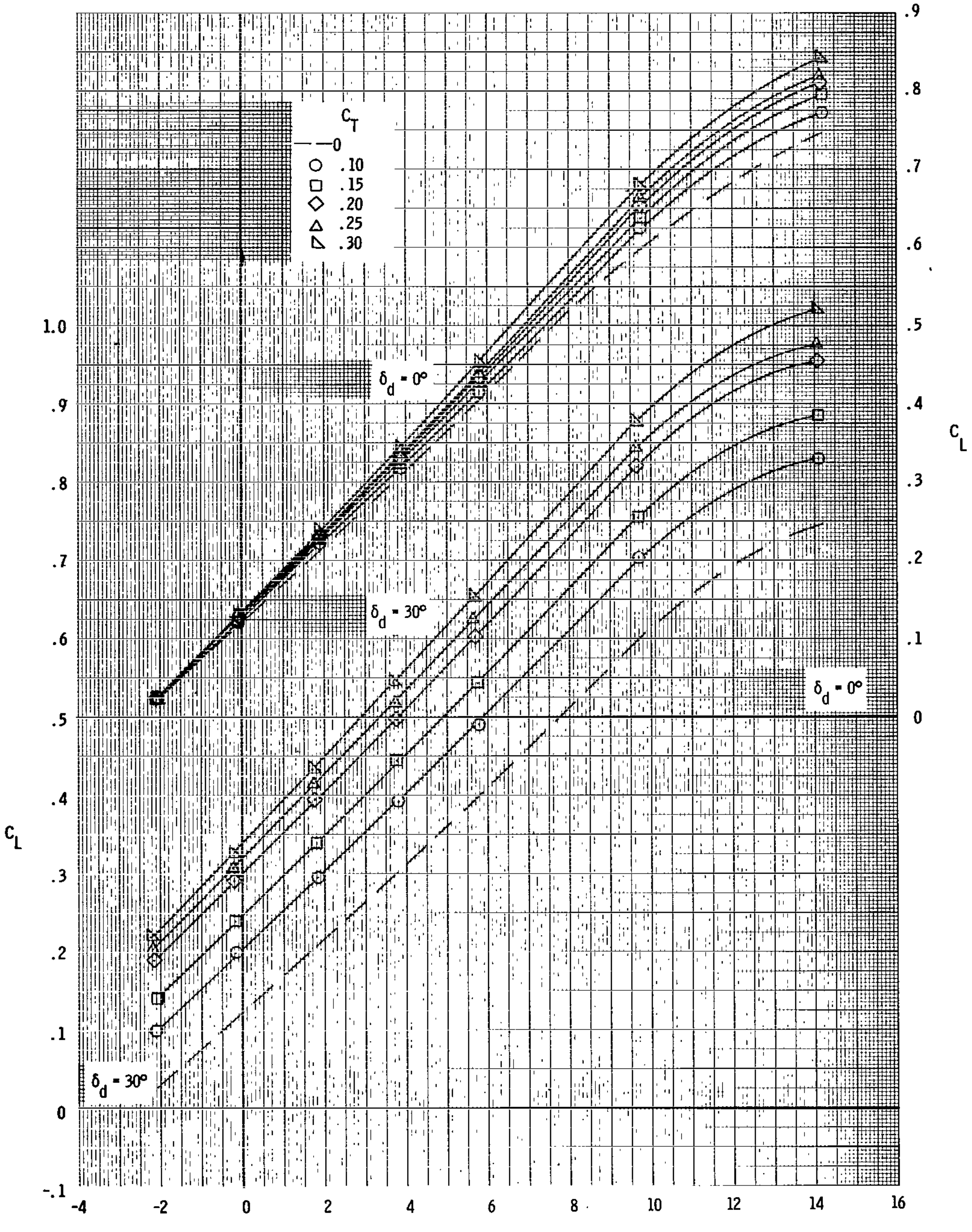

(a) M = 0.40.

Figure 28.- Variation of total lift with angle of attack at constant values of thrust coefficient for the nozzles tested.

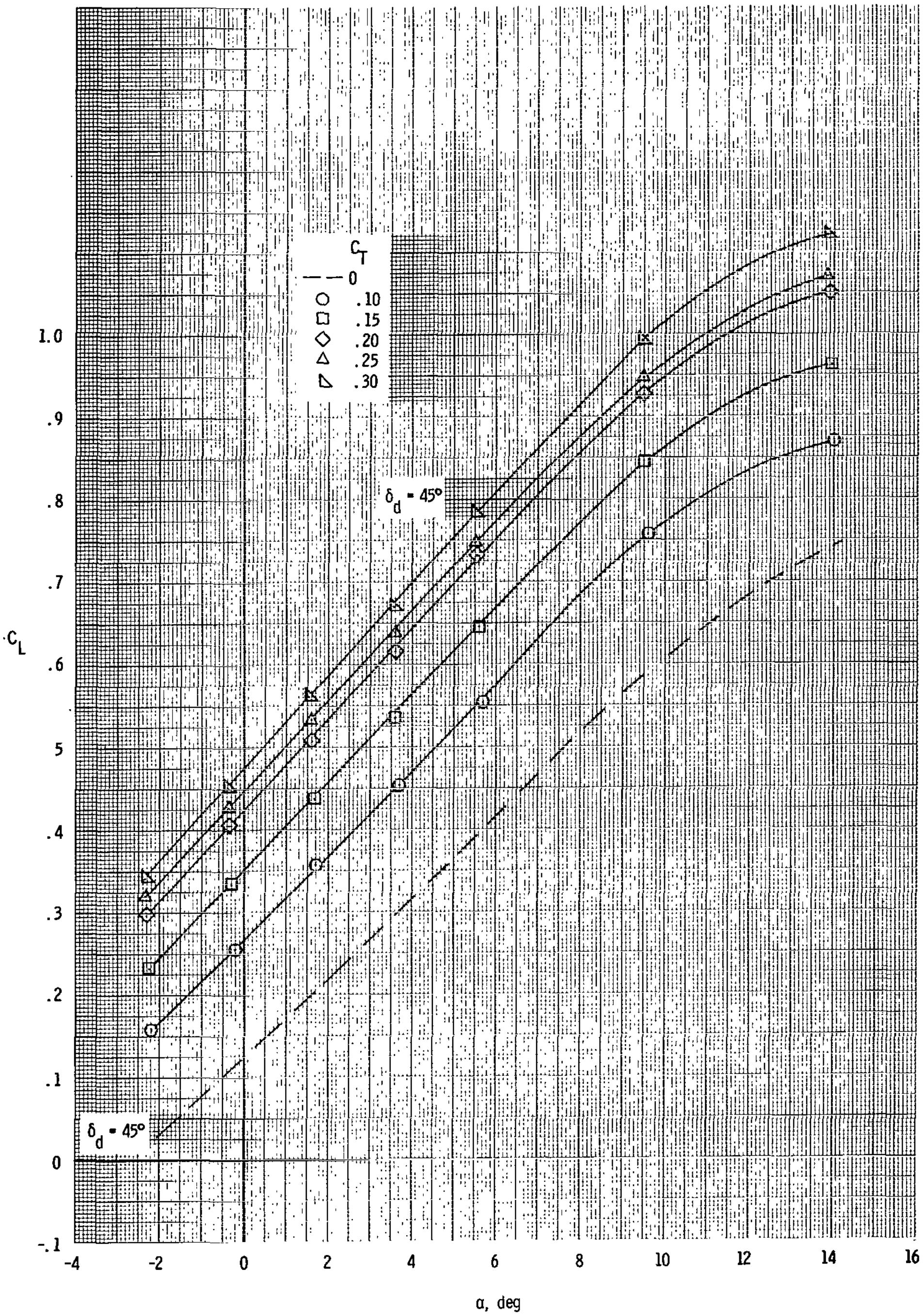

(a) Concluded.

Figure 28.- Continued.

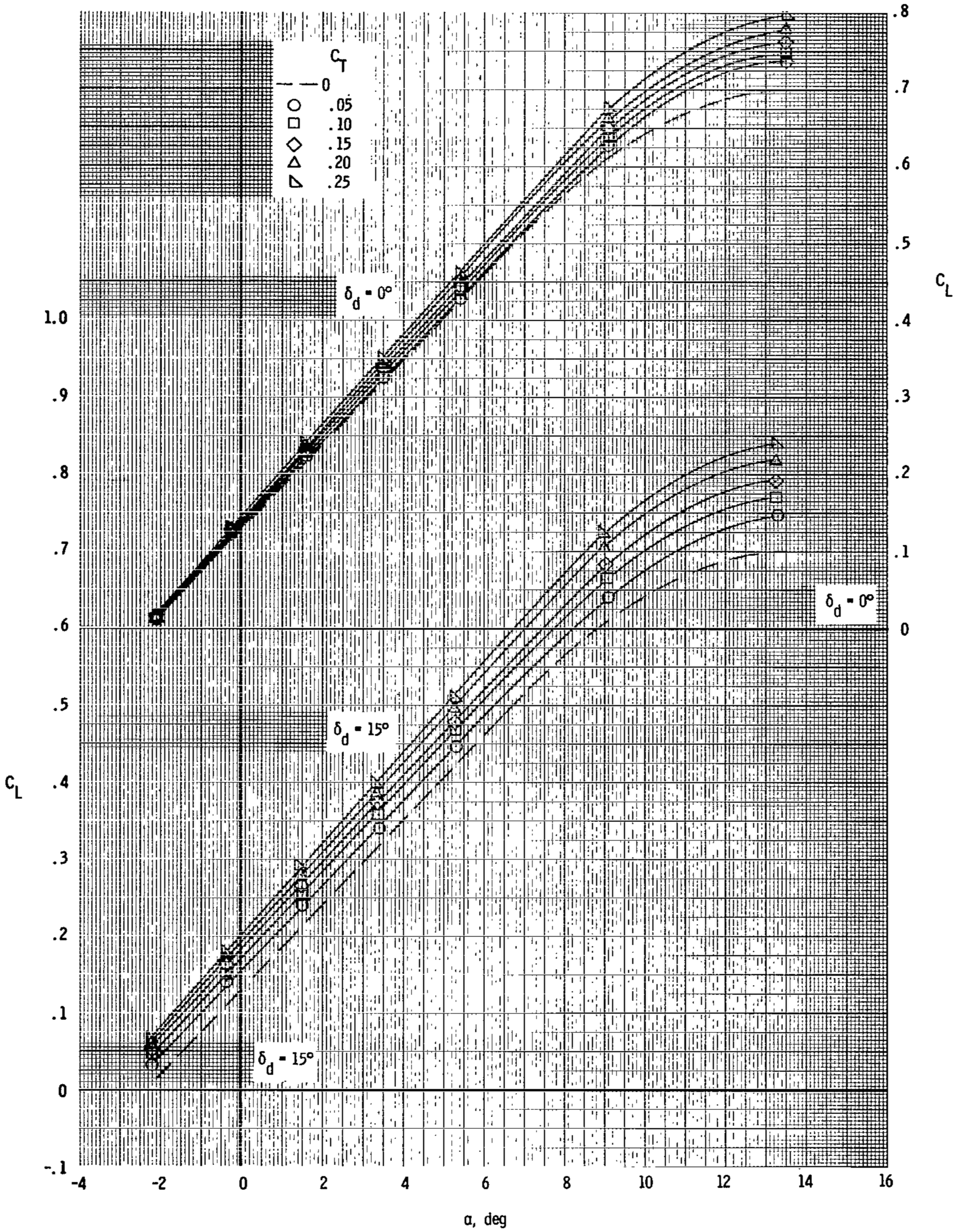

(b) M = 0.70.

Figure 28.- Continued.

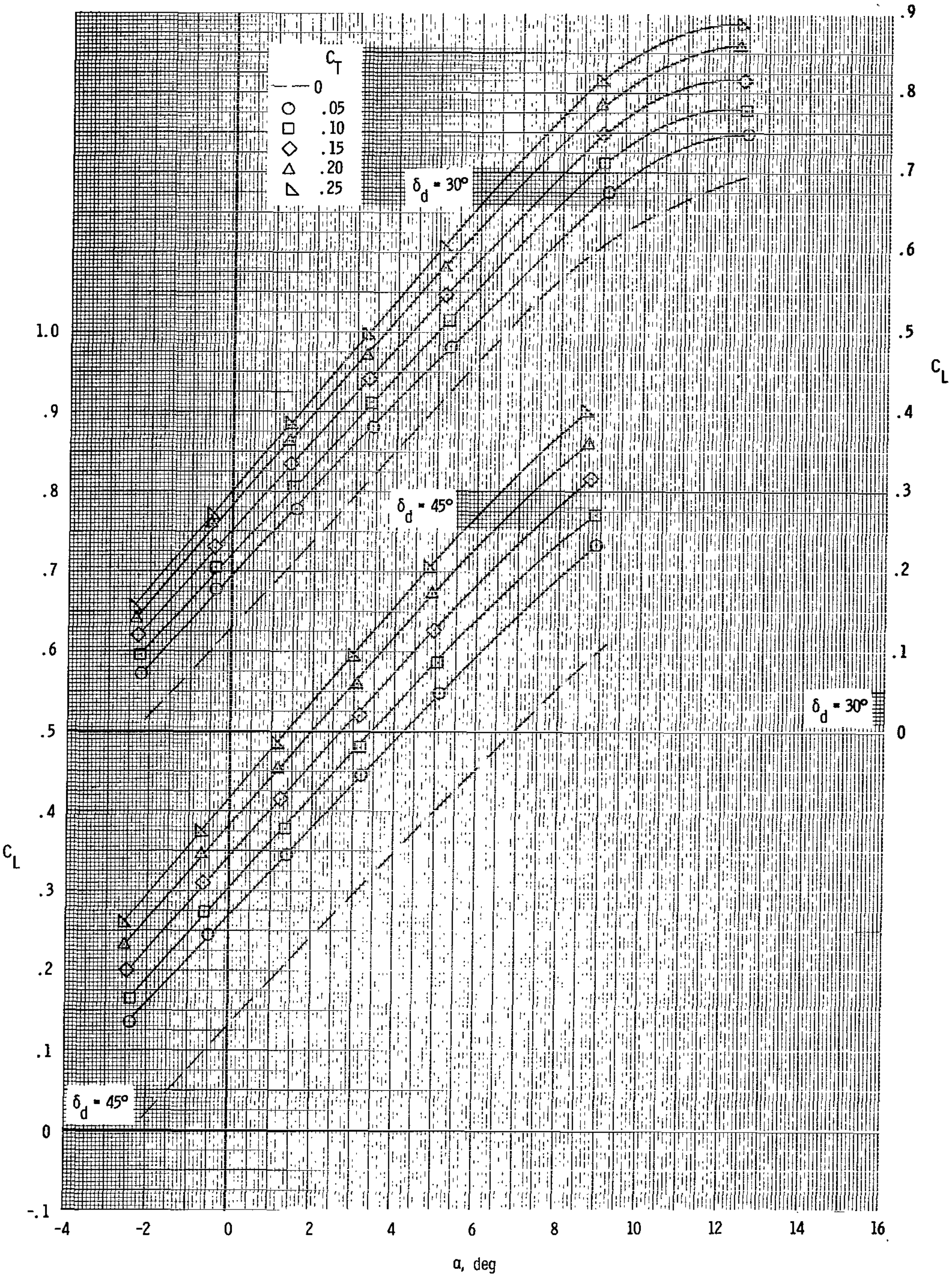

(b) Concluded.

Figure 28.- Continued.

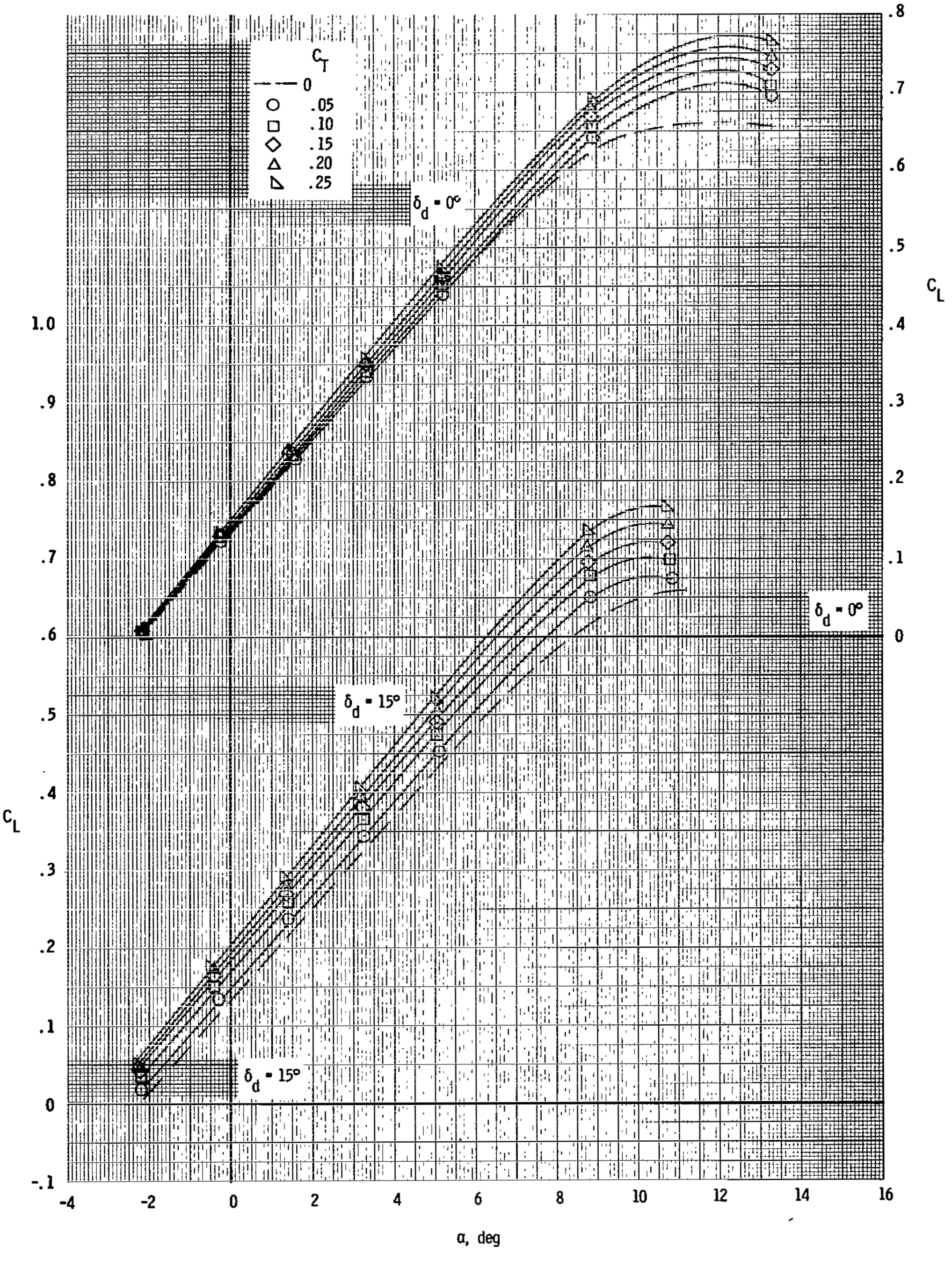

(c) M = 0.80.

Figure 28.- Continued.

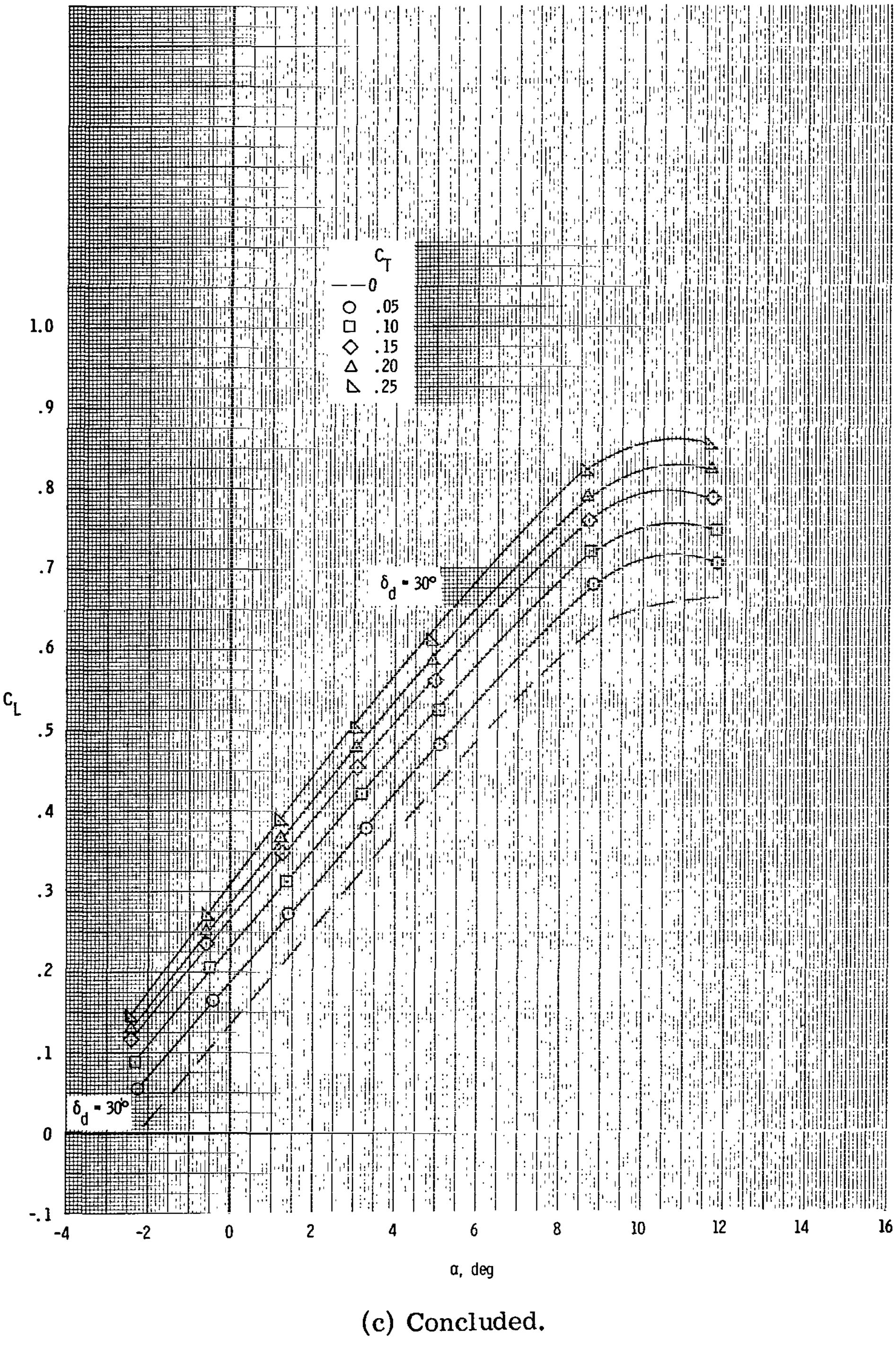

(c) Concluded.

Figure 28.- Continued.

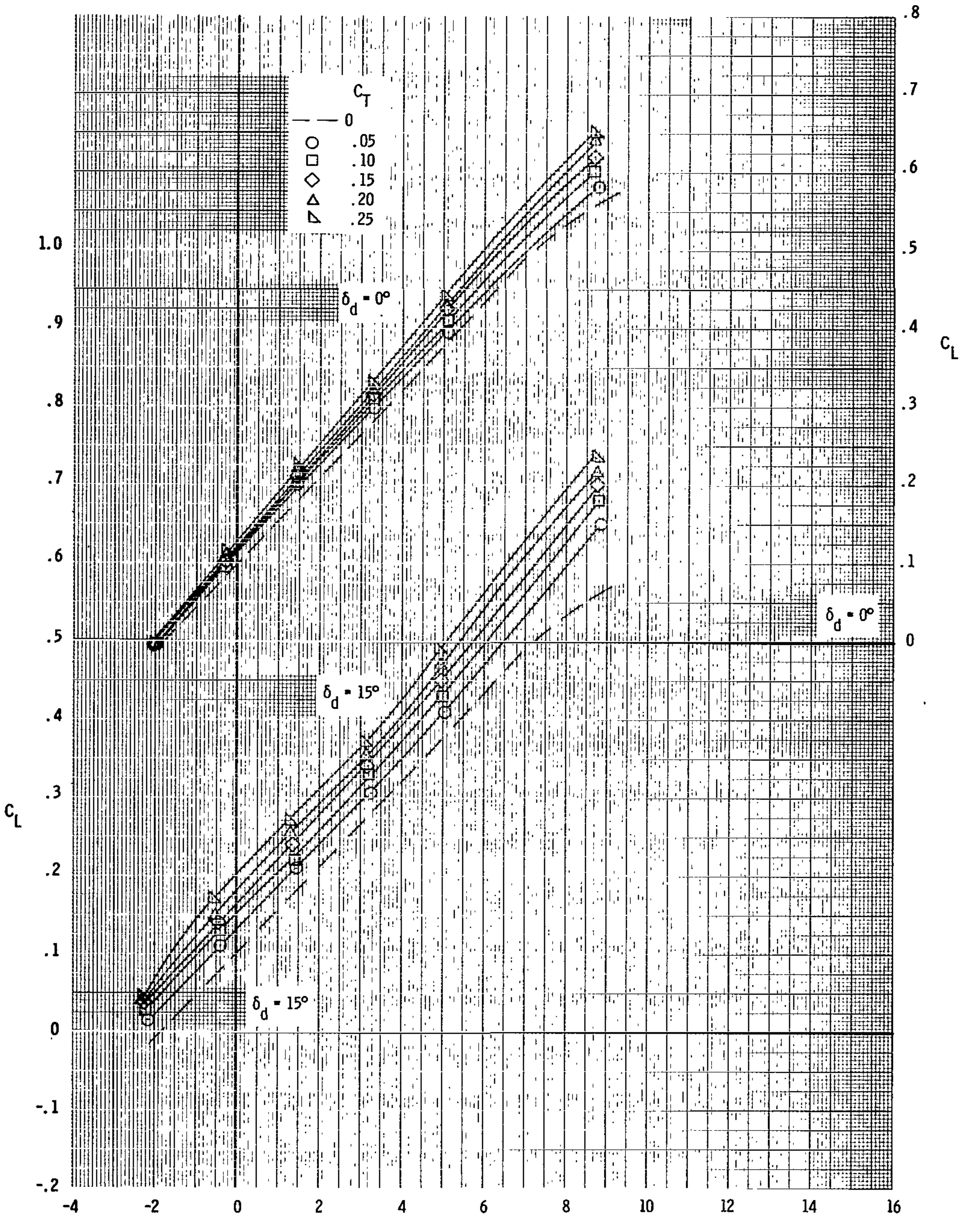

(d) M = 0.90.

Figure 28.- Continued.

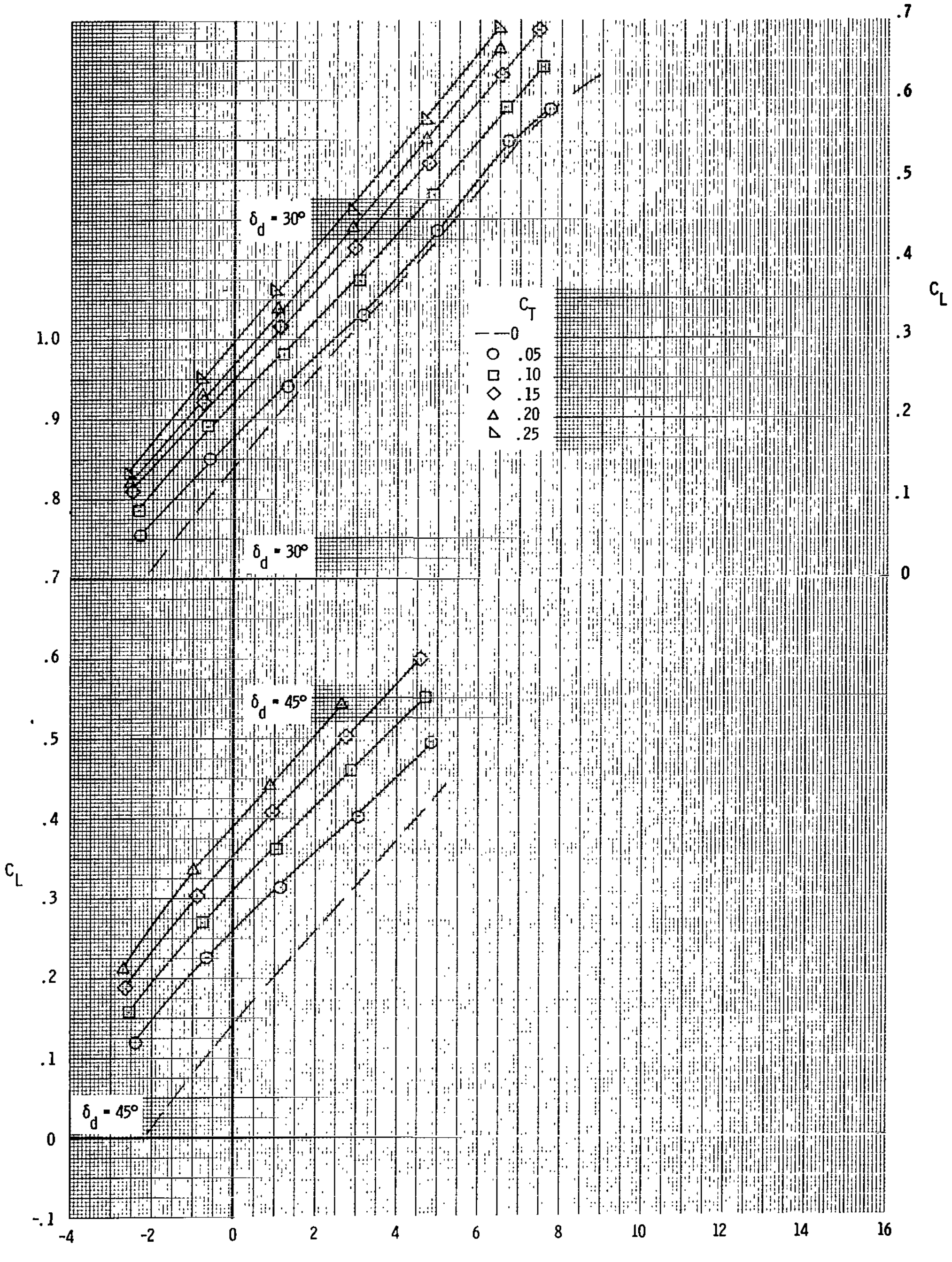

(d) Concluded.

Figure 28.- Continued.

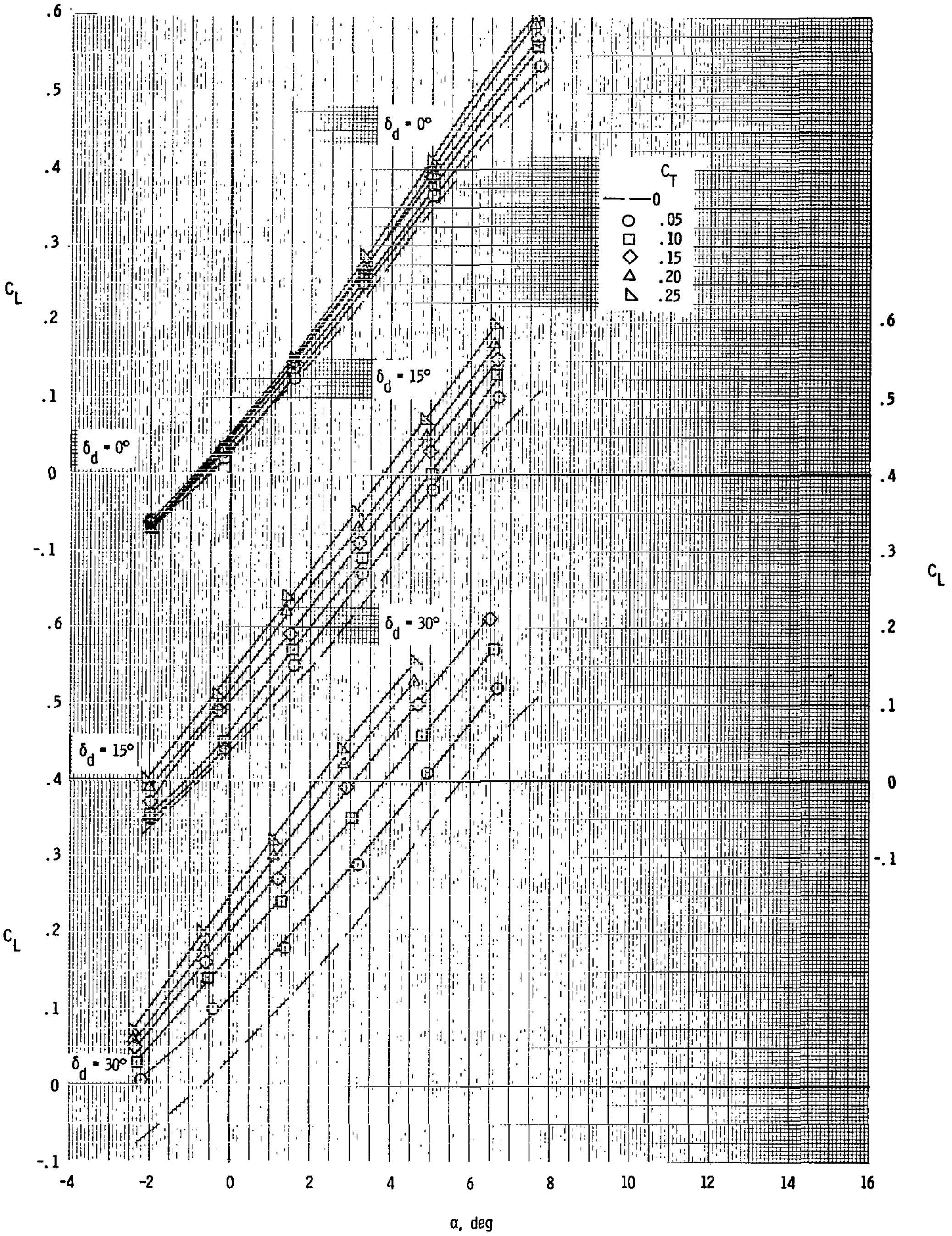

(e) M = 0.95.

Figure 28.- Continued.

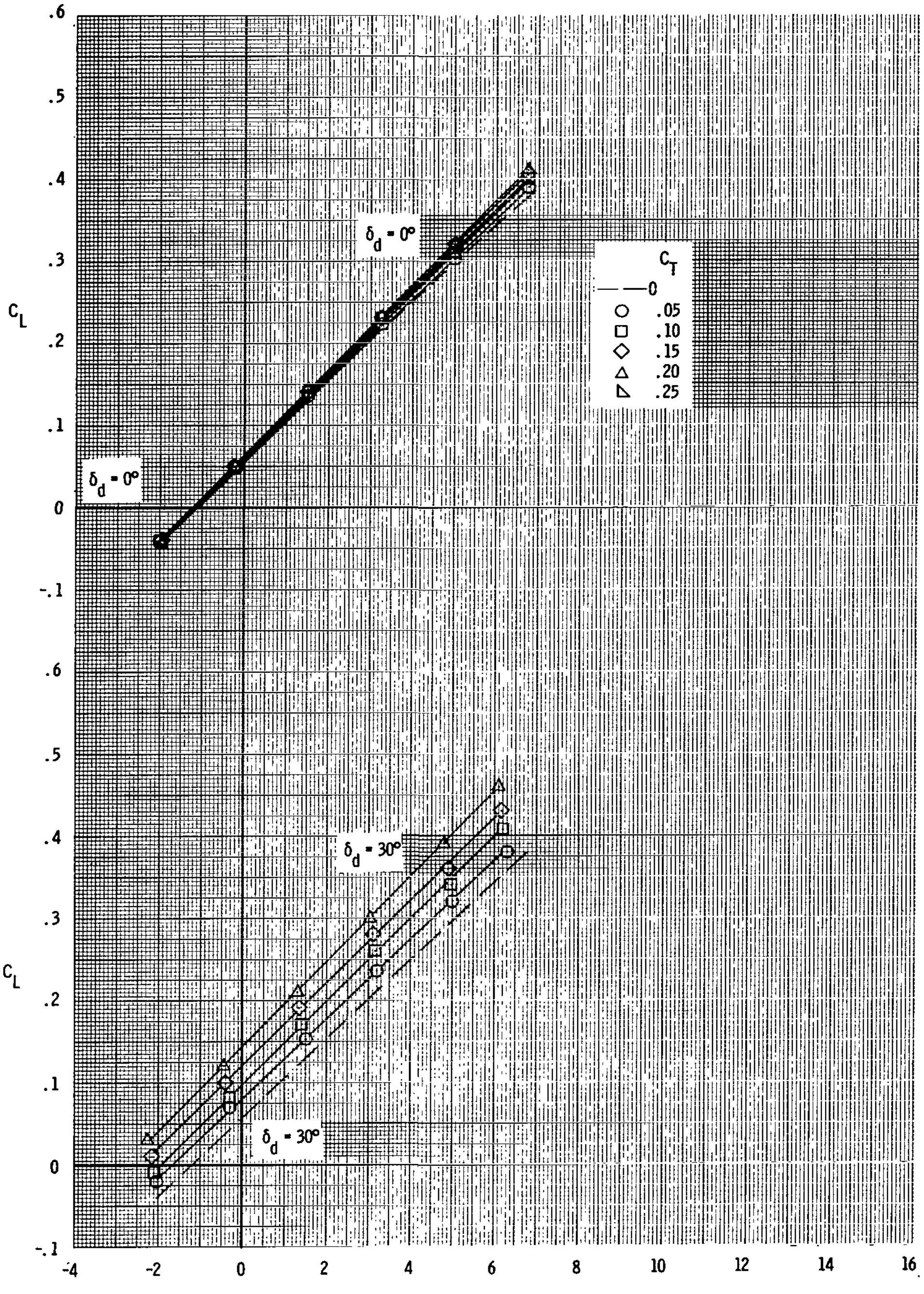

(f) M = 1.20.

Figure 28.- Concluded.

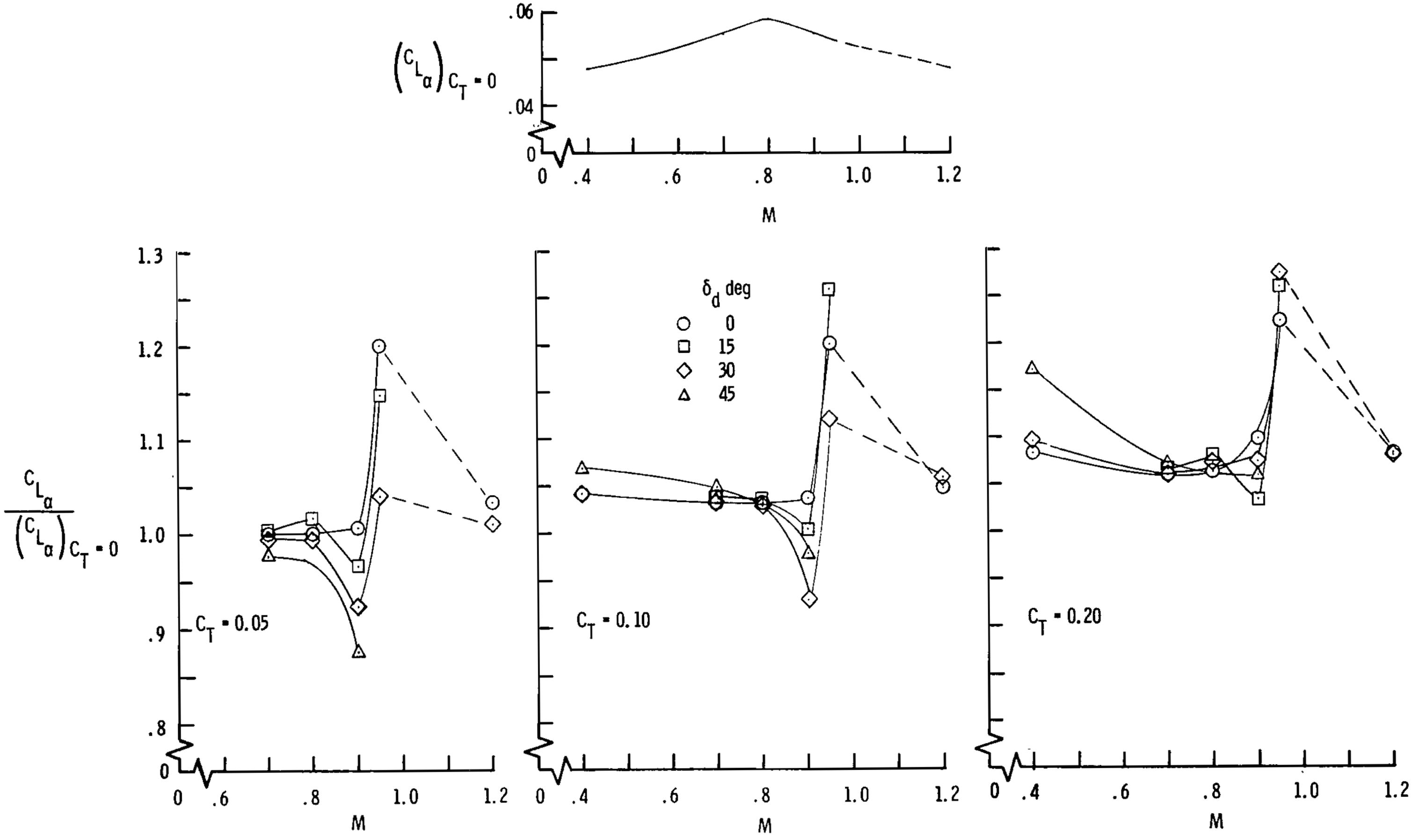

Figure 29.- Variation of lift-curve-slope ratio with Mach number for various nozzles at selected thrust coefficients.

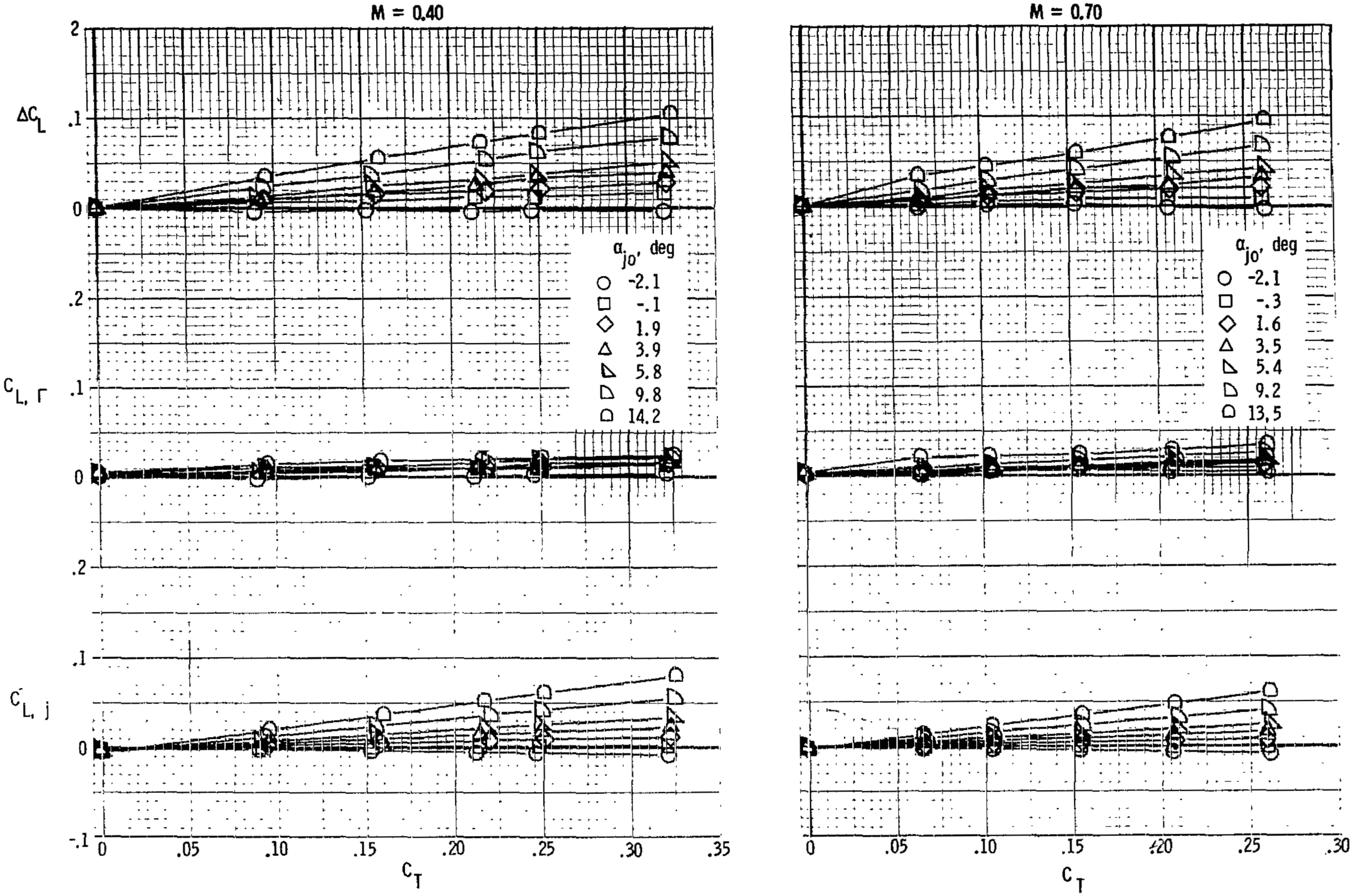

(a) M = 0.40 and 0.70.

Figure 30.- Jet lift, induced lift, and incremental lift characteristics. $\delta_d = 0^o$.

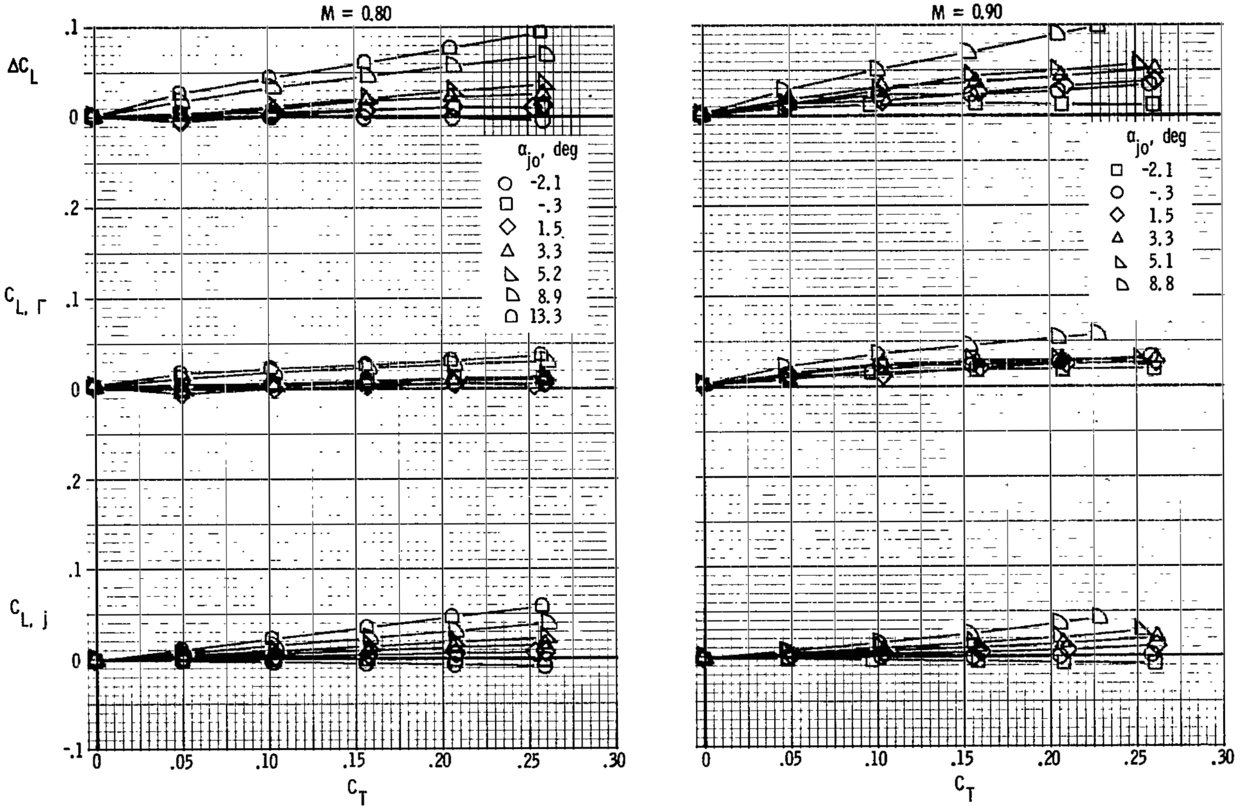

(b) M = 0.80 and 0.90.

Figure 30.- Continued.

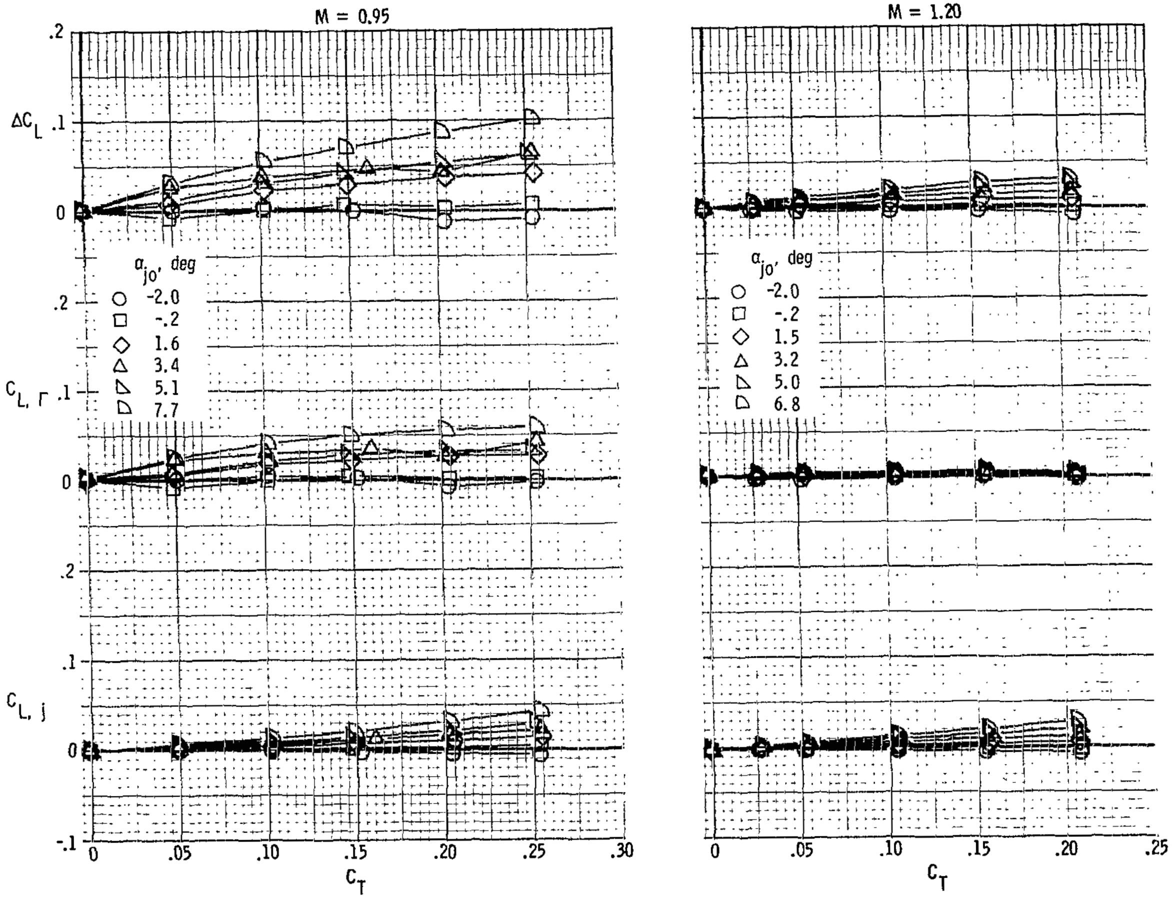

(c) M = 0.95 and 1.20.

Figure 30.- Concluded.

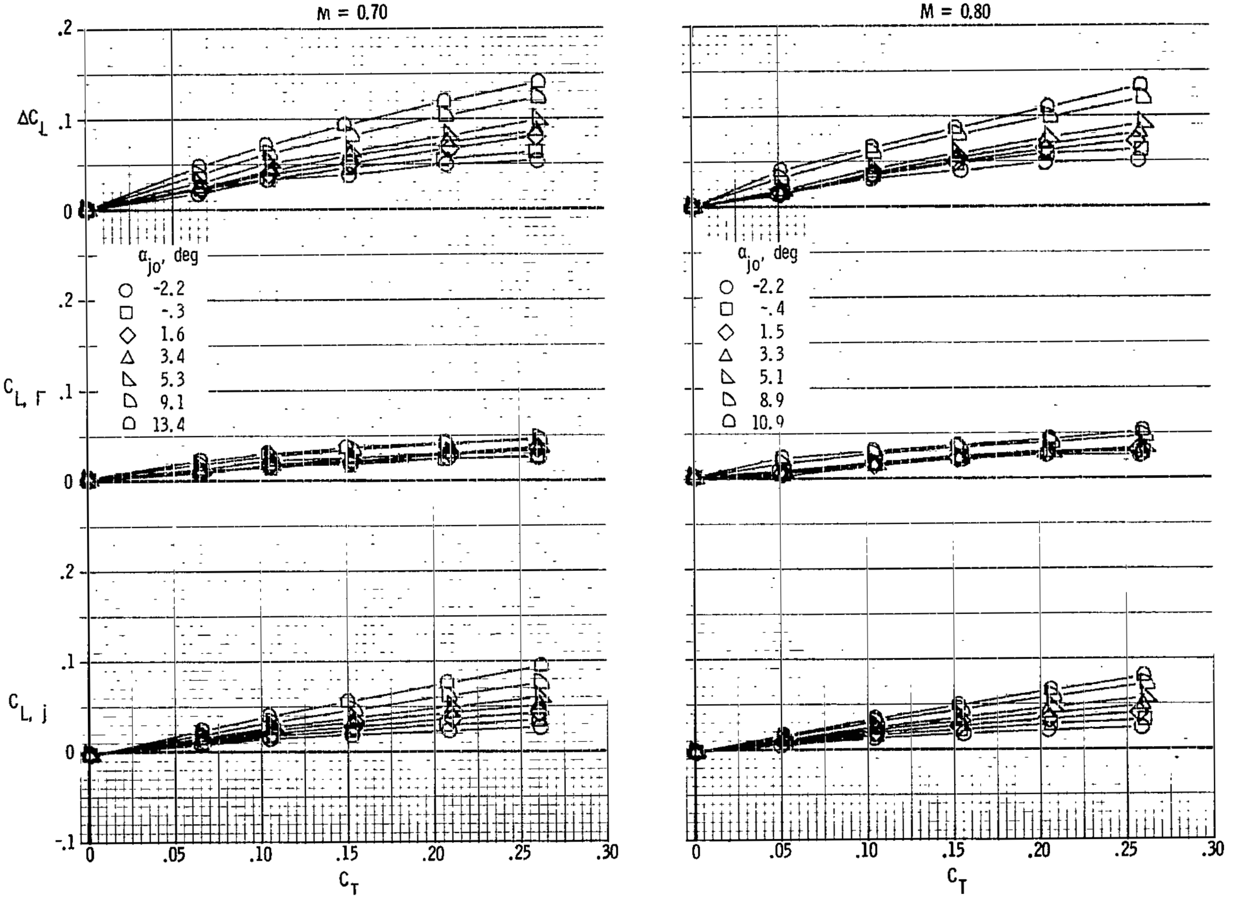

(a) M = 0.70 and 0.80.

Figure 31.- Jet lift, induced lift, and incremental lift characteristics. $\delta_d = 15^{\circ}$.

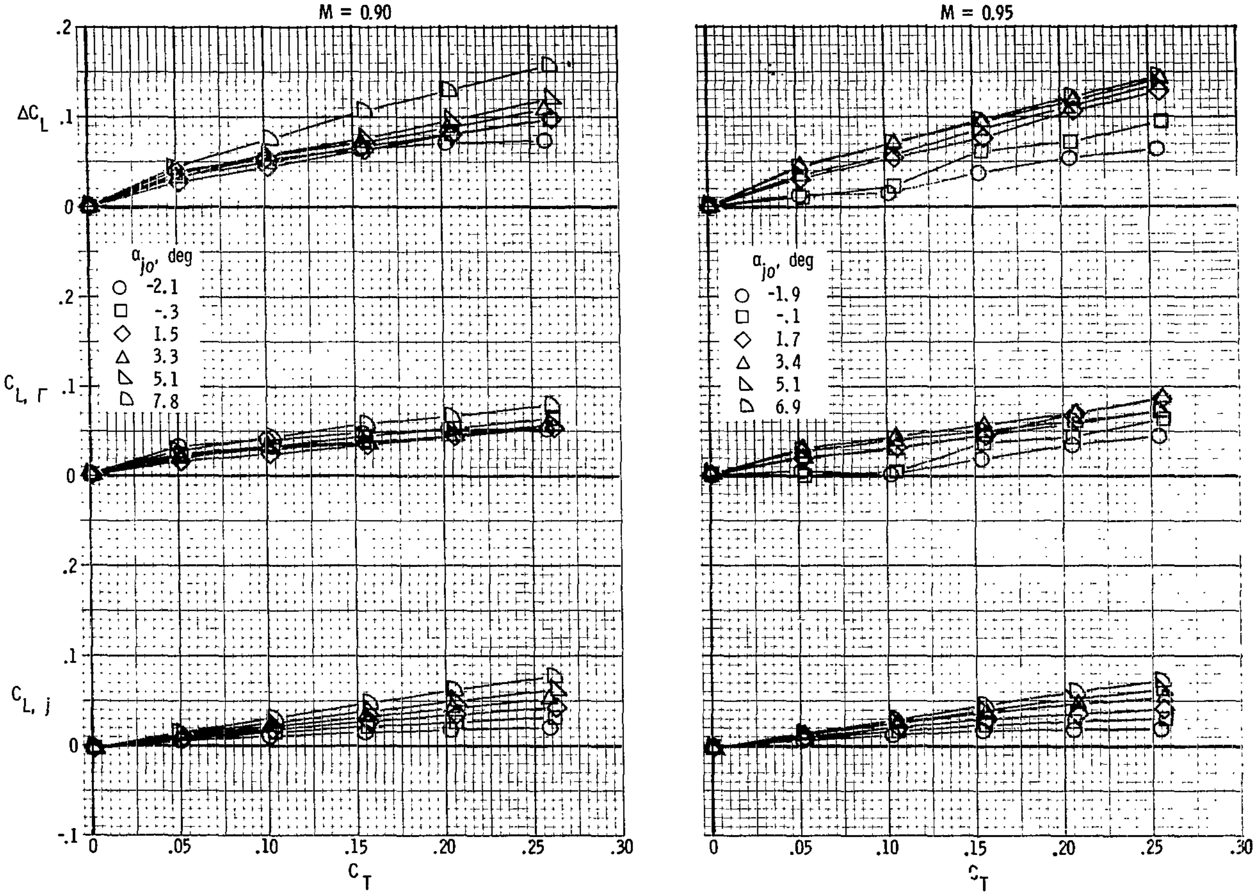

(b) M = 0.90 and 0.95.

Figure 31.- Concluded.

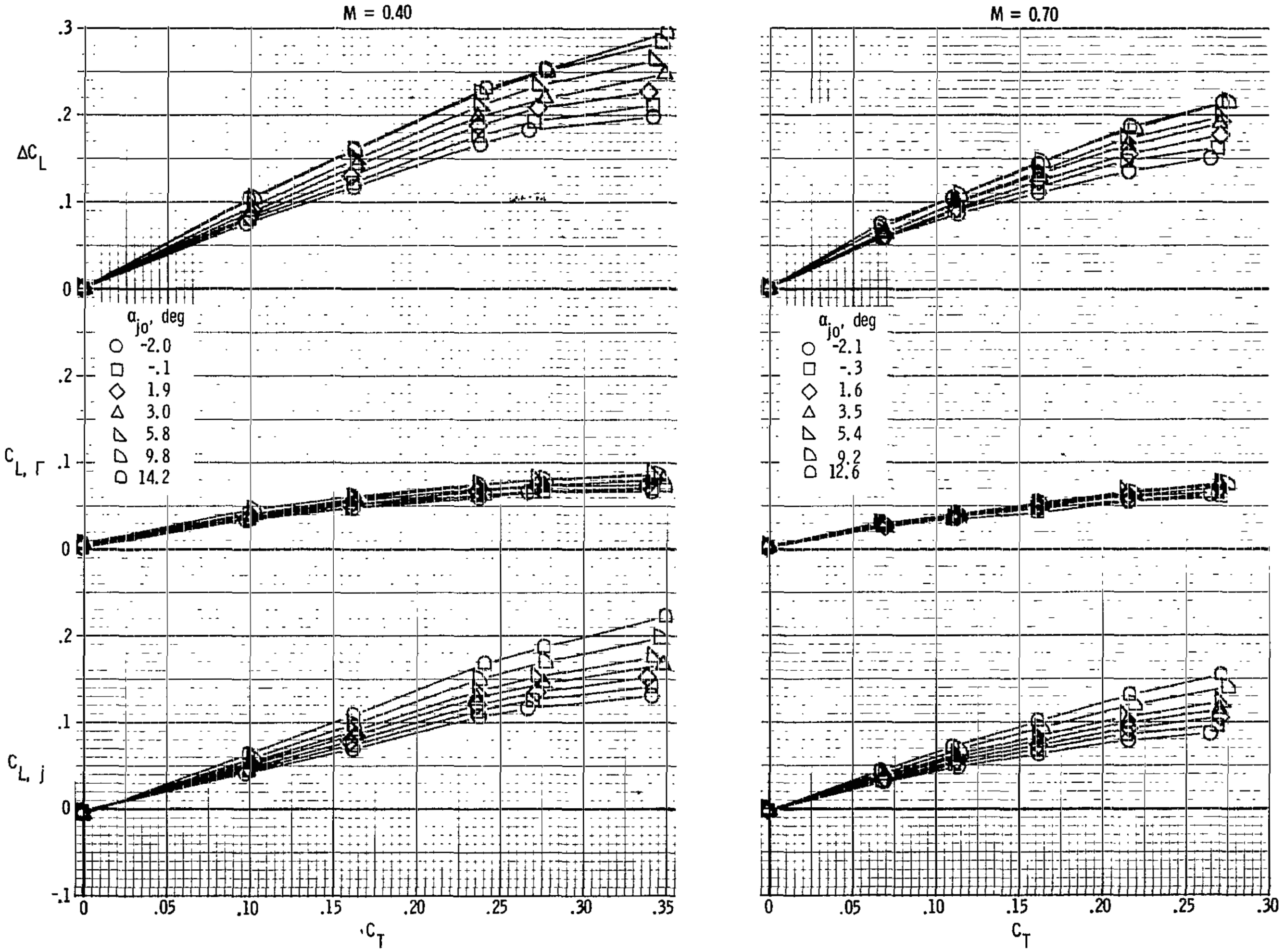

(a) M = 0.40 and 0.70.

Figure 32.- Jet lift, induced lift, and incremental lift characteristics. $\delta_d = 30^o$.

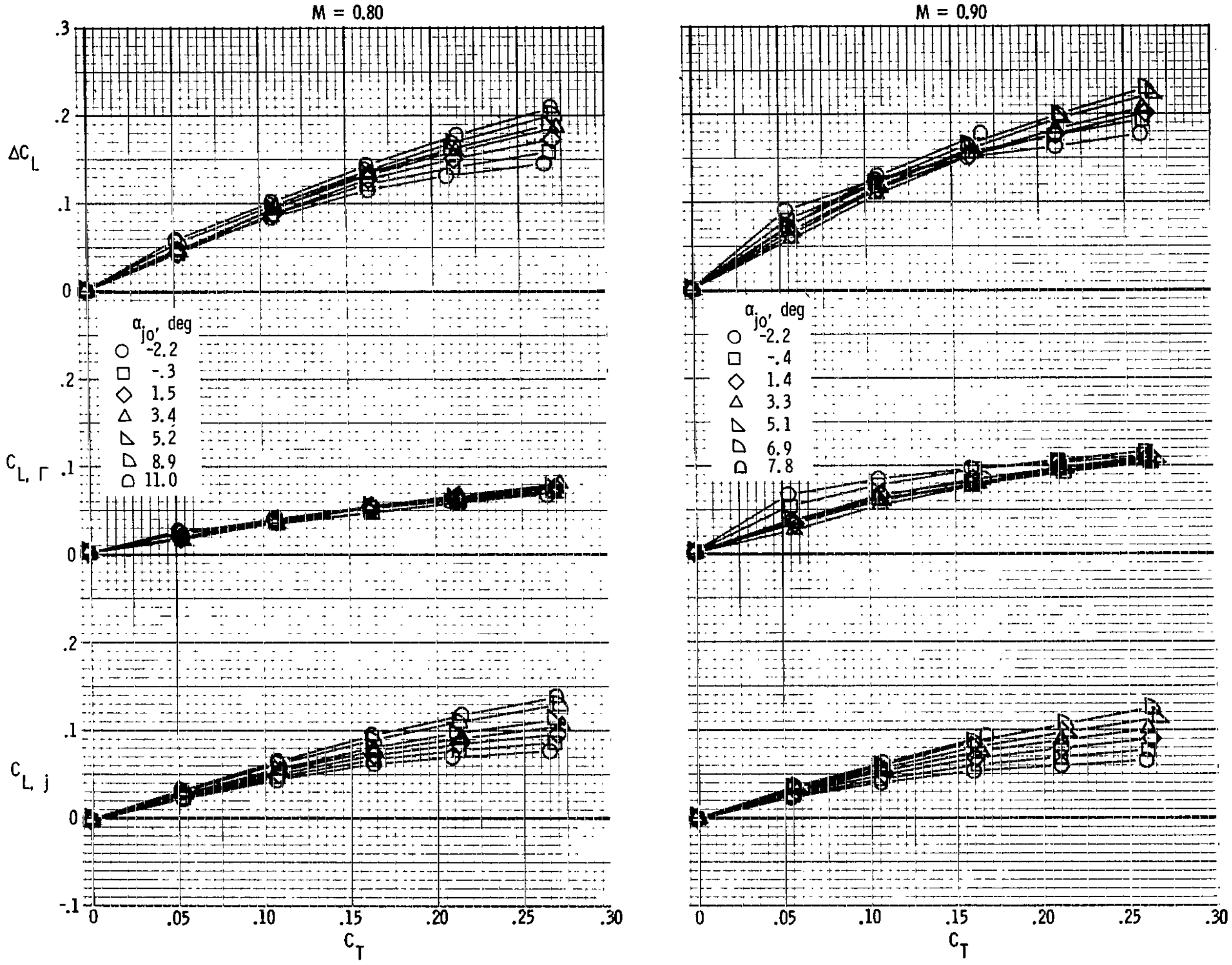

(b) M = 0.80 and 0.90.

Figure 32.- Continued.

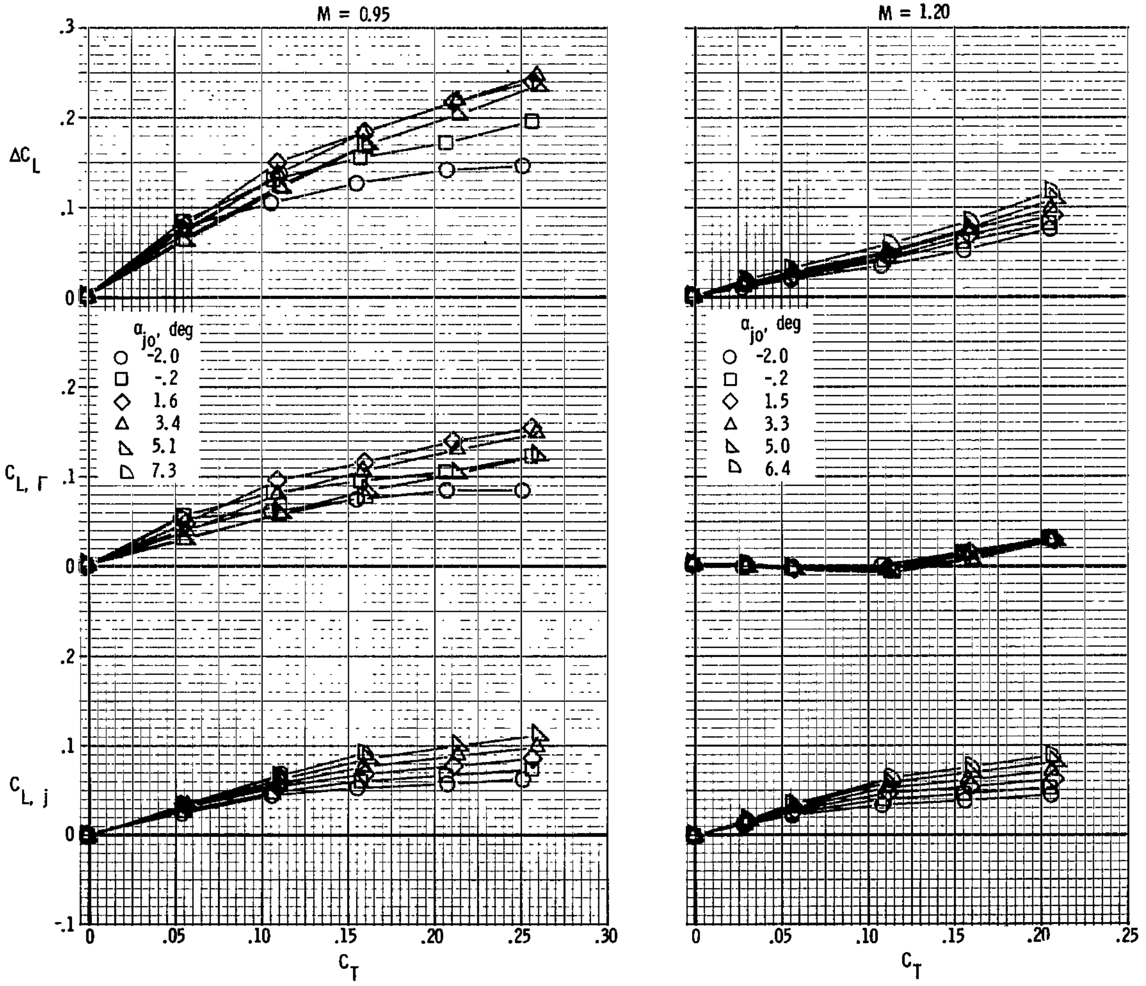

(c) M = 0.95 and 1.20.

Figure 32. - Concluded.

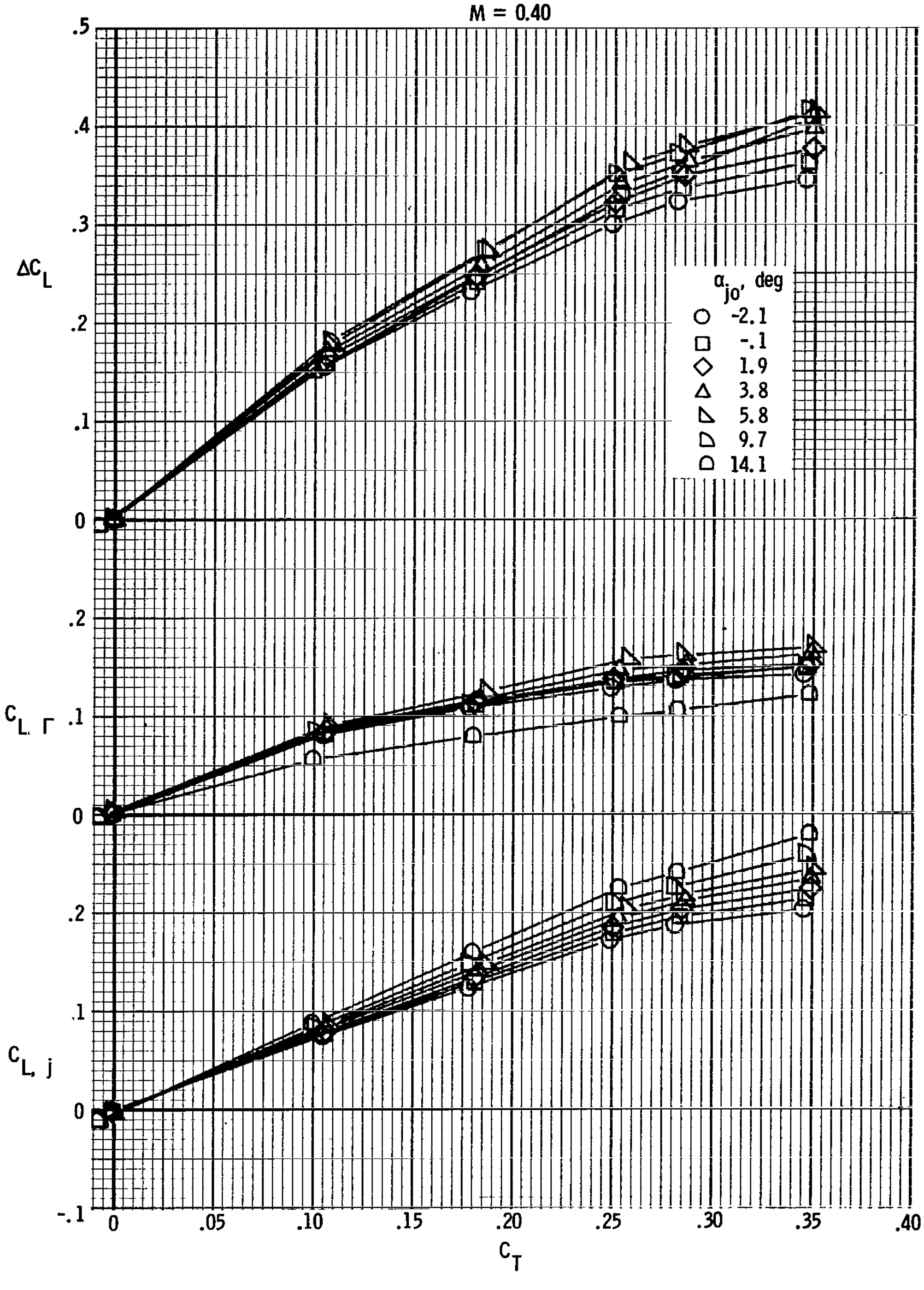

(a) M = 0.40.

Figure 33.- Jet lift, induced lift, and incremental lift characteristics. $\delta_d = 45^\circ$.

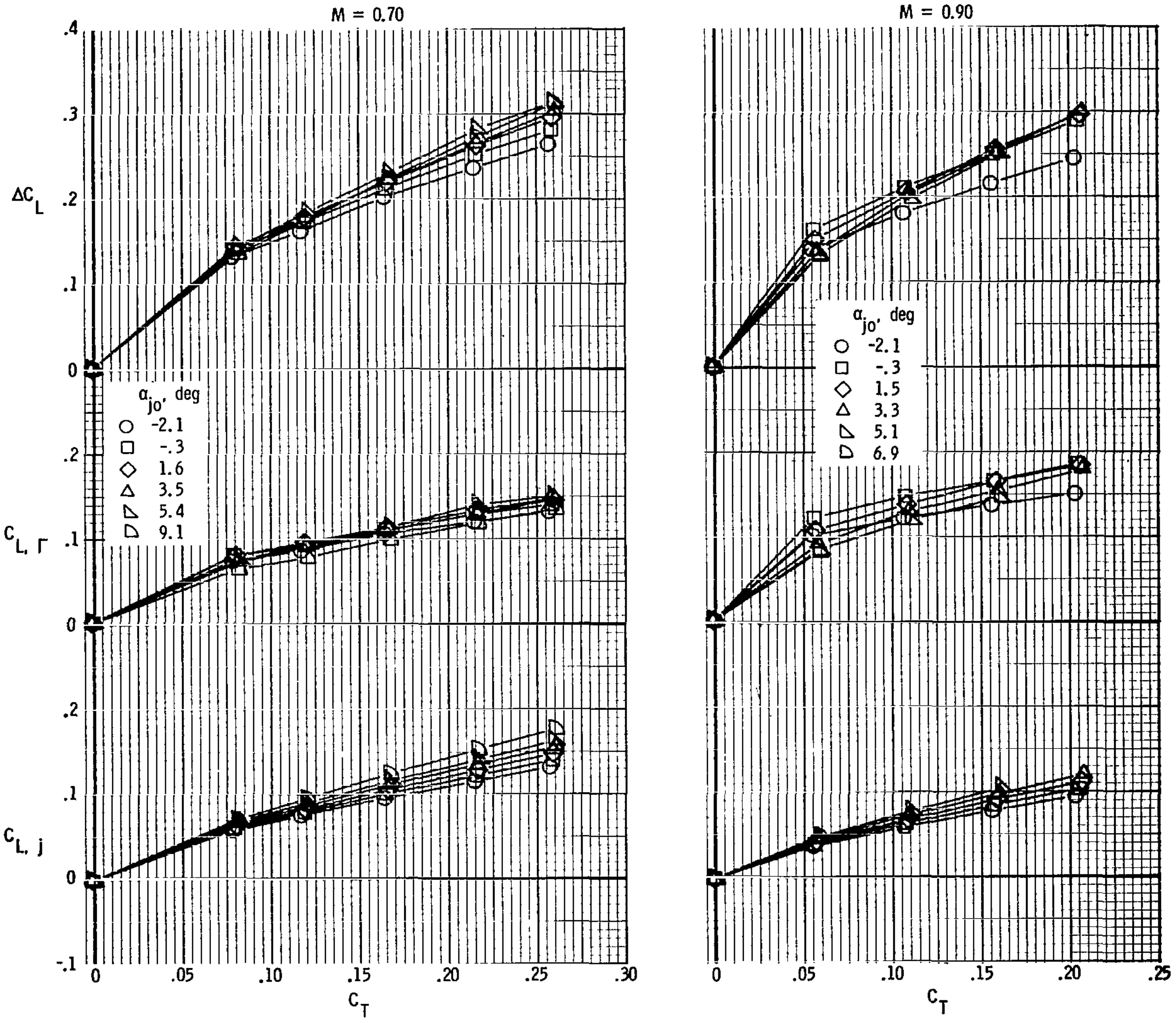

(b) M = 0.70 and 0.90.

Figure 33.- Concluded.

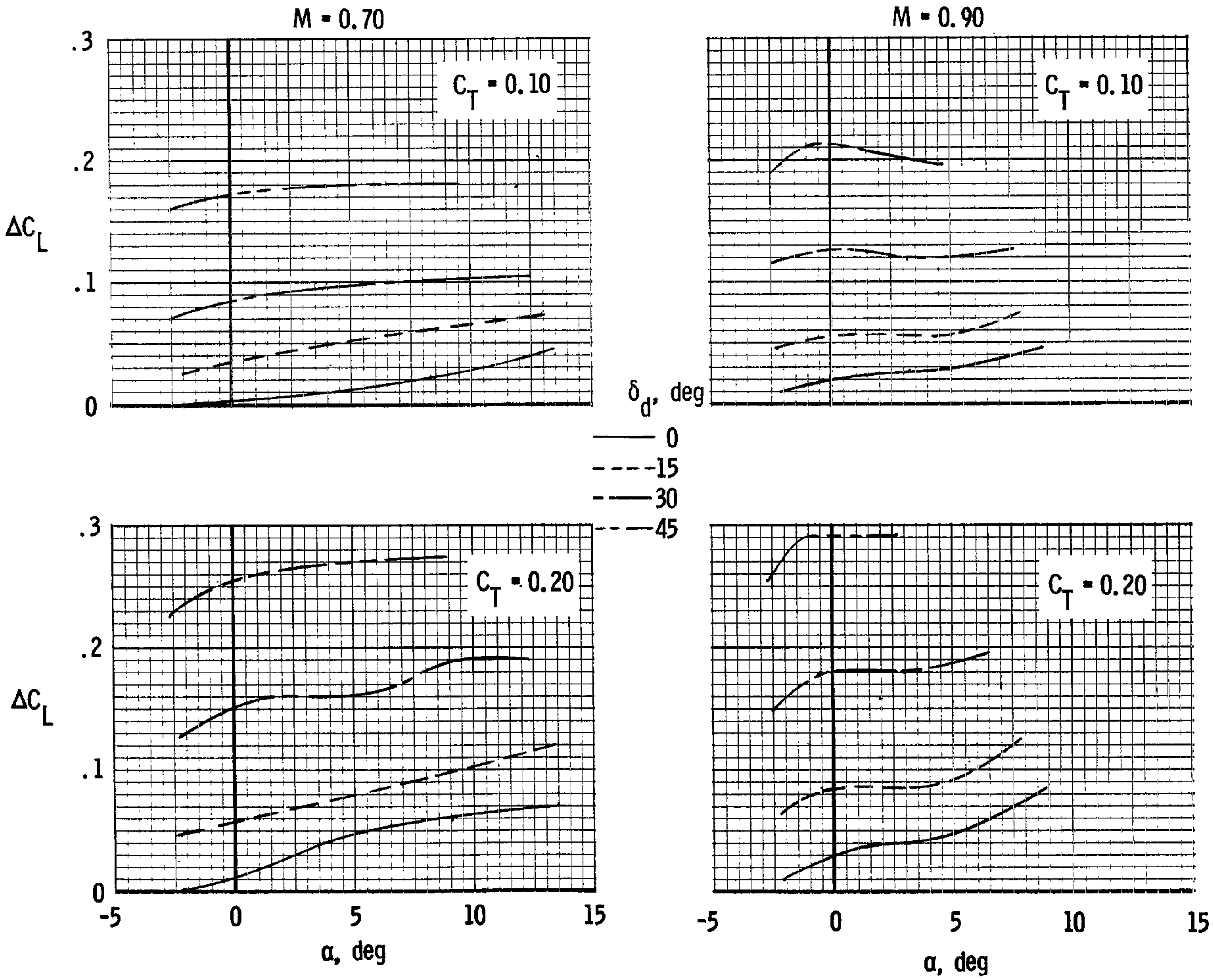

Figure 34.- Typical variation of incremental lift with angle of attack for selected thrust coefficients and Mach numbers.

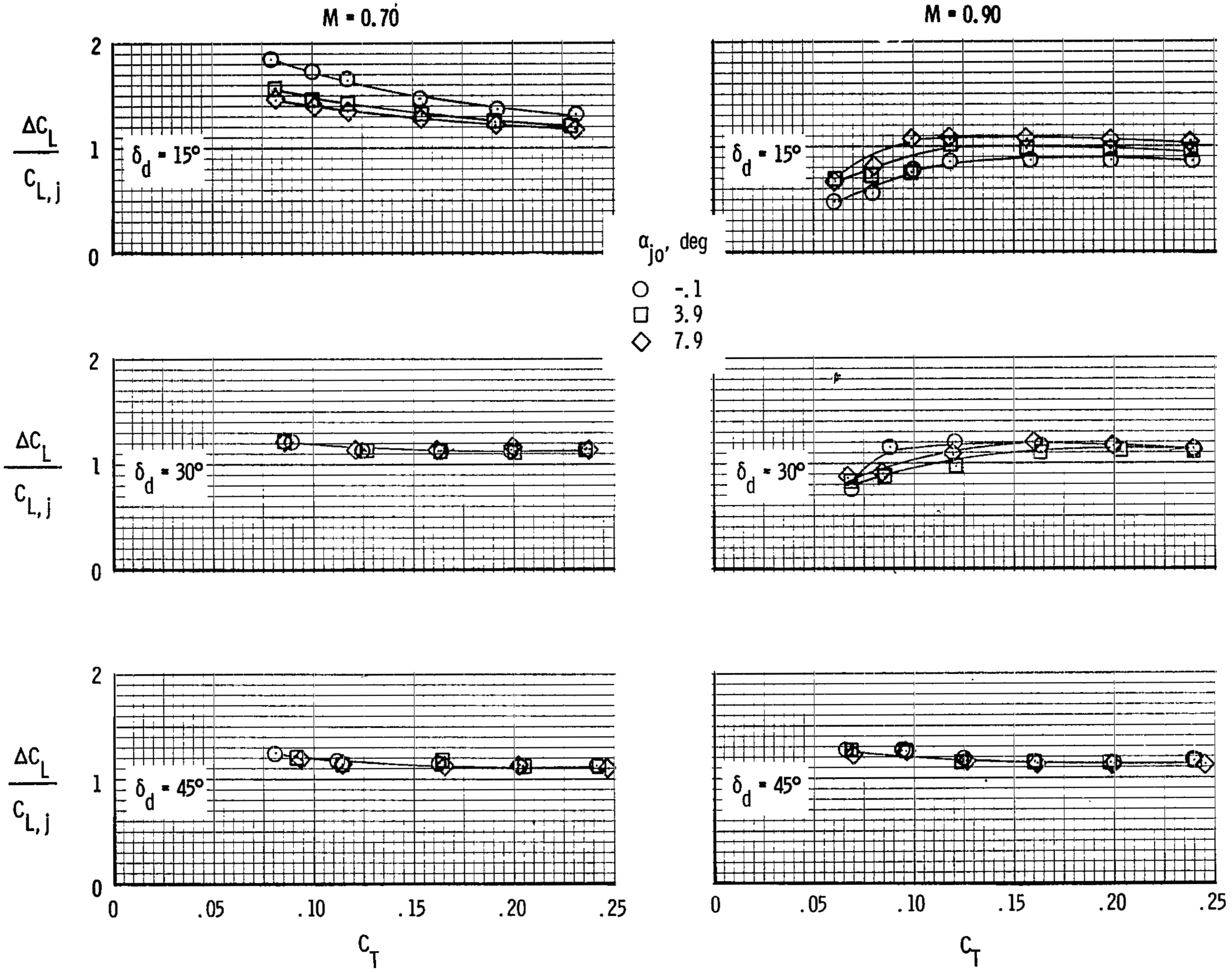

Figure 35.- Variation of lift-augmentation ratio with thrust coefficient. Wings off.

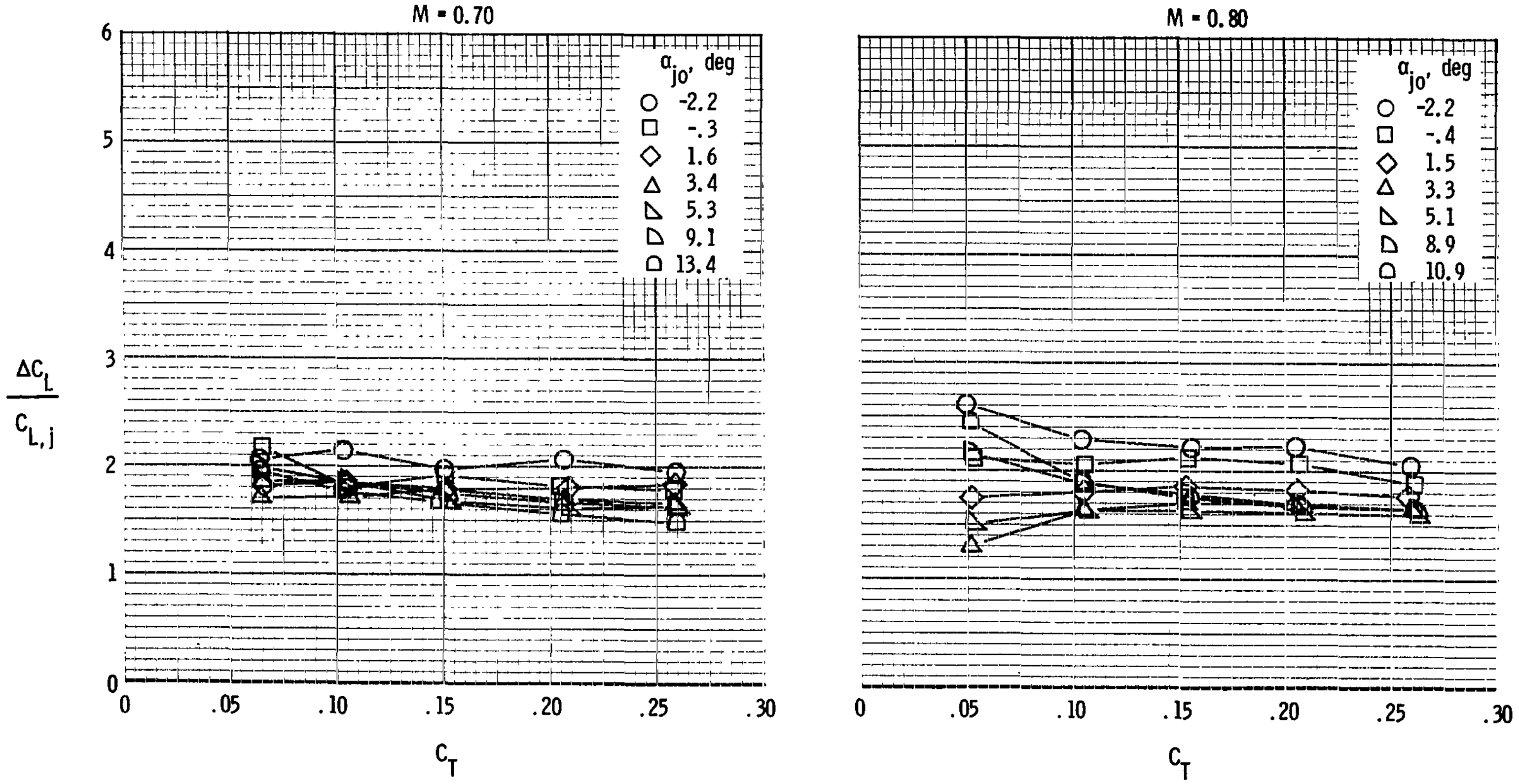

(a) M = 0.70 and 0.80.

Figure 36.- Variation of lift-augmentation ratio with thrust coefficient. $\delta_d = 15^o$.

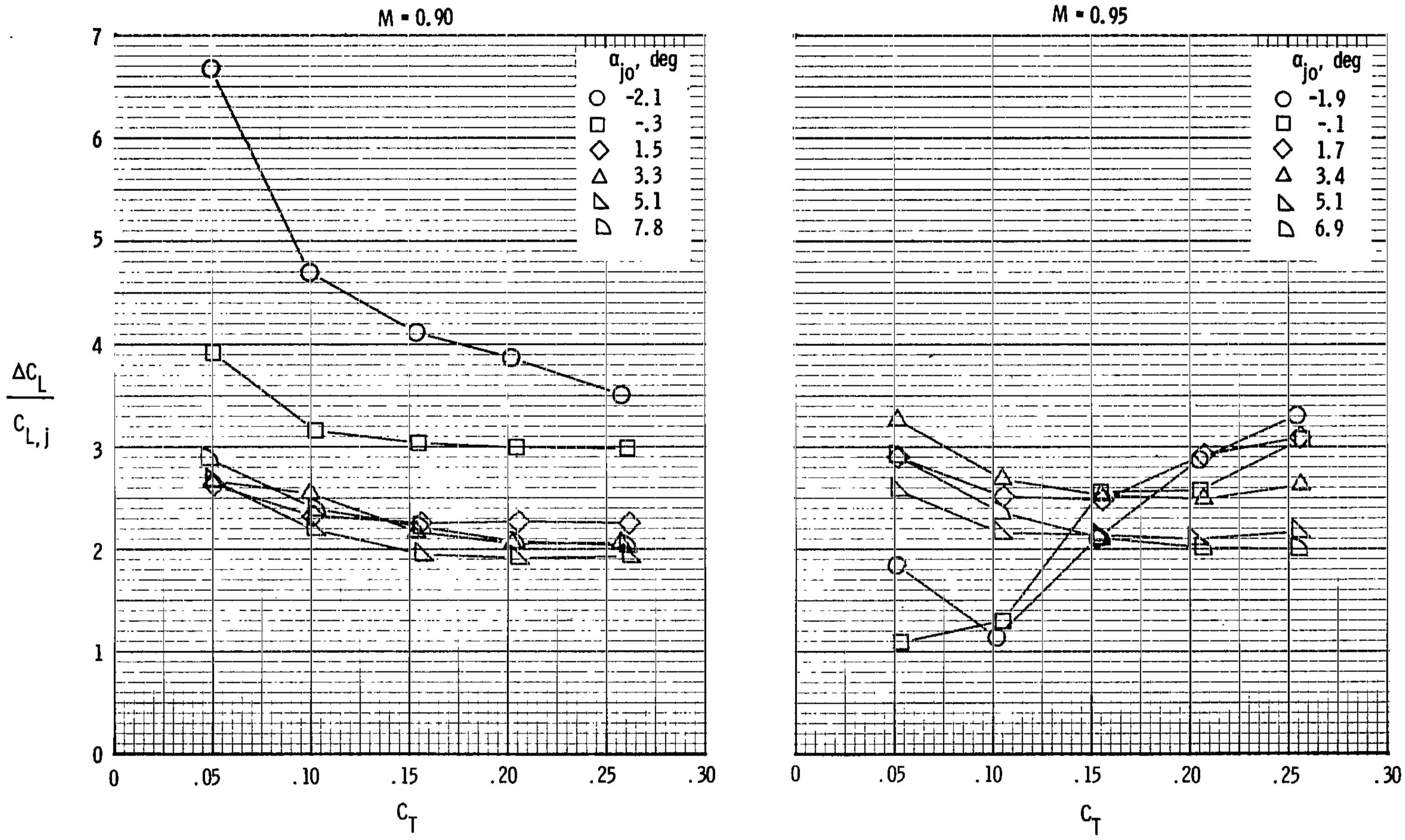

(b) M = 0.90 and 0.95.

Figure 36.- Concluded.

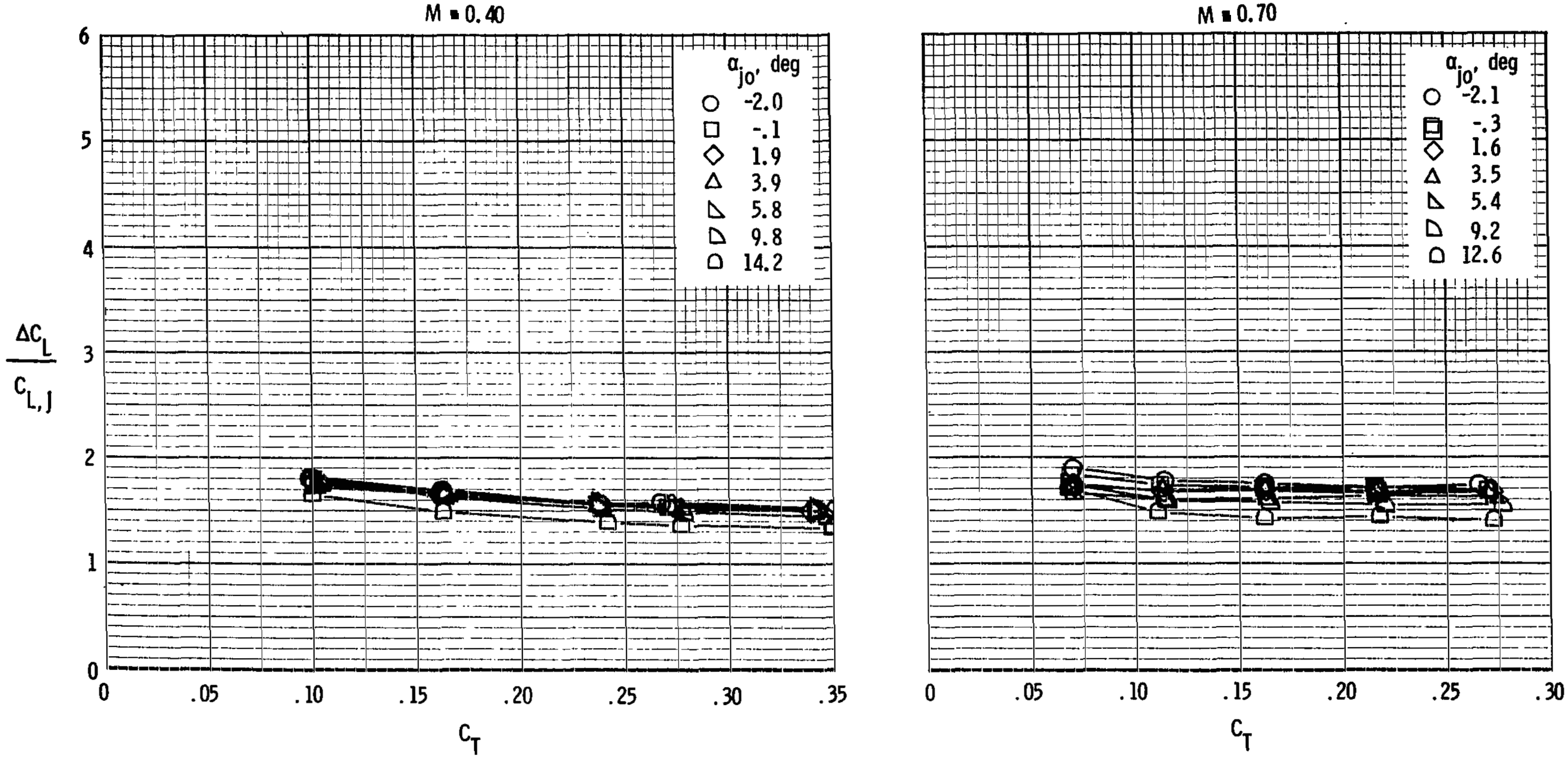

(a) M = 0.40 and 0.70.

Figure 37.- Variation of lift-augmentation ratio with thrust coefficient. $\delta_d = 30^{\circ}$.

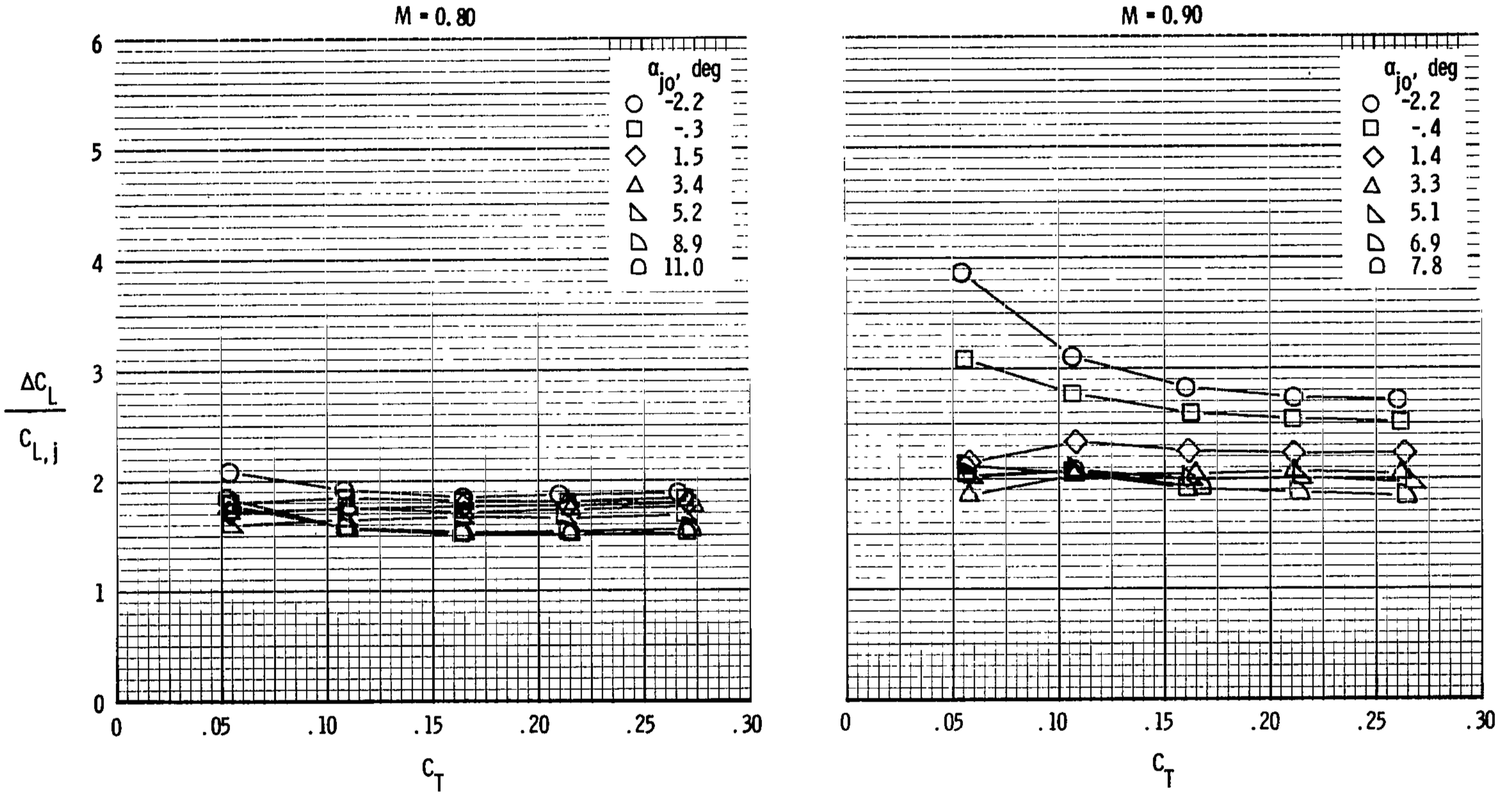

(b) M = 0.80 and 0.90.

Figure 37.- Continued.

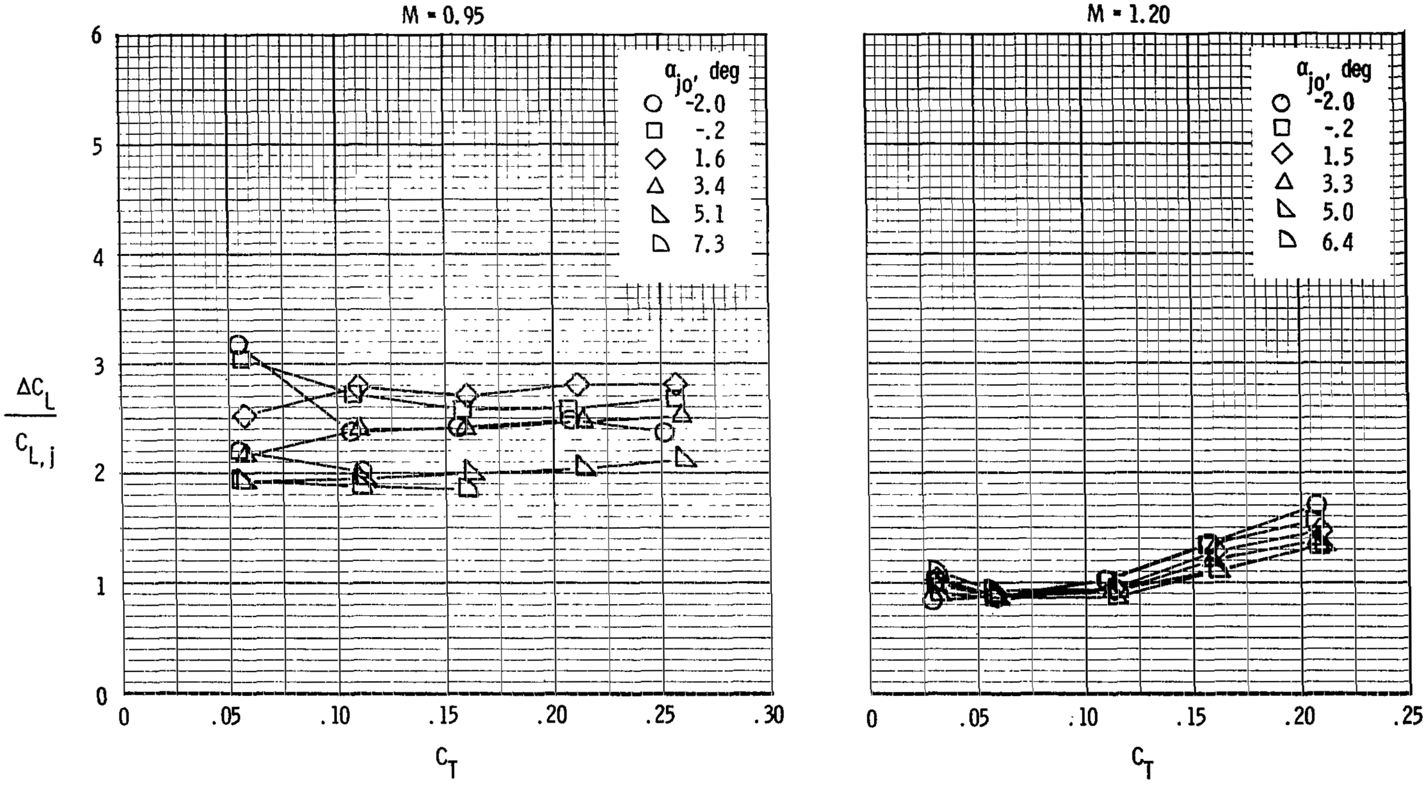

(c) M = 0.95 and 1.20.

Figure 37.- Concluded.

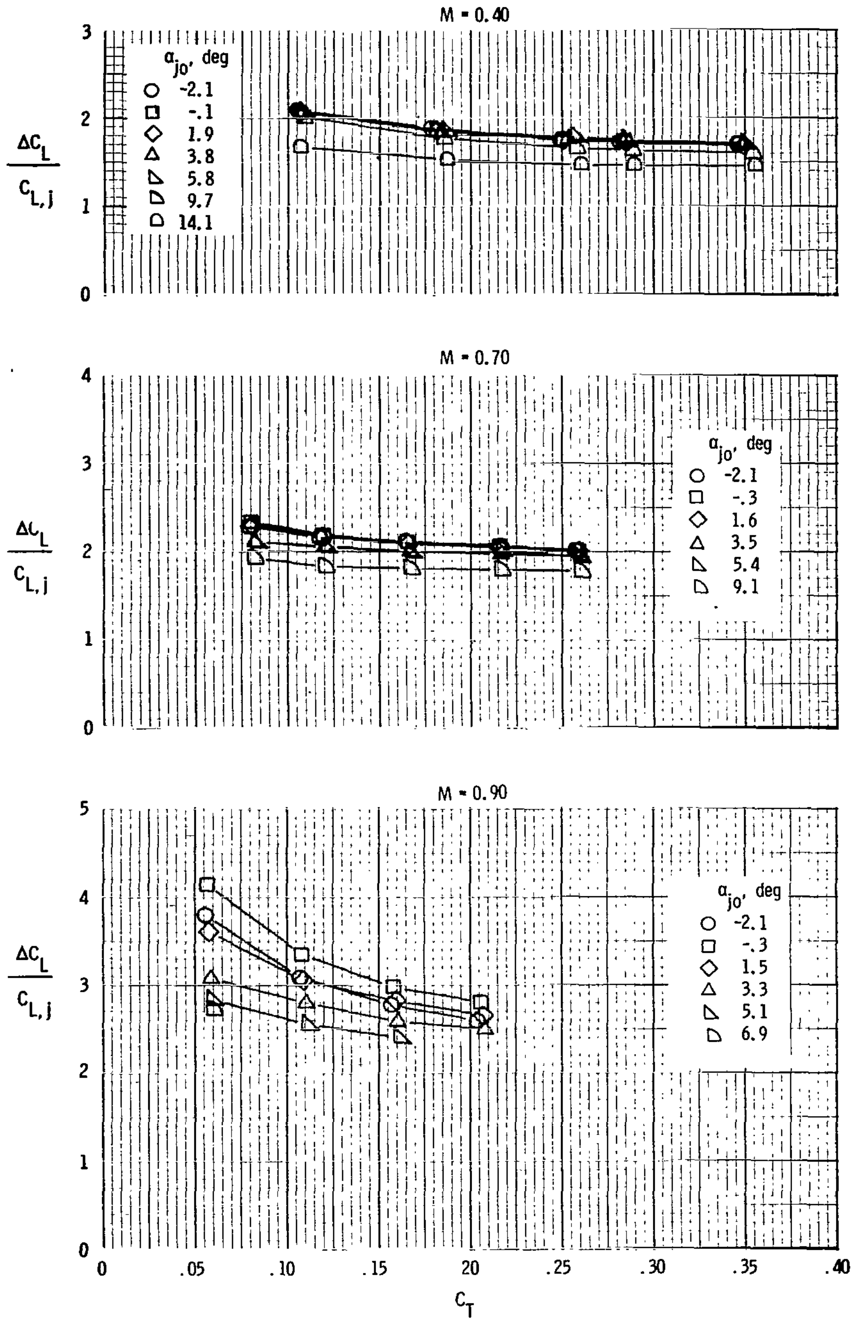

Figure 38.- Variation of lift-augmentation ratio with thrust coefficient. $\delta_d = 45^{\circ}$.

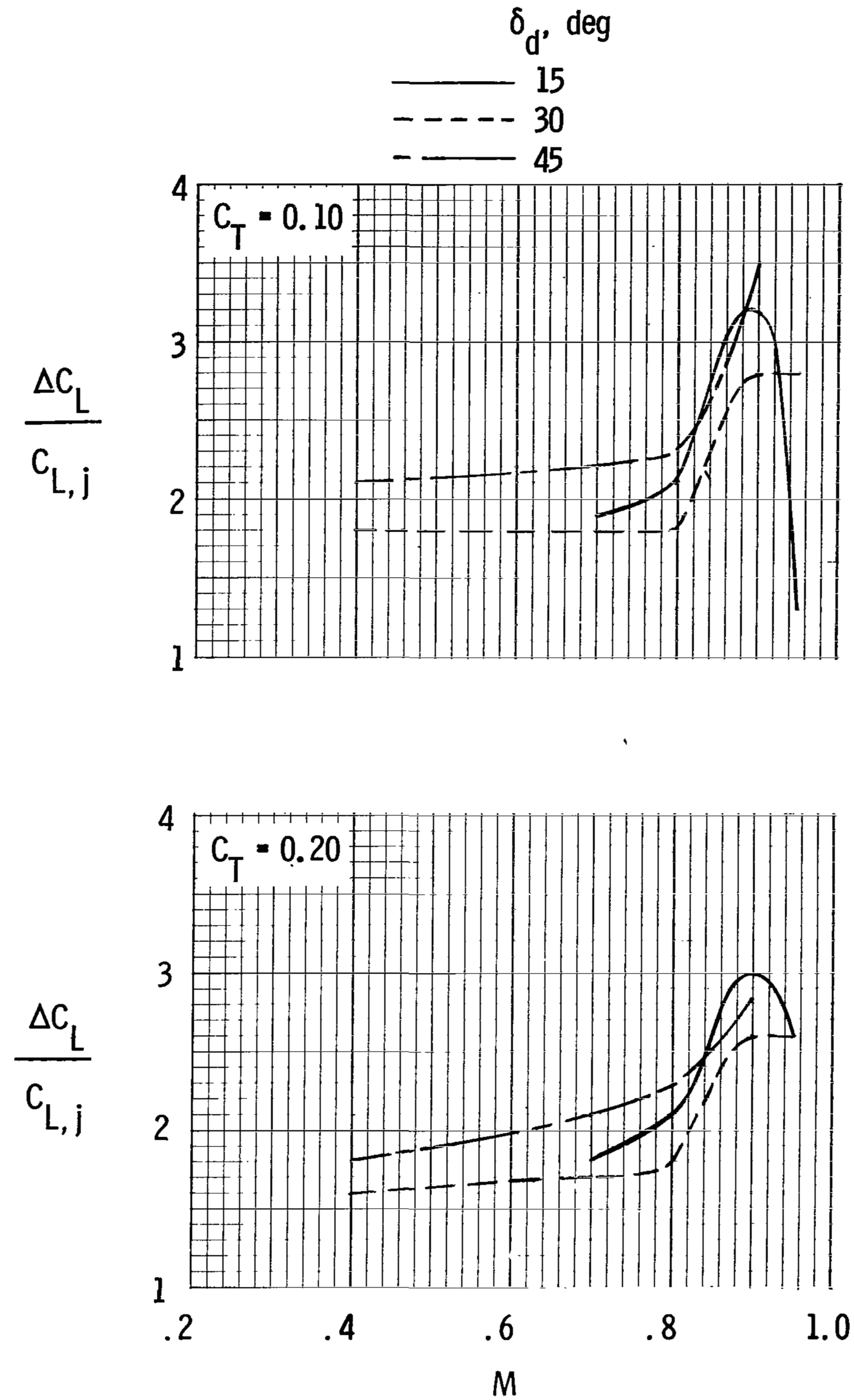

Figure 39.- Variation of lift-augmentation ratio with Mach number for selected conditions. $\alpha \approx 0^{\circ}$.

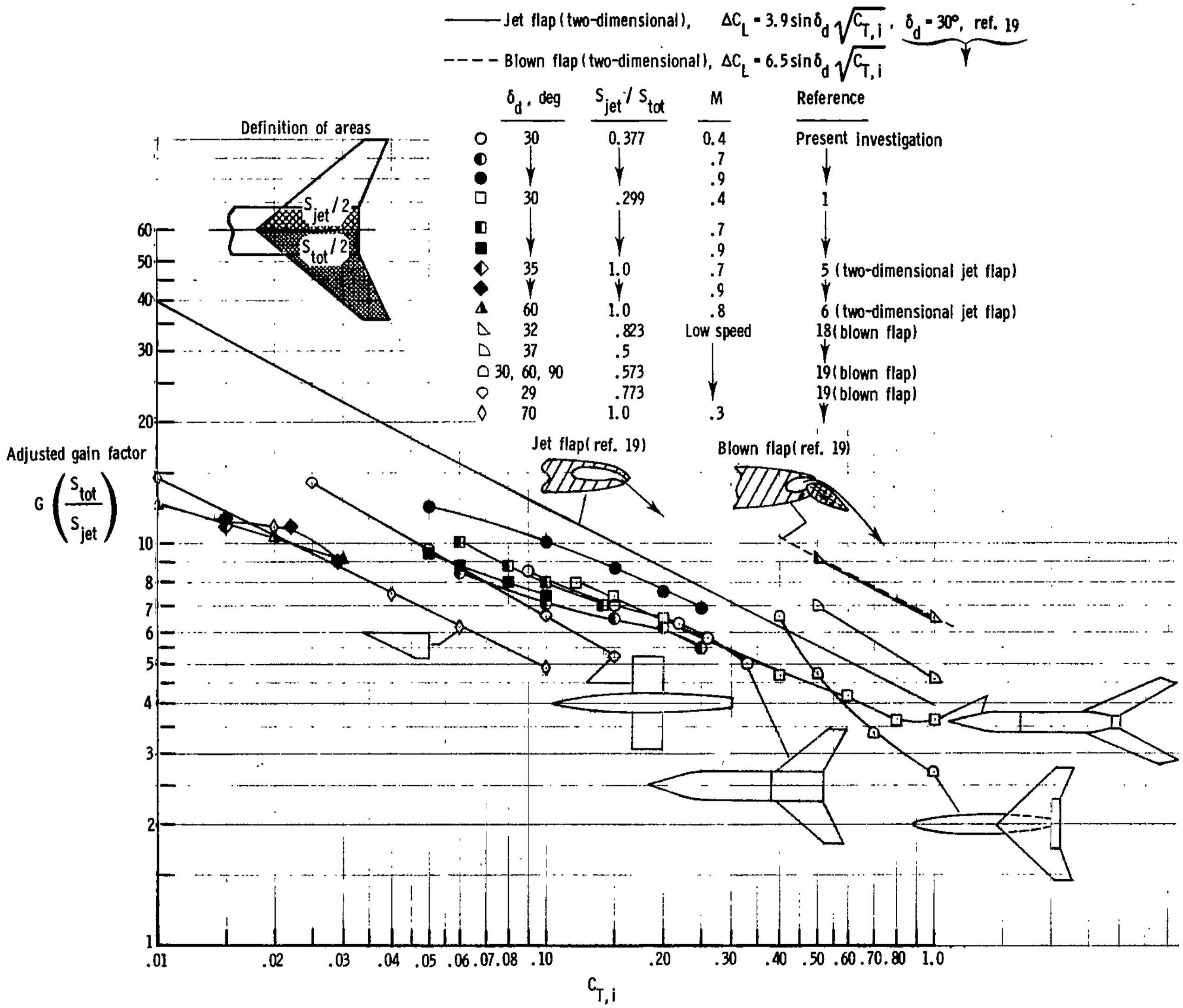

Figure 40.- Comparison of gain factor adjusted for partial span effects from present investigation with theoretical and other experimental data. Gain factor is based on measured turning static angle.

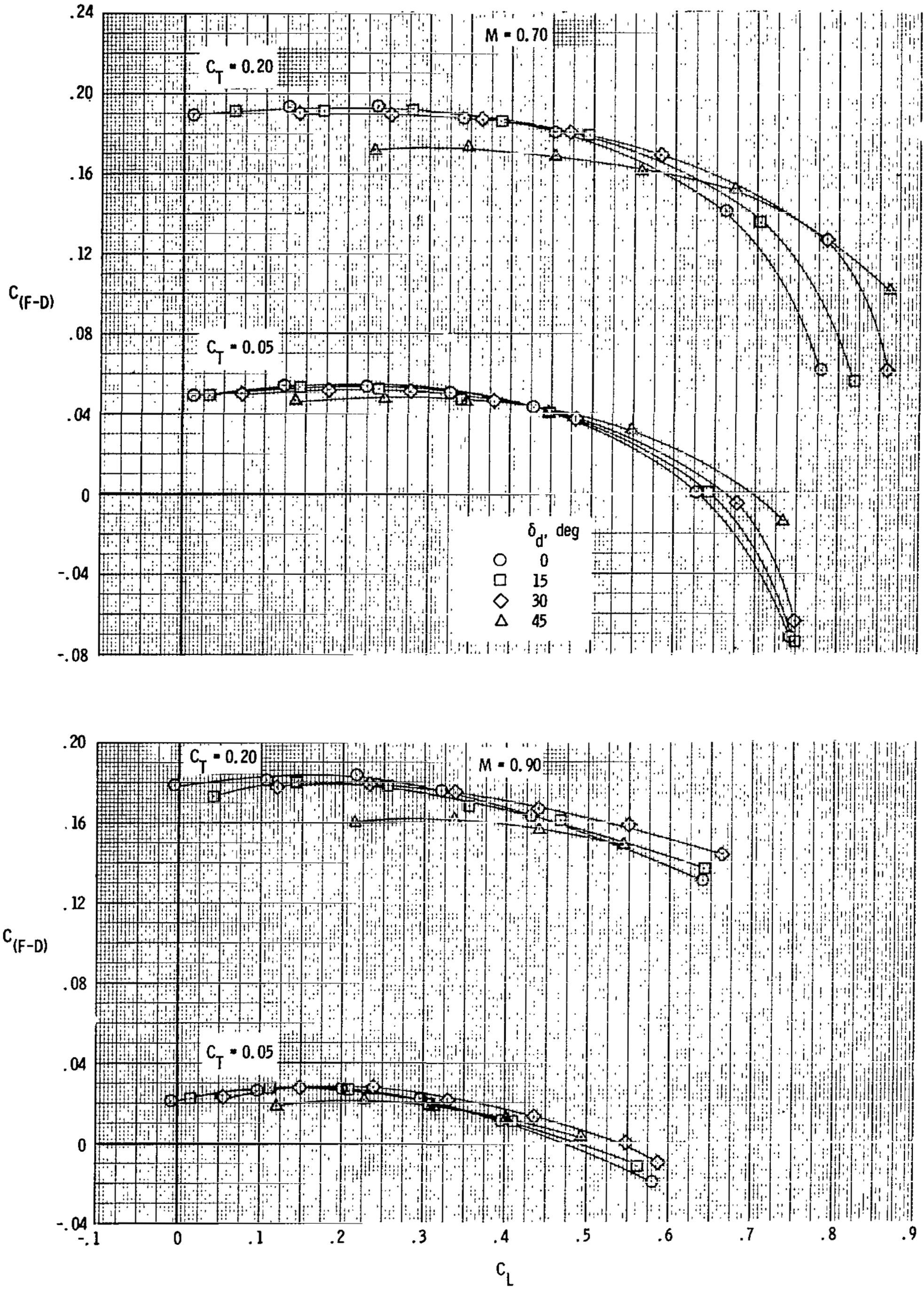

Figure 41.- Typical variation of thrust-minus-drag coefficient with total lift coefficient at constant values of thrust coefficient for two Mach numbers.

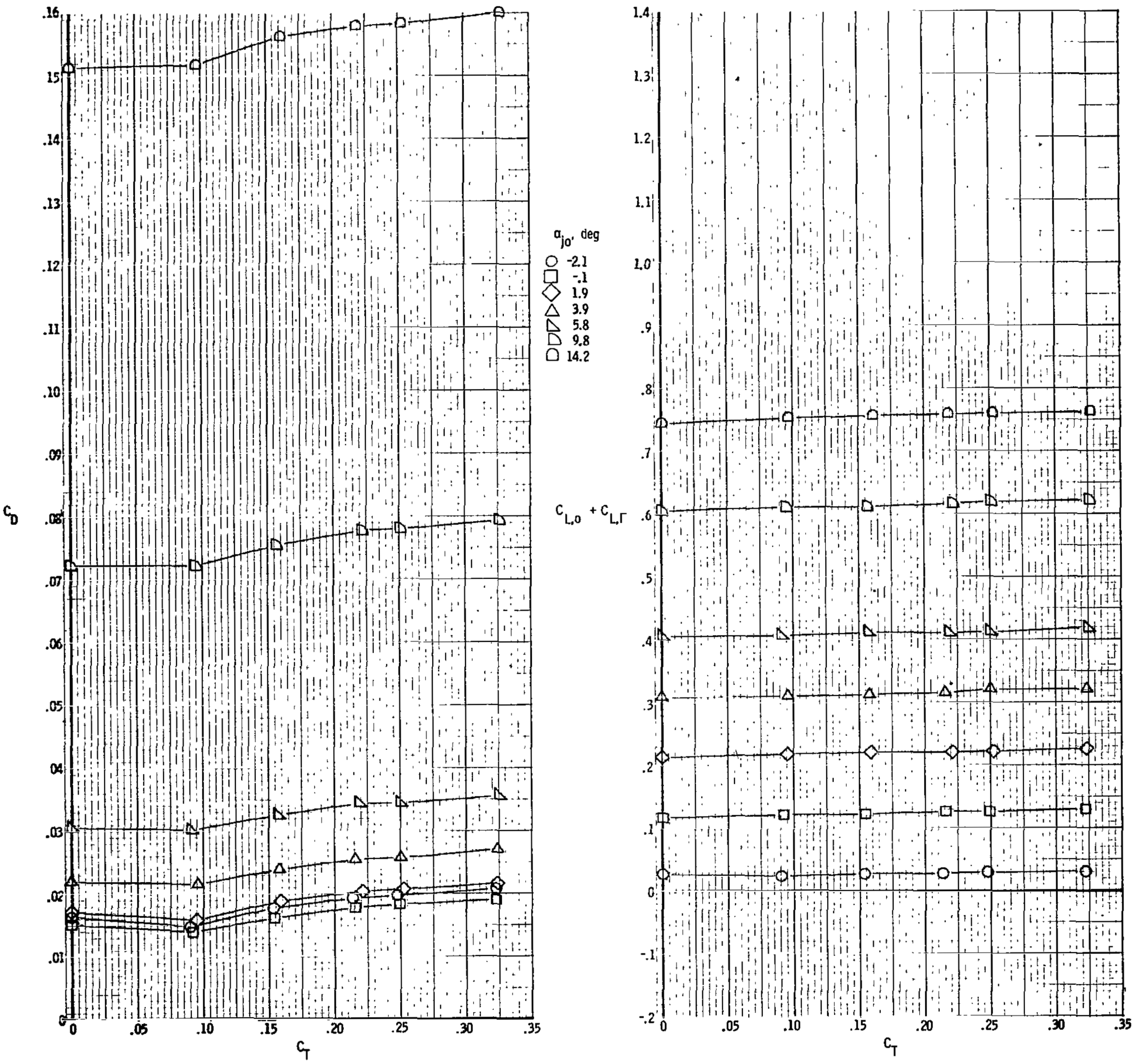

(a) M = 0.40.

Figure 42.- Lift and drag characteristics. $\delta_d = 0^{\circ}$.

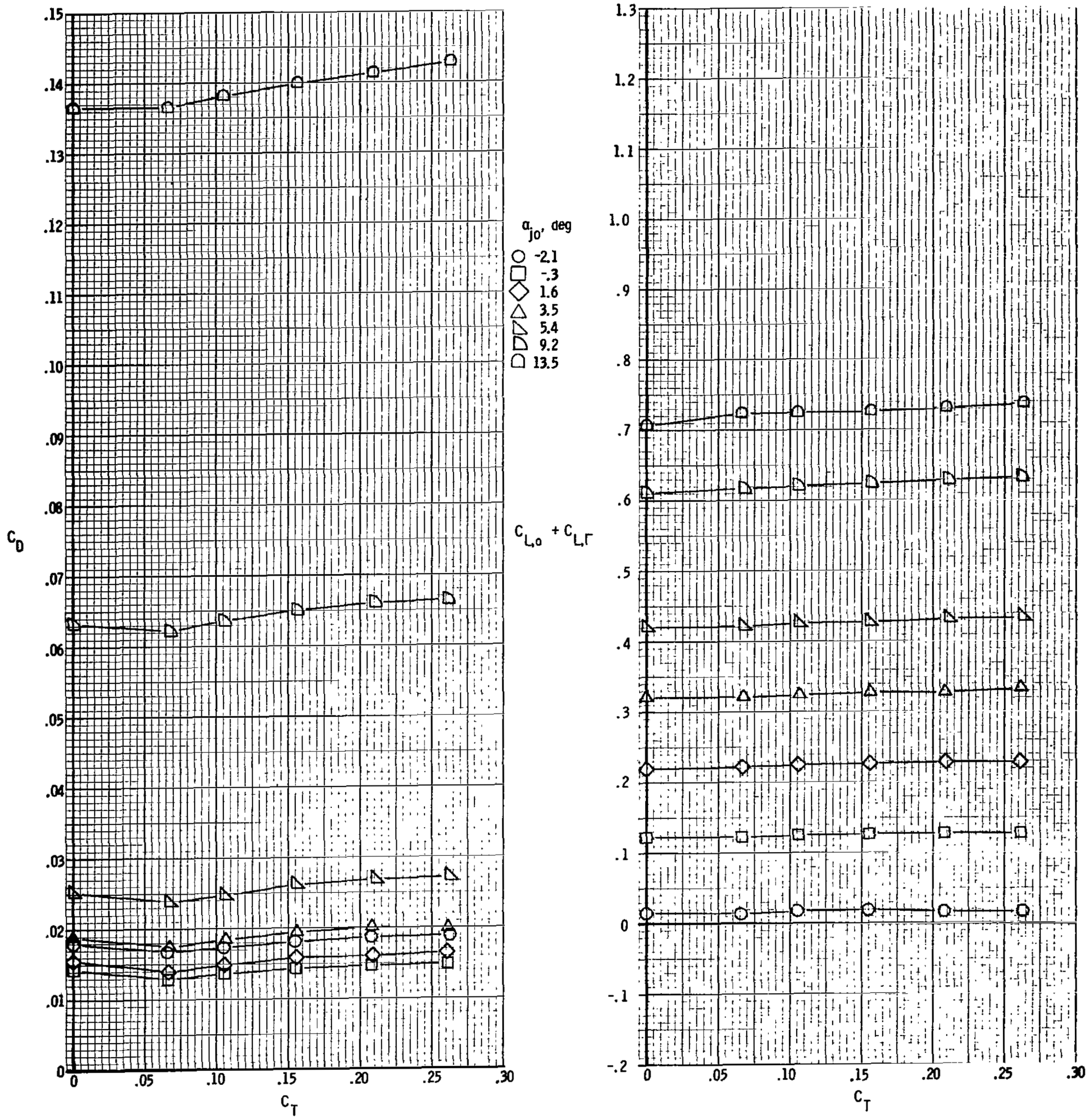

(b) M = 0.70.

Figure 42.- Continued.

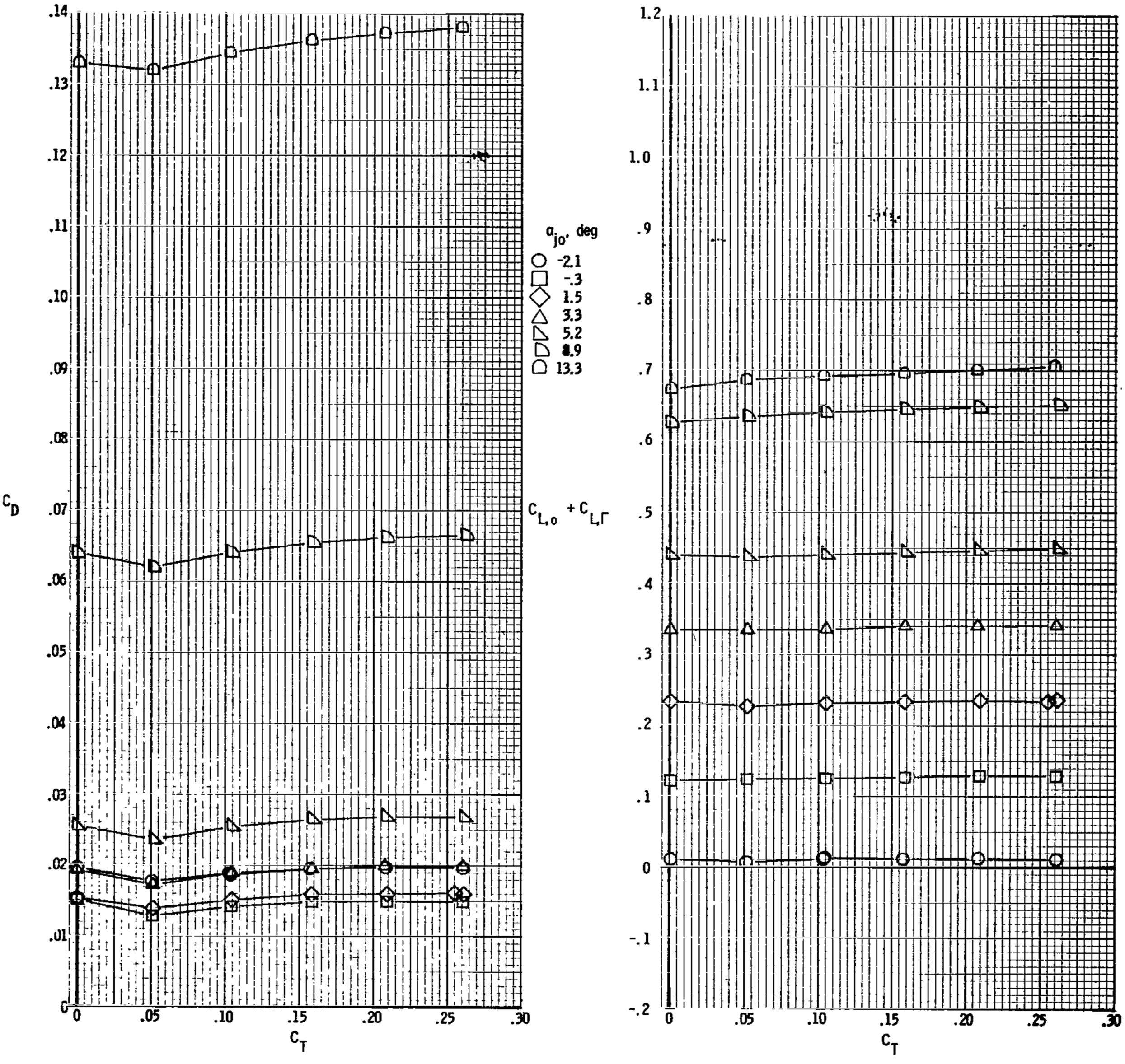

(c) M = 0.80.

Figure 42.- Continued.

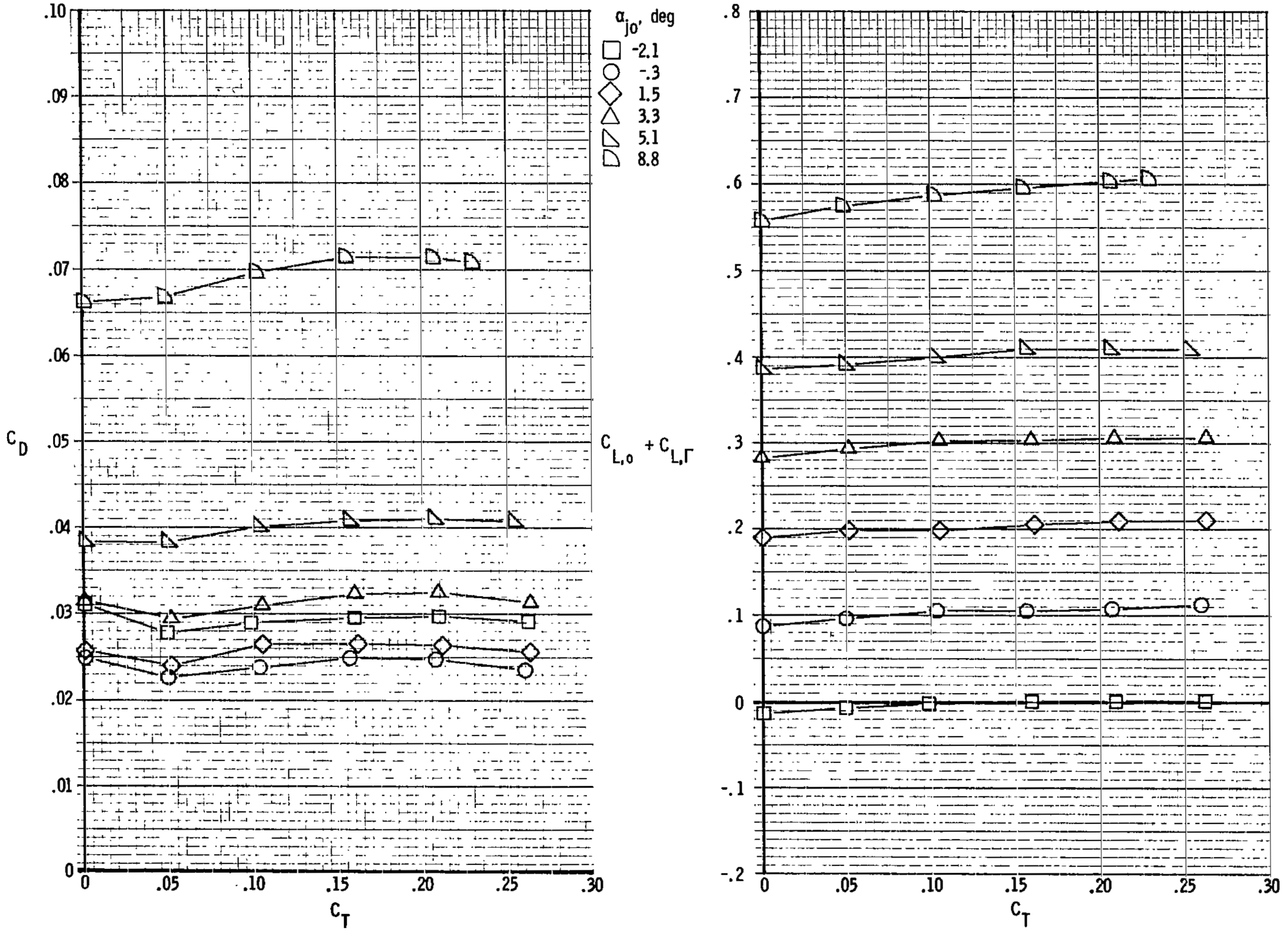

(d) M = 0.90.

Figure 42.- Continued.

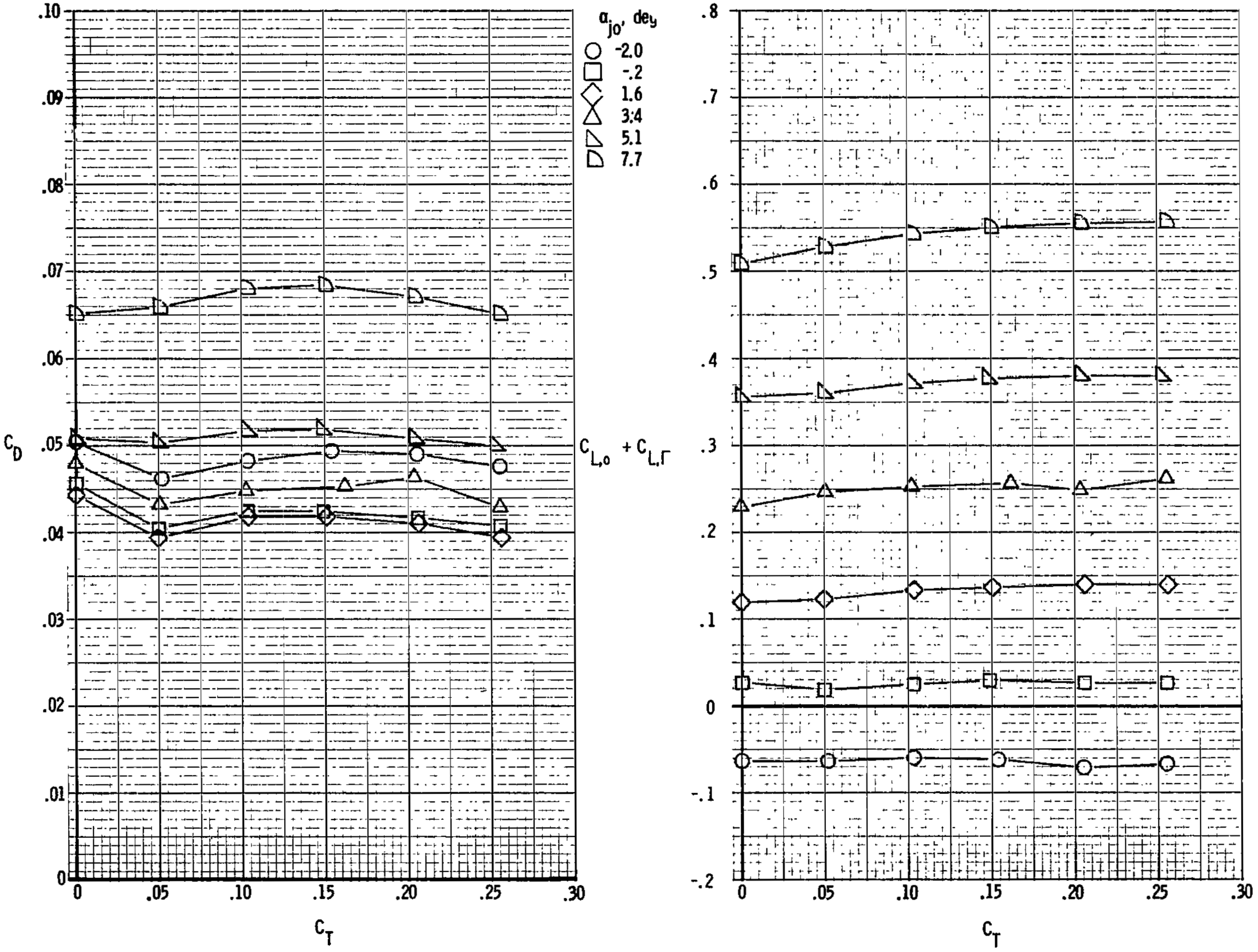

(e) M = 0.95.

Figure 42.- Continued.

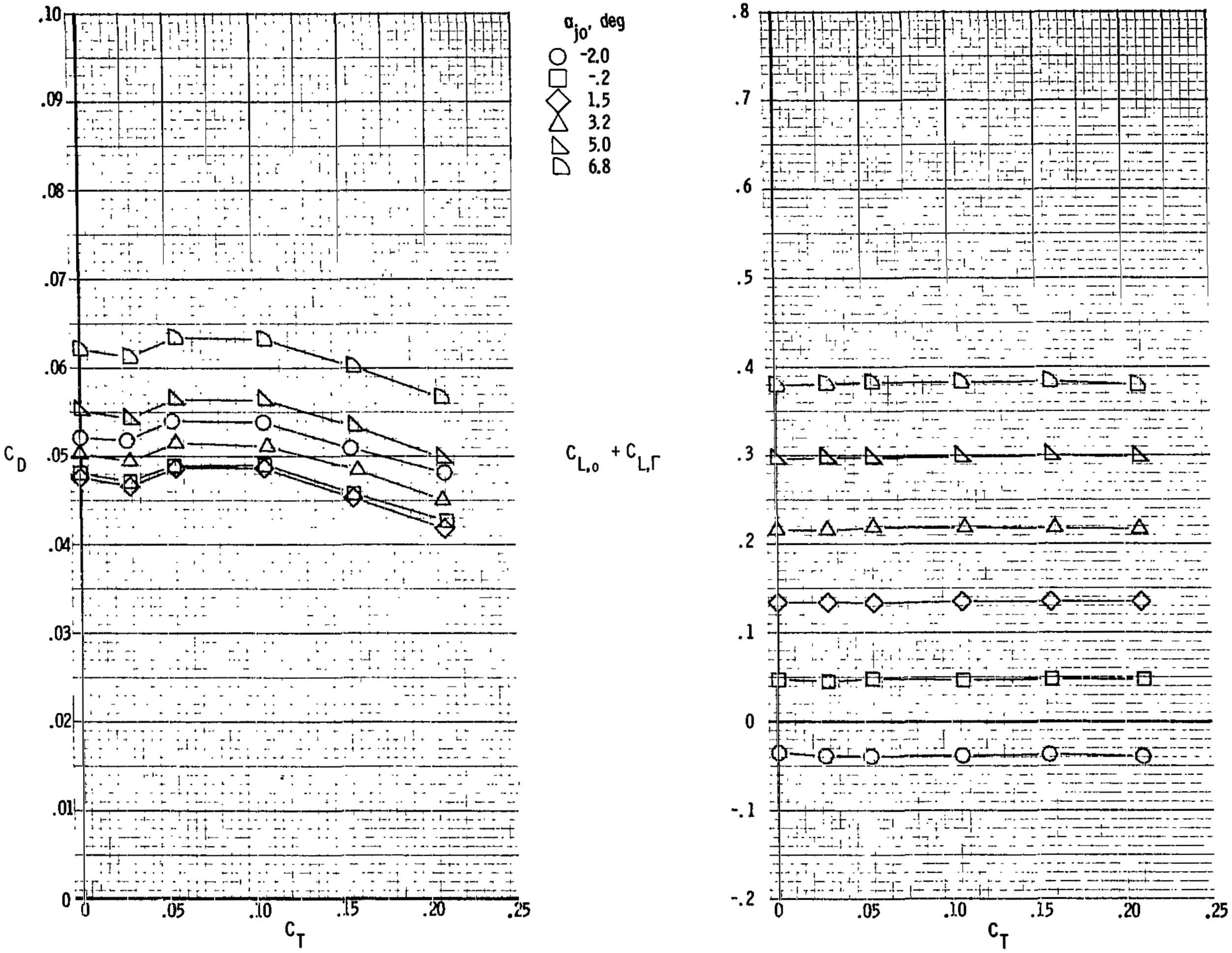

(f) M = 1.20.

Figure 42.- Concluded.

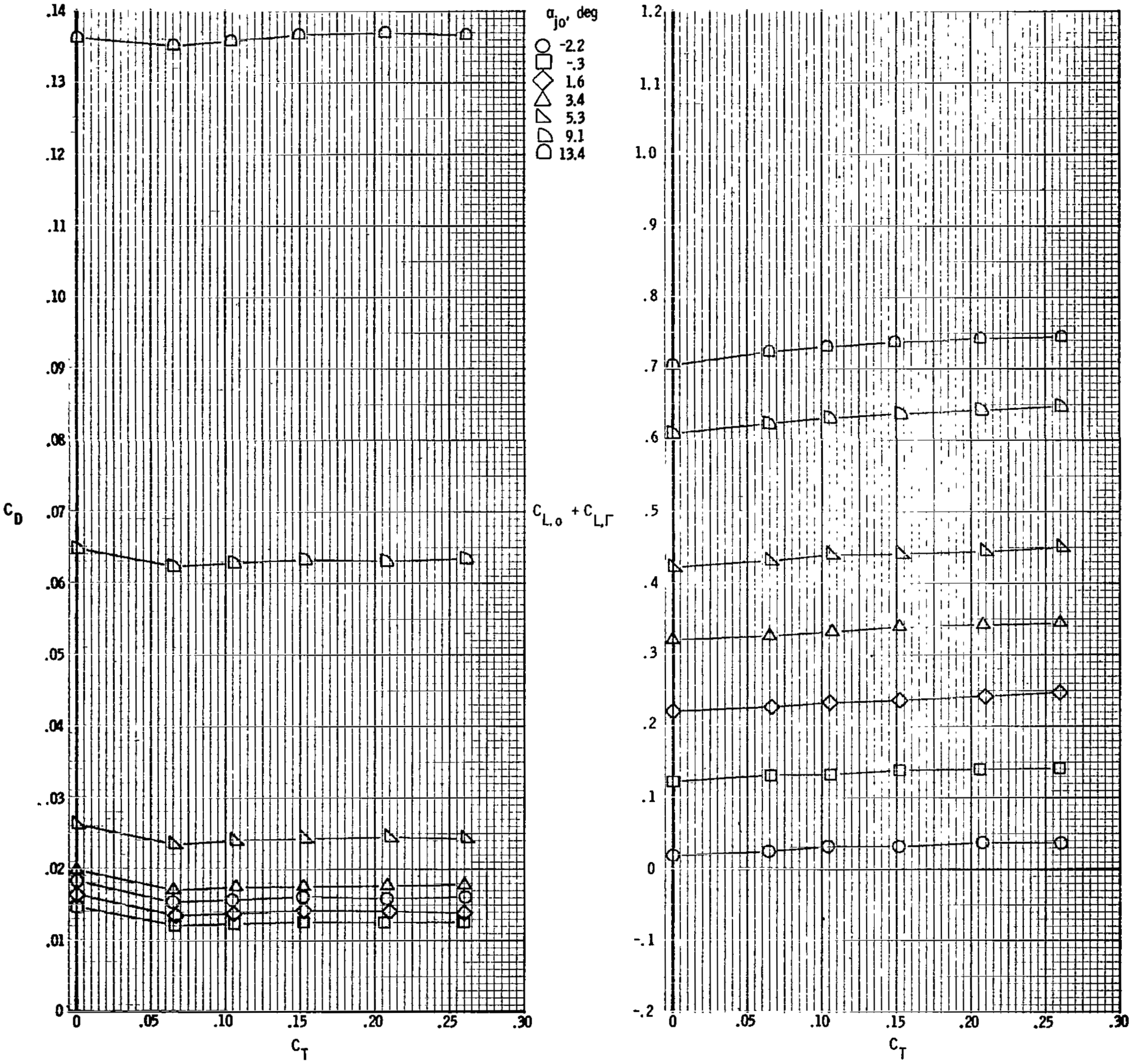

(a) M = 0.70.

Figure 43.- Lift and drag characteristics. $\delta_d = 15^o$.

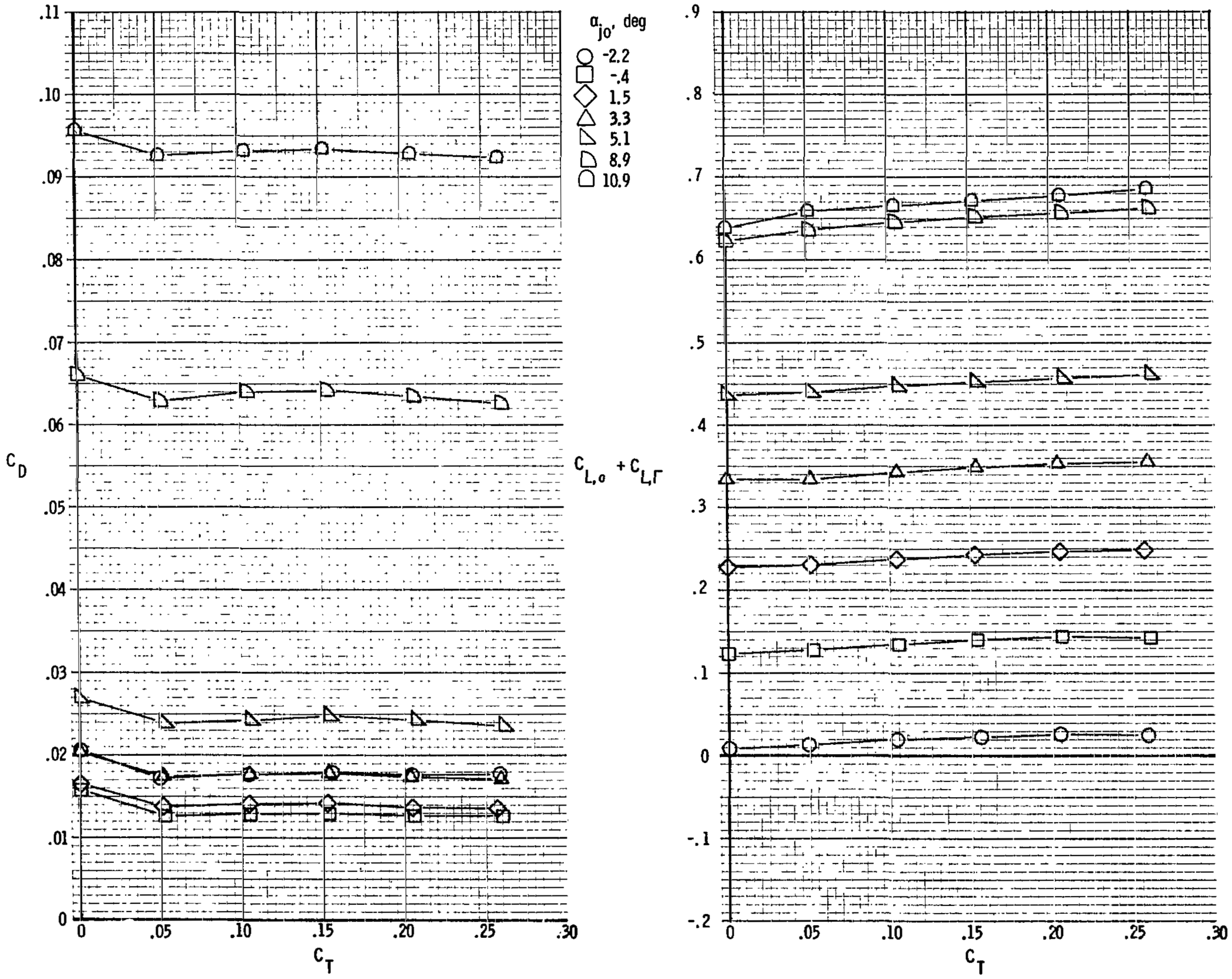

(b) M = 0.80.

Figure 43.- Continued.

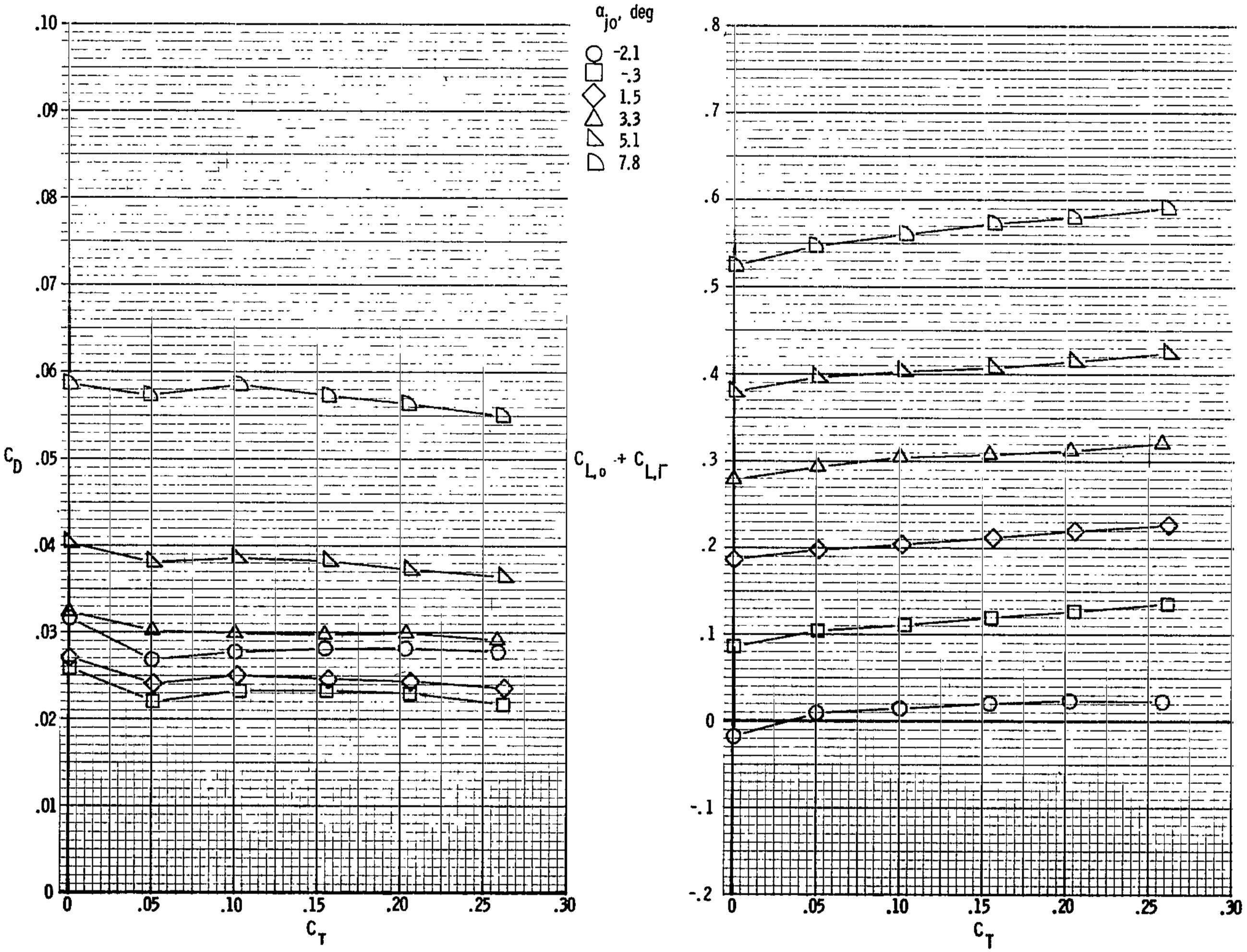

(c) M = 0.90.

Figure 43.- Continued.

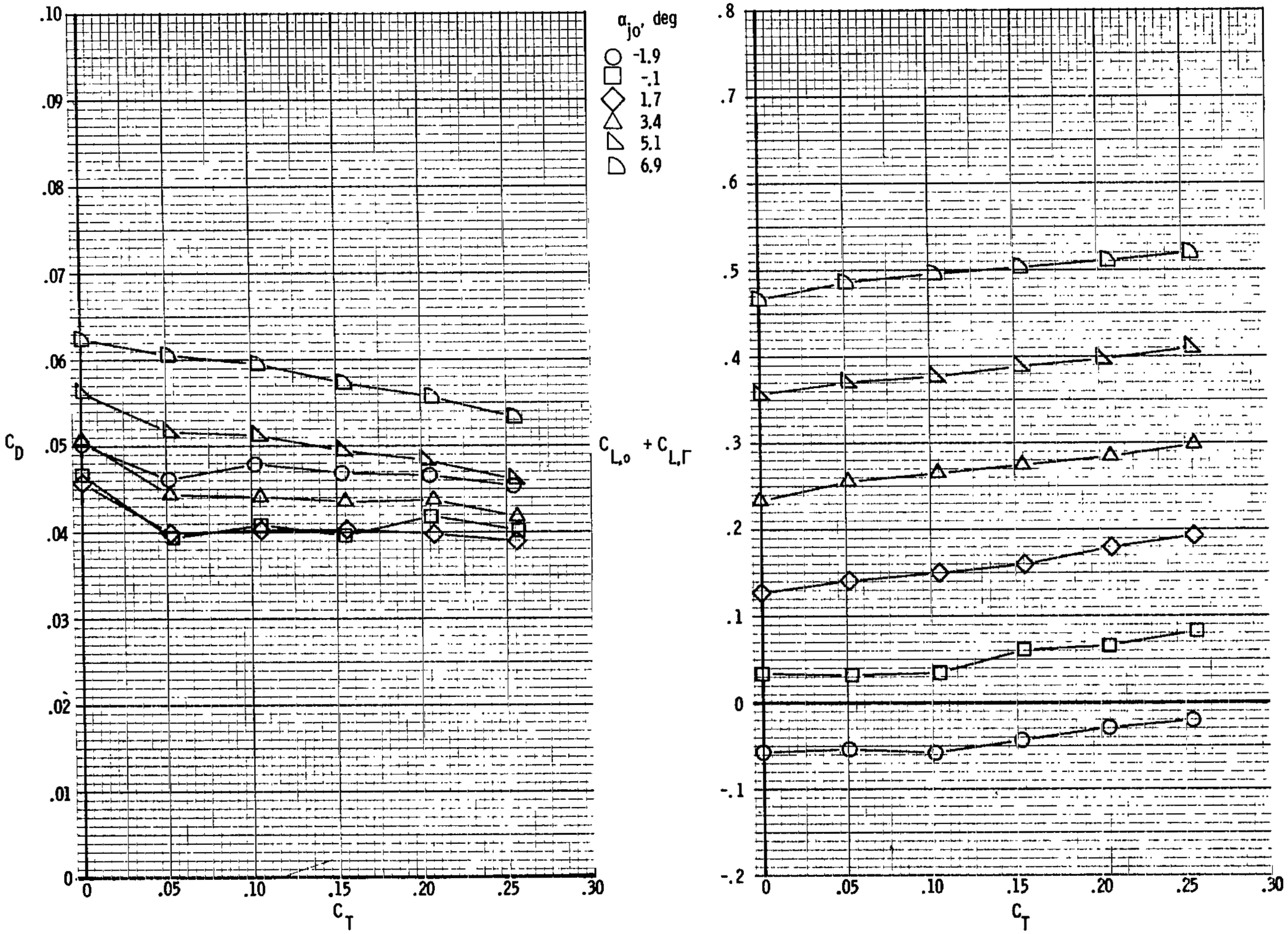

(d) M = 0.95.

Figure 43.- Concluded.

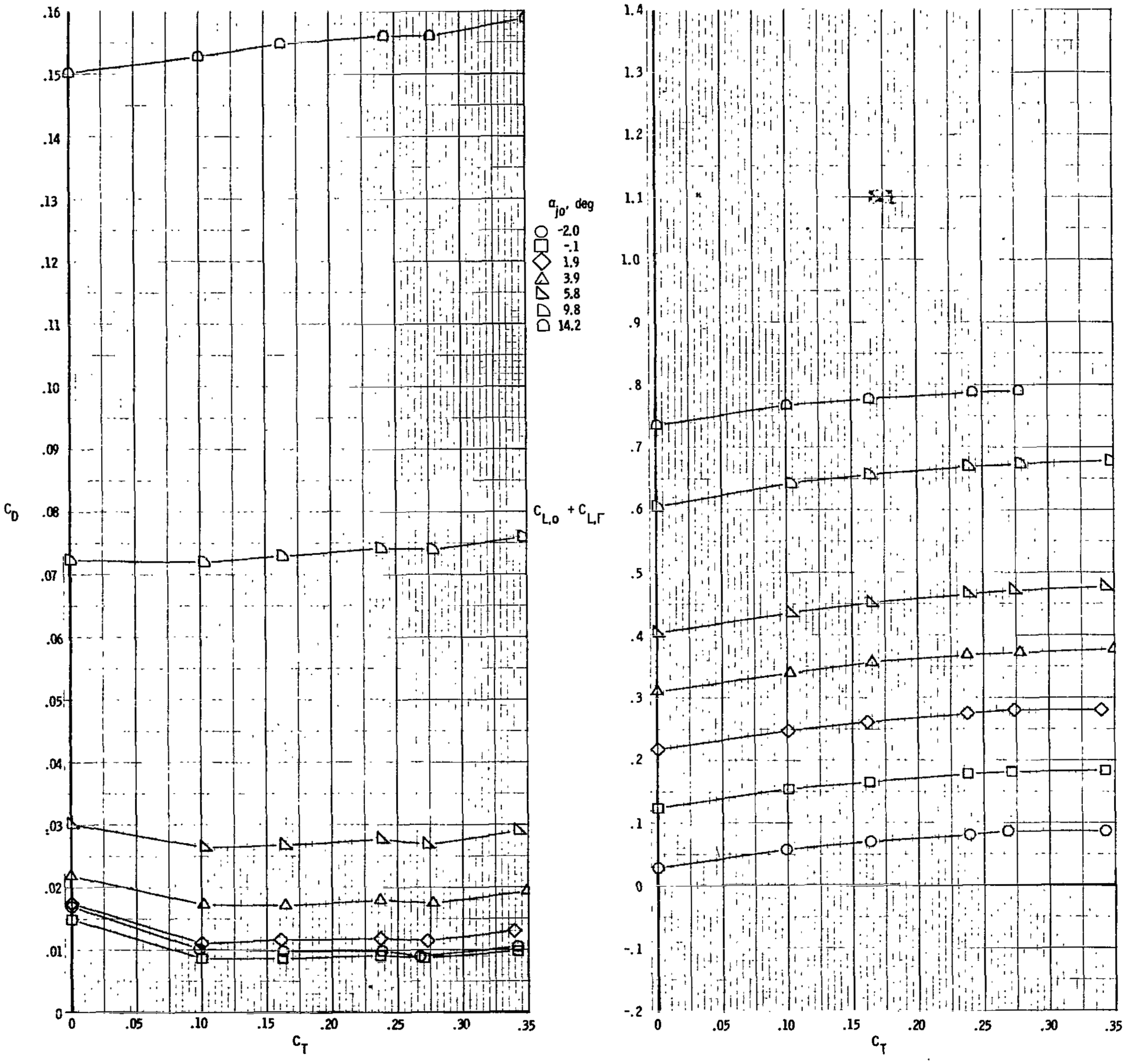

(a) M = 0.40.

Figure 44.- Lift and drag characteristics. $\delta_d = 30^o$.

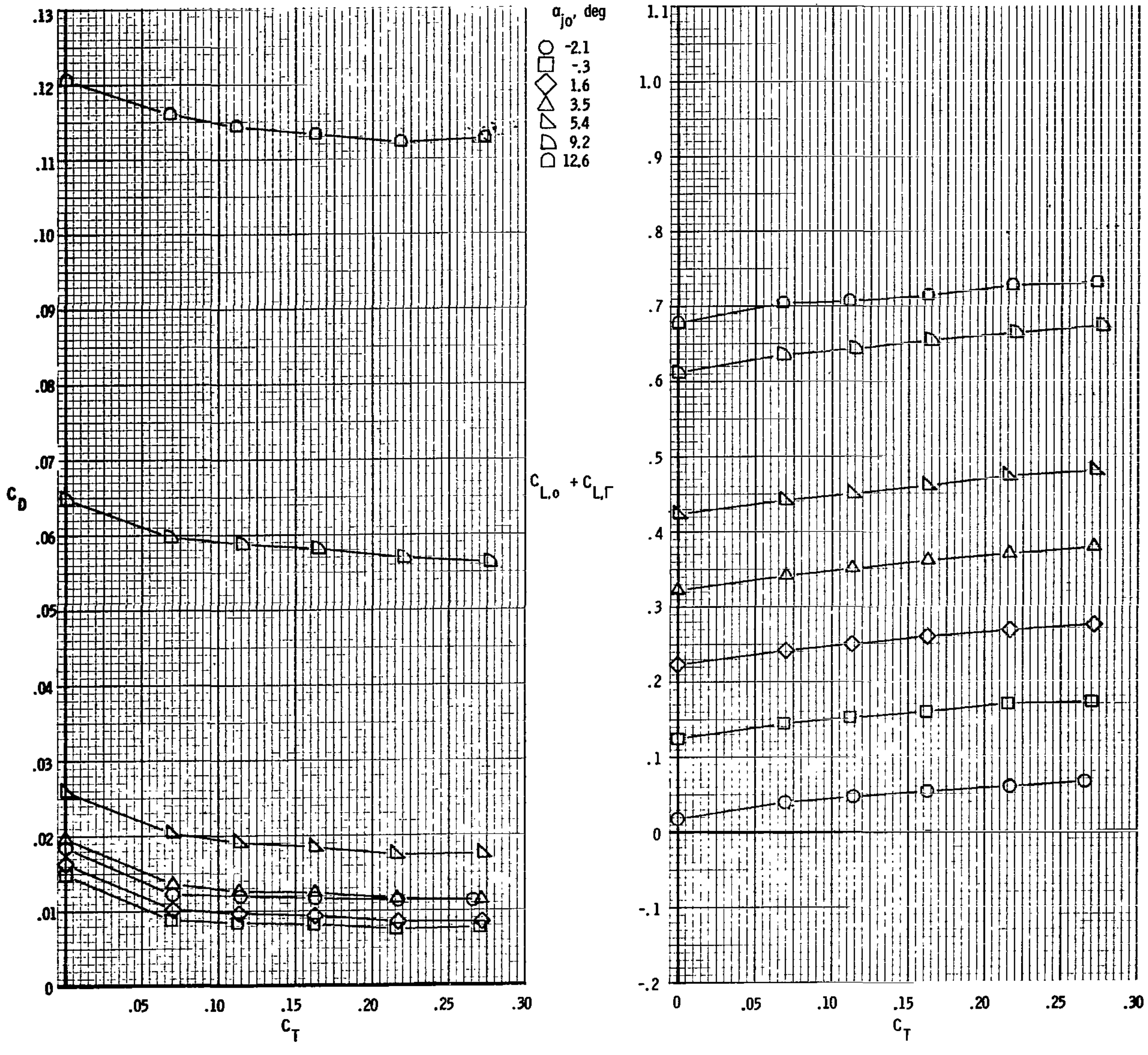

(b) M = 0.70.

Figure 44.- Continued.

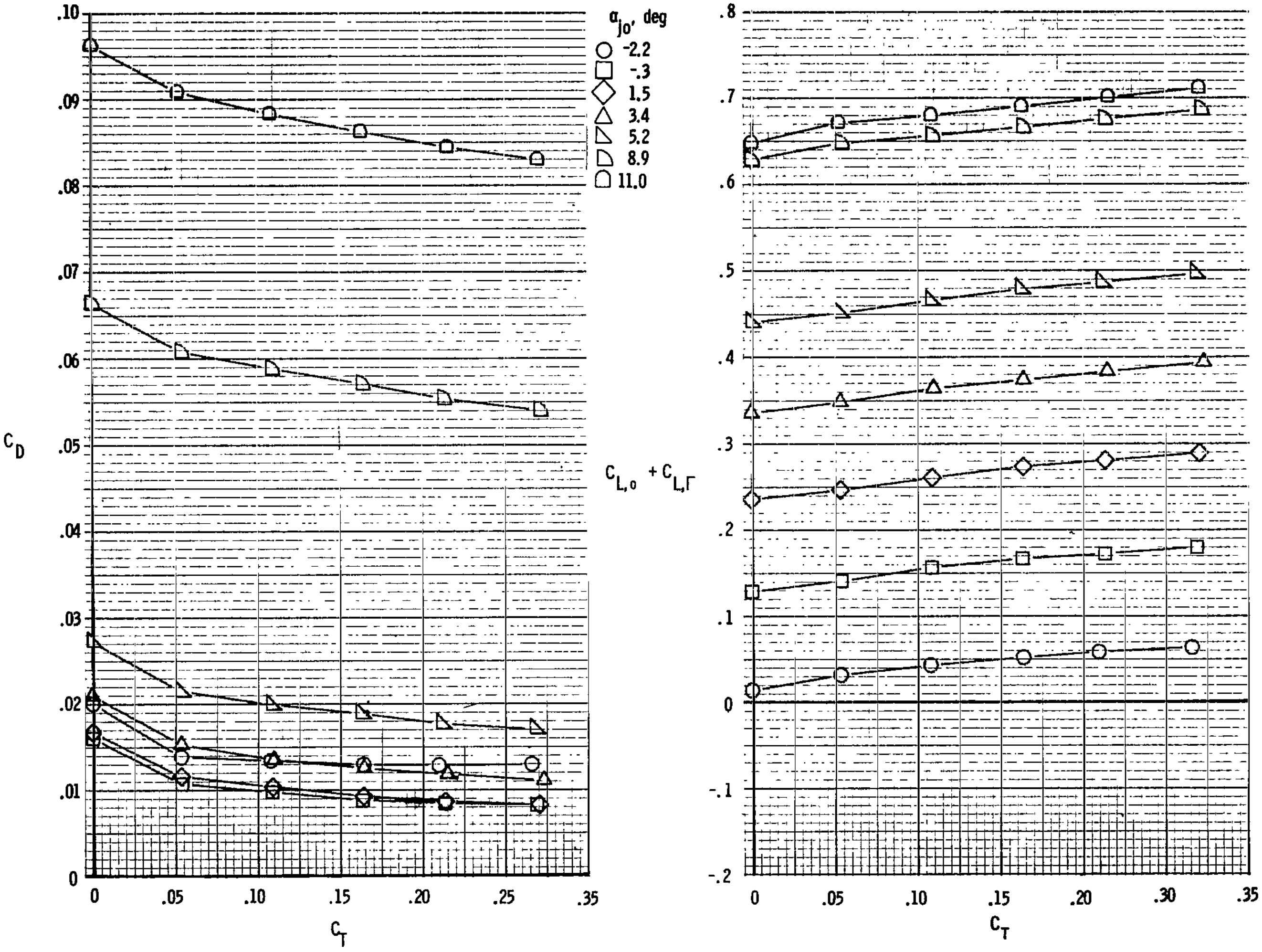

(c) M = 0.80.

Figure 44.- Continued.

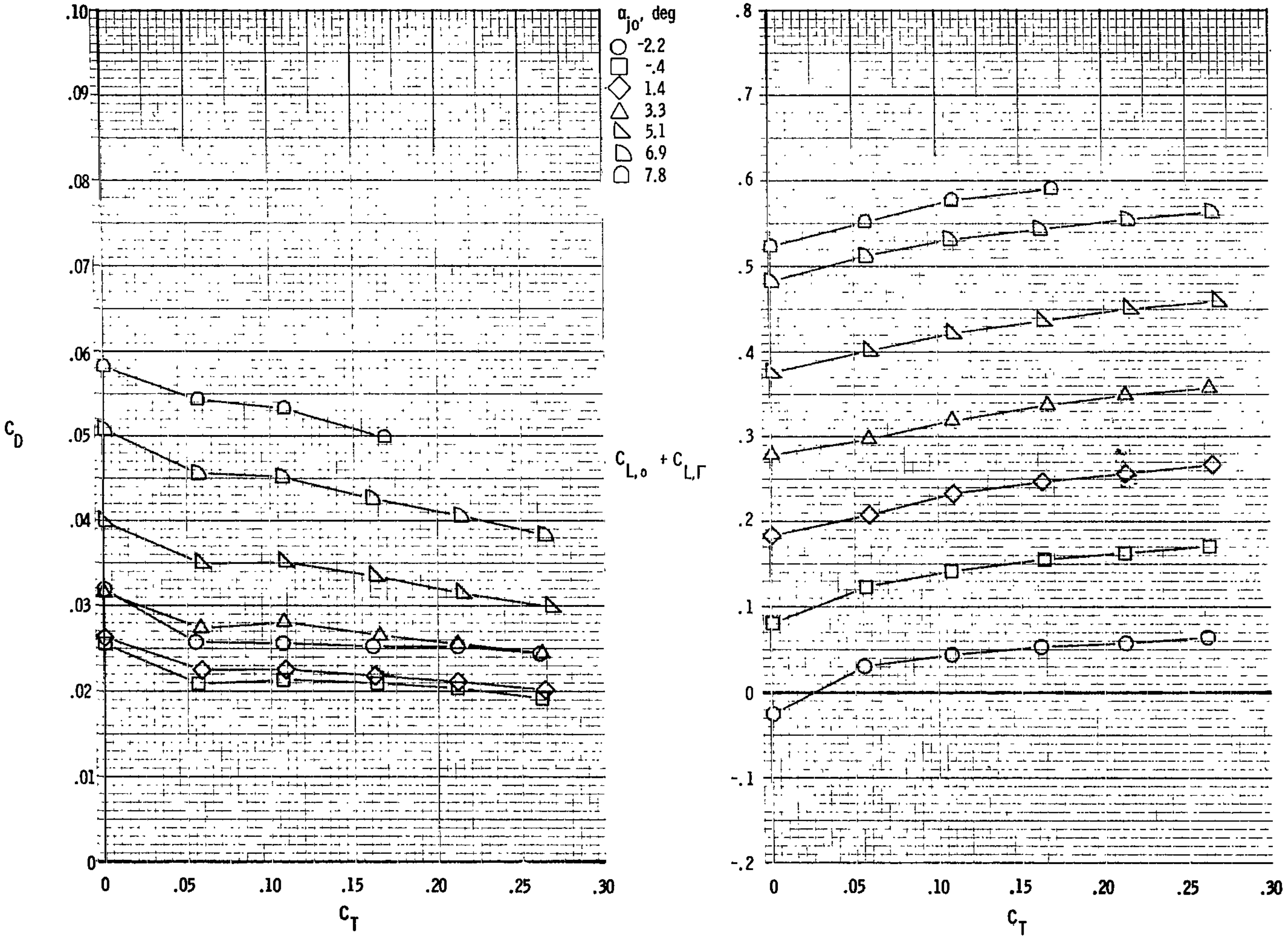

(d) M = 0.90.

Figure 44.- Continued.

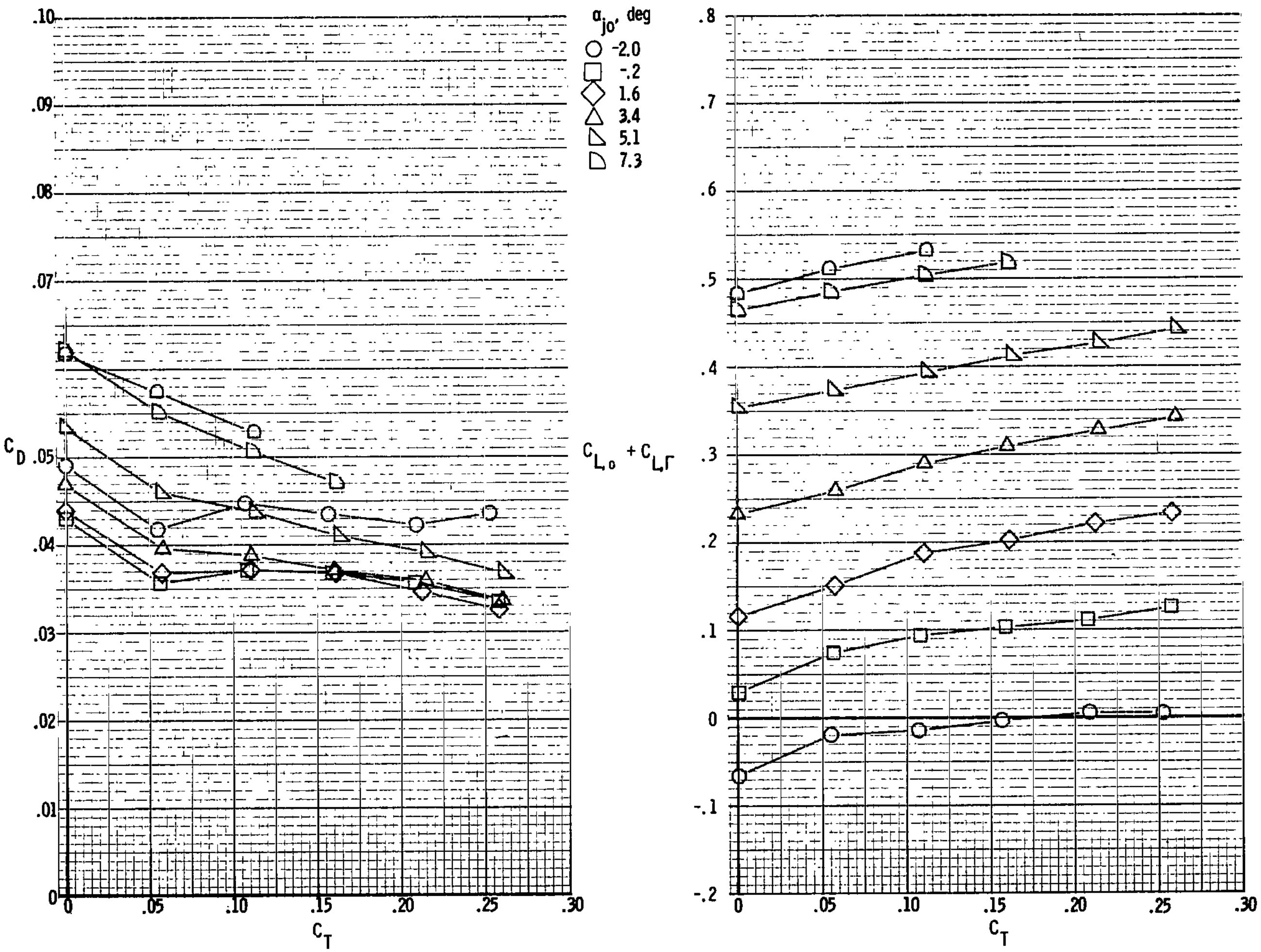

(e) M = 0.95.

Figure 44.- Continued.

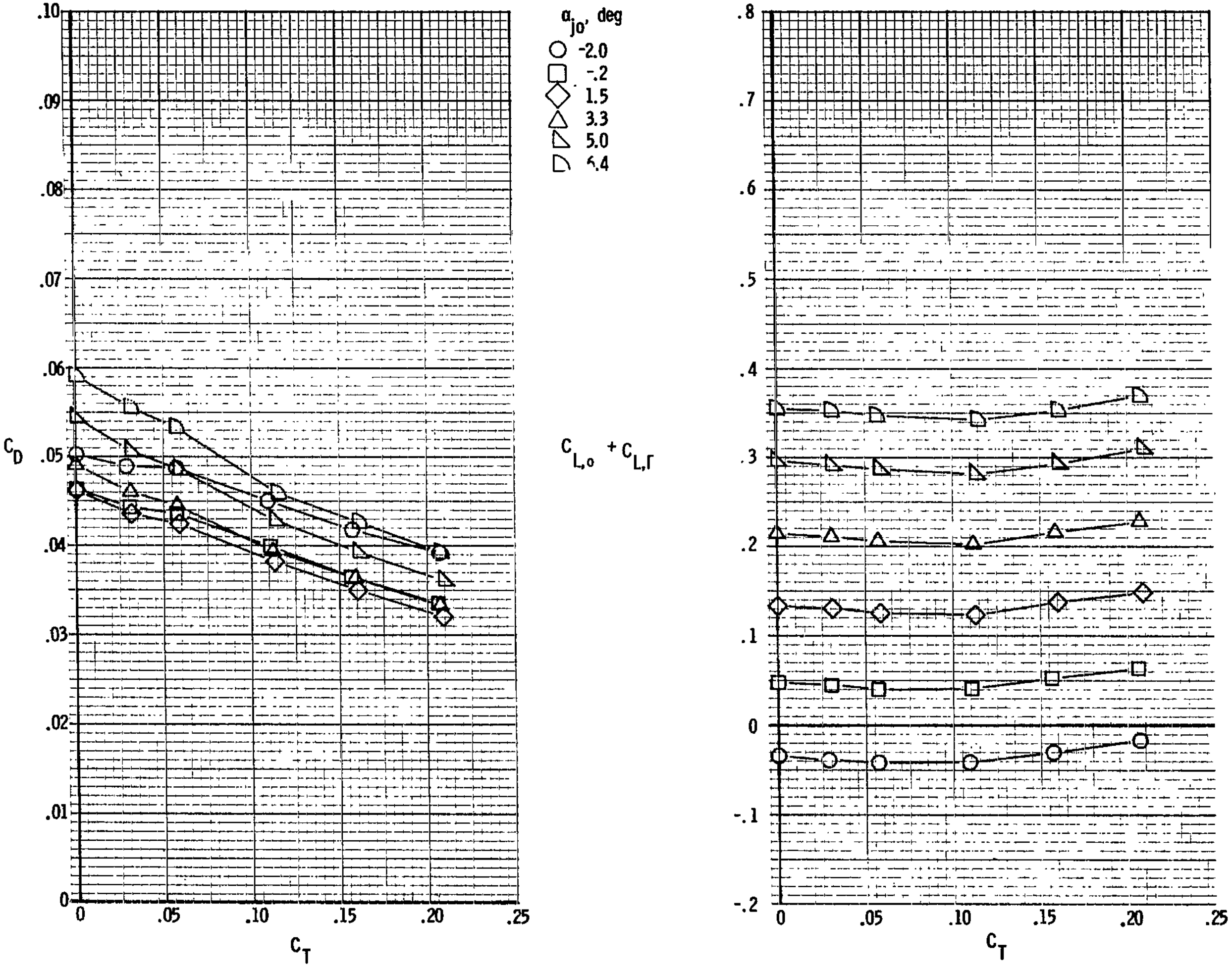

(f) M = 1.20.

Figure 44.- Concluded.

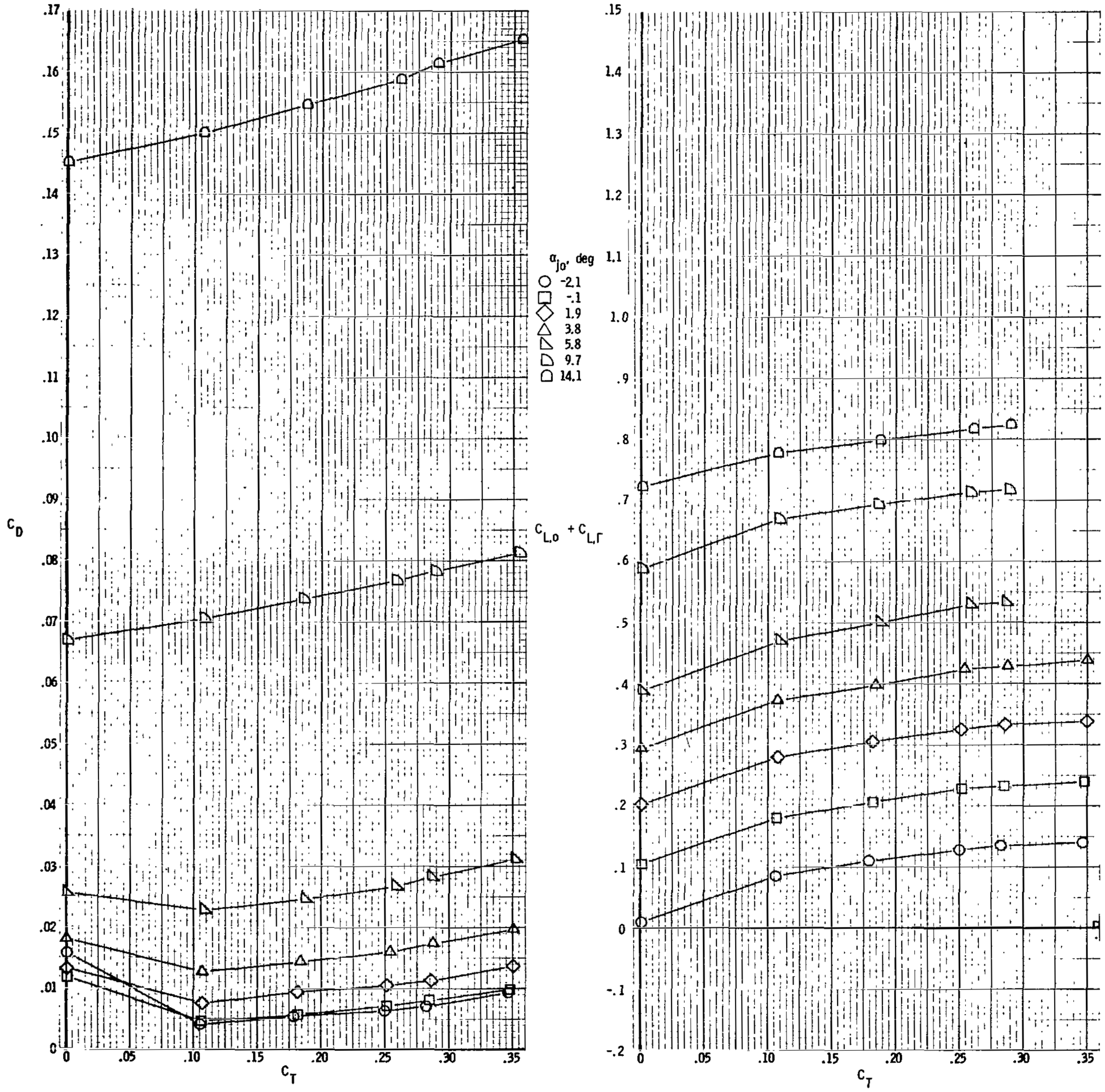

(a) M = 0.40.

Figure 45.- Lift and drag characteristics. $\delta_d = 45^{\circ}$.

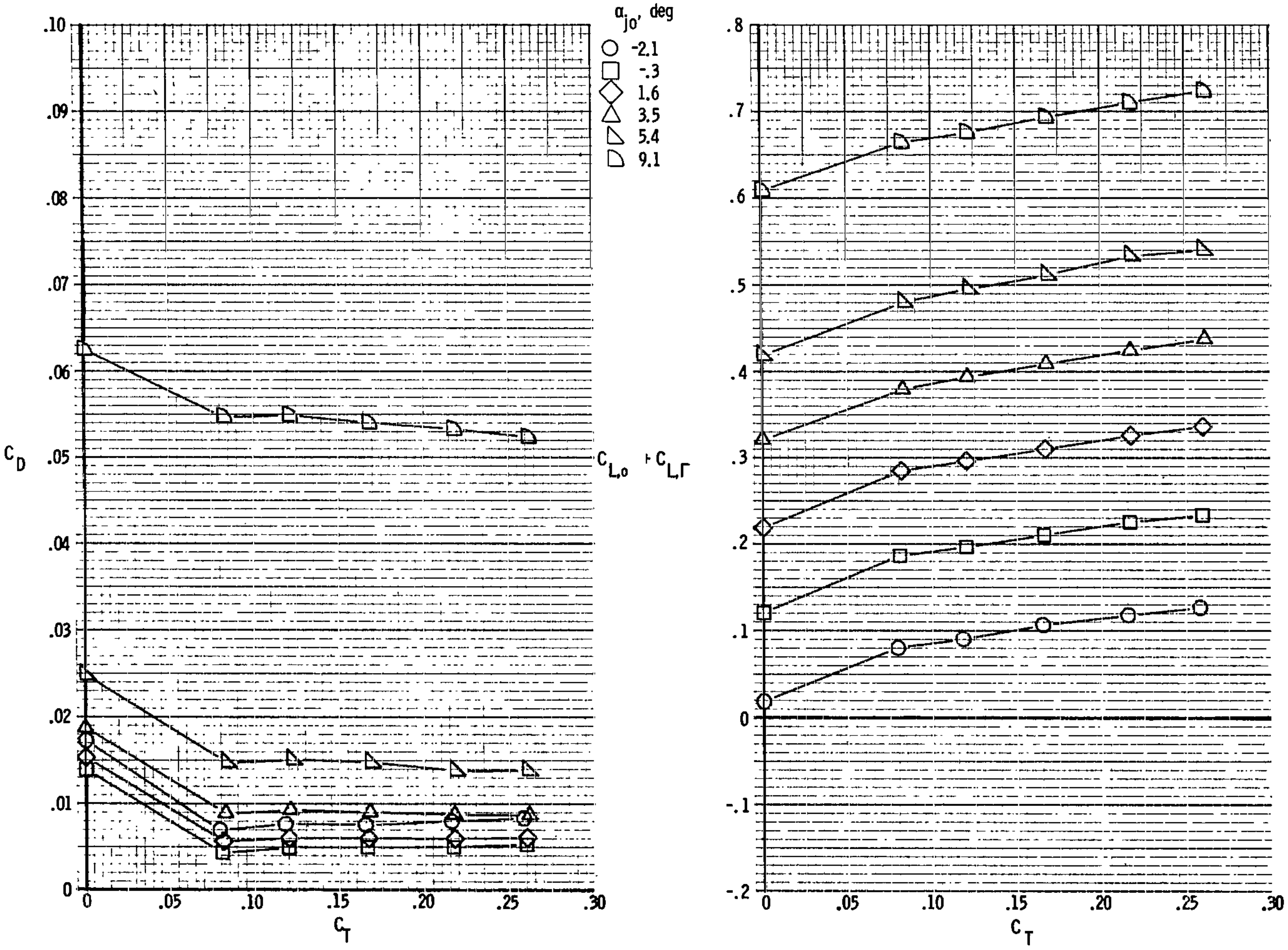

(b) M = 0.70.

Figure 45.- Continued.

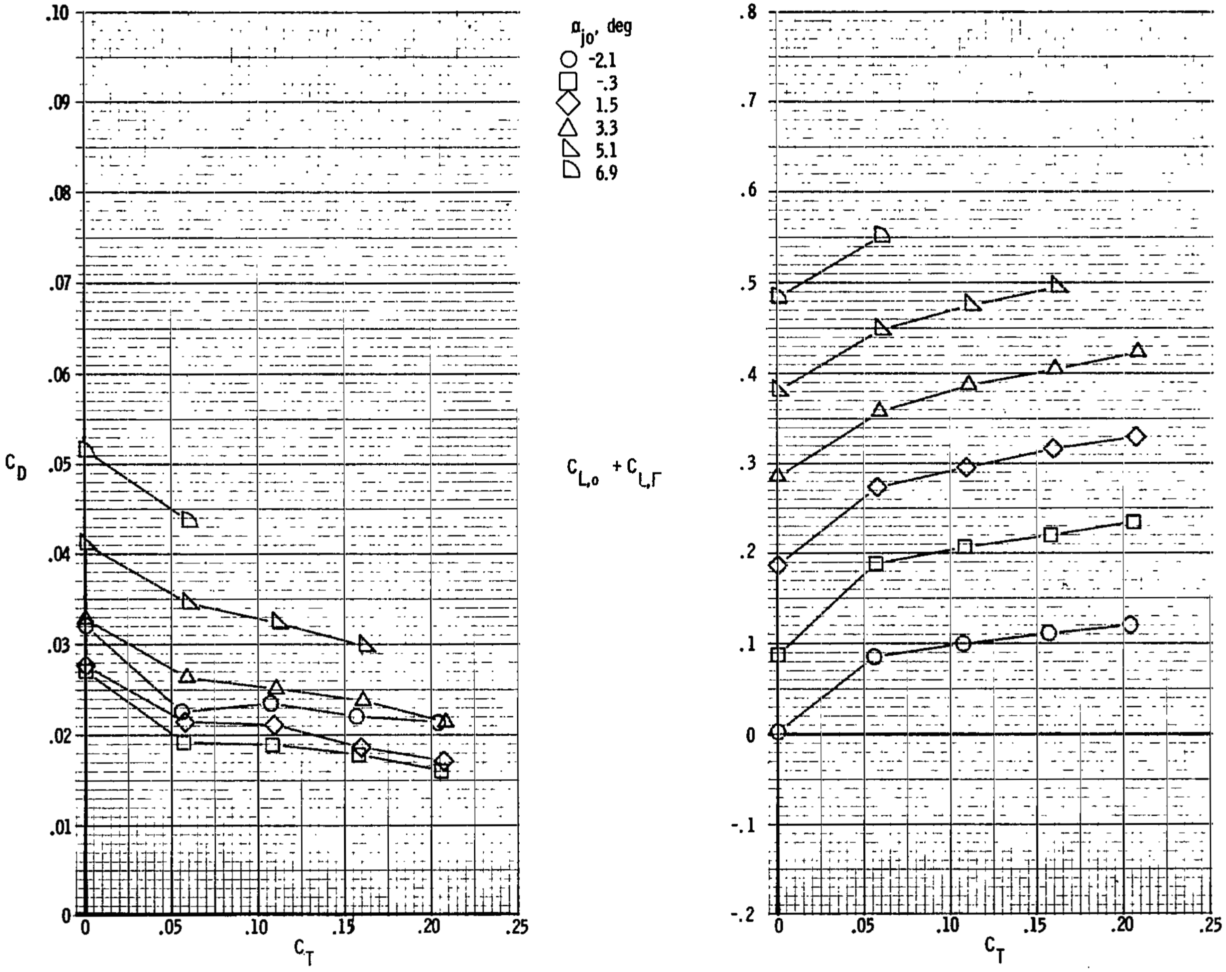

(c) M = 0.90.

Figure 45.- Concluded.

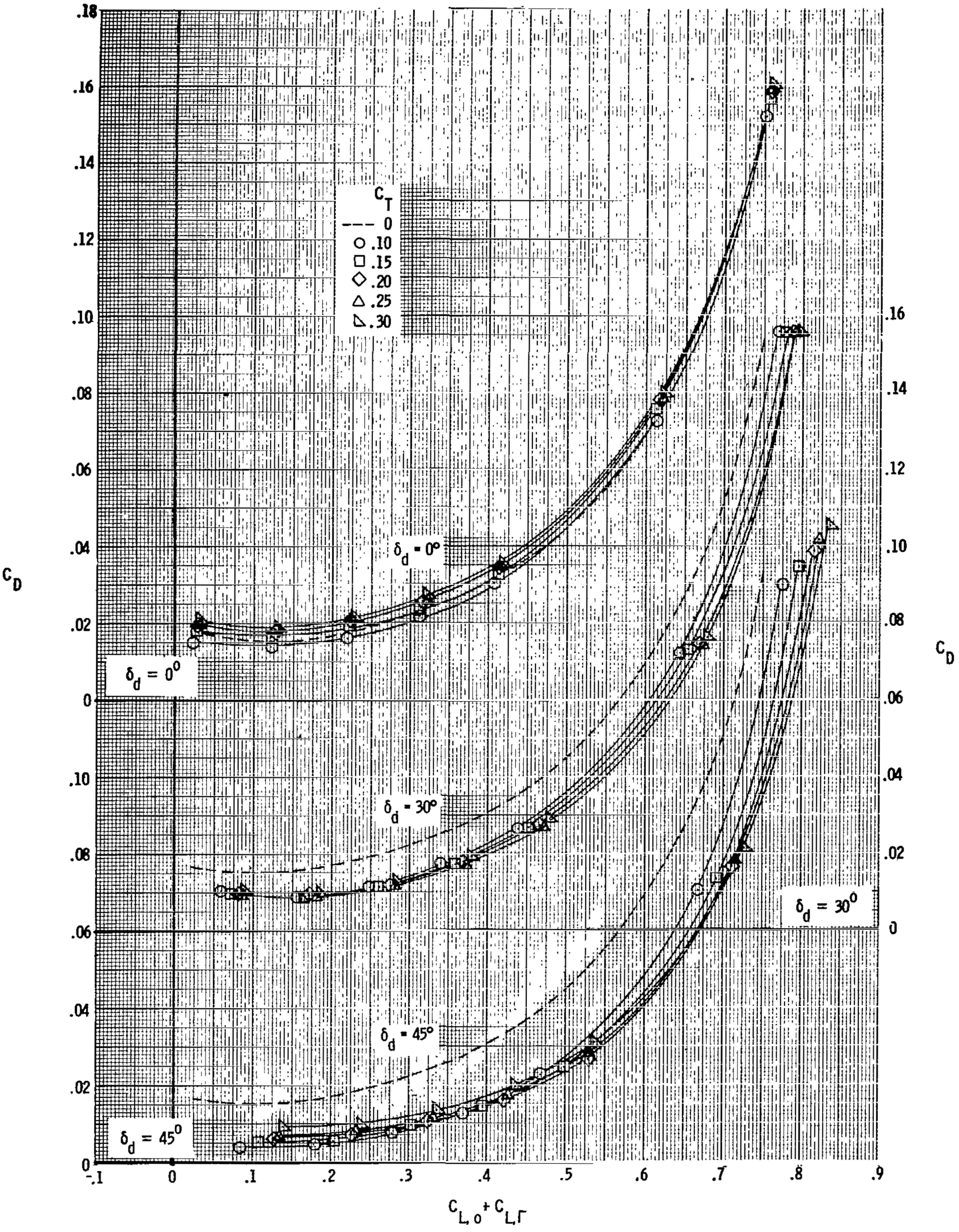

(a) $M = 0.40$.

Figure 46.- Variation of drag coefficient with jet off plus supercirculation lift for the various nozzles.

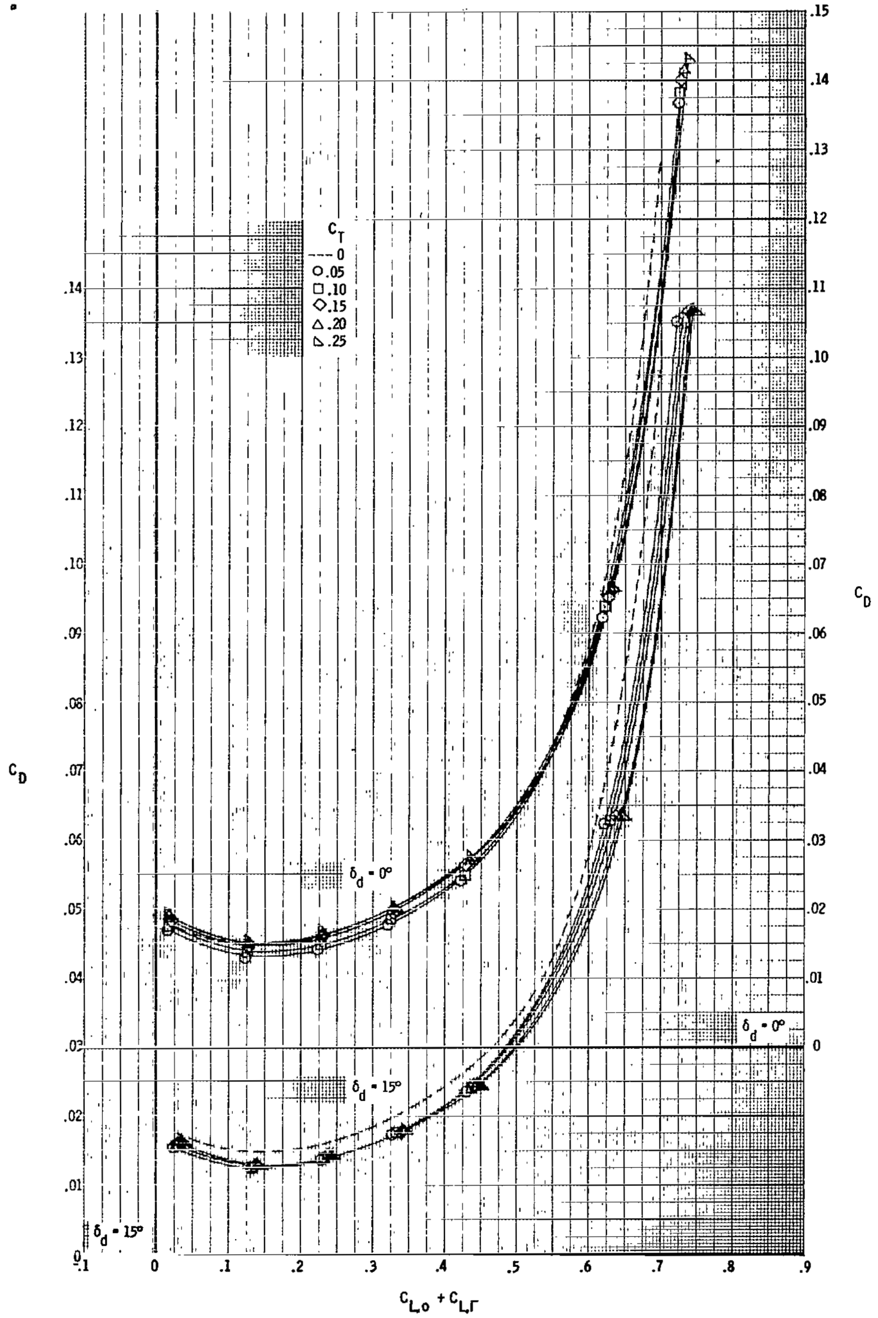

(b) M = 0.70.

Figure 46.- Continued.

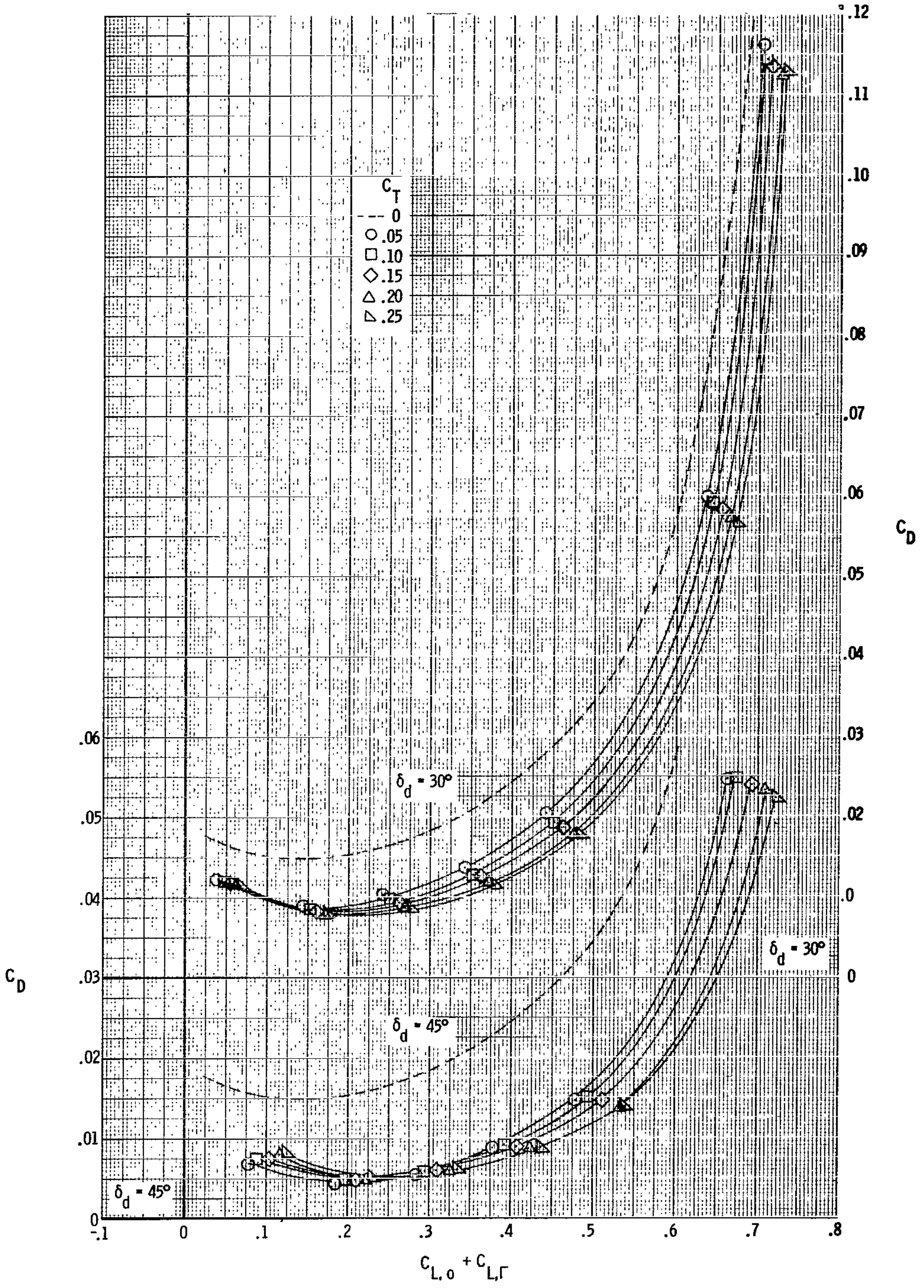

(b) Concluded.

Figure 46.- Continued.

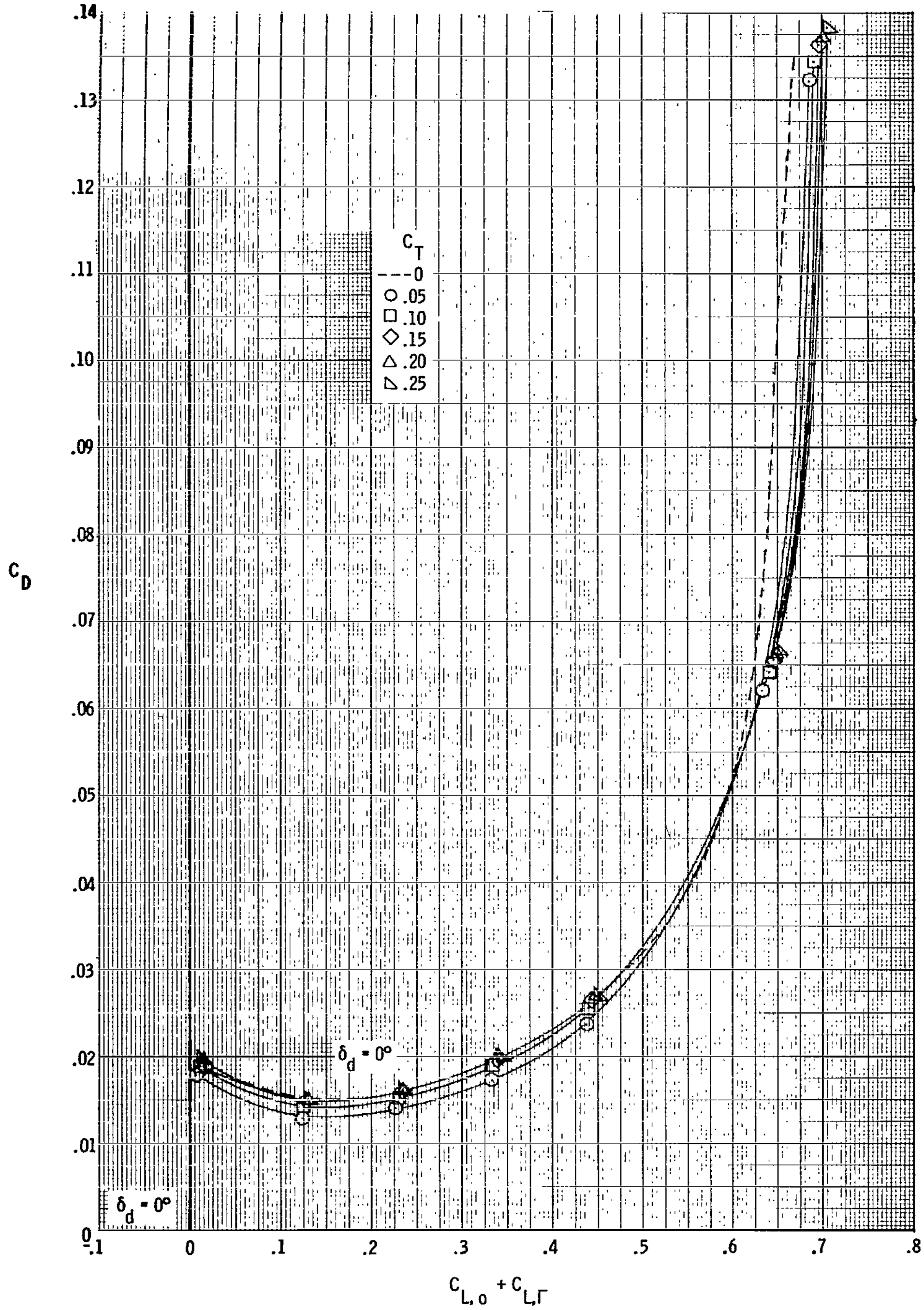

(c) M = 0.80.

Figure 46.- Continued.

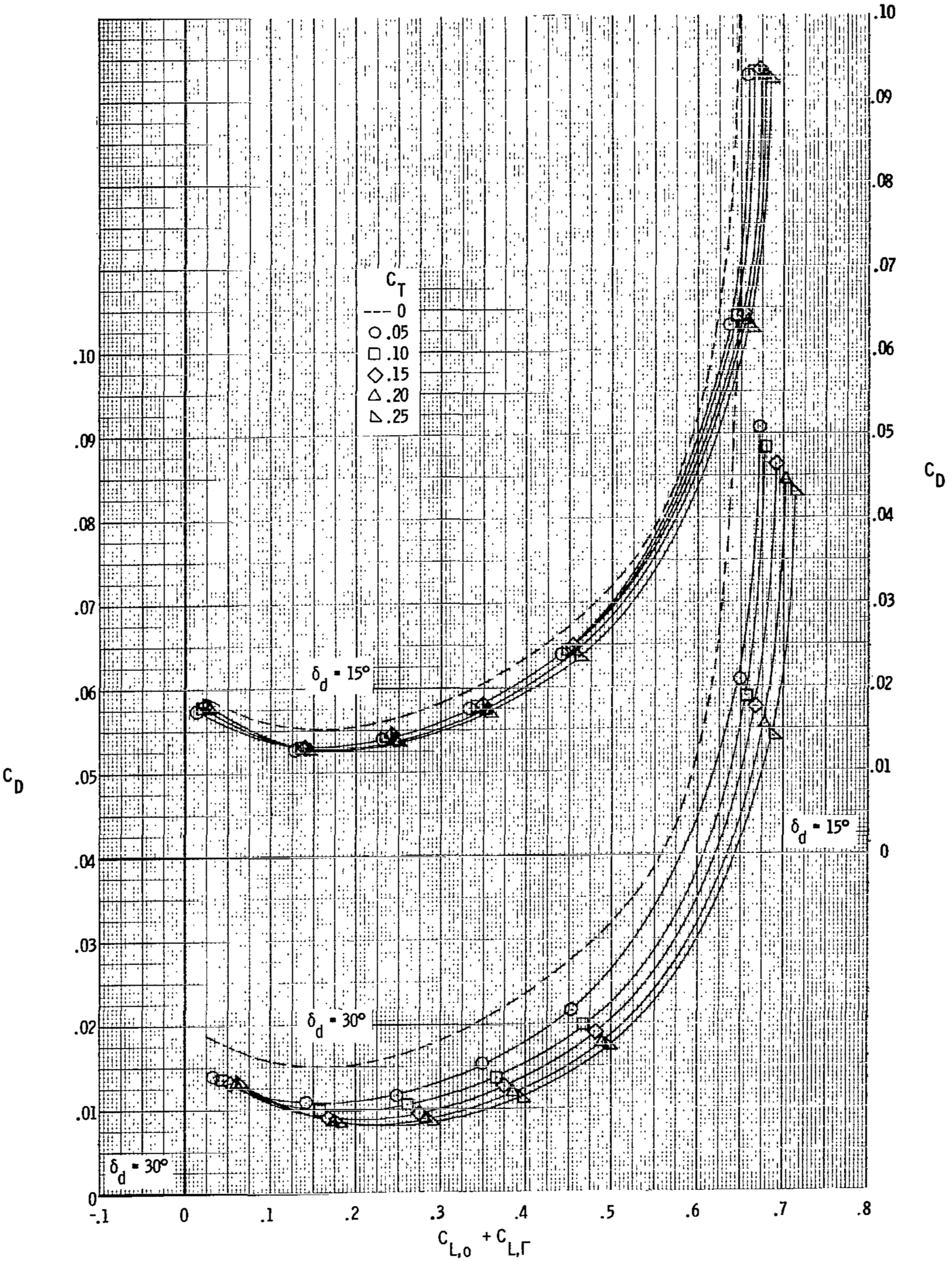

(c) Concluded.

Figure 46.- Continued.

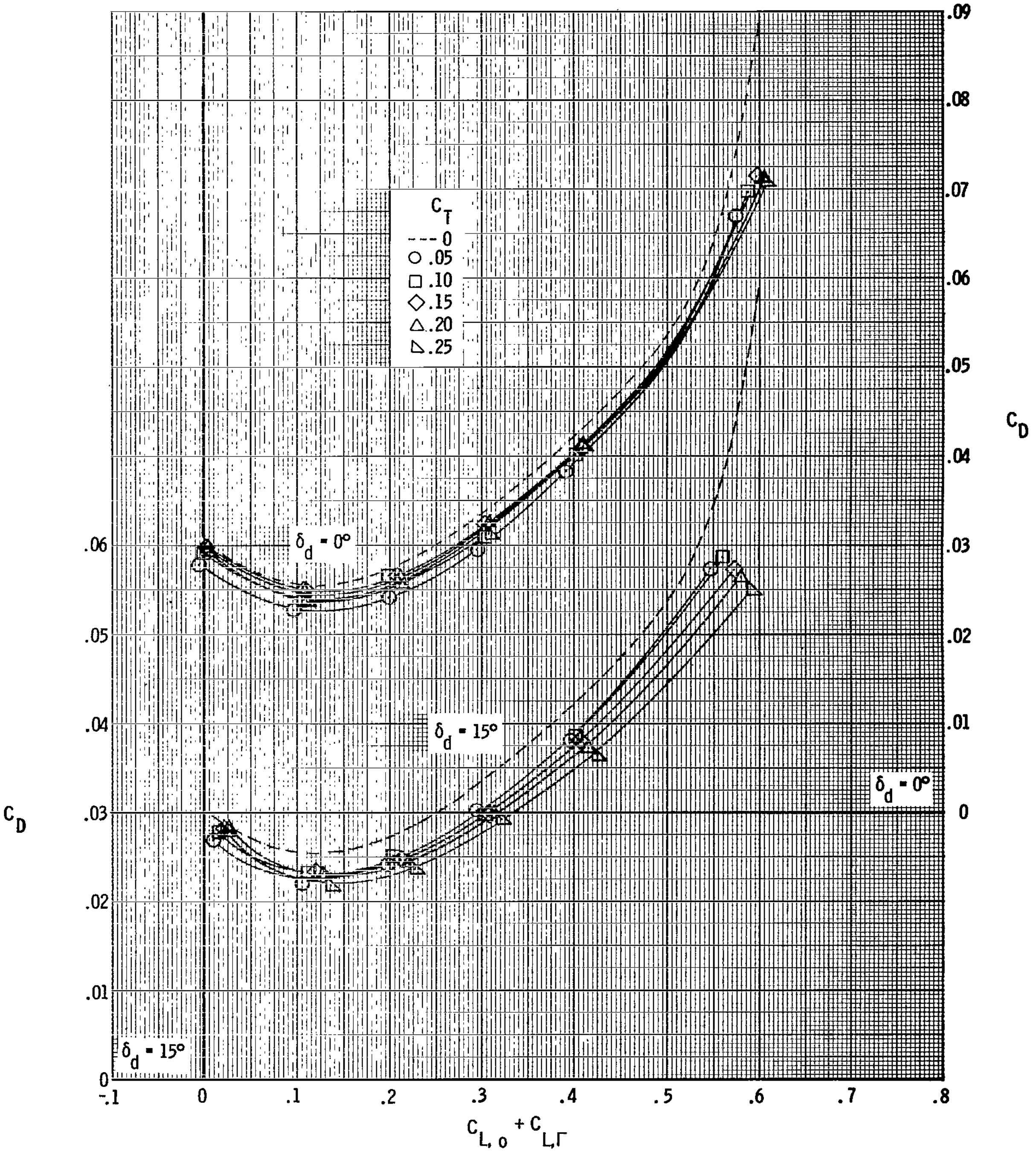

(d) M = 0.90.

Figure 46.- Continued.

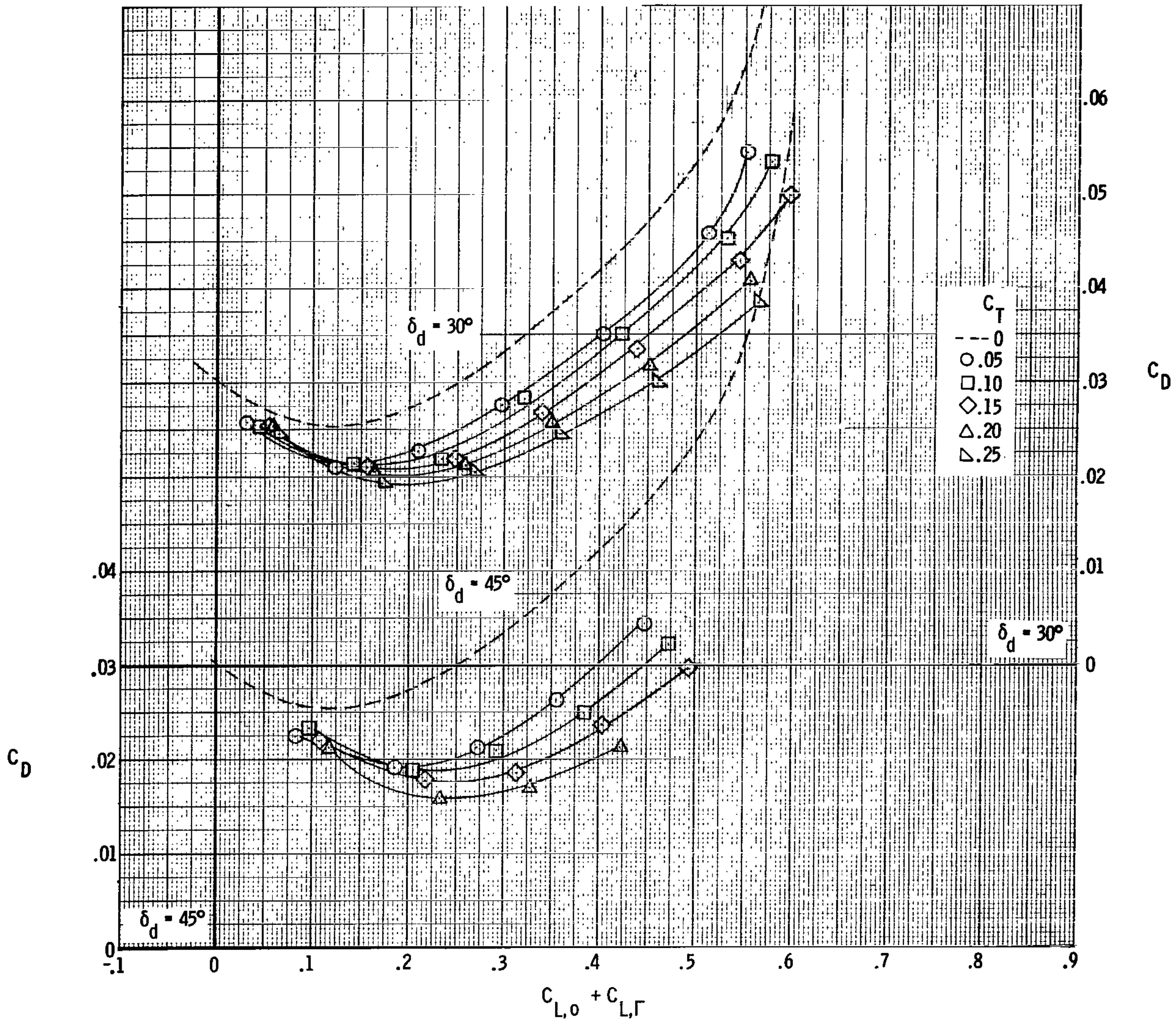

(d) Concluded.

Figure 46.- Continued.

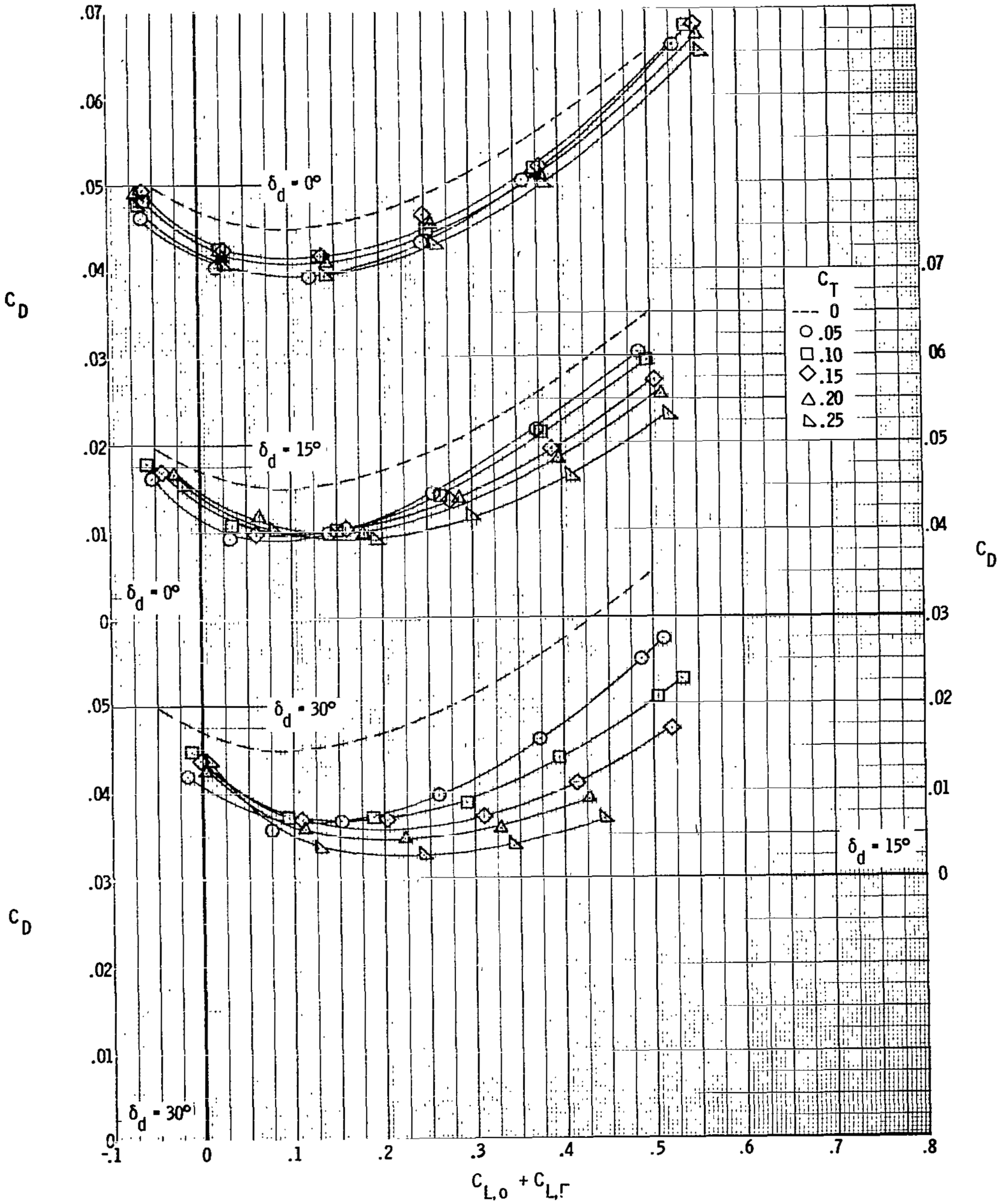

(e) M = 0.95.

Figure 46.- Continued.

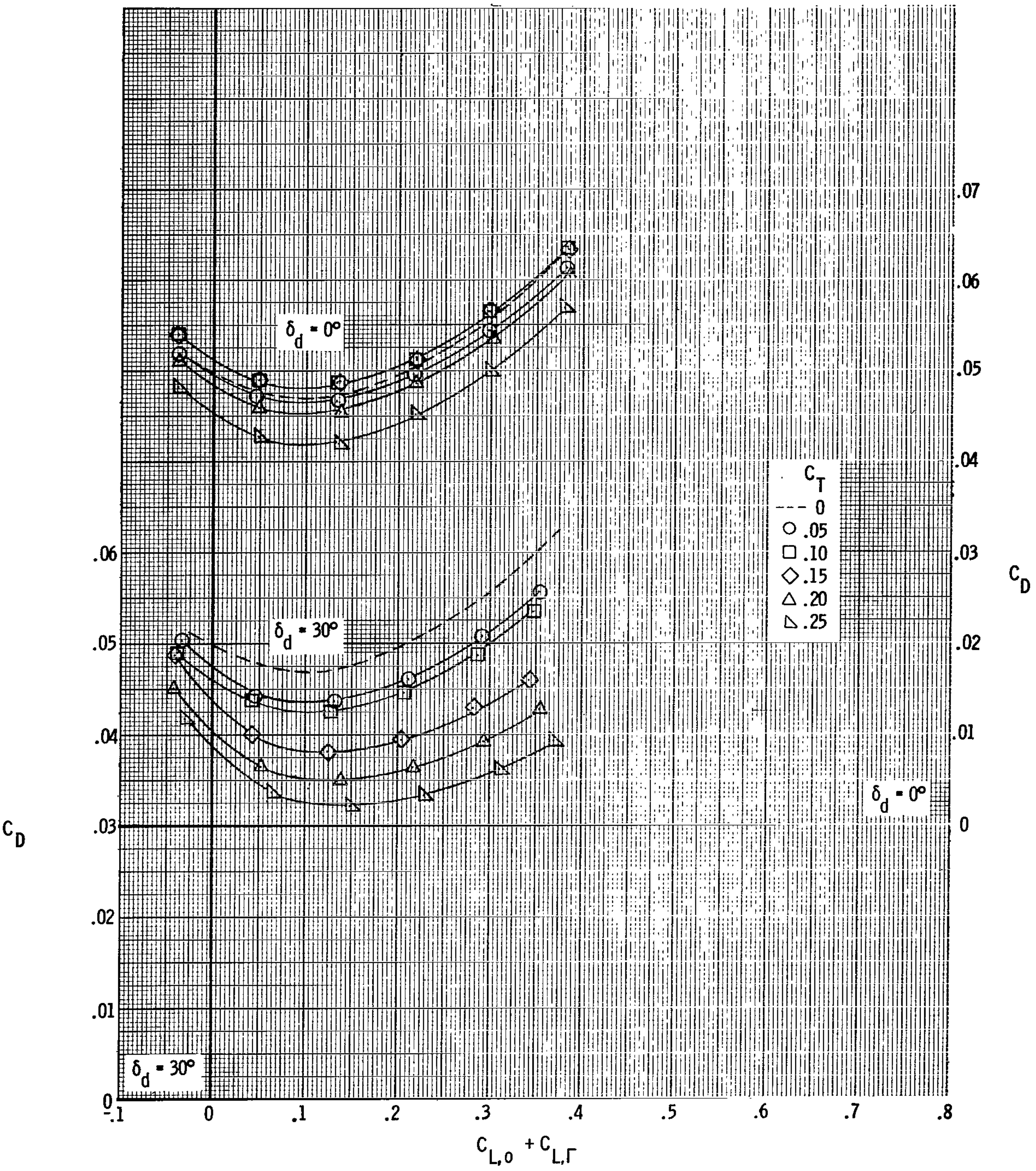

(f) M = 1.20.

Figure 46.- Concluded.

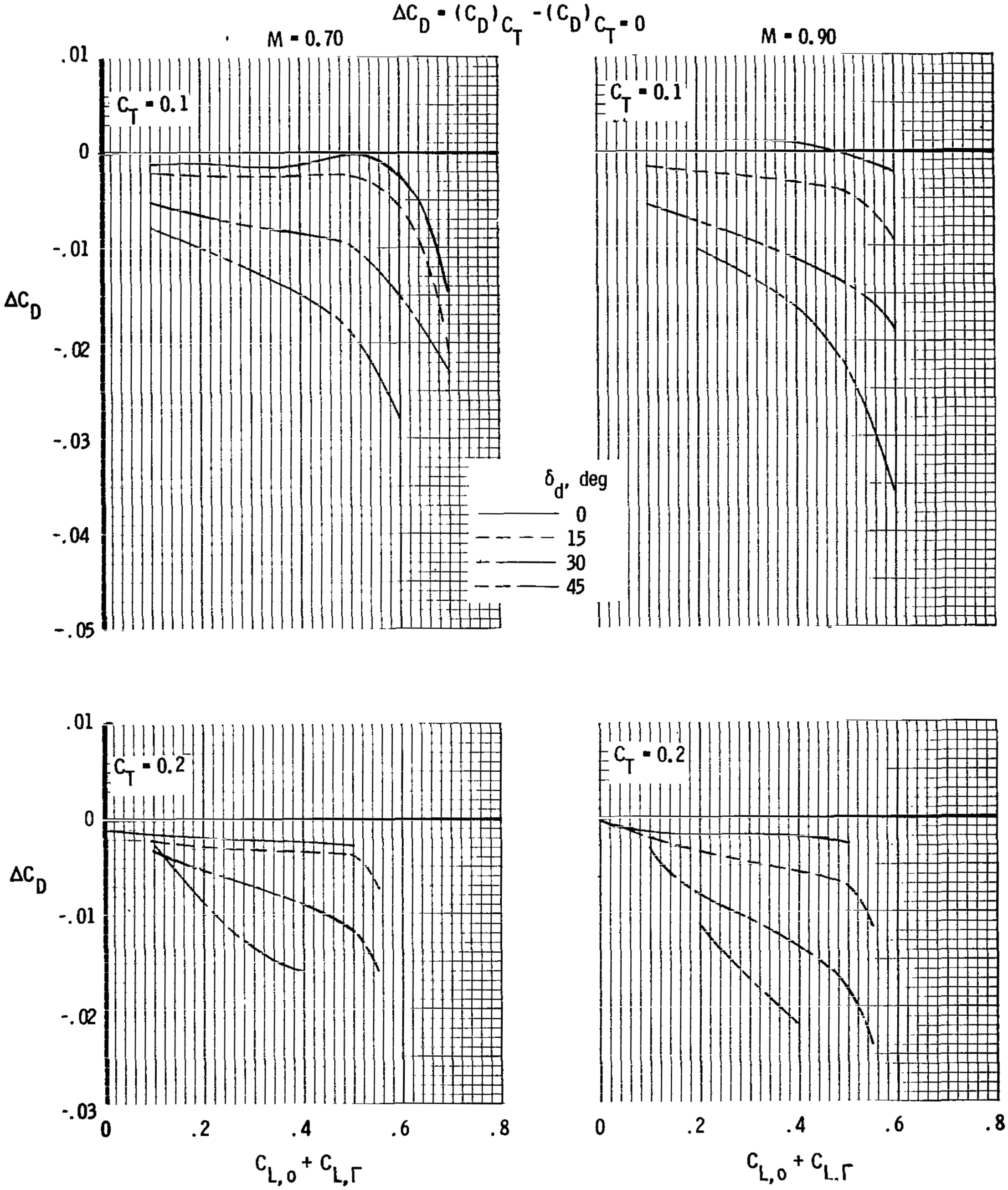

Figure 47. - Effect of jet operation on incremental drag.

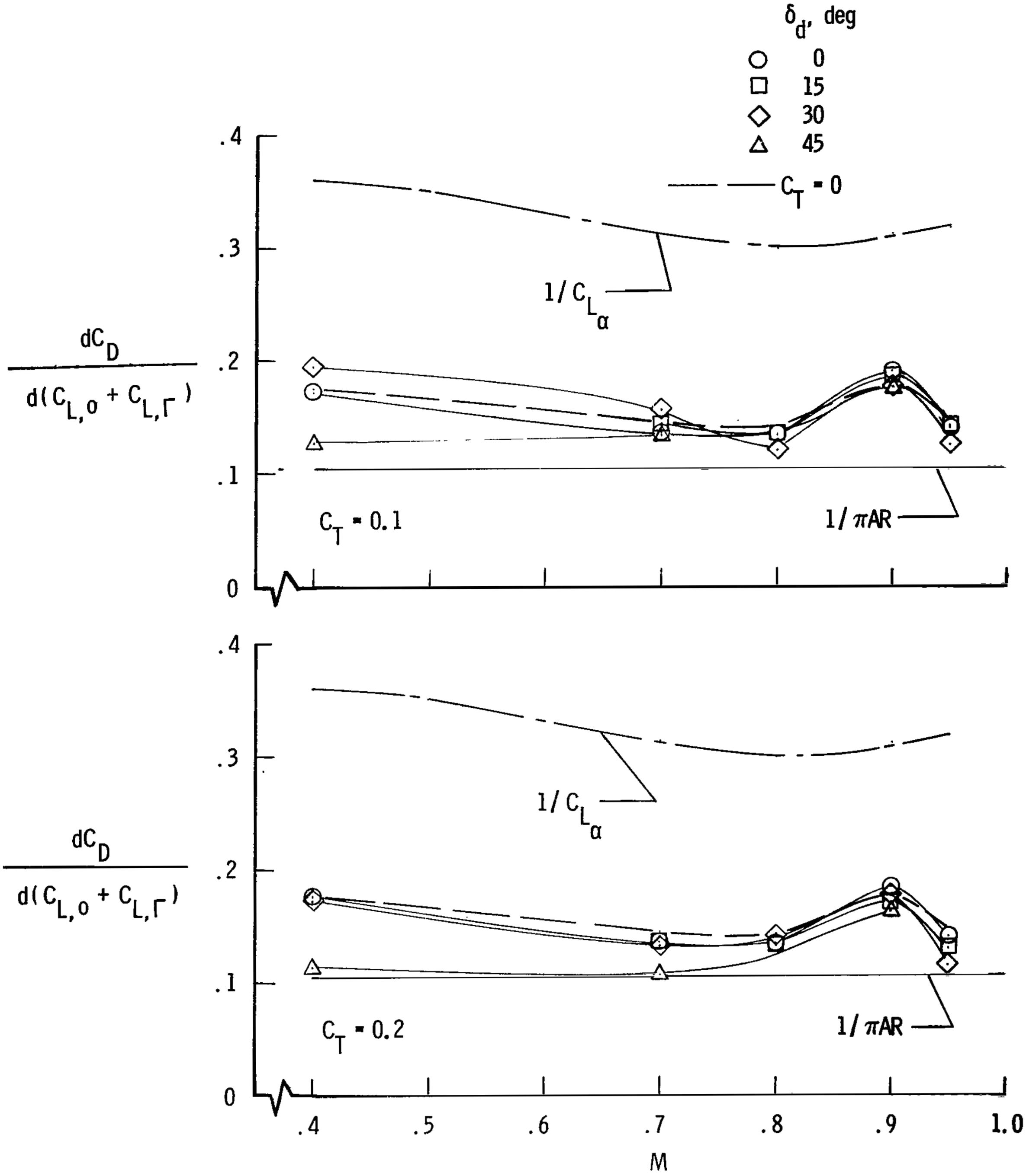

Figure 48.- Summary of drag-due-to-lift characteristics with Mach number for nozzles tested at selected pressure ratio. Symbols represent interpolated points.

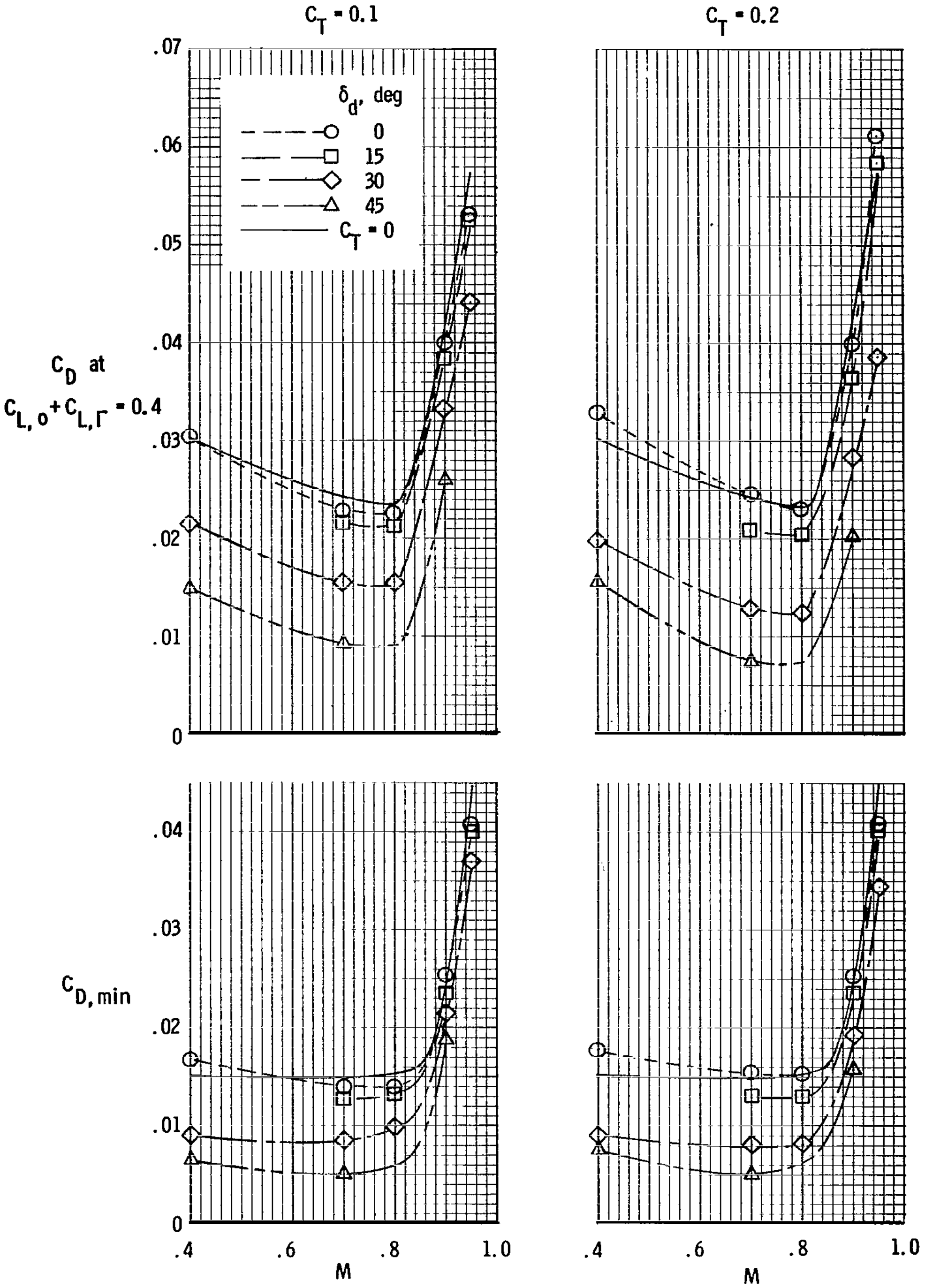

Figure 49.- Variation of drag coefficient with Mach number at selected values of lift and thrust coefficient. Symbols represent interpolated points.

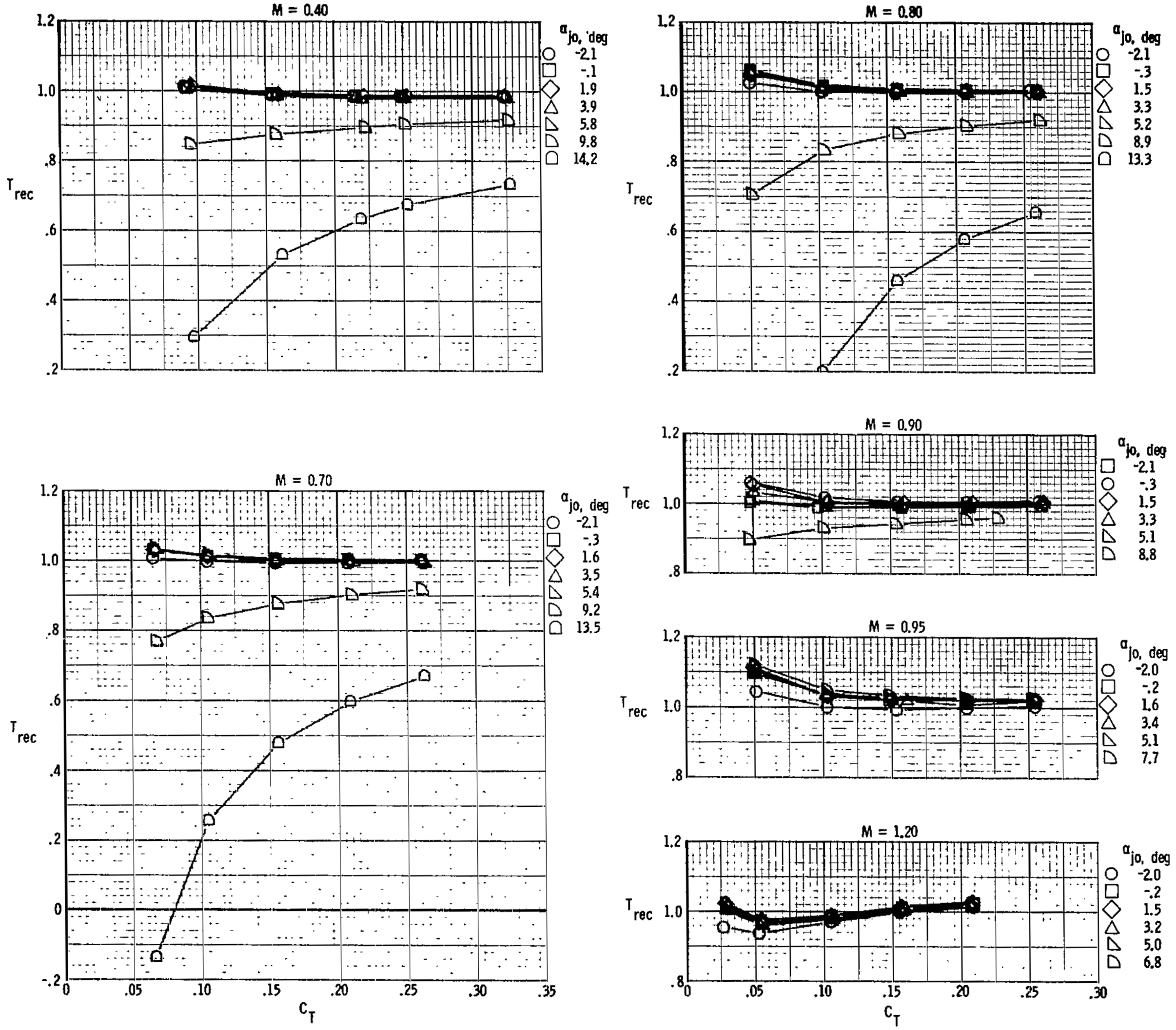

Figure 50.- Variation of thrust recovery with thrust coefficient. $\delta_d = 0^{\circ}$.

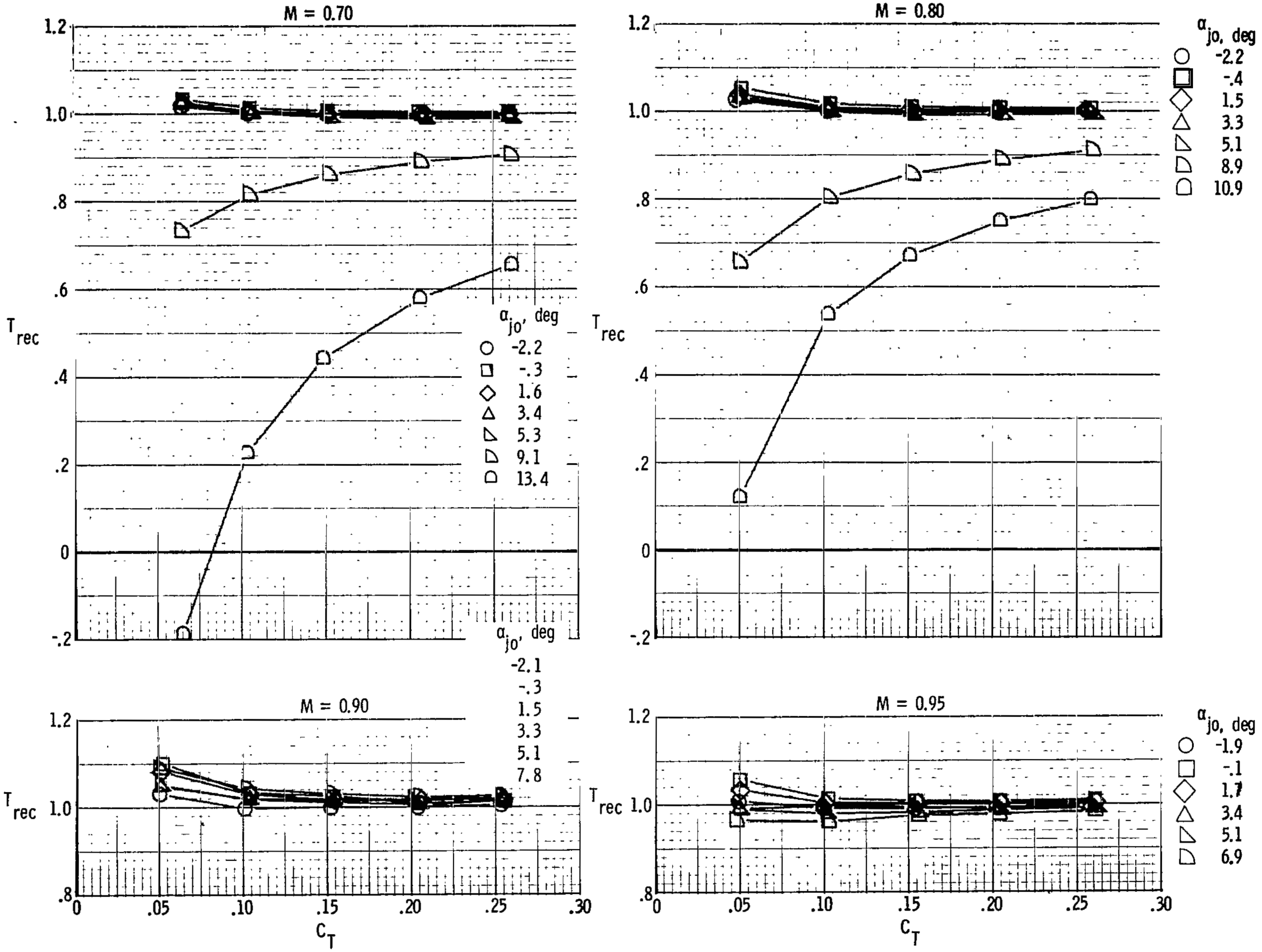

Figure 51.- Variation of thrust recovery with thrust coefficient. $\delta_d = 15^o$.

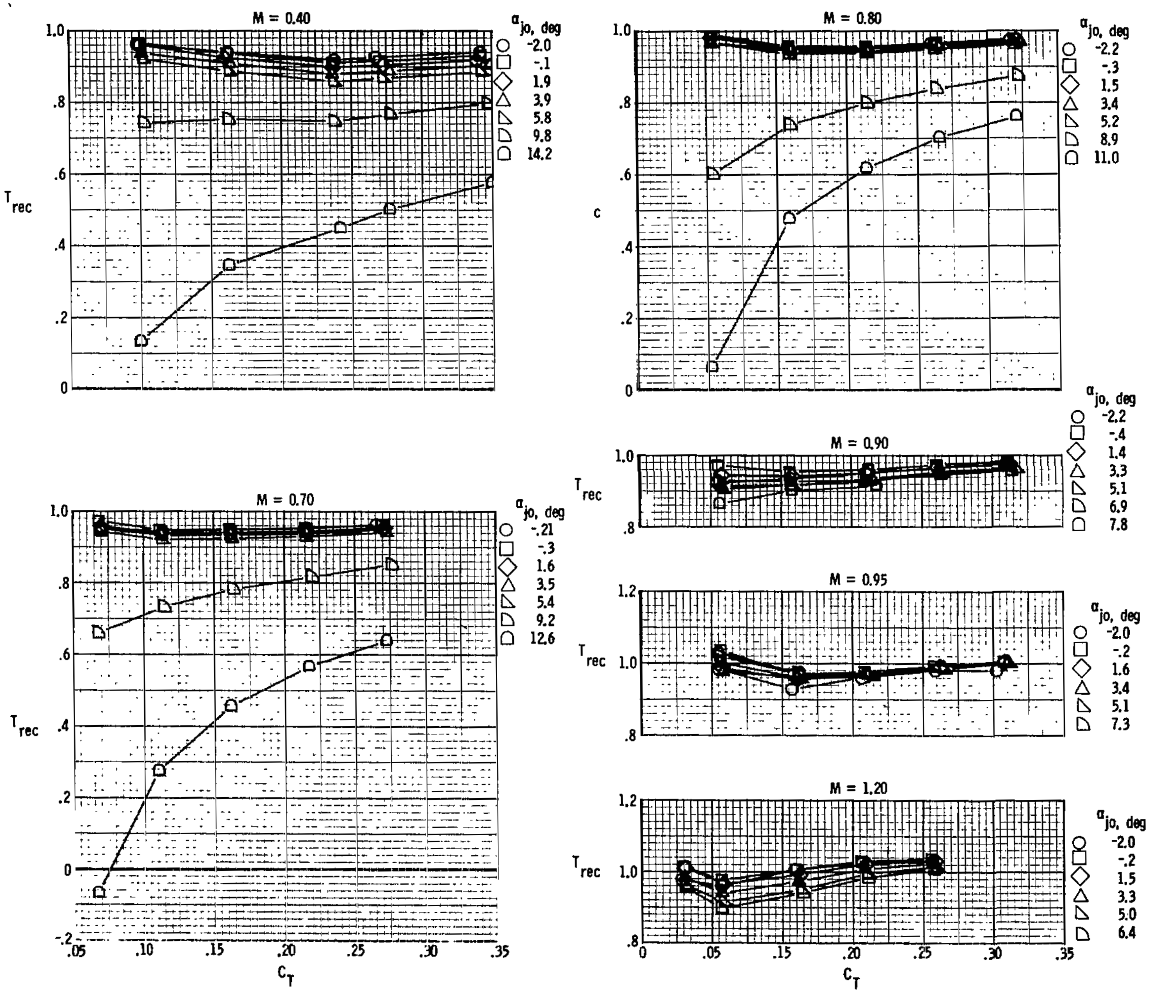

Figure 52.- Variation of thrust recovery with thrust coefficient. $\delta_d = 30^o$.

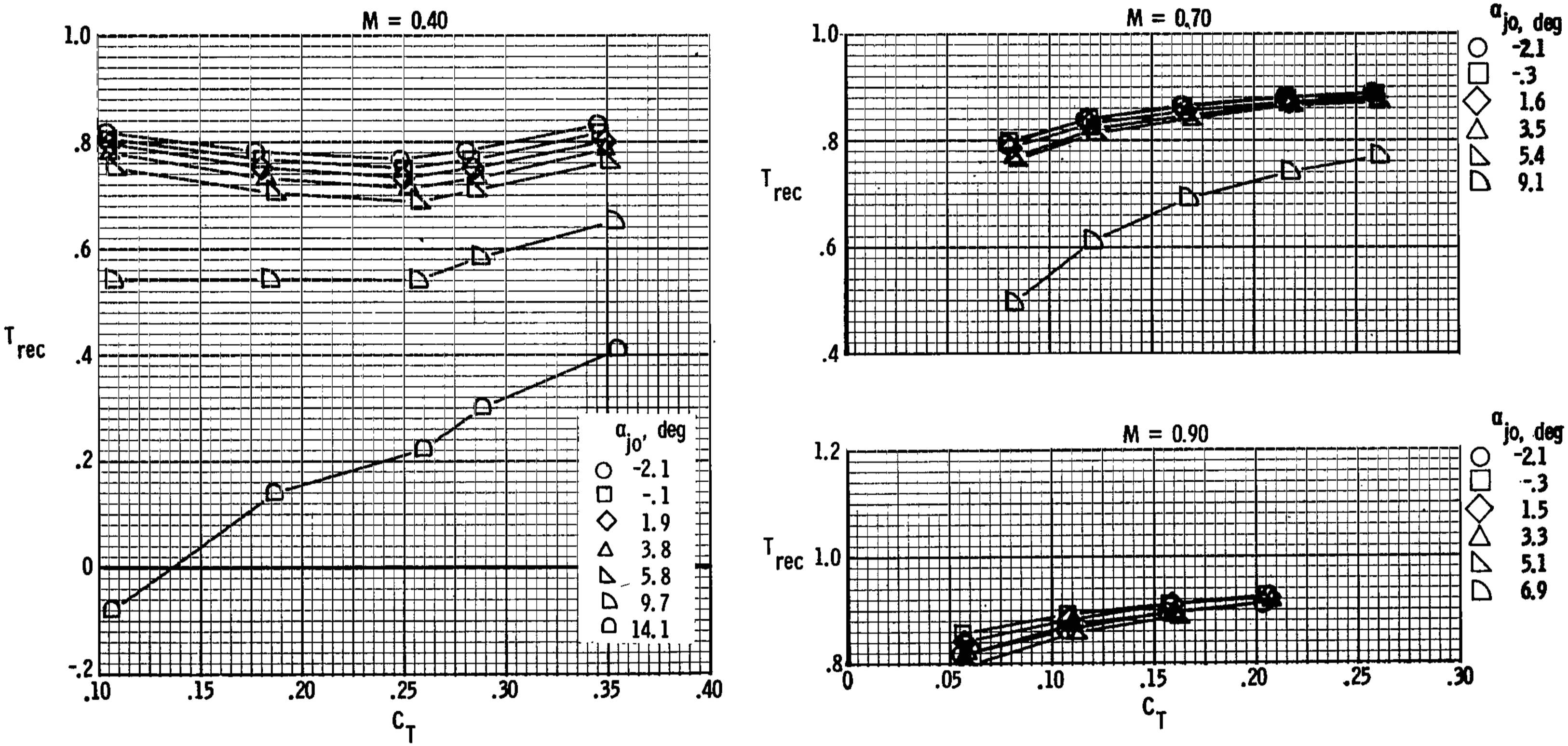

Figure 53.- Variation of thrust recovery with thrust coefficient. $\delta_d = 45^{\circ}$.

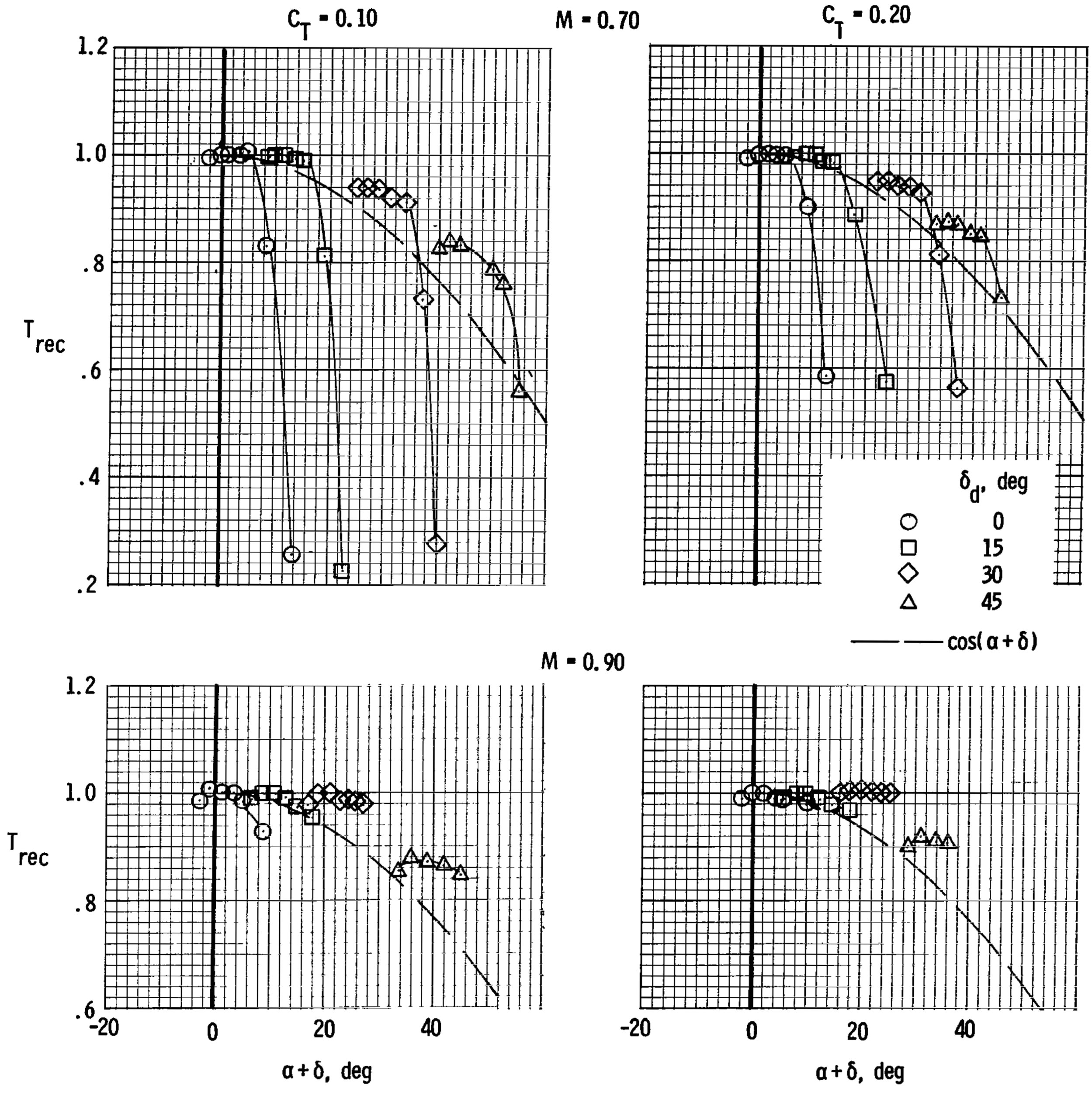

Figure 54.- Variation of thrust recovery with thrust vector angle for selected thrust coefficients and Mach numbers.

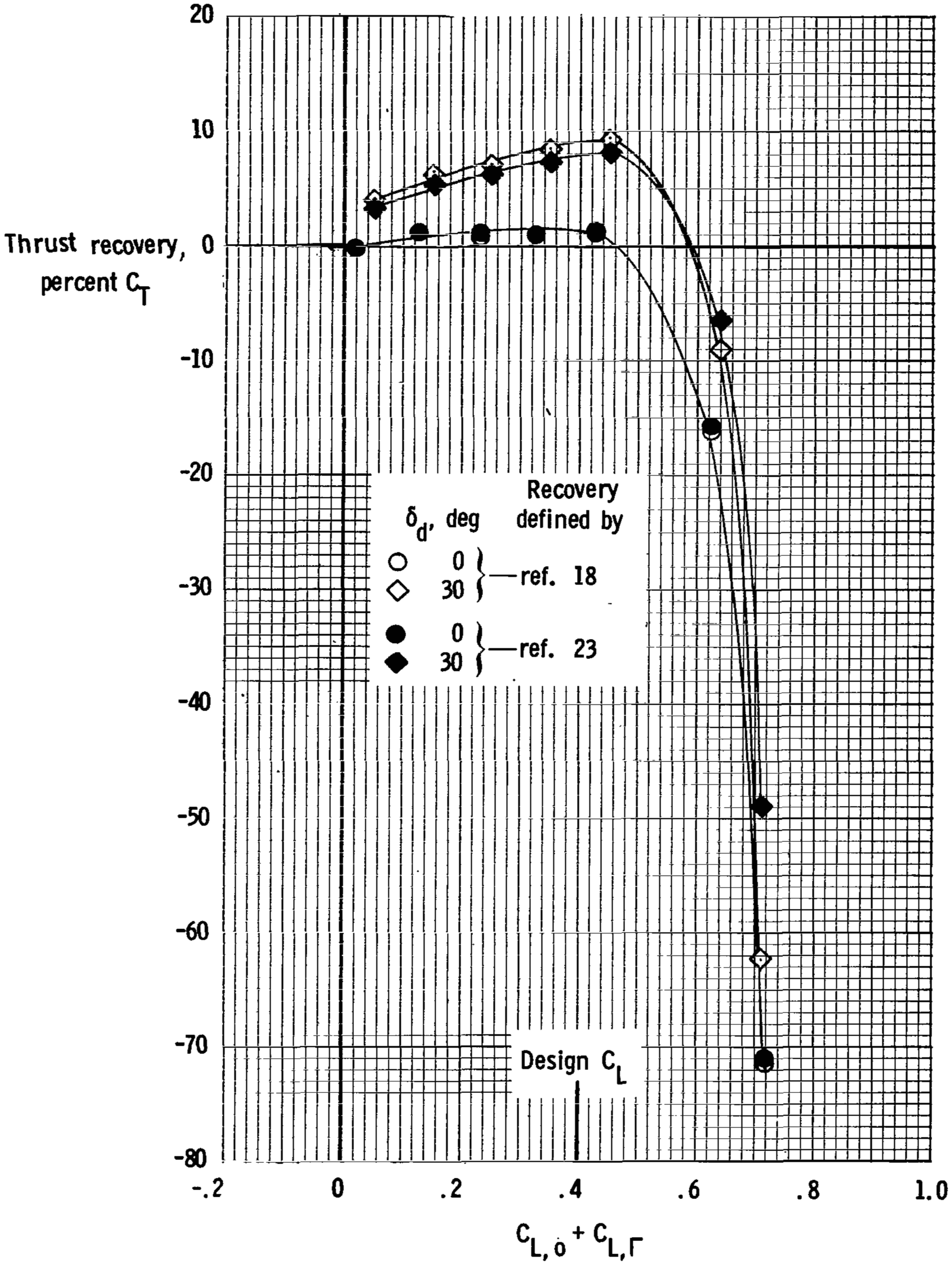

Figure 55.- Variation of thrust recovery in terms of percent C_T with aerodynamic lift coefficient at $M = 0.70$. $C_T = 0.10$.

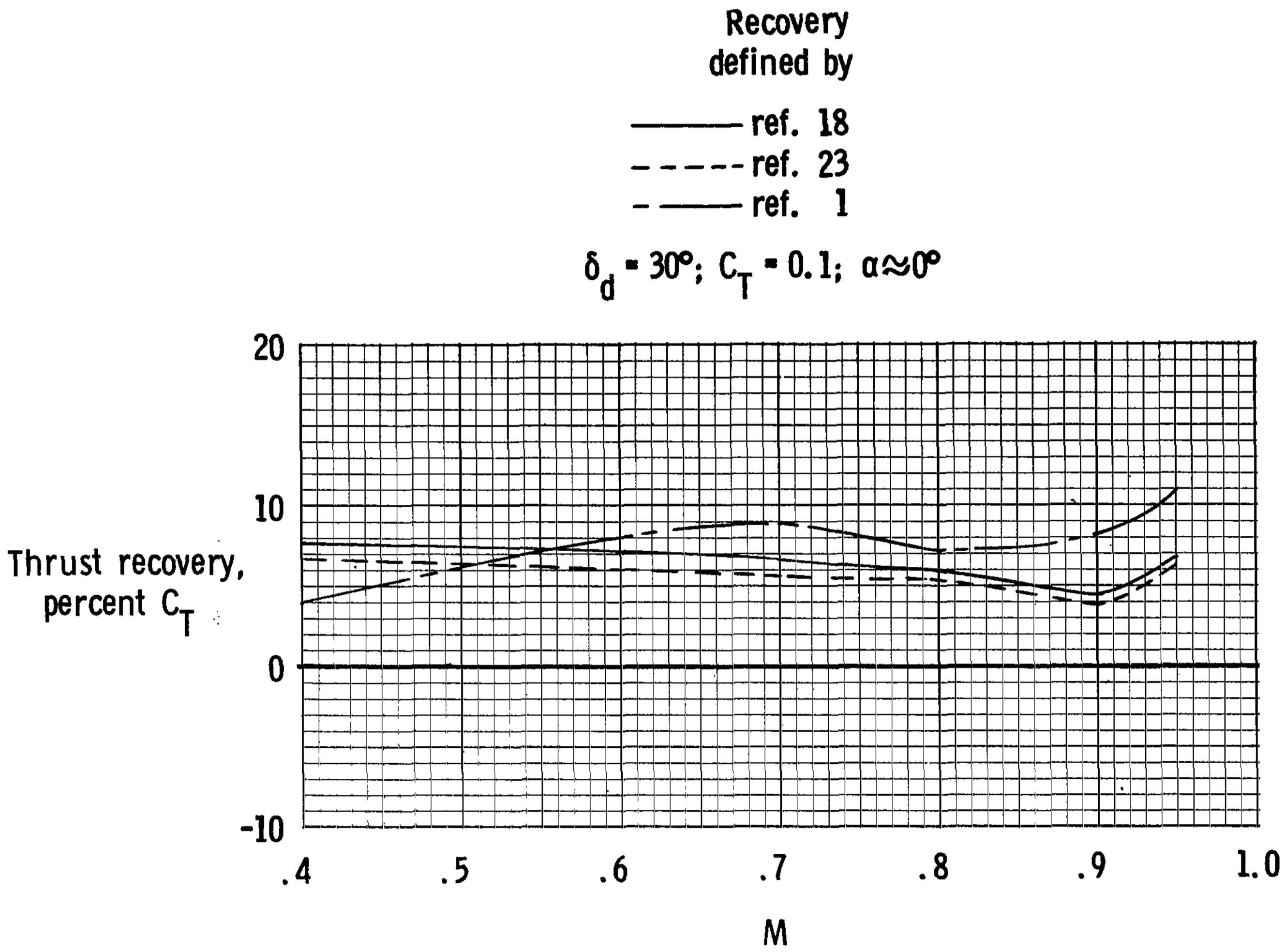

Figure 56.- Comparison of variation of thrust recovery in terms of percent thrust coefficient with Mach number as determined by three methods.

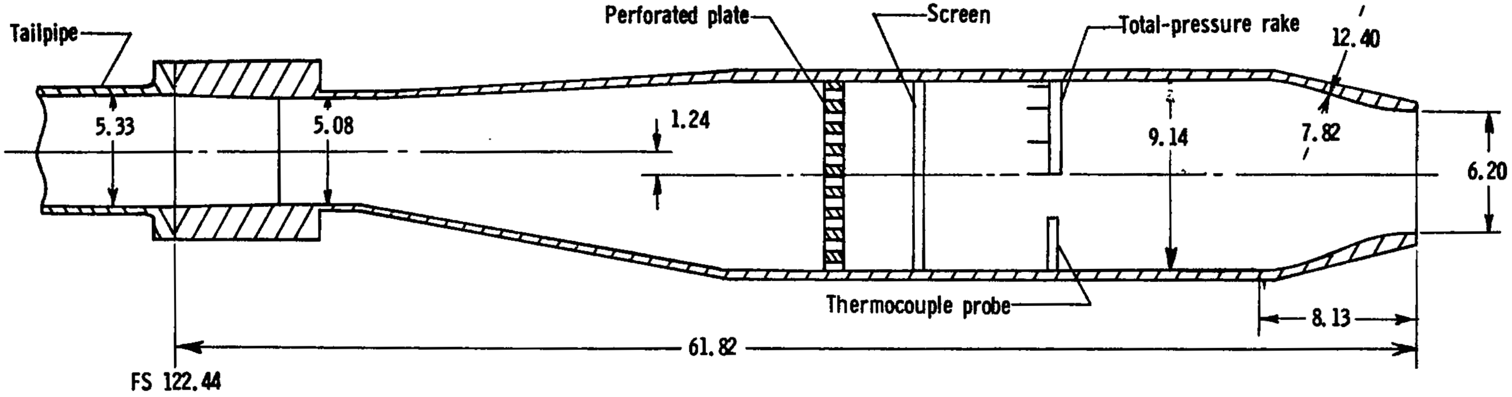

Figure 57.- Sketch of top view of calibration nozzles. All dimensions are in centimeters.

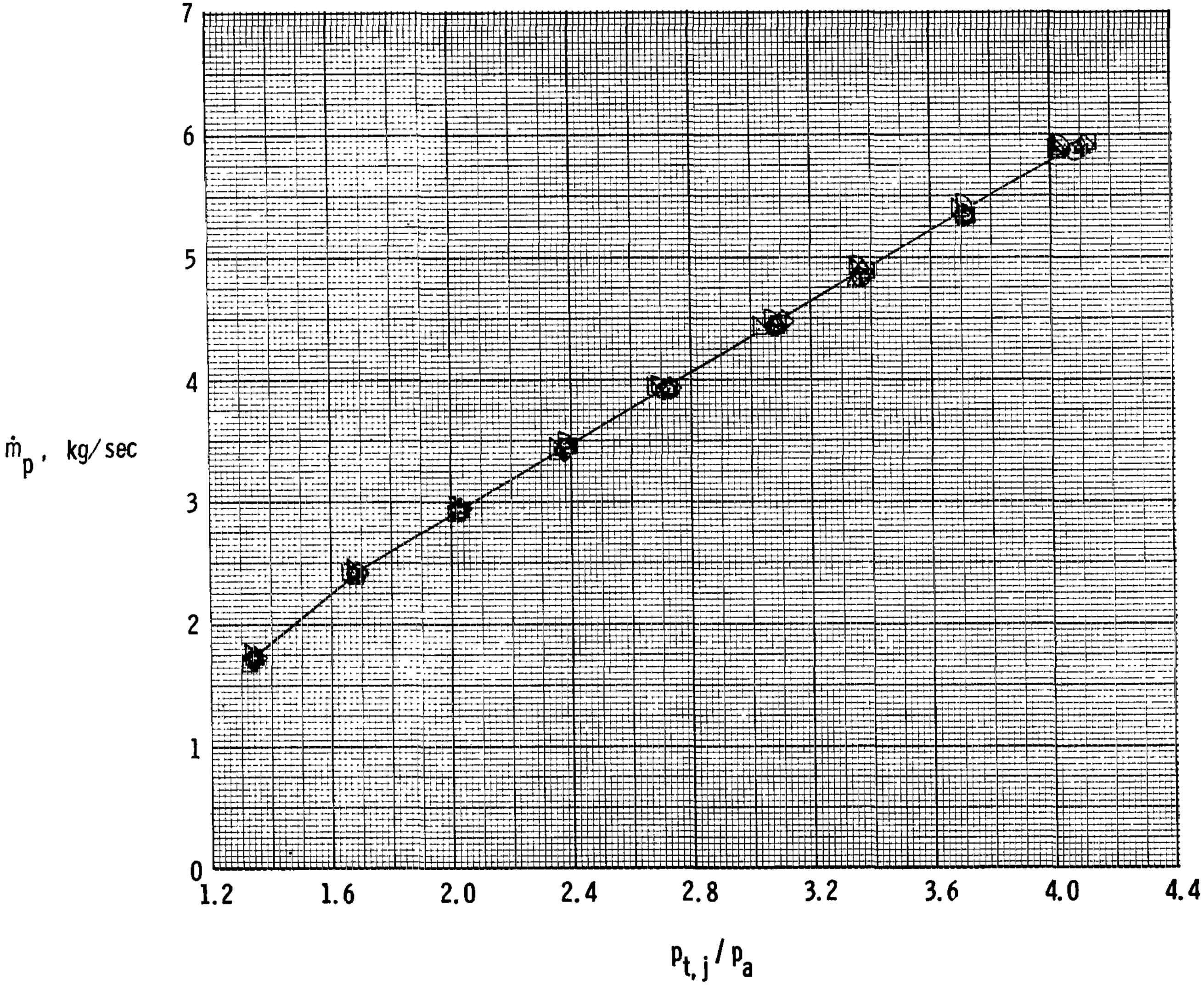

Figure 58.- Variation of mass-flow rate with nozzle pressure ratio. Each symbol denotes a static run.

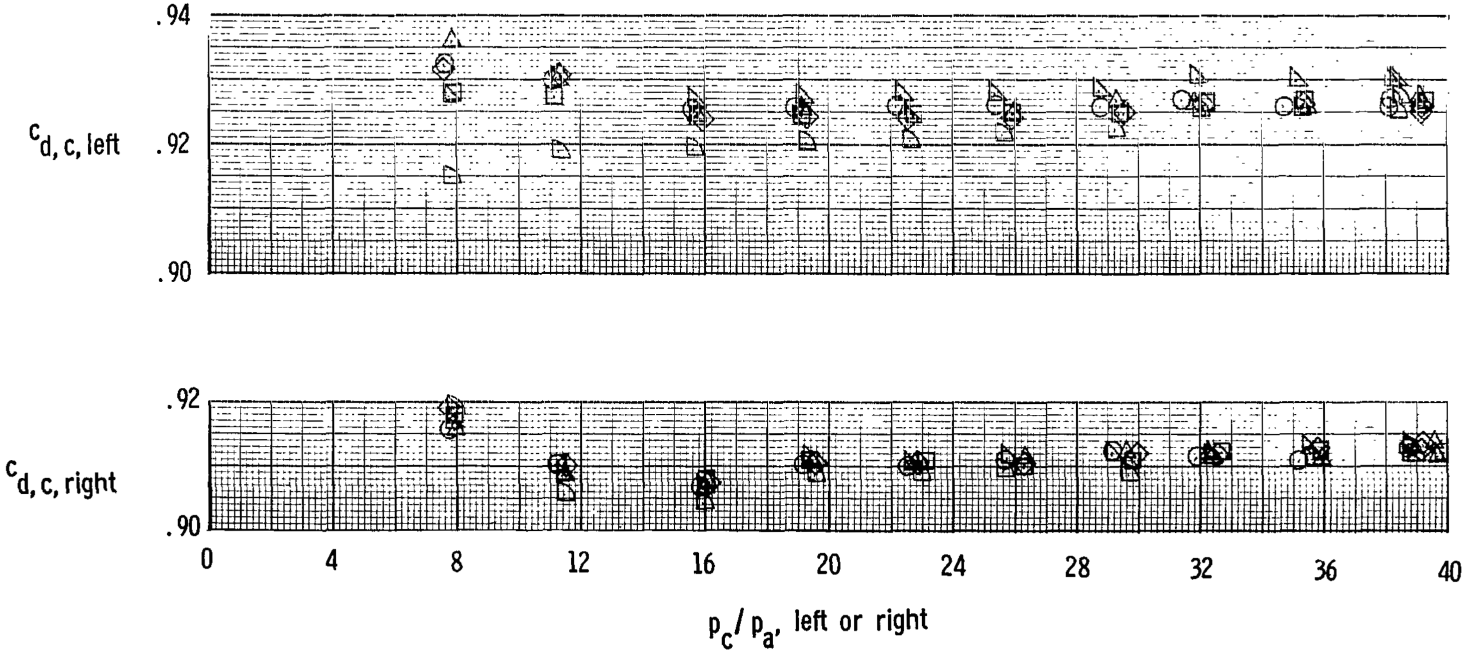

Figure 59.- Variation of orifice discharge coefficient with chamber pressure ratio. Each symbol represents a static run.

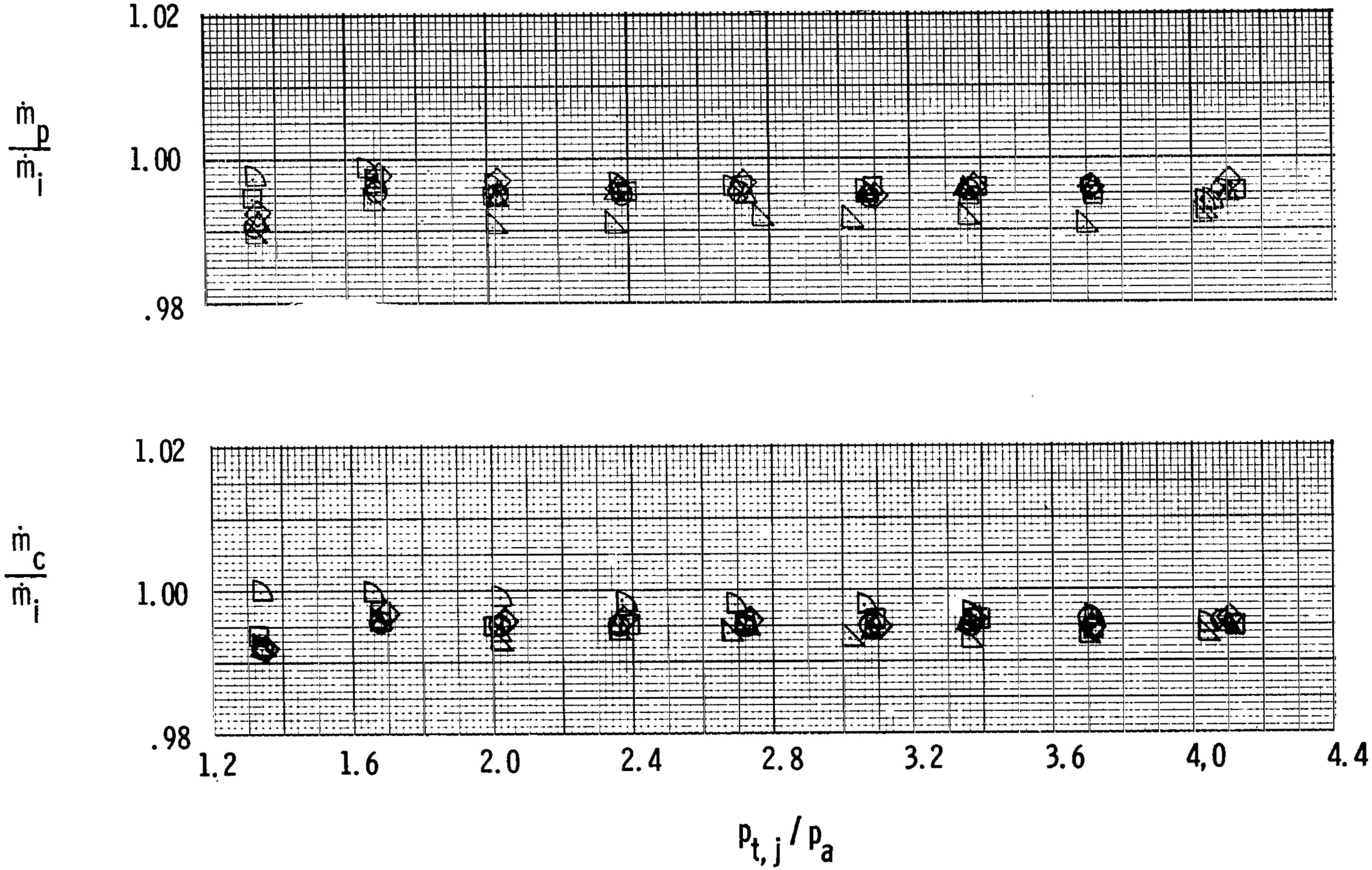

Figure 60. - Variation of mass-flow ratios with nozzle pressure ratio. Each symbol represents a static run.

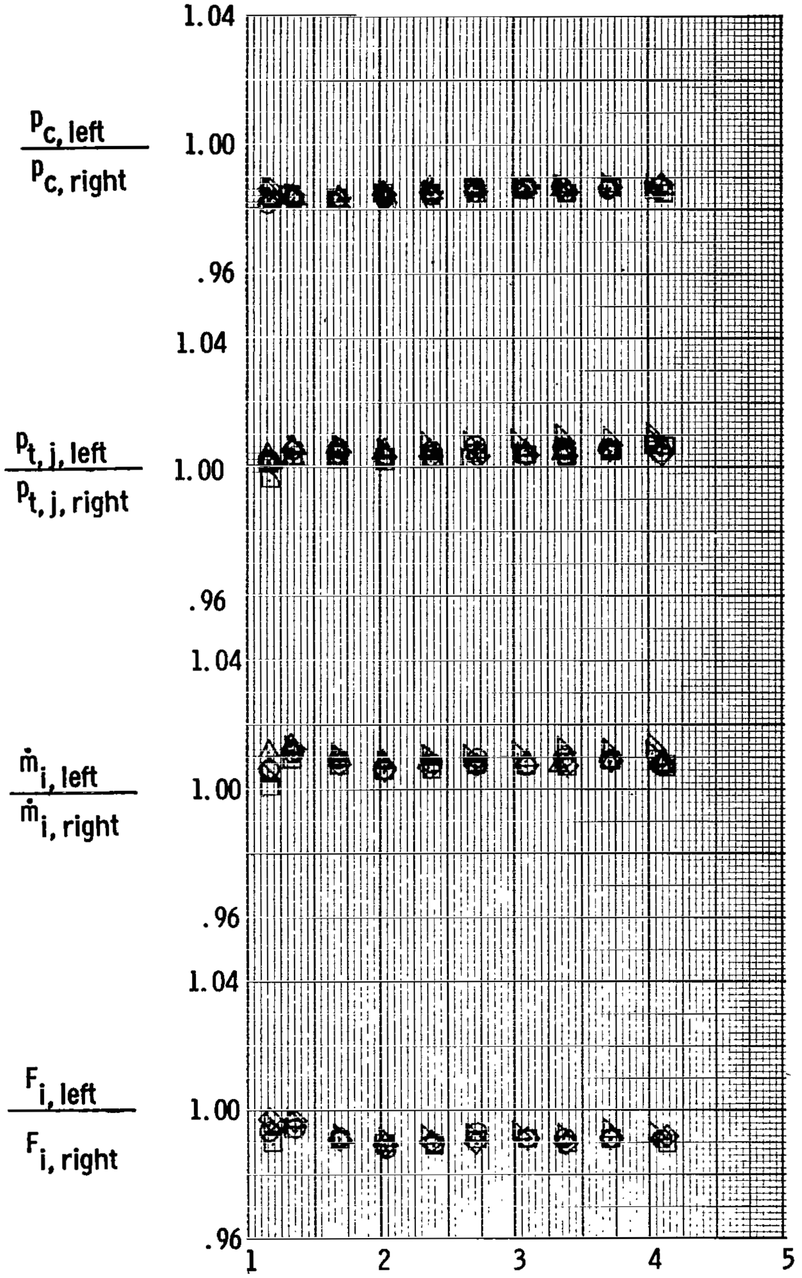

Figure 61. - Flow control valve performance. Each symbol represents a static run.

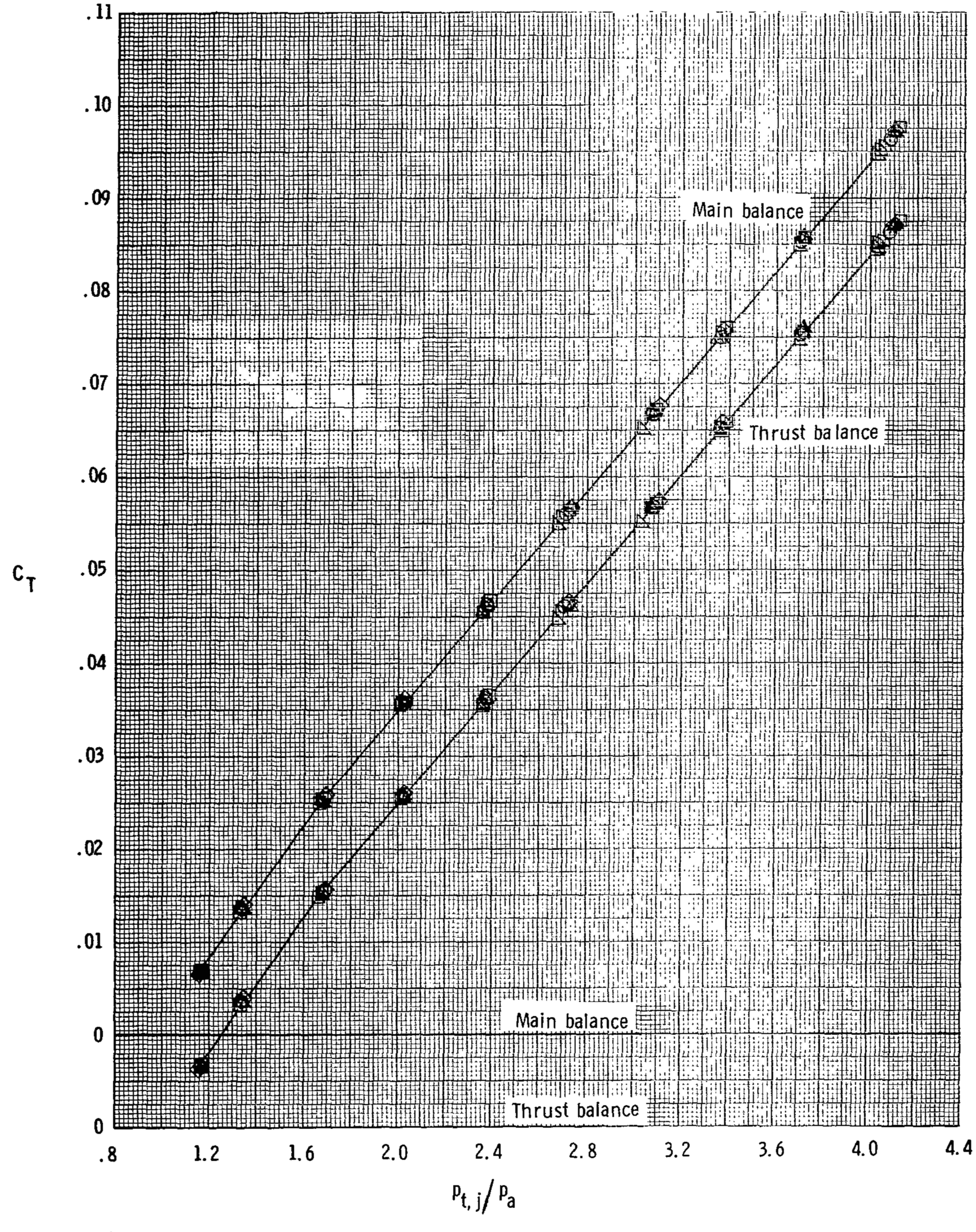

Figure 62. - Variation of measured thrust coefficient with nozzle pressure ratio. Each symbol represents a static run.

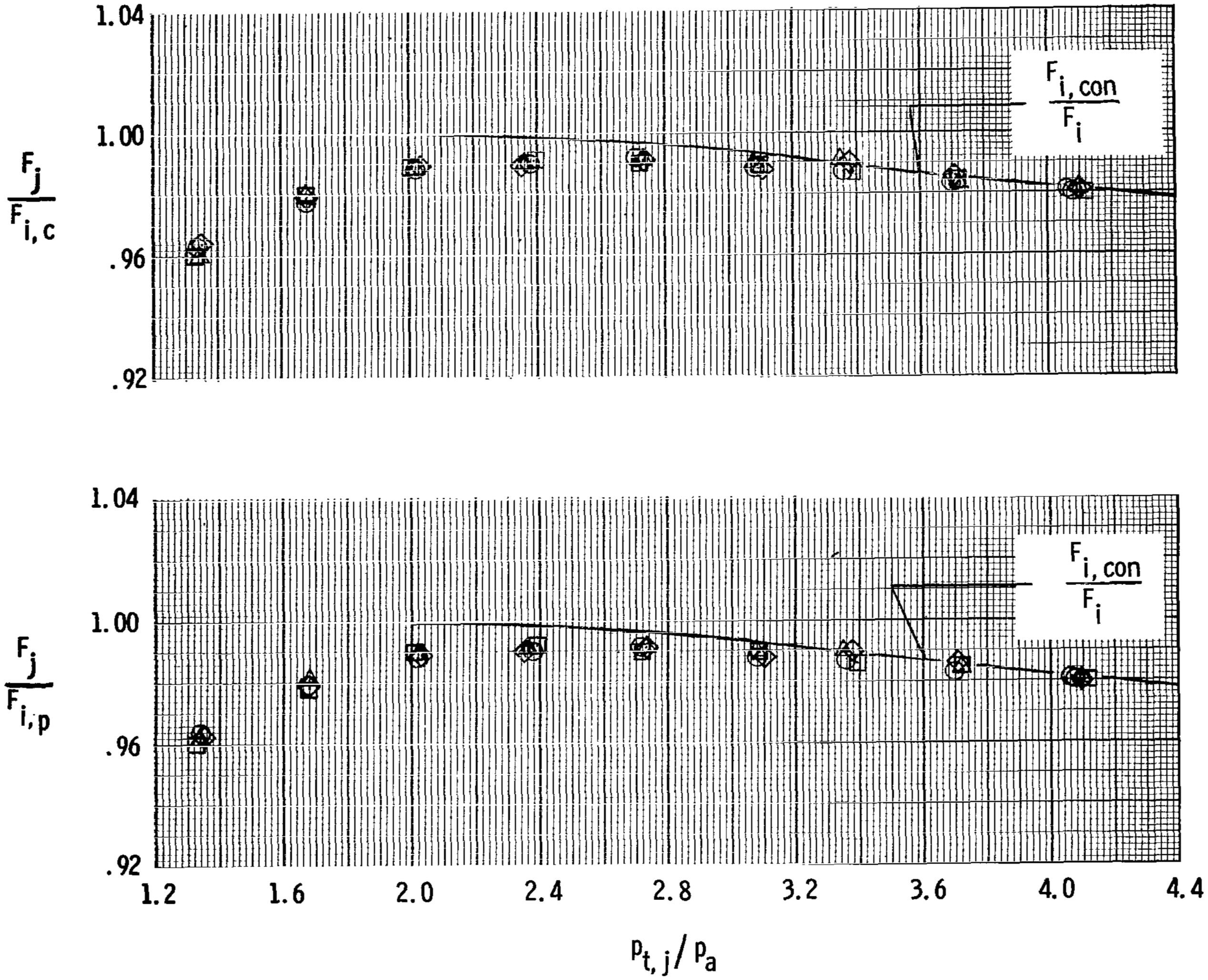

Figure 63.- Variation of thrust force ratio with jet total pressure ratio.

*U.S. GOVERNMENT PRINTING OFFICE: 1975 - 635-275/44

NATIONAL AERONAUTICS AND SPACE ADMINISTRATION
WASHINGTON, D.C. 20546

OFFICIAL BUSINESS
PENALTY FOR PRIVATE USE $300

SPECIAL FOURTH-CLASS RATE
BOOK

POSTAGE AND FEES PAID
NATIONAL AERONAUTICS AND
SPACE ADMINISTRATION
451

U.S.MAIL

082 001 C1 U A 751121 S00903DS
DEPT OF THE AIR FORCE
AF WEAPONS LABORATORY
ATTN: TECHNICAL LIBRARY (SUL)
KIRTLAND AFB NM 87117

POSTMASTER: If Undeliverable (Section 158 Postal Manual) Do Not Return

> *"The aeronautical and space activities of the United States shall be conducted so as to contribute . . . to the expansion of human knowledge of phenomena in the atmosphere and space. The Administration shall provide for the widest practicable and appropriate dissemination of information concerning its activities and the results thereof."*
>
> —NATIONAL AERONAUTICS AND SPACE ACT OF 1958

NASA SCIENTIFIC AND TECHNICAL PUBLICATIONS

TECHNICAL REPORTS: Scientific and technical information considered important, complete, and a lasting contribution to existing knowledge.

TECHNICAL NOTES: Information less broad in scope but nevertheless of importance as a contribution to existing knowledge.

TECHNICAL MEMORANDUMS: Information receiving limited distribution because of preliminary data, security classification, or other reasons. Also includes conference proceedings with either limited or unlimited distribution.

CONTRACTOR REPORTS: Scientific and technical information generated under a NASA contract or grant and considered an important contribution to existing knowledge.

TECHNICAL TRANSLATIONS: Information published in a foreign language considered to merit NASA distribution in English.

SPECIAL PUBLICATIONS: Information derived from or of value to NASA activities. Publications include final reports of major projects, monographs, data compilations, handbooks, sourcebooks, and special bibliographies.

TECHNOLOGY UTILIZATION PUBLICATIONS: Information on technology used by NASA that may be of particular interest in commercial and other non-aerospace applications. Publications include Tech Briefs, Technology Utilization Reports and Technology Surveys.

Details on the availability of these publications may be obtained from:

SCIENTIFIC AND TECHNICAL INFORMATION OFFICE
NATIONAL AERONAUTICS AND SPACE ADMINISTRATION
Washington, D.C. 20546